frontiers | Research Topics

Case reports in PET imaging 2023

Edited by
Carmelo Caldarella, Ramin Sadeghi and Matteo Bauckneht

Published in
Frontiers in Medicine

ISSN 1664-8714
ISBN 978-2-8325-5197-4
DOI 10.3389/978-2-8325-5197-4

About Frontiers

Frontiers is more than just an open access publisher of scholarly articles: it is a pioneering approach to the world of academia, radically improving the way scholarly research is managed. The grand vision of Frontiers is a world where all people have an equal opportunity to seek, share and generate knowledge. Frontiers provides immediate and permanent online open access to all its publications, but this alone is not enough to realize our grand goals.

Frontiers journal series

The Frontiers journal series is a multi-tier and interdisciplinary set of open-access, online journals, promising a paradigm shift from the current review, selection and dissemination processes in academic publishing. All Frontiers journals are driven by researchers for researchers; therefore, they constitute a service to the scholarly community. At the same time, the *Frontiers journal series* operates on a revolutionary invention, the tiered publishing system, initially addressing specific communities of scholars, and gradually climbing up to broader public understanding, thus serving the interests of the lay society, too.

Dedication to quality

Each Frontiers article is a landmark of the highest quality, thanks to genuinely collaborative interactions between authors and review editors, who include some of the world's best academicians. Research must be certified by peers before entering a stream of knowledge that may eventually reach the public - and shape society; therefore, Frontiers only applies the most rigorous and unbiased reviews. Frontiers revolutionizes research publishing by freely delivering the most outstanding research, evaluated with no bias from both the academic and social point of view. By applying the most advanced information technologies, Frontiers is catapulting scholarly publishing into a new generation.

What are Frontiers Research Topics?

Frontiers Research Topics are very popular trademarks of the *Frontiers journals series*: they are collections of at least ten articles, all centered on a particular subject. With their unique mix of varied contributions from Original Research to Review Articles, Frontiers Research Topics unify the most influential researchers, the latest key findings and historical advances in a hot research area.

Find out more on how to host your own Frontiers Research Topic or contribute to one as an author by contacting the Frontiers editorial office: frontiersin.org/about/contact

Case reports in PET imaging 2023

Topic editors

Carmelo Caldarella — Fondazione Policlinico Universitario A. Gemelli IRCCS, Italy

Ramin Sadeghi — Mashhad University of Medical Sciences, Iran

Matteo Bauckneht — University of Genoa, Italy

Citation

Caldarella, C., Sadeghi, R., Bauckneht, M., eds. (2024). *Case reports in PET imaging 2023*. Lausanne: Frontiers Media SA. doi: 10.3389/978-2-8325-5197-4

Table of contents

frontiers | Frontiers in Medicine

TYPE Editorial
PUBLISHED 10 July 2024
DOI 10.3389/fmed.2024.1455227

OPEN ACCESS

EDITED AND REVIEWED BY
Giorgio Treglia,
Ente Ospedaliero Cantonale (EOC), Switzerland

*CORRESPONDENCE
Carmelo Caldarella
carmelo.caldarella@policlinicogemelli.it

RECEIVED 26 June 2024
ACCEPTED 27 June 2024
PUBLISHED 10 July 2024

CITATION
Caldarella C, Bauckneht M and Sadeghi R (2024) Editorial: Case reports in PET imaging 2023. *Front. Med.* 11:1455227. doi: 10.3389/fmed.2024.1455227

Editorial: Case reports in PET imaging 2023

Carmelo Caldarella[1]*, Matteo Bauckneht[2,3] and Ramin Sadeghi[4]

[1]Nuclear Medicine Unit, Dipartimento di Diagnostica per Immagini e Radioterapia Oncologica, Fondazione Policlinico Universitario Agostino Gemelli IRCCS, Rome, Italy, [2]Nuclear Medicine, IRCCS Ospedale Policlinico San Martino, Genoa, Italy, [3]Department of Health Sciences (DISSAL), University of Genoa, Genoa, Italy, [4]Nuclear Medicine Research Center, Mashhad University of Medical Sciences, Mashhad, Iran

KEYWORDS

case report, PET-CT imaging, uncommon disease, diagnostic performances, ^{18}F-FDG

Editorial on the Research Topic
Case reports in PET imaging 2023

In recent years, the increasing need for early diagnosis, precise disease staging/restaging and patient-tailored treatment has highlighted the benefits of using advanced hybrid Nuclear Medicine imaging, such as Positron Emission Tomography-Computed Tomography (PET-CT) in clinical practice. Its ability to simultaneously collect functional and anatomical information and to detect pathology without concurrent morphological alterations allows it to guide the clinical management of patients and is of increasing interest in clinical research. This Research Topic includes 14 case reports that highlight the role of PET-CT in patients with uncommon pathological conditions as a valuable tool for differential diagnosis, staging/restaging, guiding therapeutic strategy, or introducing possible developments in acquisition techniques that may be suitable for the critically ill patient.

The incidence of renal tumors has been increasing worldwide in recent years, with an estimated 400,000 new cases annually (1): the most common histotypes are renal clear cell carcinoma (RCC) and urothelial carcinoma. In this Research Topic, an uncommon case of Xp11.2 translocation/TFE3 gene fusion-associated RCC is presented in which ^{18}F-FDG PET-CT was used to detect multiple retroperitoneal lymph nodes and was used to exclude disease recurrence and metastasis in long-term post-surgery follow-up (Huang, Peng et al.). ^{18}F-FDG PET-CT may exhibit high uptake in other rare malignant kidney diseases, such as myxoid liposarcoma, a soft-tissue sarcoma associated with the chromosomal translocation $t_{(12:16)}$ (q13:p11) (2, 3), which rarely arises predominantly in the kidney: in one case report, ^{18}F-FDG PET-CT was used to stage primary renal myxoid liposarcoma, demonstrating disease extension beyond the kidney with pancreatic body involvement, and excluding distant metastases (Huang, Chao et al.).

Uncommon malignancies may pose a significant challenge due to unpredictable behavior and unusual metastatic spread, which in most cases is more extensive than seen on morphological imaging. It is well known that the extent and activity of metastatic involvement as shown by ^{18}F-FDG PET-CT has an impact on treatment response, recurrence risk and, ultimately, patient prognosis (4–9).

This is relevant for therapeutic schemes that include immune system-regulating drugs such as pembrolizumab or nivolumab. In this Research Topic, an exceptionally uncommon case of non-gestational choriocarcinoma is presented, in which ^{18}F-FDG PET-CT confirmed metastatic spread to lungs, brain, bone, and retroperitoneal lymph nodes, with markedly increased uptake; the patient was treated with pembrolizumab, although with serious adverse effects and an inadequate response, leading to a rapid increase in the size of the lung and brain lesions, and ultimately to the patient's death only 5 months after diagnosis (Huang, Zheng, Bao et al.). In another paper, ^{18}F-FDG PET-CT performed for restaging in an operated post-pubertal testicular teratoma revealed increased uptake at the edges of an irregular mass below the left renal hilum. The lesion exhibited low uptake in the center due to necrosis (a marker of aggressiveness), but no other disease sites were found. The patient was then re-operated, and despite initial PET-CT evidence of multi-site abdominal-pelvic progression after surgery, he showed a complete metabolic response on a subsequent PET-CT scan (Jiao et al.).

Attention should be paid to patients undergoing therapy with immune checkpoint inhibitors since pseudo-progression (increase in uptake/size by known lesions or appearance of new lesions and subsequent response) may complicate the evaluation of treatment efficacy. A case of unresectable liver recurrence of uveal melanoma treated with pembrolizumab, and long-term follow-up ^{18}F-FDG PET-CT is published in this Research Topic. The patient ultimately showed a dramatic response to pembrolizumab after 28 months of therapy, despite three episodes of pseudo-progression which appeared on ^{18}F-FDG PET-CT as increased uptake in the known liver lesion and the appearance of other liver lesions (Amrane et al.). This points to the need for new response criteria, such as iPERCIST and imPERCIST, which reduce the risk of overdiagnosis (10, 11).

PET-CT plays a role in the staging of rare malignancies by detecting distant diseases. In this Research Topic, a case of primary intracardiac diffuse large B-cell lymphoma is presented: the patient exhibited multiple nodular soft tissue density lesions in the heart and pericardium with increased ^{18}F-FDG uptake, and multiple lymph nodes with a variable increase in ^{18}F-FDG uptake in the mediastinum, left axilla and near the left kidney (Huang Z. et al.). Moreover, the distribution of an uncommon malignancy may mimic another more frequently observed condition, as illustrated by the case of a 57-year-old woman complaining of dizziness and headaches, with multiple sites of bone destruction in the skull, spine and pelvis on MRI, and multiple ^{18}F-FDG-avid foci throughout the skeleton (including the sternum, bilateral clavicles, scapulae and ribs). This distribution, in the absence of a primary tumor, was consistent with multiple myeloma; however, histology of the most active skull lesion revealed a multicentric primary angiosarcoma of the bone, an exceptionally unusual occurrence (Huang, Xiao et al.). Moreover, an uncommon benign condition may be the first clinical manifestation of a common malignant disease, as in the case of a woman with retroperitoneal fibrosis and renal insufficiency, associated with a histologic finding of breast cancer metastasis in the right kidney: as morphological imaging failed to detect the primary lesion, ^{18}F-FDG PET-CT was performed which revealed bilateral breast cancer (histologically confirmed as lobular carcinoma) with bone, lymph node and kidney metastases, thus underlying the advantages of functional imaging (Song et al.). The whole-body performance of PET-CT can also be highlighted in some benign conditions: in particular, in this Research Topic a case of sporadic schwannomatosis is reported, in which PET-CT revealed an uncommon involvement of the lumbar spinal canal, not seen on MRI, and a correlation between ^{18}F-FDG uptake and histological characteristics (Li et al.).

Transplantation is a well-recognized treatment for many severe diseases and the only chance for survival when irreversible damage to vital functions occurs; however, immunosuppression is required to avoid rejection, which can lead to a wide spectrum of complications, either infectious, tumoral or non-neoplastic lymphoproliferative ones. In this context, two papers in this Research Topic address the role of ^{18}F-FDG PET-CT in detecting and monitoring two rare post-transplant complications. Specifically, in a patient with blastic plasmacytoid dendritic cell neoplasm (BPDCN) involving the left cheek, lymph nodes and bone marrow, PET-CT performed after allogeneic hematopoietic stem cell transplantation and immunosuppressive therapy revealed multiple ^{18}F-FDG-avid lymph nodes in the chest and abdomen, not seen on a pre-treatment scan, and the disappearance of known BPDCN lesions. A biopsy of the most ^{18}F-FDG-avid mesenteric lesion revealed a post-transplant lymphoproliferative disorder. This demonstrated the potential of ^{18}F-FDG PET-CT in detecting and monitoring such severe and exceptionally rare conditions, and in suggesting a lesion for biopsy (Chen et al.). The other case highlights the role of ^{18}F-FDG PET-CT in detecting three complications that occurred sequentially in the same patient after renal transplantation: the first was a multifocal diffuse large B-cell lymphoma in the liver (without other disease sites on PET-CT); then, during chemotherapy for the lymphoma, an ^{18}F-FDG-active bronchial thickening was revealed to be aspergillosis; finally, after successful antifungal treatment ^{18}F-FDG PET-CT revealed a necrotizing granulomatous inflammation in the right vastus lateralis. Such complications would not have been detected without functional imaging (Huang, Zheng, Zhang et al.).

The liver is a typical site of metastasis, especially for gastrointestinal malignancies, whereas primary hepatic malignancies are less common and are mostly represented by hepatocellular carcinoma (HCC), accounting for more than 800,000 deaths annually (12). However, much more unusual pathological entities can occur in the liver, as reported in two articles in which PET-CT was useful for lesion characterization and staging. In particular, ^{18}F-FDG PET-CT excluded distant disease in a patient with an incidentally found liver lesion suspected of being HCC; however, immunohistochemistry revealed that the lesion was a peri-vascular epithelioid tumor, a mesenchymal malignancy that only rarely involves the liver primarily (Yang et al.). Somatostatin receptor ligands are routinely used in PET-CT evaluation of patients with neuroendocrine tumors (NETs), with better performance than ^{18}F-FDG due to more specific uptake and a higher lesion-to-background ratio; the liver is usually involved by metastases, while primary hepatic NETs are extremely rare (only 0.8% of all NETs) (13). In the case of a woman with an incidentally found liver mass, suspected of

metastatic malignant tumor, ^{18}F-FDG PET-CT showed uptake in two liver lesions and multiple lymph nodes in the hepatogastric ligament, therefore raising the suspicion of HCC. However, since A-fetoprotein was normal, [^{18}F]Al-F-octreotide PET-CT, an emerging approach for somatostatin receptor functional imaging, was performed and showed even higher uptake than ^{18}F-FDG in liver lesions and lymph nodes, which were subsequently confirmed as a primary hepatic NET with lymph node metastases (Zhang et al.).

Finally, recent advances in PET-CT technology, such as long-axial field-of-view (LAFOV) which result in a dramatic reduction in acquisition time and injected activity (14), may make PET-CT suitable for intensive care unit patients, as demonstrated in the case of Hemophilus influenza sepsis and pericarditis in which LAFOV allowed a 12-min whole-body scan revealing FDG uptake in the pericardial layers, pleura and right knee synovitis (van Snick et al.).

Author contributions

CC: Conceptualization, Methodology, Supervision, Writing – original draft, Writing – review & editing. MB: Conceptualization, Methodology, Supervision, Writing – original draft, Writing – review & editing. RS: Conceptualization, Methodology, Supervision, Writing – original draft, Writing – review & editing.

Funding

The author(s) declare that no financial support was received for the research, authorship, and/or publication of this article.

Acknowledgments

We wish to thank all the authors who contributed articles to this Research Topic and all those who participated as reviewers.

Conflict of interest

The authors declare that the research was conducted in the absence of any commercial or financial relationships that could be construed as a potential conflict of interest.

Publisher's note

References

1. Cirillo L, Innocenti S, Becherucci F. Global epidemiology of kidney cancer. *Nephrol Dial Transplant.* (2024) 39:920–8. doi: 10.1093/ndt/gfae036

2. Pérez-Losada J, Pintado B, Gutiérrez-Adán A, Flores T, Bañares-González B, del Campo JC, et al. The chimeric FUS/TLS-CHOP fusion protein specifically induces liposarcomas in transgenic mice. *Oncogene.* (2000) 19:2413–22. doi: 10.1038/sj.onc.1203572

3. Antonescu CR, Tschernyavsky SJ, Decuseara R, Leung DH, Woodruff JM, Brennan MF, et al. Prognostic impact of P53 status, TLS-CHOP fusion transcript structure, and histological grade in myxoid liposarcoma: a molecular and clinicopathologic study of 82 cases. *Clin Cancer Res.* (2001) 7:3977–87.

4. Wen W, Piao Y, Xu D, Li X. Prognostic Value of MTV and TLG of 18F-FDG PET in patients with stage I and II non-small-cell lung cancer: a meta-analysis. *Contrast Media Mol Imaging.* (2021) 2021:7528971. doi: 10.1155/2021/7528971

5. Albano D, Treglia G, Dondi F, Calabrò A, Rizzo A, Annunziata S, et al. 18F-FDG PET/CT maximum tumor dissemination (Dmax) in lymphoma: a new prognostic factor? *Cancers (Basel).* (2023) 15:2494. doi: 10.3390/cancers15092494

6. Evangelista L, Zucchetta P, Moletta L, Serafini S, Cassarino G, Pegoraro N, et al. The role of FDG PET/CT or PET/MRI in assessing response to neoadjuvant therapy for patients with borderline or resectable pancreatic cancer: a systematic literature review. *Ann Nucl Med.* (2021) 35:767–76. doi: 10.1007/s12149-021-01629-0

7. Wen W, Xu D, Piao Y, Li X. Prognostic value of maximum standard uptake value, metabolic tumour volume, and total lesion glycolysis of 18F-FDG PET/CT in patients with malignant pleural mesothelioma: a systematic review and meta-analysis. *Cancer Cell Int.* (2022) 22:60. doi: 10.1186/s12935-022-02482-5

8. Wen W, Xuan D, Hu Y, Li X, Liu L, Xu D. Prognostic value of maximum standard uptake value, metabolic tumor volume, and total lesion glycolysis of positron emission tomography/computed tomography in patients with breast cancer: a systematic review and meta-analysis. *PLoS ONE.* (2019) 14:e0225959. doi: 10.1371/journal.pone.0225959

9. Ayati N, Sadeghi R, Kiamanesh Z, Lee ST, Zakavi SR, Scott AM. The value of 18F-FDG PET/CT for predicting or monitoring immunotherapy response in patients with metastatic melanoma: a systematic review and meta-analysis. *Eur J Nucl Med Mol Imaging.* (2021) 48:428–48. doi: 10.1007/s00259-020-04967-9

10. Goldfarb L, Duchemann B, Chouahnia K, Zelek L, Soussan M. Monitoring anti- PD-1-based immunotherapy in non-small cell lung cancer with FDG PET: introduction of iPERCIST. *EJNMMI Res.* (2019) 9:8. doi: 10.1186/s13550-019-0473-1

11. Guan Y, Feng D, Yin B, Li K, Wang J. Immune-related dissociated response as a specific atypical response pattern in solid tumors with immune checkpoint blockade. *Ther Adv Med Oncol.* (2022) 14:17588359221096877. doi: 10.1177/17588359221096877

12. Oh JH, Jun DW. The latest global burden of liver cancer: a past and present threat. *Clin Mol Hepatol.* (2023) 29:355–57. doi: 10.3350/cmh.2023.0070

13. Strosberg JR, Halfdanarson TR, Bellizzi AM, Chan JA, Dillon JS, Heaney AP, et al. The north American neuroendocrine tumor society consensus guidelines for surveillance and medical management of midgut neuroendocrine tumors. *Pancreas.* (2017) 46:707–14. doi: 10.1097/MPA.0000000000000850

14. Calderón E, Schmidt FP, Lan W, Castaneda-Vega S, Brendlin AS, Trautwein NF, et al. Image quality and quantitative PET parameters of low-dose [18F]FDG PET in a long axial field-of-view PET/CT scanner. *Diagnostics.* (2023) 13:3240. doi: 10.3390/diagnostics13203240

frontiers | Frontiers in Medicine

TYPE Case Report
PUBLISHED 27 July 2023
DOI 10.3389/fmed.2023.1235843

OPEN ACCESS

EDITED BY
Carmelo Caldarella,
Fondazione Policlinico Universitario A. Gemelli IRCCS, Italy

REVIEWED BY
Apurva Patel,
Gujarat Cancer & Research Institute, India
Romina Grazia Giancipoli,
Agostino Gemelli University Polyclinic (IRCCS), Italy

*CORRESPONDENCE
Lei Kang
✉ kanglei@bjmu.edu.cn

†These authors have contributed equally to this work

RECEIVED 06 June 2023
ACCEPTED 14 July 2023
PUBLISHED 27 July 2023

CITATION
Huang W, Chao F, Zhang Y, Li L, Gao Y, Qiu Y, Gao J and Kang L (2023) Primary renal myxoid liposarcoma with pancreatic invasion on ^{18}F-FDG PET/CT: first case report and literature review.
Front. Med. 10:1235843.
doi: 10.3389/fmed.2023.1235843

Primary renal myxoid liposarcoma with pancreatic invasion on ^{18}F-FDG PET/CT: first case report and literature review

Wenpeng Huang[1†], Fangfang Chao[2†], Yongbai Zhang[1], Liming Li[3], Yuan Gao[1], Yongkang Qiu[1], Jianbo Gao[3] and Lei Kang[1*]

[1]Department of Nuclear Medicine, Peking University First Hospital, Beijing, China, [2]Department of Nuclear Medicine, The First Affiliated Hospital of Zhengzhou University, Zhengzhou, China, [3]Department of Radiology, The First Affiliated Hospital of Zhengzhou University, Zhengzhou, China

Background: Myxoid liposarcoma (MLS) is a rare malignant soft tissue sarcoma that predominantly manifests in the deep soft tissues of the extremities, particularly within the musculature of the thigh. Unlike other types of liposarcoma, MLS demonstrates a propensity for metastasis to atypical sites, including the lung parenchyma, soft tissues, retroperitoneum, mediastinum, breast, liver, thymus, lymph nodes, and bones. The definitive diagnosis primarily relies on histology with HE staining. Imaging modalities such as ultrasound, CT, MRI, and ^{18}F-FDG PET/CT scans serve as valuable tools for tumor identification.

Case report: A 57-year-old man presented with symptoms of abdominal distention and vomiting 1 month ago. Contrast-enhancement CT revealed a heterogeneous hypodense mass in the upper-middle part of the left kidney, displaying irregular morphology and protrusion towards the exterior of the kidney, with abundant blood supply and had a maximum dimension of approximately 10.7 cm × 9.0 cm. Additionally, a rounded soft tissue density was identified in the pancreatic body. Multiplanar reconstruction demonstrated a connection between the pancreatic lesion and the kidney mass. ^{18}F-FDG PET/CT was conducted for staging, revealing significant growth of the lesion in the upper-middle part of the left kidney, extending beyond the kidney and infiltrating the pancreatic body. The lesion demonstrated remarkably high ^{18}F-FDG uptake (SUVmax = 10.2, MTV = 136.13 cm^3, TLG = 484.62). The postoperative pathological examination confirmed the diagnosis of MLS. On the 10th day post-surgery, the patient presented with tumor recurrence and underwent another surgical resection. Unfortunately, during the operation, the patient experienced a sudden cardiac arrest and died.

Conclusion: Renal MLS with invasion into the pancreas is very rare in clinical practice. Due to the limited research on the utilization of ^{18}F-FDG PET/CT in this particular context, given the rarity and low incidence of MLS, its role remains largely unexplored. As PET/CT imaging becomes increasingly prevalent, thorough imaging of disease sites becomes indispensable for the development of treatment protocols and the monitoring of treatment response.

KEYWORDS

myxoid liposarcoma, kidney, pancreas, recurrence, computed tomography, ^{18}F-FDG

Introduction

Malignant tumors of adipocytic origin encompass well-differentiated liposarcoma, myxoid liposarcoma (MLS), dedifferentiated liposarcoma, pleomorphic liposarcoma, and myxoid pleomorphic liposarcoma (1). MLS is a rare malignant soft tissue sarcoma (STS) that accounts for approximately 30% of all liposarcomas and 10% of all STS (2, 3). The incidence of MLS reaches its peak during the fourth and fifth decades of life, affecting both genders equally (4). MLS predominantly manifests in the deep soft tissues of the extremities, particularly within the musculature of the thigh, and exhibits slow growth (5, 6). MLS is a sarcoma associated with a chromosomal translocation *t(12:16) (q13:p11)*, leading to the formation of the FUS-CHOP oncoprotein. This oncoprotein interacts with DNA promoters, causing dysregulation of downstream protein expression (7, 8). Unlike other types of liposarcoma, MLS exhibits a propensity for metastasis to atypical sites, encompassing the lung parenchyma, soft tissues (abdominal or chest wall), retroperitoneum, mediastinum, epidural space, breast, liver, thymus, pancreas, lymph nodes, and bones (9–14). Choosing the appropriate imaging modality is crucial for the accurate diagnosis and effective management of patients with STS (15). Positron emission tomography (PET) is a functional imaging technique that enables the assessment of tumor or physiologic tissue metabolism *in vivo* using positron-emitting radionuclides. Specifically, the uptake of fluorine-18 deoxyglucose (^{18}F-FDG) is utilized to identify the heightened metabolic activity of tumorous cells through glucose metabolism (16). ^{18}F-FDG PET/CT plays a significant role in the staging, restaging, detection of local recurrence and metastatic disease, as well as the prediction of prognosis and assessment of therapeutic response in STS (17, 18).

Here, we present a unique case of MLS of the left kidney invading the pancreas, exhibited a dismal clinical course and prognosis. In addition, we summarized the ^{18}F-FDG PET/CT findings of MLS from the literature in Table 1 (19–29).

Case presentation

A 57-year-old man presented with symptoms of abdominal distention and vomiting 1 month ago and has lost 15 kg since the onset of his illness. Physical examination revealed no abnormalities. Laboratory tests showed elevated levels of D-dimer (0.42 mg/L), fibrinogen (4.95 g/L), and C-reactive protein (141.50 mg/L), while tumor markers were within the normal range. The patient had a history of hypertension for 10 years and paroxysmal supraventricular tachycardia for 1 year.

The patient underwent an abdominal ultrasound examination, which revealed a heterogeneous hypoechoic mass in the upper middle part of the left kidney, measuring approximately 7.8 cm × 7.0 cm with unclear boundaries. Color Doppler flow imaging demonstrated grade II blood flow signal within the mass (Figures 1A,B). Additionally, a cystic solid mass measuring approximately 4.8 cm × 4.4 cm was detected in the posterior part of the pancreas, located immediately adjacent to the superior pole of the left kidney (Figures 1C,D). CT examination revealed a heterogeneous hypodense mass in the upper middle part of the left kidney, exhibiting irregular morphology and protrusion towards the exterior of the kidney, along with blurring of the perirenal fat gap. The lesion measured approximately 7.0 cm × 9.0 cm × 10.7 cm, showing significant enhancement (Figure 1E). The mass displayed rich blood supply, with visible branches of the left renal artery entering the mass (Figure 1F). Additionally, a rounded soft tissue density was identified in the pancreatic body. Multiplanar reconstruction revealed a connection between the pancreatic lesion and the mass in the left kidney (Figures 1G,H). ^{18}F-FDG PET/CT was conducted for lesion staging, demonstrating a prominent growth of a lesion in the upper middle part of the left kidney, extending beyond the kidney and infiltrating the pancreatic body. The lesion exhibited significantly high FDG uptake (SUVmax = 10.2, MTV = 136.13 cm^3, TLG = 484.62) and had a maximum dimension of approximately 6.8 cm × 8.9 cm (Figure 2).

The patient underwent a percutaneous pathology biopsy of the lesion, which resulted in a diagnosis of liposarcoma. Subsequently, the patient underwent surgical resection, revealing a left renal mass with dimensions of approximately 8.0 cm × 7.0 cm × 5.0 cm. The mass exhibited a grayish-yellowish-grayish-red color and a soft texture. Additionally, an exophytic growth of the tumor was observed, invading the pancreatic body, with a pancreatic lesion measuring approximately 6.5 cm × 5.5 cm × 3.0 cm. Hematoxylin and eosin staining of the lesion demonstrated a diffuse distribution of tumor cells, with round cell areas accounting for approximately 10% of the tumor cells. Notably, frequent nuclear atypia and a mucus-like stroma were observed, along with a significant presence of proliferating small vessels and abundant cytoplasm (Figure 3A). Immunohistochemical results exhibited that the MDM2, CD34, Vimentin, S-100, and STAT-6 were positive in tumor cells (Figures 3B–F). The postoperative pathological examination confirmed the diagnosis of myxoid liposarcoma (MLS).

On the 10th day after surgery, the patient presented with symptoms of abdominal distension and vomiting. Physical examination revealed a palpable solid mass in the left upper abdomen, measuring approximately 20 cm × 15 cm, with limited mobility and tenderness upon pressure. Subsequent CT examination confirmed tumor recurrence (Figure 4). Despite the lack of the intended chemotherapy regimen, the patient underwent another surgical resection, revealing a retroperitoneal mass measuring approximately 20 cm × 15 cm. The mass invaded the pancreas, transverse colonic mesentery, duodenum, and spleen. Unfortunately, at the conclusion of the operation, the patient experienced a sudden cardiac arrest and could not be revived despite aggressive resuscitation efforts. The cardiac arrest was considered to be associated with the patient's previous history of cardiac disease.

Discussion

The kidney is an uncommon site for MLS. In our case, MLS originated from the fatty component of the left renal sinus, and its infiltrative growth invaded the pancreas, which is exceptionally rare. The patient presented with symptoms of abdominal distention and vomiting, attributed to the rapid tumor growth exerting pressure on the stomach.

Chromosomal translocations represent the most prevalent molecular abnormalities identified in sarcomas (30). MLS is distinguished by the *t(12:16) (q13:p11)* chromosomal translocation, which occurs in 95% of patients and gives rise to the FUS-CHOP oncoprotein (10). In a minority of cases, the *EWSR1* gene on

TABLE 1 Previous cases of myxoid liposarcoma with ^{18}F-FDG PET/CT.

Case	Authors	Patient sex	Age	Clinical presentation	Primary sites	Max diameter (cm)	Grade	SUVmax	Invasion and metastasis	Management	Prognosis
1	Paladino et al. (19)	F	31	Acute back pain	The left thigh	NA	NA	NA	Vertebrae	Surgery + chemotherapy + radiotherapy + cellular therapy	Alive at 1 y
2	Lunn et al. (20)	F	37 y	NA	Right gluteus medius muscle	NA	II	3.9	NA	NA	NA
3	Lunn et al. (20)	M	48 y	NA	Proximal left thigh, subcutaneous	NA	II	2.2	NA	NA	NA
4	Lunn et al. (20)	M	37 y	NA	Right sartorius muscle	NA	I	2.8	NA	NA	NA
5	Lunn et al. (20)	M	15 y	NA	Proximal left thigh, subcutaneous	NA	I	1.6	NA	NA	NA
6	Lunn et al. (20)	F	42 y	NA	NA	NA	II	4.2	NA	NA	NA
7	Suzuki et al. (21)	F	48 y	NA	Intramuscular	3	NA	0.79	NA	NA	NA
8	Suzuki et al. (21)	M	36 y	NA	Subcutaneous	6	NA	1.29	NA	NA	NA
9	Suzuki et al. (21)	F	39 y	NA	Intermuscular	15	NA	1.9	NA	NA	NA
10	Suzuki et al. (21)	M	36 y	NA	Subcutaneous	9	NA	2.4	NA	NA	NA
11	Suzuki et al. (21)	M	42 y	NA	Intermuscular	22	NA	2.4	NA	NA	NA
12	Suzuki et al. (21)	M	42 y	NA	Intermuscular	16	NA	2.4	NA	NA	NA
13	Suzuki et al. (21)	F	79 y	NA	Intermuscular	25	NA	2.5	NA	NA	NA
14	Suzuki et al. (21)	F	59 y	NA	Intramuscular	17	NA	2.57	NA	NA	NA
15	Suzuki et al. (21)	F	78 y	NA	Subcutaneous	8	NA	3.1	NA	NA	NA
16	Sakamoto et al. (22)	M	43 y	NA	Left leg	NA	NA	NA	Right neck region, the retroperitoneum, lung and vertebrae	Surgery + chemotherapy	Alive at 10 y
17	Baffour et al. (23)	M	37 y	NA	Right sartorius muscle	NA	I	2.8	NA	NA	NA
18	Liu et al. (24)	M	29 y	A small nodule above the umbilicus	The left lobe of the liver	11.0	NA	3.1	Abdomen and pelvic cavities	Chemotherapy	Died after few weeks
19	Kudo et al. (25)	M	52 y	A slowly enlarging, painless mass at the dorsal aspect of the left foot	The deep portion of the plantar aspect of the left foot	8	NA	5.5	Para-aortic lymph node	Surgery + chemotherapy + radiotherapy	NA
20	Ramamurthy et al. (26)	F	53	Shortness of breath, orthopnea, a dry cough, and a low-grade intermittent fever	Right atrium	5.8	NA	3.4	Multiple lymph nodes and abdomen areas	NA	NA
21	Schwab et al. (27)	F	65	Low back pain	Popliteal	NA	III	Non-elevated FDG uptake in metastasis	The second lumbar vertebrae	Surgery + radiotherapy	Died
22	Shivdasani et al. (28)	F	56	A large painless swelling in posterior aspect of the left thigh	Left thigh	11	NA	5	None	Surgery + radiotherapy	Alive
23	Ozguven et al. (29)	M	48	NA	Left thigh	NA	NA	4.1	Pelvis, paravertebra, right gluteal region, and mesenteric region of abdomen	Surgery + chemotherapy	Alive at 3 y

NA, not available.

10.3389/fmed.2023.1235843

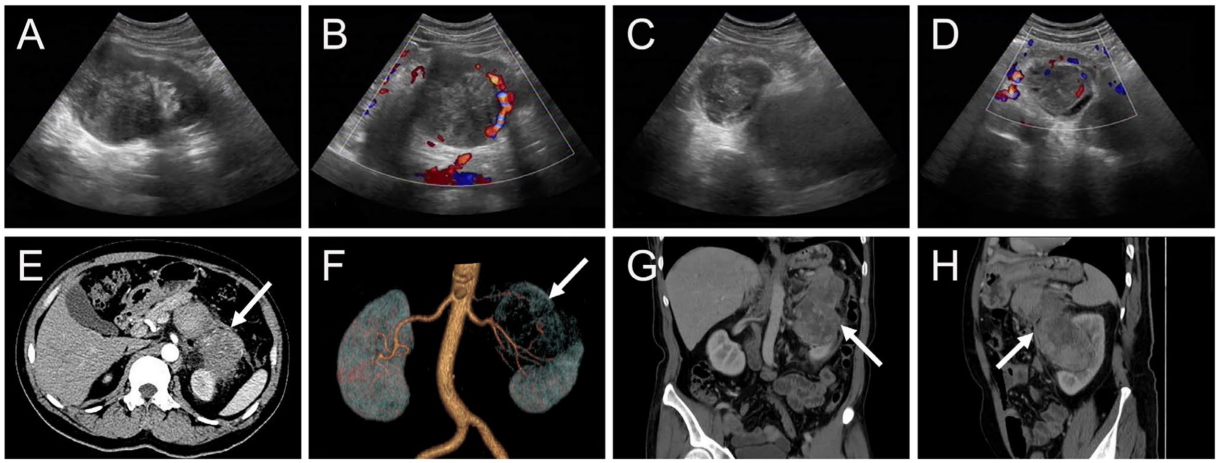

FIGURE 1
Ultrasound and contrast-enhanced computed tomography (CT) images of myxoid liposarcoma (MLS) of the left kidney invading the pancreas. **(A,B)** A heterogeneous hypoechoic mass measuring approximately 7.8 cm × 7.0 cm was observed in the upper middle part of the left kidney with indistinct borders. Color Doppler flow imaging (CDFI) revealed the presence of grade II flow signal within the mass. **(C,D)** Additionally, a cystic solid mass measuring approximately 4.8 cm × 4.4 cm was identified in the posterior part of the pancreas, immediately adjacent to the superior pole of the left kidney. CDFI indicated the presence of grade I blood flow signal within the mass. **(E)** The arterial phase transverse CT image depicted a protruding mass in the upper middle part of the left kidney, exhibiting extrarenal growth (long arrows), blurring of the perirenal fat gap, and significant enhancement (76 HU). **(F)** A volume rending (VR) image demonstrated abundant blood supply to the mass, with multiple branches of the left renal artery entering the lesion. **(G,H)** Coronal and sagittal images obtained from the venous phase displayed invasion of the pancreas by the left kidney mass (98 HU).

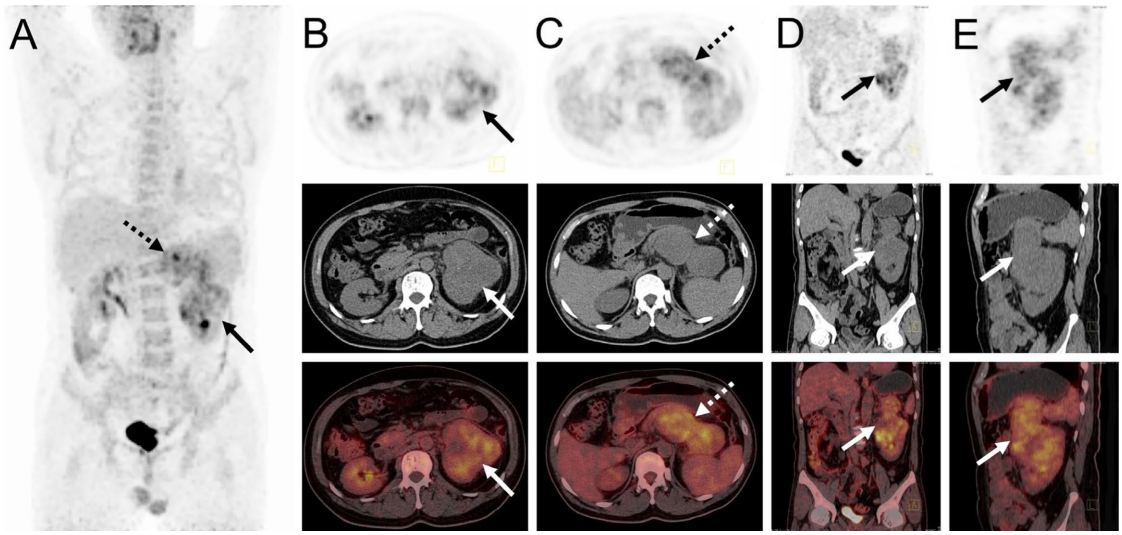

FIGURE 2
^{18}F-FDG PET/CT images of myxoid liposarcoma of the left kidney invading the pancreas. **(A)** The anteroposterior 3-dimensional maximum intensity projection image (MIP) revealed increased metabolic activity in the left kidney (long arrows) and the pancreatic body region (dashed arrows). **(B)** Transverse images exhibited irregular morphology of the left kidney, accompanied by significantly high FDG uptake (SUVmax = 9.3). **(C)** Transverse images showed a pancreatic body lesion with significantly high FDG uptake (SUVmax = 10.2). **(D,E)** Coronal and sagittal images demonstrated an extra-renal protrusion of the left renal lesion and invasion of the pancreas.

chromosome 22 may be implicated, resulting in the *EWSR1-DDIT3* fusion. The diagnosis of MLS relies on histopathological features, which include a nodular growth pattern characterized by a combination of uniform non-lipogenic cells and small lipoblasts exhibiting a signet-ring appearance. These cells are found within a prominent myxoid stroma that is characterized by an abundance of hyaluronic acid and distinctive plexiform vasculature (31). Occasionally, metaplastic cartilaginous and osseous elements may be observed. High-grade MLS is defined as tumors in which the round cell component constitutes over 5% of the total tumor (3). While immunohistochemistry is not essential for the differential diagnosis, molecular investigations should be performed to explore specific mutations. In this case, both MDM2 and CD34 were positive, and the definitive diagnosis was primarily based on HE-stained histology.

The diagnosis of MLS poses an enduring challenge (26). Imaging modalities, including ultrasound, CT, MRI, and PET scans, serve as

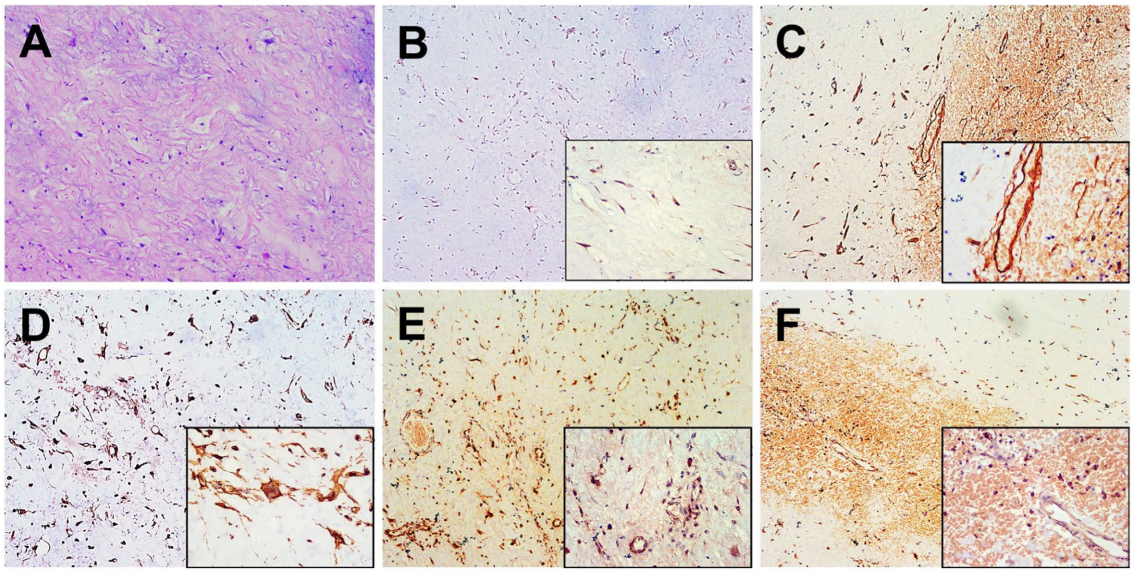

FIGURE 3
Histopathological and immunohistochemical images. **(A)** Hematoxylin–eosin (HE) staining (magnification ×100) showed a diffuse distribution of tumor cells and a mucus-like stroma, along with a significant presence of proliferating small vessels and abundant cytoplasm. Immunohistochemistry showed that the short spindle cells were positive for MDM2 **(B)**, CD34 **(C)**, Vimentin **(D)**, S-100 **(E)** and STAT-6 **(F)** was observed to be positive of the tumor cells (magnification ×40 and ×200).

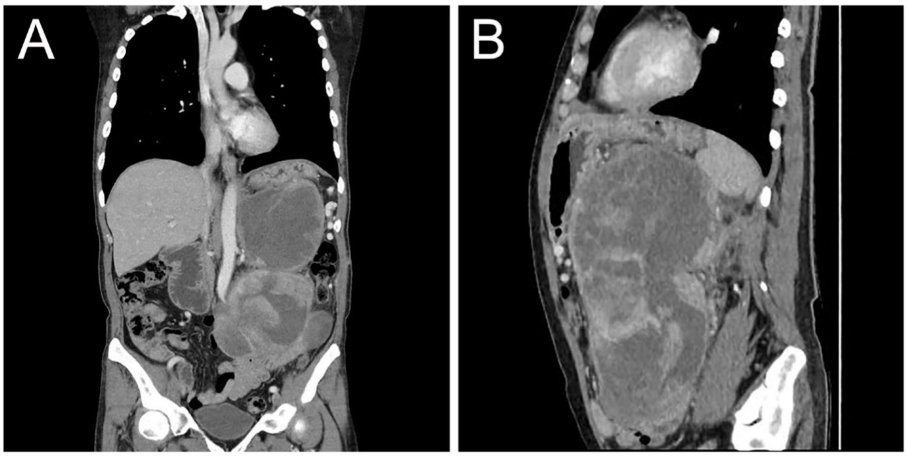

FIGURE 4
Postoperative contrast-enhanced CT images showed recurrence of MLS. Coronal **(A)** and sagittal **(B)** images obtained from the venous phase showed moderate inhomogeneous enhancement of the recurrent tumor in the abdominal cavity with compression and displacement of adjacent organs.

invaluable tools for tumor identification (32). However, there is currently no established standard regarding the timing and type of imaging surveillance in MLS (9). MLS is distinguished by its distinct pattern of metastatic spread, underscoring the importance of detecting metastatic disease to determine prognosis and guide management decisions (5). In our case, the CT features of MLS included an extra-renal distending, infiltrative growth invading the pancreas with cystic necrosis. Multiple renal artery branches were observed entering the mass, consistent with the pathology of a mucus-like interstitial stroma rich in vascular structures, thereby demonstrating noticeable enhancement. While the presence of fat content is a characteristic feature of MLS, histologically, the mucus component predominates and the fat content is minimal. Consequently, the fat component was not distinctly evident on CT in this particular case. Several studies have documented the substantial clinical efficacy of ^{18}F-FDG PET/CT in the initial diagnosis, staging, biopsy site selection, restaging, and prediction of prognosis and response to therapy in the management of soft tissue sarcomas (33–37). We have summarized the previously reported manifestations of MLS using ^{18}F-FDG PET/CT in Table 1 (19–29), which revealed low ^{18}F-FDG activity ranging from (0.79 to 5.5, median, 2.535). The utility of FDG PET/CT in tumor follow-up has been questioned in some reports (16, 18). However, our case demonstrates a notable ^{18}F-FDG uptake associated with a high-grade pathology (with at least a 10% round cell component), showing increased ^{18}F-FDG uptake by round cells. A unique advantage of ^{18}F-FDG PET/CT was its ability to confirm that the tumor in our case

originated from the renal sinus, with direct invasion of the pancreas, thereby excluding the diagnosis of metastatic MLS.

Renal MLS should be differentiated from clear cell renal cell carcinoma (RCC) and renal leiomyosarcoma (RLMS). Clear cell RCC represents approximately 75%–80% of all cases of renal cell carcinoma and originates from the epithelium of the proximal tubule. Typically, clear cell RCC manifests as a heterogeneous mass in the renal cortex, characterized by rapid enhancement followed by contrast wash-out (38, 39). On MRI, T1WI demonstrates iso-or hypo-signal intensity, while T2WI shows inhomogeneous high signal (40, 41). Additionally, there is high ^{18}F-FDG uptake on PET/CT (42). RLMS is an aggressive mesenchymal tumor that typically originates from the smooth muscle cells of the intrarenal blood vessels or the renal pelvis (43). CT scans reveal isointensity or slight hyperintensity, along with delayed or persistent enhancement. Tumors frequently exhibit external extension, easily encircling and infiltrating the inferior vena cava, while also showing a tendency to form tumor emboli and develop distant lymph node metastasis. MRI can provide additional insight into the tumor composition, elucidating hemorrhage and necrosis at different stages. On T1WI, the tumor shows iso-signal intensity, while on T2WI, there is distinct hypointensity (44). Furthermore, ^{18}F-FDG PET/CT demonstrates increased uptake (45). Therefore, from an imaging perspective, our case is not easily distinguishable from clear cell RCC and RLMS, necessitating a reliance on pathological diagnosis.

The utility of ^{18}F-FDG PET in evaluating liposarcomas has been well-established. According to a meta-analysis conducted by Ioannidis and Lau (46), which included 15 studies comprising 441 soft-tissue tumors, PET/CT demonstrated positive results in all intermediate-and high-grade liposarcomas (95% confidence interval 97.3–100). Brenner et al. (47) discovered that SUVmax has the potential to be clinically useful for risk stratification and patient management in liposarcoma. In their study, the SUVmax for MLS was determined to be 3.5 ± 1.5, and a tumor SUVmax exceeding the group mean value of 3.6 was significantly associated with reduced disease-free survival and served as an indicator for identifying patients at a high risk of developing early local recurrences or metastases. ^{18}F-FDG PET/CT plays a significant role in determining treatment and follow-up strategies in MLS by detecting early metastatic disease and highlighting primary and metastatic soft tissue sites (19, 48). Ozguven et al. (29) performed ^{18}F-FDG PET/CT for restaging a patient with MLS, revealing multiple metastases in the mesenteric region. This finding led to a change in the therapeutic management, with the addition of systemic chemotherapy to the wide surgical excision of the gluteal mass. Yokouchi et al. (49) reported the detection of a solitary metastatic breast tumor arising from MLS of the lower limbs using ^{18}F-FDG PET/CT. Liu et al. (24) utilized ^{18}F-FDG PET/CT for a comprehensive evaluation of primary hepatic MLS, confirming its origin and ruling out a metastatic diagnosis. Additionally, ^{18}F-FDG PET/CT may serve as a valuable non-invasive modality for malignant grading and differentiating between subtypes of liposarcoma. Suzuki et al. (21) demonstrated that the mean ^{18}F-FDG SUVs of MLS and other types of liposarcoma were significantly higher than those of well-differentiated liposarcoma by two-and three-fold, respectively. These accumulation rates were remarkably well related to their biological malignant grades.

Several prognostic factors have been identified in MLS, including age over 45 years, tumor size exceeding 10 cm, round cell differentiation exceeding 5%, and the presence of tumor necrosis, all of which are associated with a poor prognosis (50). Surgical resection remains the primary treatment option for MLS (51–53), with the resection margin playing a crucial role in patient survival (54). Inadequate excision is considered the primary cause of local recurrence. Both radiotherapy and chemotherapy are employed in the management of MLS (55, 56). Radiotherapy is administered both pre-and post-operatively for early-stage disease and for palliative purposes in cases of metastatic disease. Chemotherapy is primarily utilized for palliation in cases of metastatic disease. A phase II clinical trial investigating neoadjuvant trabectedin in patients with advanced localized MLS demonstrated significant efficacy and minimal toxicity, using a dosage of 1.5 mg/m^2 trabectedin every 3 weeks (57). Unfortunately, our patient experienced early recurrence, had not yet undergone chemotherapy, and succumbed to the disease following re-surgical resection.

Conclusion

In conclusion, we present an exceptionally rare case of MLS involving the left kidney with invasion into the pancreas. Due to the limited research on the utilization of ^{18}F-FDG PET/CT in this particular context, given the rarity and low incidence of MLS, its role remains largely unexplored. However, as PET/CT imaging becomes increasingly prevalent, a comprehensive assessment of disease sites becomes indispensable for the development of treatment protocols and the monitoring of treatment response. This capability also enables the exploration of various interventions in terms of their type and timing, with the potential to enhance patient outcomes and mitigate morbidity and mortality.

Data availability statement

The original contributions presented in the study are included in the article/supplementary material, further inquiries can be directed to the corresponding author.

Ethics statement

Written informed consent was obtained from the individual(s) for the publication of any potentially identifiable images or data included in this article.

Author contributions

WH and FC: manuscript draft and editing. LL and YG: imaging data collection. YZ and YQ: imaging data analysis. JG: supervision. LK: writing-review and editing. All authors contributed to the article and approved the submitted version.

Funding

This work was supported by the National Natural Science Foundation of China (82171970), the Beijing Science Foundation for Distinguished Young Scholars (JQ21025), the Beijing Municipal Science & Technology Commission (Z221100007422027), National

High Level Hospital Clinical Research Funding (Interdisciplinary Research Project of Peking University First Hospital, 2023IR17).

Conflict of interest

The authors declare that the research was conducted in the absence of any commercial or financial relationships that could be construed as a potential conflict of interest.

Publisher's note

References

1. Creytens D. What's new in adipocytic neoplasia? *Virchows Arch*. (2020) 476:29–39. doi: 10.1007/s00428-019-02652-3

2. Conyers R, Young S, Thomas DM. Liposarcoma: molecular genetics and therapeutics. *Sarcoma*. (2011) 2011:483154. doi: 10.1155/2011/483154

3. Saifuddin A, Andrei V, Rajakulasingam R, Oliveira I, Seddon B. Magnetic resonance imaging of trunk and extremity myxoid liposarcoma: diagnosis, staging, and response to treatment. *Skelet Radiol*. (2021) 50:1963–80. doi: 10.1007/s00256-021-03769-w

4. Huh WW, Yuen C, Munsell M, Hayes-Jordan A, Lazar AJ, Patel S, et al. Liposarcoma in children and young adults: a multi-institutional experience. *Pediatr Blood Cancer*. (2011) 57:1142–6. doi: 10.1002/pbc.23095

5. Conill C, Setoain X, Colomo L, Palacín A, Combalia-Aleu A, Pomés J, et al. Diagnostic efficacy of bone scintigraphy, magnetic resonance imaging, and positron emission tomography in bone metastases of myxoid liposarcoma. *J Magn Reson Imaging*. (2008) 27:625–8. doi: 10.1002/jmri.21298

6. Ho TP. Myxoid liposarcoma: how to stage and follow. *Curr Treat Options in Oncol*. (2023) 24:292–9. doi: 10.1007/s11864-023-01064-5

7. Pérez-Losada J, Pintado B, Gutiérrez-Adán A, Flores T, Bañares-González B, del Campo JC, et al. The chimeric FUS/TLS-CHOP fusion protein specifically induces liposarcomas in transgenic mice. *Oncogene*. (2000) 19:2413–22. doi: 10.1038/sj.onc.1203572

8. Antonescu CR, Tschernyavsky SJ, Decuseara R, Leung DH, Woodruff JM, Brennan MF, et al. Prognostic impact of P53 status, TLS-CHOP fusion transcript structure, and histological grade in myxoid liposarcoma: a molecular and clinicopathologic study of 82 cases. *Clin Cancer Res*. (2001) 7:3977–87.

9. Visgauss JD, Wilson DA, Perrin DL, Colglazier R, French R, Mattei J-C, et al. Staging and surveillance of myxoid liposarcoma: follow-up assessment and the metastatic pattern of 169 patients suggests inadequacy of current practice standards. *Ann Surg Oncol*. (2021) 28:7903–11. doi: 10.1245/s10434-021-10091-1

10. Antonescu CR, Elahi A, Healey JH, Brennan MF, Lui MY, Lewis J, et al. Monoclonality of multifocal myxoid liposarcoma: confirmation by analysis of TLS-CHOP or EWS-CHOP rearrangements. *Clin Cancer Res*. (2000) 6:2788–93.

11. Dürr HR, Rauh J, Baur-Melnyk A, Knösel T, Lindner L, Roeder F, et al. Myxoid liposarcoma: local relapse and metastatic pattern in 43 patients. *BMC Cancer*. (2018) 18:304. doi: 10.1186/s12885-018-4226-8

12. Estourgie SH, Nielsen GP, Ott MJ. Metastatic patterns of extremity myxoid liposarcoma and their outcome. *J Surg Oncol*. (2002) 80:89–93. doi: 10.1002/jso.10093

13. Farmer RP, Schowinsky JT, Lindeque BGP. Myxoid liposarcoma of the thigh with metastasis to the left ventricle of the heart: a case report. *JBJS Case Connect*. (2015) 5:e91. doi: 10.2106/JBJS.CC.N.00038

14. Wang D, Wu J, Yu J, Zhang H, Liu H. Solitary pancreatic metastasis of extremity myxoid liposarcoma: a case report and literature review. *BMC Cancer*. (2018) 18:1121. doi: 10.1186/s12885-018-5059-1

15. Ilaslan H, Schils J, Nageotte W, Lietman SA, Sundaram M. Clinical presentation and imaging of bone and soft-tissue sarcomas. *Cleve Clin J Med*. (2010) 77:S2–7. doi: 10.3949/ccjm.77.s1.01

16. Younis MH, Abu-Hijleh HA, Aldahamsheh OO, Abualruz A, Thalib L. Meta-analysis of the diagnostic accuracy of primary bone and soft tissue sarcomas by 18F-FDG-PET. *Med Princ Pract*. (2020) 29:465–72. doi: 10.1159/000505651

17. Gabriel M, Rubello D. 18F-FDG PET-CT in soft tissue sarcomas: staging, restaging, and prognostic value? *Nucl Med Commun*. (2016) 37:3–8. doi: 10.1097/MNM.0000000000000407

18. Lee L, Kazmer A, Colman MW, Gitelis S, Batus M, Blank AT. What is the clinical impact of staging and surveillance PET-CT scan findings in patients with bone and soft tissue sarcoma? *J Surg Oncol*. (2022) 125:901–6. doi: 10.1002/jso.26789

19. Paladino LP, Belzarena AC, Henderson-Jackson E, Joyce DM. Metastatic vertebral lesion mimicking an atypical hemangioma with negative 18F-FDG positron emission tomography-computed tomography. *Radiol Case Rep*. (2019) 14:1401–6. doi: 10.1016/j.radcr.2019.09.008

20. Lunn BW, Littrell LA, Wenger DE, Broski SM. 18F-FDG PET/CT and MRI features of myxoid liposarcomas and intramuscular myxomas. *Skelet Radiol*. (2018) 47:1641–50. doi: 10.1007/s00256-018-3000-y

21. Suzuki R, Watanabe H, Yanagawa T, Sato J, Shinozaki T, Suzuki H, et al. PET evaluation of fatty tumors in the extremity: possibility of using the standardized uptake value (SUV) to differentiate benign tumors from liposarcoma. *Ann Nucl Med*. (2005) 19:661–70. doi: 10.1007/BF02985114

22. Sakamoto A, Fukutoku Y, Matsumoto Y, Harimaya K, Oda Y, Iwamoto Y. Myxoid liposarcoma with negative features on bone scan and [18F]-2-fluoro-2-deoxy-D-glucose-positron emission tomography. *World J Surg Oncol*. (2012) 10:214. doi: 10.1186/1477-7819-10-214

23. Baffour FI, Wenger DE, Broski SM. 18F-FDG PET/CT imaging features of lipomatous tumors. *Am J Nucl Med Mol Imaging*. (2020) 10:74–82.

24. Liu W, Liang W, Peng Z. Positron emission tomography/computed tomography manifestations of primary hepatic myxoid liposarcoma: a case report. *Medicine (Baltimore)*. (2018) 97:e12307. doi: 10.1097/MD.0000000000012307

25. Kudo H, Inaoka T, Tokuyama W, Hiruta N, Nakagawa K, Hayashi A, et al. Round cell liposarcoma arising in the left foot: MRI and PET findings. *Jpn J Radiol*. (2012) 30:852–7. doi: 10.1007/s11604-012-0119-y

26. Thoddi Ramamurthy M, Kumar Balakrishnan V, Sunny S, Rajkumar A, Sundaram S, Krishnamurthy P, et al. Case report: metastatic myxoid liposarcoma arising from the right atrium extends as cardiac tamponade-a rare case of atrial oncology. *Front Cardiovasc Med*. (2022) 9:1046436. doi: 10.3389/fcvm.2022.1046436

27. Schwab JH, Healey JH. FDG-PET lacks sufficient sensitivity to detect myxoid liposarcoma spinal metastases detected by MRI. *Sarcoma*. (2007) 2007:36785–3. doi: 10.1155/2007/36785

28. Shivdasani D, Singh N, Pereira M, Zade A. Unusual asymptomatic fluorodeoxyglucose avid pheochromocytoma in a case of myxoid liposarcoma of the extremity on 18-F fluorodeoxyglucose positron emission tomography-computed tomography. *World J Nucl Med*. (2017) 16:237–9. doi: 10.4103/1450-1147.207275

29. Ozguven S, Aras M, Inanir S. Mesenteric metastases of purely myxoid liposarcoma: an unusual behavior of primary tumor depicted on fludeoxyglucose positron emission tomography/computerized tomography. *Indian J Nucl Med*. (2015) 30:82–3. doi: 10.4103/0972-3919.147556

30. Mertens F, Antonescu CR, Hohenberger P, Ladanyi M, Modena P, D'Incalci M, et al. Translocation-related sarcomas. *Semin Oncol*. (2009) 36:312–23. doi: 10.1053/j.seminoncol.2009.06.004

31. Öz Atalay F, Akyol S, Bozdogan Ö. Primary low grade myxoid liposarcoma of the ovary: a case report and review of literature. *J Obstet Gynaecol Res*. (2020) 46:1921–6. doi: 10.1111/jog.14395

32. von Mehren M, Randall RL, Benjamin RS, Boles S, Bui MM, Ganjoo KN, et al. Soft tissue sarcoma, version 2.2018, NCCN clinical practice guidelines in oncology. *J Natl Compr Cancer Netw*. (2018) 16:536–63. doi: 10.6004/jnccn.2018.0025

33. Li C-P, Liu D-N, Zhou N-N, Tian X-Y, Wang Z, Liu B-N, et al. Prediction of histologic subtype and FNCLCC grade by SUVmax measured on 18F-FDG PET/CT in patients with retroperitoneal Liposarcoma. *Contrast Media Mol Imaging*. (2021) 2021:1–8. doi: 10.1155/2021/7191363

34. Fuglø HM, Jørgensen SM, Loft A, Hovgaard D, Petersen MM. The diagnostic and prognostic value of ^{18}F-FDG PET/CT in the initial assessment of high-grade bone and soft tissue sarcoma. A retrospective study of 89 patients. *Eur J Nucl Med Mol Imaging*. (2012) 39:1416–24. doi: 10.1007/s00259-012-2159-z

35. Kubo T, Furuta T, Johan MP, Ochi M. Prognostic significance of (18)F-FDG PET at diagnosis in patients with soft tissue sarcoma and bone sarcoma; systematic review and meta-analysis. *Eur J Cancer*. (2016) 58:104–11. doi: 10.1016/j.ejca.2016.02.007

36. Lim HJ, Johnny Ong C-A, Tan JW-S, Ching Teo MC. Utility of positron emission tomography/computed tomography (PET/CT) imaging in the evaluation of sarcomas: a systematic review. *Crit Rev Oncol Hematol*. (2019) 143:1–13. doi: 10.1016/j.critrevonc.2019.07.002

37. Shin D-S, Shon O-J, Han D-S, Choi J-H, Chun K-A, Cho I-H. The clinical efficacy of (18)F-FDG-PET/CT in benign and malignant musculoskeletal tumors. *Ann Nucl Med*. (2008) 22:603–9. doi: 10.1007/s12149-008-0151-2

38. Woo S, Kim SH. Differentiation of small, solid renal masses: a pattern recognition approach. *Semin Ultrasound CT MR*. (2017) 38:28–36. doi: 10.1053/j.sult.2016.08.008

39. Razik A, Das CJ, Sharma S. Angiomyolipoma of the kidneys: current perspectives and challenges in diagnostic imaging and image-guided therapy. *Curr Probl Diagn Radiol*. (2019) 48:251–61. doi: 10.1067/j.cpradiol.2018.03.006

40. Jhaveri KS, Elmi A, Hosseini-Nik H, Hedgire S, Evans A, Jewett M, et al. Predictive value of chemical-shift MRI in distinguishing clear cell renal cell carcinoma from non-clear cell renal cell carcinoma and minimal-fat Angiomyolipoma. *AJR Am J Roentgenol*. (2015) 205:W79–86. doi: 10.2214/AJR.14.13245

41. Schieda N, Davenport MS, Pedrosa I, Shinagare A, Chandarana H, Curci N, et al. Renal and adrenal masses containing fat at MRI: proposed nomenclature by the society of abdominal radiology disease-focused panel on renal cell carcinoma. *J Magn Reson Imaging*. (2019) 49:917–26. doi: 10.1002/jmri.26542

42. Takahashi M, Kume H, Koyama K, Nakagawa T, Fujimura T, Morikawa T, et al. Preoperative evaluation of renal cell carcinoma by using 18F-FDG PET/CT. *Clin Nucl Med*. (2015) 40:936–40. doi: 10.1097/RLU.0000000000000875

43. Miller JS, Zhou M, Brimo F, Guo CC, Epstein JI. Primary leiomyosarcoma of the kidney: a clinicopathologic study of 27 cases. *Am J Surg Pathol*. (2010) 34:238–42. doi: 10.1097/PAS.0b013e3181cad8c9

44. Choudhury M, Singh SK, Pujani M, Pathania OP. A case of leiomyosarcoma of kidney clinically and radiologically misdiagnosed as renal cell carcinoma. *Indian J Cancer*. (2009) 46:241–3. doi: 10.4103/0019-509X.52962

45. Makis W, Brimo F, Probst S. Primary renal Leiomyosarcoma presenting with subcutaneous and osseous metastases: staging and follow-up with 18F-FDG PET/CT. *Nucl Med Mol Imaging*. (2018) 52:69–73. doi: 10.1007/s13139-016-0467-0

46. Ioannidis JPA, Lau J. 18F-FDG PET for the diagnosis and grading of soft-tissue sarcoma: a meta-analysis. *J Nucl Med*. (2003) 44:717–24.

47. Brenner W, Eary JF, Hwang W, Vernon C, Conrad EU. Risk assessment in liposarcoma patients based on FDG PET imaging. *Eur J Nucl Med Mol Imaging*. (2006) 33:1290–5. doi: 10.1007/s00259-006-0170-y

48. Ak I, Can C. F-18 FDG PET in detecting renal cell carcinoma. *Acta Radiol*. (2005) 46:895–9. doi: 10.1080/02841850500335002

49. Yokouchi M, Nagano S, Kijima Y, Yoshioka T, Tanimoto A, Natsugoe S, et al. Solitary breast metastasis from myxoid liposarcoma. *BMC Cancer*. (2014) 14:482. doi: 10.1186/1471-2407-14-482

50. Hashimoto K, Nishimura S, Mitani S, Ito T, Akagi M. Myxoid liposarcoma originating in the retroperitoneum with metastasis to the calcaneus: a rare case report and review of literature. *Skelet Radiol*. (2022) 51:2053–8. doi: 10.1007/s00256-022-04028-2

51. Tfayli Y, Baydoun A, Naja AS, Saghieh S. Management of myxoid liposarcoma of the extremity. *Oncol Lett*. (2021) 22:596. doi: 10.3892/ol.2021.12857

52. Hoffman A, Ghadimi MPH, Demicco EG, Creighton CJ, Torres K, Colombo C, et al. Localized and metastatic myxoid/round cell liposarcoma: clinical and molecular observations. *Cancer*. (2013) 119:1868–77. doi: 10.1002/cncr.27847

53. Zheng K, Yu X-C, Xu M, Yang Y. Surgical outcomes and prognostic factors of myxoid liposarcoma in extremities: a retrospective study. *Orthop Surg*. (2019) 11:1020–8. doi: 10.1111/os.12566

54. Kim HS, Lee J, Yi SY, Jun HJ, Choi Y-L, Ahn GH, et al. Liposarcoma: exploration of clinical prognostic factors for risk based stratification of therapy. *BMC Cancer*. (2009) 9:205. doi: 10.1186/1471-2407-9-205

55. Crago AM, Dickson MA. Liposarcoma: multimodality management and future targeted therapies. *Surg Oncol Clin N Am*. (2016) 25:761–73. doi: 10.1016/j.soc.2016.05.007

56. Chowdhry V, Goldberg S, DeLaney TF, Cote GM, Chebib I, Kim J, et al. Myxoid liposarcoma: treatment outcomes from chemotherapy and radiation therapy. *Sarcoma*. (2018) 2018:1–6. doi: 10.1155/2018/8029157

57. Gronchi A, Hindi N, Cruz J, Blay J-Y, Lopez-Pousa A, Italiano A, et al. Trabectedin and radiotherapy in soft tissue sarcoma (TRASTS): results of a phase I study in myxoid liposarcoma from Spanish (GEIS), Italian (ISG), French (FSG) sarcoma groups. *EClinicalMedicine*. (2019) 9:35–43. doi: 10.1016/j.eclinm.2019.03.007

frontiers | Frontiers in Medicine

TYPE Case Report
PUBLISHED 17 August 2023
DOI 10.3389/fmed.2023.1258310

OPEN ACCESS

EDITED BY
Carmelo Caldarella,
Fondazione Policlinico Universitario A. Gemelli IRCCS, Italy

REVIEWED BY
Domenico Albano,
University of Brescia, Italy
Andor W. J. M. Glaudemans,
University Medical Center Groningen, Netherlands

*CORRESPONDENCE
Zhanli Fu
✉ fuzhanli2002@163.com
Meng Liu
✉ louisa_liu@bjmu.edu.cn

†These authors have contributed equally to this work

RECEIVED 13 July 2023
ACCEPTED 31 July 2023
PUBLISHED 17 August 2023

CITATION
Chen J, Zhang X, Ma L, Gao Y, Fu Z and Liu M (2023) ^{18}F-FDG PET/CT findings in a patient with blastic plasmacytoid dendritic cell neoplasm and post-transplant lymphoproliferative disorder after hematopoietic stem cell transplantation: a case report.
Front. Med. 10:1258310.
doi: 10.3389/fmed.2023.1258310

^{18}F-FDG PET/CT findings in a patient with blastic plasmacytoid dendritic cell neoplasm and post-transplant lymphoproliferative disorder after hematopoietic stem cell transplantation: a case report

Jinzhi Chen†, Xi Zhang†, Linlin Ma, Yuan Gao, Zhanli Fu* and Meng Liu*

Department of Nuclear Medicine, Peking University First Hospital, Beijing, China

Background: Blastic plasmacytoid dendritic cell neoplasm (BPDCN) is an extremely rare hematopoietic malignancy, which originating from precursors of plasmacytoid dendritic cells. Allogeneic hematopoietic stem cell transplantation (HSCT) is normally considered in the treatment of BPDCN patients to acquire sustained remission. Post-transplant lymphoproliferative disorder (PTLD) is a group of conditions involving abnormal lymphoid cells proliferation in the context of extrinsic immunosuppression after solid organ transplantation (SOT) or HSCT. Herein, we report a patient with BPDCN, who suffered from PTLD after allogeneic HSCT.

Case presentation: A 66-year-old man was diagnosed with BPDCN, confirmed by pathologic examination after splenectomy. The post-surgery ^{18}F-fluoro-2-deoxy-D-glucose-positron emission tomography/computed tomography (^{18}F-FDG PET/CT) showed multifocal ^{18}F-FDG avidity in the left cheek, lymph nodes and bone marrow. The patient started chemotherapy, followed by allogeneic HSCT and immunosuppressive therapy. Four months after the HSCT, the patient developed intermittent fever and recurrent lymphadenopathy, accompanied with progressively elevated Epstein–Barr virus (EBV)-DNA both in serum and lymphocytes. ^{18}F-FDG PET/CT was performed again and found multiple new enlarged ^{18}F-FDG-avid lymph nodes, while the previous hypermetabolic lesions all disappeared. The pathology of mesenteric lymph node indicated a monomorphic PTLD (diffuse large B-cell lymphoma). Then the immunosuppressive medications were stopped and two cycles of Rituximab were given, and the follow-up CT scan indicated a complete response.

Conclusion: When patients with BPDCN recurred new enlarged lymph nodes after allogeneic HSCT and immunosuppressive therapy, PTLD should be taken into consideration. ^{18}F-FDG PET/CT may provide additional evidence for supporting or refuting the suspicion of PTLD, and suggest lesions accessible for biopsy.

KEYWORDS

blastic plasmacytoid dendritic cell neoplasm, hematopoietic stem cell transplantation, post-transplant lymphoproliferative disorder, ^{18}F-FDG, PET/CT

1. Introduction

Blastic plasmacytoid dendritic cell neoplasm (BPDCN), originating from the precursor of plasmacytoid dendritic cells, is an extremely rare and aggressive hematopoietic malignancy (1). It typically involves skin, lymph nodes and bone marrow, while its exact incidence remains unknown (2). The diagnosis of BPDCN is mainly based on histology, immunohistochemistry, and flow cytometry (3, 4). ^{18}F-fluoro-2-deoxy-D-glucose-positron emission tomography/computed tomography (^{18}F-FDG PET/CT) is helpful in staging of BPDCN (5). Given the highly aggressive clinical behavior, the overall prognosis of BPDCN is poor (6–8). There have been no standard treatments for BPDCN, and leukemia-type chemotherapy followed by allogeneic hematopoietic stem cell transplantation (HSCT) can be considered as a consolidative strategy (9). Post-transplant lymphoproliferative disorder (PTLD) is a group of conditions involving abnormal lymphoid cells proliferation in the context of extrinsic immunosuppression after solid organ transplantation (SOT) or HSCT (10). Herein, we report a patient with BPDCN, who suffered from PTLD after allogeneic HSCT. The unique ^{18}F-FDG PET/CT patterns at the initial diagnosis of BPDCN and at the time of PTLD after HSCT indicated that ^{18}F-FDG PET/CT might be helpful for the differential diagnosis and suggesting lesions accessible for biopsy.

2. Case report

A 66-year-old man presented with continuous fever with the highest temperature of 38.6°C and left upper abdominal pain for 1 month. The laboratory examination showed a progressive decrease of blood platelets, with a minimum of 32×10^9/L. Ultrasound examination showed splenomegaly and multiple enlarged lymph nodes in bilateral supraclavicular regions, bilateral axillas, and bilateral groins. Contrast-enhanced magnetic resonance imaging (MRI) revealed massive splenomegaly with an abnormal signal lesion in the spleen (Figures 1A–D), and multiple enlarged lymph nodes in the hepatic hilum and around the pancreas. Combining the patient's progressive thrombocytopenia and massive splenomegaly, hypersplenism was considered, and splenectomy was performed subsequently. Hematoxylin and eosin (HE)-stained specimens of the splenic lesion revealed diffuse distribution of small to medium monomorphic round cells with moderate cytoplasm and inconspicuous nucleoli, and the result of immunohistochemistry (IHC) showed CD56 (++), CD123 (+), CD4 (++), CD43 (++), which was consistent with BPDCN involving the spleen (Figures 1E–G).

Further physical examination revealed a brown rash on the patient's left cheek (Figure 2A), and ^{18}F-FDG PET/CT was performed for evaluating the systemic involvement of BPDCN. The patient fasted for at least 6 h before PET/CT examination, and his blood sugar concentration on the day of examination was 6.2 mmol/L. PET/CT (Philips Gemini GXL, Philips Medical Systems, United States) scan was performed 60 min after the intravenous administration of ^{18}F-FDG (3.7 MBq/kg body weight, provided by Atom high-tech Co., Ltd., Beijing, China). Image acquisition began with CT for attenuation correction and anatomical reference, using a standardized protocol with a tube voltage of 120 kV, a tube current of 100 mA/s, and a matrix of 512×512. Then PET scan was performed with a matrix of 144×144, 1.5 min per bed position, 8 bed positions.

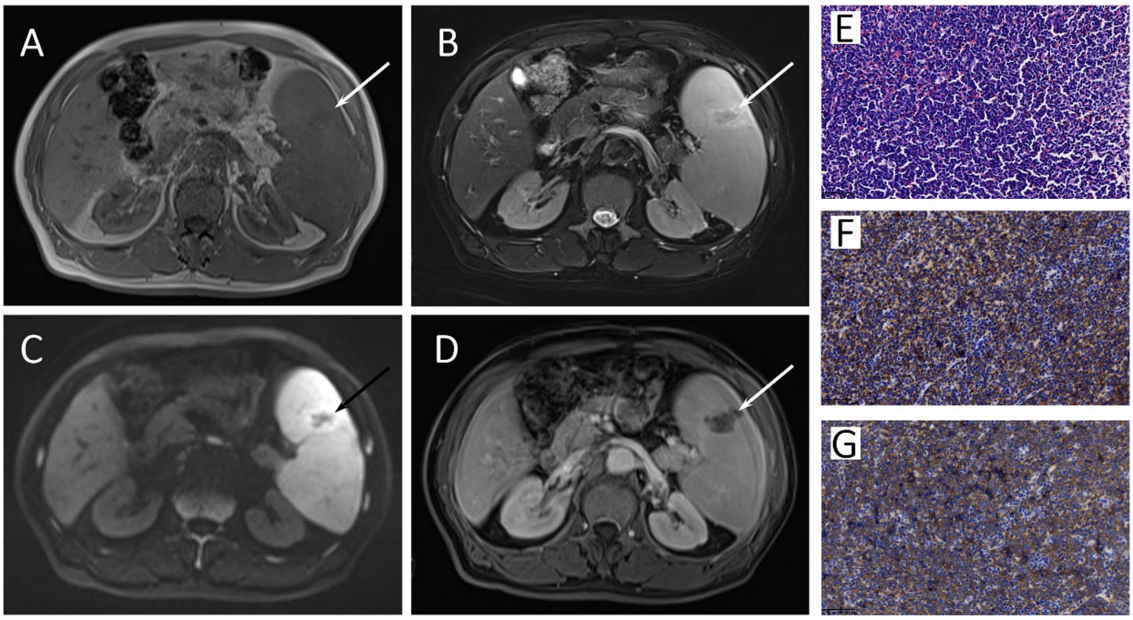

FIGURE 1
The axial image of T1-weighted **(A)**, Fat-suppressed T2-weighted **(B)**, diffusion-weighted **(C)**, and gadolinium-enhanced T1-weighted **(D)** MRI images showed massive splenomegaly with an abnormal signal lesion (arrows) in the spleen. The HE staining specimen of spleen **(E)** showed diffuse distribution of small to medium monomorphic round cells with moderate cytoplasm and inconspicuous nucleoli, and the neoplastic cells showed both positive for CD56 **(F)** and CD123 **(G)** in immunohistochemistry.

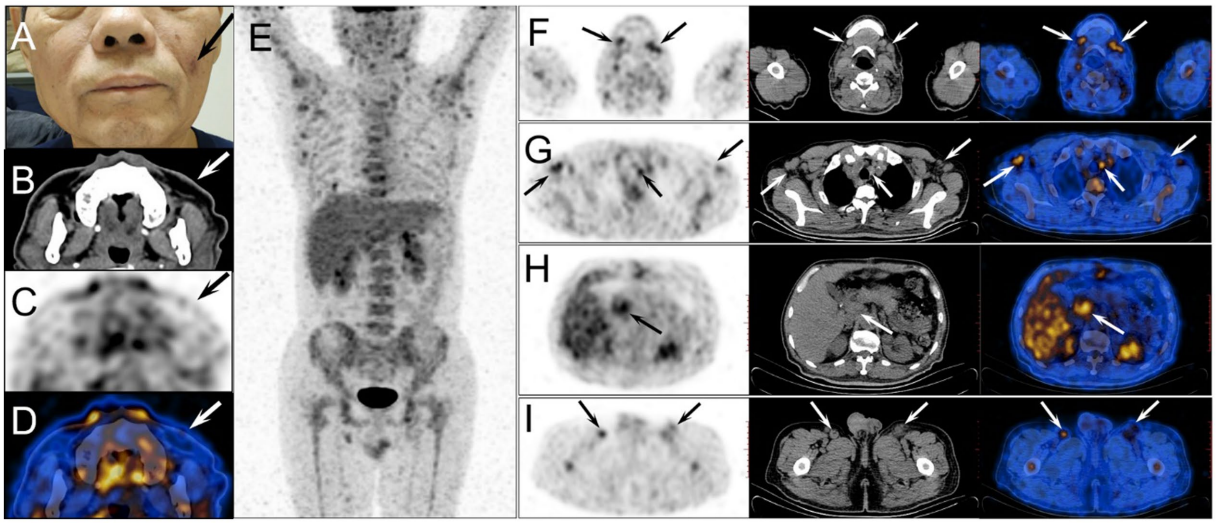

FIGURE 2
The physical examination revealed a brown rash on the patient's left cheek [**(A)**, arrow]. The axial image of head CT revealed slightly skin thickening in the left cheek [**(B)**, arrow], with mild ^{18}F-FDG avidity (SUVmax 1.1) on the corresponding PET [**(C)**, arrow] and PET/CT fusion [**(D)**, arrow] images. The body MIP image **(E)** demonstrated diffuse ^{18}F-FDG uptake in bone marrow (SUVmax 4.0) and multiple metabolic foci as described in the following axial images. On the axial images of PET, CT and PET/CT fusion, multiple enlarged lymph nodes were found in bilateral submaxillary regions **(F)**, bilateral axillas and mediastinum **(G)**, hepatic hilum **(H)**, and bilateral groins **(I)** (arrows), which exhibited varying ^{18}F-FDG avidity with the maximal SUVmax of 4.2 in the left submaxillary lymph nodes.

Pulmonary breath-holding CT was carried out with a tube voltage of 120 kV, a tube current of 100 mA/s. All images were reconstructed by Fusion Viewer software in the Extended Brilliance Workstation (EBW, Philips Medical Systems, United States).

The images revealed slightly skin thickening in the left cheek with mild ^{18}F-FDG avidity with maximum standardized uptake value (SUVmax) of 1.1 (Figures 2B–D), diffuse uptake in the bone marrow with SUVmax of 4.0, and multiple metabolic enlarged lymph nodes with SUVmax of 4.2 (Figures 2E–I). The SUVmax of liver and blood pool was 3.3 and 2.1, respectively. The pathological findings of the left cheek rash, bone marrow, and cervical lymph node were all consistent with BPDCN.

Subsequently, the patient received chemotherapy with one cycle of VDLP (vincristine, daunorubicin, L-asparaginase and prednisone) and three cycles of CHOPE (cyclophosphamide, doxorubicin, vincristine, prednisone, and etoposide). Follow-up ultrasound showed that the previously enlarged lymph nodes disappeared, and bone marrow biopsy showed no abnormal cells. For maintaining a sustained remission, the patient underwent allogeneic HSCT and immunosuppressive therapy.

Four months after HSCT, the patient developed intermittent fever with the highest temperature of 39.0°C. The EBV-DNA both in serum and lymphocytes was gradually increased. All these clues leaded the clinicians to the suspicion of PTLD, but more evidences were required to exclude the acute infection, graft-versus-host disease (GVHD), graft rejection or malignancy relapse. Hence, the patient was referred to a second ^{18}F-FDG PET/CT examination. On the examination day, the patient's fasting blood sugar concentration was 7.5 mmol/L. The images showed multiple new ^{18}F-FDG-avid enlarged lymph nodes in the chest and abdomen with SUVmax of 13.9, while the previous hypermetabolic lesions all disappeared (Figure 3). The SUVmax of liver and blood pool was 4.1 and 2.7, respectively.

Based on the ^{18}F-FDG PET/CT results, a core needle biopsy was performed on the ^{18}F-FDG-avid mesenteric lymph node. The HE result showed diffuse medium-large cell infiltration with nuclear irregularity, and the IHC results showed CD20 (+++), CD3 (−), CD56 (−), CD10 (−), Bcl-6 (−), MUM1 (+), Bcl-2 (80%+), CD123 (−), with EBV-positive in the *in-situ* hybridization for EBV-encoded RNA (Figure 4). The pathology of the mesenteric lymph node proved a diffuse large B-cell lymphoma, indicating the diagnosis of monomorphic PTLD.

Then the immunosuppressive medications were stopped and two cycles of Rituximab were given. One month after the treatment, the EBV DNA in the patient's serum and lymphocytes was undetectable. The follow-up CT showed the lesions disappeared completely, characterized as complete response.

3. Discussion

BPDCN, derived from precursors of plasmacytoid dendritic cells, is an extremely rare hematopoietic malignancy (11). It commonly affects elderly males, with a male/female incidence ratio of at least 3:1 (12, 13). Ninety percent of patients have cutaneous involvement, and skin lesions are often the first manifestation that typically result in medical attention (14, 15). The skin lesions are usually manifested as bruise-like lesions, plaques or nodules on the head, trunk, and extremities (6). A small percentage of patients will present with isolated skin disease, while the majority of patients has extracutaneous manifestations, including lymphadenopathy, fever, fatigue, or testicular swelling, but rarely have massive splenomegaly or hypersplenism (15–19).

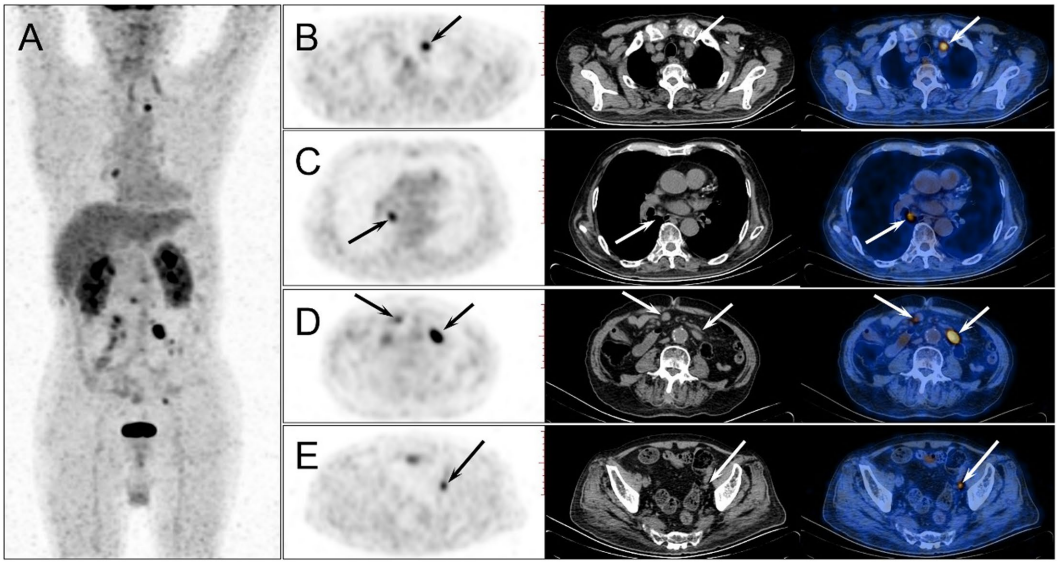

FIGURE 3
The second ^{18}F-FDG PET/CT was performed 4 months after the HSCT. The MIP image **(A)** showed multiple new ^{18}F-FDG-avid lesions in the chest and abdomen, while the previous hypermetabolic lesions all disappeared. On the axial images of PET, CT and PET/CT fusion, enlarged lymph nodes were observed in mediastinum **(B,C)**, and abdominal and pelvic cavity **(D,E)** (arrows), which demonstrated intense ^{18}F-FDG uptake with the highest SUVmax of 13.9 in the mesenteric lymph node.

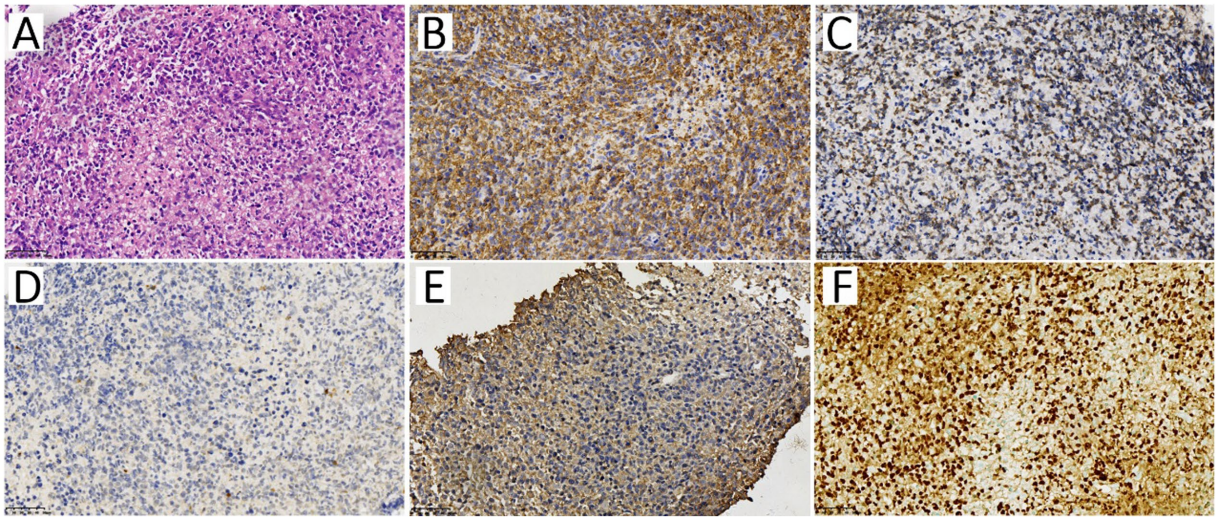

FIGURE 4
The pathology of the mesenteric lymph node. The HE staining specimen **(A)** showed diffuse medium-large cell infiltration with nuclear irregularity. Immunophenotype of the neoplastic cells showed CD20 **(B)** and Bcl-2 **(C)** were positive, while CD56 **(D)** and CD123 **(E)** were negative. The *in-situ* hybridization (ISH) staining of EBV-encoded RNA [EBER, **(F)**] showed EBV positive.

The diagnosis of BPDCN is mainly based on histology, immunohistochemistry, and flow cytometry (3, 4, 20). Under microscope, the tumor cells are medium sized with a slightly irregular-shaped nucleus and smooth chromatin, similar to lymphoblasts (14). IHC usually demonstrates that the characteristic markers of plasmacyte-like dendritic cells, such as CD4, CD56, CD123, CD303 and T-cell leukemia/lymphoma protein 1 (TCL-1), are positive, while the markers of myelocyte, T/B lymphocyte, and NK cell are negative (3, 4, 21).

Currently, only a few case reports have described the imaging features of BPDCN on ^{18}F-FDG PET/CT. Typical presentations include mildly hypermetabolic cutaneous lesions with thickened skin or subcutaneous mass, mildly hypermetabolic enlarged lymph nodes in multiple regions, and slightly higher ^{18}F-FDG uptake in bone marrow, with reported SUVmax range of 1.9–2.4 (17, 22–24). Although the imaging features of BPDCN on ^{18}F-FDG PET/CT are nonspecific, ^{18}F-FDG PET/CT is crucial in staging of BPDCN by detecting the involvement of regional lymph

node, bone marrow, and other organs, which is related to prognosis of the disease (5, 17).

BPDCN is an aggressive hematopoietic malignancy and exhibits a poor prognosis, with median survival of less than 2 years (25). There is no standard treatment-protocol for BPDCN, and the commonly used chemotherapy regimens derive from other more common hematological malignancies, such as non-Hodgkin lymphoma (NHL), acute lymphoblastic leukemia (ALL) and acute myeloid leukemia (AML) (6, 8, 26). Patients with BPDCN can achieve remission after receiving leukemia-type chemotherapy, but the disease usually tends to relapse after a few months. Consequently, allogeneic HSCT is considered as a consolidative strategy to maintain sustained complete remission (20). In addition, in view of the highly aggressive clinical behavior of BPDCN, it is recommended to start HSCT as soon as possible (9, 22).

PTLD is a group of conditions involving abnormal lymphoid cells proliferation in the context of extrinsic immunosuppression after SOT or HSCT. It is one of the most serious complications after the transplantation (10). The incidence of PTLD is 1 to 20% of recipients overall and varies by transplanted organs. Recipients of intestine and multi-organ transplantation have the highest risk (12%–17%), followed by lung (6%–10%), heart (3%–5%), liver (2%–3%) and kidney (1.5%–2.5%), while the recipients of HSCT have the lowest risk (< 2%) (27, 28). Although the incidence of PTLD in HSCT recipients is relatively low, patients with the following risk factors are more prone to develop PTLD: the use of antithymocyte globulin or alemtuzumab, *in-vivo* T-cell depletion, EBV serology donor/recipient mismatch (recipient-negative/donor-positive), human leukocyte antigen (HLA) mismatch, splenectomy, a second HSCT, and so on (29).

Compared with the SOT-associated PTLDs, which usually demonstrated a bimodal time distribution, with an early peak in the first 2 years and a second peak between 5 and 10 years after transplantation, most of the HSCT-associated PTLDs only show the early-onset pattern (10, 30). In many early-onset cases, carcinogenic EBV is a key pathogenic driver. The immunosuppressive therapy after allogeneic HSCT may disrupt the normal balance between the proliferation of potentially infected B-cells and the EBV-specific T-cell response, while the increased number of latently infected B cells may develop into PTLD (31). Furthermore, the splenectomy before HSCT may impair the function of CD5 positive B cell and lead to explosive growth of EBV load (32).

According to the World Health Organization (WHO), PTLDs was classified into four main types, namely, early lesions, polymorphic PTLD, monomorphic PTLD (with many subtypes), and classic Hodgkin lymphoma-like PTLD. EBV-related PTLD may evolve from a polyclonal disorder to a more aggressive monoclonal variant. Therefore, early diagnosis, accurate staging, and timely treatment are of vital importance to reduce morbidity and mortality. The European Conference in Infections in Leukemia recommended in the evidence-based guidelines that weekly EBV-DNA screening should be carried out on high-risk allogeneic HSCT recipients for at least 3 months (33).

The clinical manifestations of PTLD are usually nonspecific, and the patients commonly present with fever, anorexia, lethargy, night sweats, and weight loss. When latently-infected lymphocytes expand within the reticuloendothelial system, patients can present with lymphadenopathy, symptomatic hepatosplenomegaly, ascites, abdominal pain and cytopenias (34). Clinicians should differentiate PTLD from an acute infection, GVHD, graft rejection or malignancy relapse. Surveillance and diagnostic strategies for high-risk population of PTLD include routine blood test, weekly EBV DNA monitoring, imaging and tissue biopsy. Pathological diagnosis is the gold standard of PTLD, and most importantly, it can determine the PTLD subtype, which forms the basis for the subsequent treatment planning.

^{18}F-FDG PET/CT may provide additional evidence for supporting or refuting the suspicion of PTLD, and suggest lesions accessible for biopsy (21, 35–37). As ^{18}F-FDG PET/CT can provide both anatomic and metabolic information of lesions, it can increase the sensitivity of detecting occult metabolically active lesions or small lesions neglected on CT scan due to not meeting size criteria (35). Besides, it was reported that ^{18}F-FDG PET/CT had advantage in detecting extra-nodal lesions due to its additional metabolic information (38). A recent retrospective study including 91 patients with clinical suspicion of PTLD showed that the sensitivity and specificity of ^{18}F-FDG PET/CT for the detection of PTLD were 85 and 90%, respectively (30). Another monocentric retrospective analysis involving 170 cases showed that ^{18}F-FDG uptake in PTLD was generally high with a median SUVmax of 17.4 (range 2.6–26.4) (39). However, ^{18}F-FDG uptake will also increase in other conditions in patients after transplantation, such as postsurgical inflammation, infection, bone marrow activation and transplant rejection. In these cases, the detection of non-specific ^{18}F-FDG-avid lesions will make the diagnosis of PTLD challenging.

It is worth noting that in this case, there were small foci of slightly increased uptake in the bone marrow (heterogenous uptake), slightly increased uptake in lymph nodes and skin in BPDCN, whereas there was intense uptake in evidently enlarged lymph nodes in PTLD, consistent with previous reports (17, 22–24, 39). This indicates that the differences in ^{18}F-FDG uptake patterns may also be a distinguishing point between these two diseases.

As a whole-body functional and molecular imaging method, ^{18}F-FDG PET/CT has unique advantages in staging and re-staging. Accurate staging is required for clinicians to decide the management strategy, as well as to evaluate the treatment response promptly and accurately. At present, the ^{18}F-FDG PET/CT staging procedures of lymphoma are adopted for PTLD staging in many centers (40).

According to the National Comprehensive Cancer Network (NCCN) guideline (41), the main treatment options for PTLD include reducing immunosuppression, rituximab monotherapy, chemotherapy with or without rituximab, sequential chemo-immunotherapy, and so on.

In summary, we herein report a rare case of a patient with BPDCN who suffered from PTLD after allogeneic HSCT. This case indicates when new enlarged lymph nodes after HSCT and immunosuppressive therapy in patients with BPDCN are discovered, PTLD should be taken into consideration. ^{18}F-FDG PET/CT examination may provide additional evidence for supporting or refuting the suspicion of PTLD, and suggest lesions accessible for biopsy.

Data availability statement

The original contributions presented in the study are included in the article/supplementary material, further inquiries can be directed to the corresponding authors.

Ethics statement

Written informed consent was obtained from the individual(s) for the publication of any potentially identifiable images or data included in this article.

Author contributions

JC and XZ: imaging data analysis, manuscript draft, and editing. LM and YG: imaging data collection. ZF and ML: supervision, writing review, and editing. All authors contributed to the article and approved the submitted version.

Funding

The author(s) declare that no financial support was received for the research, authorship, and/or publication of this article.

Conflict of interest

The authors declare that the research was conducted in the absence of any commercial or financial relationships that could be construed as a potential conflict of interest.

Publisher's note

References

1. Chaperot L, Bendriss N, Manches O, Gressin R, Maynadie M, Trimoreau F, et al. Identification of a leukemic counterpart of the plasmacytoid dendritic cells. *Blood*. (2001) 97:3210–7. doi: 10.1182/blood.v97.10.3210

2. Pemmaraju N, Lane AA, Sweet KL, Stein AS, Vasu S, Blum W, et al. Tagraxofusp in blastic plasmacytoid dendritic-cell neoplasm. *N Engl J Med*. (2019) 380:1628–37. doi: 10.1056/NEJMoa1815105

3. Laribi K, Denizon N, Besancon A, Farhi J, Lemaire P, Sandrini J, et al. Blastic plasmacytoid dendritic cell neoplasm: from origin of the cell to targeted therapies. *Biol Blood Marrow Transplant*. (2016) 22:1357–67. doi: 10.1016/j.bbmt.2016.03.022

4. Wang W, Khoury JD, Miranda RN, Jorgensen JL, Xu J, Loghavi S, et al. Immunophenotypic characterization of reactive and neoplastic plasmacytoid dendritic cells permits establishment of a 10-color flow cytometric panel for initial workup and residual disease evaluation of blastic plasmacytoid dendritic cell neoplasm. *Haematologica*. (2021) 106:1047–55. doi: 10.3324/haematol.2020.247569

5. Li ZG, Mu HY. Blastic plasmacytoid dendritic cell neoplasm evaluated by FDG PET/CT. *Clin Nucl Med*. (2017) 42:551–2. doi: 10.1097/RLU.0000000000001665

6. Pagano L, Valentini CG, Pulsoni A, Fisogni S, Carluccio P, Mannelli F, et al. Blastic plasmacytoid dendritic cell neoplasm with leukemic presentation: an Italian multicenter study. *Haematologica*. (2013) 98:239–46. doi: 10.3324/haematol.2012.072645

7. Tsagarakis NJ, Kentrou NA, Papadimitriou KA, Pagoni M, Kokkini G, Papadaki H, et al. Acute lymphoplasmacytoid dendritic cell (DC2) leukemia: results from the Hellenic dendritic cell leukemia study group. *Leuk Res*. (2010) 34:438–46. doi: 10.1016/j.leukres.2009.09.006

8. Deotare U, Yee KW, Le LW, Porwit A, Tierens A, Musani R, et al. Blastic plasmacytoid dendritic cell neoplasm with leukemic presentation: 10-color flow cytometry diagnosis and hypercvad therapy. *Am J Hematol*. (2016) 91:283–6. doi: 10.1002/ajh.24258

9. Sapienza MR, Pileri A, Derenzini E, Melle F, Motta G, Fiori S, et al. Blastic plasmacytoid dendritic cell neoplasm: state of the art and prospects. *Cancers (Basel)*. (2019) 11:595. doi: 10.3390/cancers11050595

10. Dharnidharka VR, Webster AC, Martinez OM, Preiksaitis JK, Leblond V, Choquet S. Post-transplant lymphoproliferative disorders. *Nat Rev Dis Primers*. (2016) 2:15088. doi: 10.1038/nrdp.2015.88

11. Adimora IJ, Wilson NR, Pemmaraju N. Blastic plasmacytoid dendritic cell neoplasm (Bpdcn): a promising future in the era of targeted therapeutics. *Cancer*. (2022) 128:3019–26. doi: 10.1002/cncr.34345

12. Garnache-Ottou F, Vidal C, Biichle S, Renosi F, Poret E, Pagadoy M, et al. How should we diagnose and treat blastic plasmacytoid dendritic cell neoplasm patients? *Blood Adv*. (2019) 3:4238–51. doi: 10.1182/bloodadvances.2019000647

13. Togami K, Chung SS, Madan V, Booth CAG, Kenyon CM, Cabal-Hierro L, et al. Sex-biased ZRSR2 mutations in myeloid malignancies impair plasmacytoid dendritic cell activation and apoptosis. *Cancer Discov*. (2022) 12:522–41. doi: 10.1158/2159-8290.CD-20-1513

14. Deconinck E, Petrella T, Garnache OF. Blastic plasmacytoid dendritic cell neoplasm: clinical presentation and diagnosis. *Hematol Oncol Clin North Am*. (2020) 34:491–500. doi: 10.1016/j.hoc.2020.01.010

15. Blennerhassett R, McCaughan G, Tegg E. An unexpected diagnosis: leukaemic presentation of blastic plasmacytoid dendritic cell neoplasm with massive splenomegaly. *Pathology*. (2018) 50:773–5. doi: 10.1016/j.pathol.2018.05.007

16. Li Y, Li Z, Lin HL, Chen XH, Li B. Primary cutaneous blastic plasmacytoid dendritic cell neoplasm without extracutaneous manifestation: case report and review of the literature. *Pathol Res Pract*. (2011) 207:55–9. doi: 10.1016/j.prp.2010.05.008

17. Sugimoto KJ, Shimada A, Yamaguchi N, Imai H, Wakabayashi M, Sekiguchi Y, et al. Sustained complete remission of a limited-stage blastic plasmacytoid dendritic cell neoplasm followed by a simultaneous combination of low-dose DeVIC therapy and radiation therapy: a case report and review of the literature. *Int J Clin Exp Pathol*. (2013) 6:2603–8.

18. Pileri A, Delfino C, Grandi V, Agostinelli C, Pileri SA, Pimpinelli N. Blastic plasmacytoid dendritic cell neoplasm (BPDCN): the cutaneous sanctuary. *G Ital Dermatol Venereol*. (2012) 147:603–8.

19. Dhariwal S, Gupta M. A case of blastic plasmacytoid dendritic cell neoplasm with unusual presentation. *Turk J Haematol*. (2019) 36:55–6. doi: 10.4274/tjh.galenos.2018.2018.0181

20. Falcone U, Sibai H, Deotare U. A critical review of treatment modalities for blastic plasmacytoid dendritic cell neoplasm. *Crit Rev Oncol Hematol*. (2016) 107:156–62. doi: 10.1016/j.critrevonc.2016.09.003

21. Adachi M, Maeda K, Takekawa M, Hinoda Y, Imai K, Sugiyama S, et al. High expression of CD56 (N-CAM) in a patient with cutaneous CD4-positive lymphoma. *Am J Hematol*. (1994) 47:278–82. doi: 10.1002/ajh.2830470406

22. Lee HJ, Park HM, Ki SY, Choi YD, Yun SJ, Lim HS. Blastic plasmacytoid dendritic cell neoplasm of the breast: a case report and review of the literature. *Medicine (Baltimore)*. (2021) 100:e25699. doi: 10.1097/MD.0000000000025699

23. Matsuo T, Ichimura K, Tanaka T, Morizane S, Iwatsuki K, Eguchi M, et al. Bilateral conjunctival lesions in blastic plasmacytoid dendritic cell neoplasm. *J Clin Exp Hematop*. (2011) 51:49–55. doi: 10.3960/jslrt.51.49

24. Nizza D, Simoneaux SF. Blastic plasmacytoid dendritic cell neoplasm presenting as a subcutaneous mass in an 8-year-old boy. *Pediatr Radiol*. (2010) 40:40–2. doi: 10.1007/s00247-010-1731-6

25. Wilson NR, Konopleva M, Khoury JD, Pemmaraju N. Novel therapeutic approaches in blastic plasmacytoid dendritic cell neoplasm (BPDCN): era of targeted therapy. *Clin Lymphoma Myeloma Leuk*. (2021) 21:734–40. doi: 10.1016/j.clml.2021.05.018

26. Reimer P, Rudiger T, Kraemer D, Kunzmann V, Weissinger F, Zettl A, et al. What is CD4+CD56+ malignancy and how should it be treated? *Bone Marrow Transplant*. (2003) 32:637–46. doi: 10.1038/sj.bmt.1704215

27. Opelz G, Dohler B. Lymphomas after solid organ transplantation: a collaborative transplant study report. *Am J Transplant*. (2004) 4:222–30. doi: 10.1046/j.1600-6143.2003.00325.x

28. Rouce RH, Louis CU, Heslop HE. Epstein-Barr virus lymphoproliferative disease after hematopoietic stem cell transplant. *Curr Opin Hematol*. (2014) 21:476–81. doi: 10.1097/MOH.0000000000000083

29. Lindsay J, Othman J, Heldman MR, Slavin MA. Epstein-Barr virus posttransplant lymphoproliferative disorder: update on management and outcomes. *Curr Opin Infect Dis*. (2021) 34:635–45. doi: 10.1097/QCO.0000000000000787

30. Montes de Jesus FM, Kwee TC, Kahle XU, Nijland M, van Meerten T, Huls G, et al. Diagnostic performance of FDG-PET/CT of post-transplant lymphoproliferative disorder and factors affecting diagnostic yield. *Eur J Nucl Med Mol Imaging*. (2020) 47:529–36. doi: 10.1007/s00259-019-04481-7

31. Babcock GJ, Decker LL, Freeman RB, Thorley-Lawson DA. Epstein-Barr virus-infected resting memory B cells, not proliferating lymphoblasts, accumulate in the peripheral blood of immunosuppressed patients. *J Exp Med*. (1999) 190:567–76. doi: 10.1084/jem.190.4.567

32. Uhlin M, Wikell H, Sundin M, Blennow O, Maeurer M, Ringden O, et al. Risk factors for Epstein-Barr virus-related post-transplant lymphoproliferative disease after allogeneic hematopoietic stem cell transplantation. *Haematologica*. (2014) 99:346–52. doi: 10.3324/haematol.2013.087338

33. Styczynski J, Reusser P, Einsele H, de la Camara R, Cordonnier C, Ward KN, et al. Management of HSV, VZV and EBV infections in patients with hematological malignancies and after Sct: guidelines from the Second European Conference on Infections in Leukemia. *Bone Marrow Transplant*. (2009) 43:757–70. doi: 10.1038/bmt.2008.386

34. DeStefano CB, Desai SH, Shenoy AG, Catlett JP. Management of post-transplant lymphoproliferative disorders. *Br J Haematol*. (2018) 182:330–43. doi: 10.1111/bjh.15263

35. Song H, Guja KE, Iagaru A. ^{18}F-FDG PET/CT for evaluation of post-transplant lymphoproliferative disorder (PTLD). *Semin Nucl Med*. (2021) 51:392–403. doi: 10.1053/j.semnuclmed.2020.12.009

36. Montes de Jesus FM, Glaudemans A, Tissing WJ, Dierckx R, Rosati S, Diepstra A, et al. ^{18}F-FDG PET/CT in the diagnostic and treatment evaluation of pediatric posttransplant lymphoproliferative disorders. *J Nucl Med*. (2020) 61:1307–13. doi: 10.2967/jnumed.119.239624

37. Ballova V, Muoio B, Albano D, Bertagna F, Canziani L, Ghielmini M, et al. Diagnostic performance of ^{18}F-FDG PET or PET/CT for detection of post-transplant lymphoproliferative disorder: a systematic review and a bivariate meta-analysis. *Diagnostics (Basel)*. (2020) 10:101. doi: 10.3390/diagnostics10020101

38. Styczynski J, van der Velden W, Fox CP, Engelhard D, de la Camara R, Cordonnier C, et al. Management of Epstein-Barr virus infections and post-transplant lymphoproliferative disorders in patients after allogeneic hematopoietic stem cell transplantation: Sixth European Conference on Infections in Leukemia (ECIL-6) Guidelines. *Haematologica*. (2016) 101:803–11. doi: 10.3324/haematol.2016.144428

39. Dierickx D, Tousseyn T, Requile A, Verscuren R, Sagaert X, Morscio J, et al. The accuracy of positron emission tomography in the detection of posttransplant lymphoproliferative disorder. *Haematologica*. (2013) 98:771–5. doi: 10.3324/haematol.2012.074500

40. Cheson BD, Fisher RI, Barrington SF, Cavalli F, Schwartz LH, Zucca E, et al. Recommendations for initial evaluation, staging, and response assessment of Hodgkin and non-Hodgkin lymphoma: the Lugano classification. *J Clin Oncol*. (2014) 32:3059–67. doi: 10.1200/JCO.2013.54.8800

41. Zelenetz AD, Gordon LI, Abramson JS, Advani RH, Bartlett NL, Caimi PF, et al. NCCN guidelines insights: B-cell lymphomas, version 3.2019. *J Natl Compr Cancer Netw*. (2019) 17:650–61. doi: 10.6004/jnccn.2019.0029

frontiers | Frontiers in Medicine

TYPE Case Report
PUBLISHED 05 September 2023
DOI 10.3389/fmed.2023.1269587

OPEN ACCESS

EDITED BY
Carmelo Caldarella,
Fondazione Policlinico Universitario A. Gemelli IRCCS, Italy

REVIEWED BY
Taha Koray Sahin,
Hacettepe University, Türkiye
Giorgio Treglia,
Ente Ospedaliero Cantonale (EOC), Switzerland

*CORRESPONDENCE
Lei Kang
✉ kanglei@bjmu.edu.cn
Aixiang Wang
✉ wax20030826@126.com

†These authors have contributed equally to this work and share first authorship

RECEIVED 30 July 2023
ACCEPTED 25 August 2023
PUBLISHED 05 September 2023

CITATION
Jiao H, Qiu Y, Huang W, Zhang Y, Chen Z, Wang A and Kang L (2023) Alpha-fetoprotein-elevated postpubertal testicular teratoma with retroperitoneal metastasis on ^{18}F-FDG PET/CT: case report and literature review.
Front. Med. 10:1269587.
doi: 10.3389/fmed.2023.1269587

Alpha-fetoprotein-elevated postpubertal testicular teratoma with retroperitoneal metastasis on ^{18}F-FDG PET/CT: case report and literature review

Hao Jiao[1†], Yongkang Qiu[1†], Wenpeng Huang[1], Yongbai Zhang[1], Zhao Chen[1], Aixiang Wang[2*] and Lei Kang[1*]

[1]Department of Nuclear Medicine, Peking University First Hospital, Beijing, China, [2]Department of Urology, Peking University First Hospital, Institute of Urology, Peking University, National Urological Cancer Center, Beijing, China

Postpubertal testicular teratoma exhibits malignant biological behavior and has metastatic potential. We report a case of a 17-year-old patient diagnosed with postpubertal testicular teratoma with massive retroperitoneal metastasis. The pathological examination revealed a mature teratoma without any other components. However, the patient had a significantly increased level of AFP, and ^{18}F-FDG PET/CT showed the retroperitoneal metastasis had increased FDG uptake, with a SUVmax of 15.6, suggesting the coexistence of other germ cell tumor components, and the patient might have a poor prognosis. After resection of the retroperitoneal tumor, PET/CT further revealed multiple abdominal and pelvic metastases, with a SUVmax of 22.5. Therefore, the patient received a cycle of chemotherapy and follow-up PET/CT imaging showed the achievement of complete metabolic response after the treatment. In this case, PET/CT played a crucial role in detecting metastasis, compensating for the limitations of pathological sampling, thus establishing a definitive diagnosis and predicting prognosis. And it was evident that PET/CT also has the advantage of evaluating therapeutic efficacy.

KEYWORDS

postpubertal testicular teratoma, retroperitoneal metastasis, ^{18}F-FDG, PET/CT, alpha-fetoprotein

Introduction

The World Health Organization updated the classification of testicular tumors in the "Tumors of the urinary system and male genital organs" category in 2022, among which nonseminomatous germ cell tumors (NSGCTs) include embryonal carcinomas, yolk sac tumors, choriocarcinomas, and teratomas. Testicular teratomas can be further classified into prepubertal and postpubertal teratomas, and teratomas unrelated to germ cell neoplasia *in situ* (GCNIS) are designated as prepubertal teratomas, while the GCNIS-derived entities are designated as postpubertal type (1, 2). Prepubertal testicular teratomas typically occur in children and exhibit a benign biological behavior. On the other hand, postpubertal testicular teratomas usually occur in adults and may also occur in pediatric patients who have disorders of sex development (3). The diagnosis of teratomas relies on pathological examination. Postpubertal teratomas, whether

mature or immature teratomas, are considered as malignant components and have metastatic potential (4, 5). A significant elevation of serum alpha-fetoprotein (AFP) suggests the potential coexistence of yolk sac tumor components in the teratoma (6). However, due to sampling limitations, pathological examination failed to show the presence of yolk sac tumors. ^{18}F-fluorodeoxygluxose (FDG) positron emission tomography/computed tomography (PET/CT) is used as a favorable examination to detect systemic tumor metastasis. Mature teratomas have normal or slightly elevated FDG uptake, so if the tumor has a significantly elevated FDG uptake, it suggests that there are other components in the tumor (7, 8). Combined with high FDG uptake on PET/CT images and significantly increased AFP, patients can be diagnosed more accurately. And a patient with teratoma coexisting with yolk sac tumor components usually has a poor prognosis, PET/CT can play a role in detecting metastasis and evaluating treatment efficacy (9).

Case presentation

A 17-year-old boy accidentally found a left testicular swelling, which was hard and accompanied by pain. The patient went to the local hospital and was diagnosed as inflammation. The pain was relieved after antibiotic infusion, but there was no significant change in the size of the swelling, so he was consulted at our hospital. The patient was previously in good health and had no history of tumor, and had no familial history of hereditary diseases. Laboratory tests showed markedly increased level of AFP (>1,210 ng/mL) whereas his HCG level was normal (<0.1 mIU/mL). The ultrasound showed that there was a cystic mass in the left testis, which tended to be benign. The pelvic contrast-enhanced MRI revealed that the left testicular mass contained both solid and cystic components, and it exhibited low signal intensity on T1WI and high signal intensity on T2WI. There were multiple reticular structures in the mass, which exhibited low signal intensity on T1WI and T2WI and high signal intensity on DWI. The solid components showed significant enhancement on enhancement scan. And there were no enlarged lymph nodes in the scanning range (Figures 1A–D). Then, left side radical orchiectomy was performed. The resected specimen measured 5.5 × 4.5 × 3.3 cm, and the pathological examination revealed a mature teratoma, with mostly well-differentiated tissues, while focal areas showed markedly heterotypic epithelioid cells. Immunohistochemistry staining results demonstrated the positive expression of AE1/AE3, SALL4, CK7 and Ki-67 (20%), whereas the negative expression of CD30, EMA, CEA, PLAP, AFP2, Vim, CD117, S-100, TTF1, PSA, CK20 (Figures 1E–H).

However, half a month after the excision of testicular lesion, although the patient had no clinical symptoms, the serum level of AFP remained significantly increased (>1,210 ng/mL), so further examinations were performed. Contrast-enhanced CT of urinary system showed there was an irregular soft tissue mass on the on the left side of abdominal aorta and below the left renal hilum, at the size of 8.4 × 10.0 cm. The mass had an incomplete capsule with unclear boundary. The internal density was heterogeneous and multiple patchy necrotic areas could be found. Also, the fatty space surrounding the lesion was unclear and the lesion demonstrated uneven enhancement (Figures 2A–C). To further evaluate the whole-body situation and re-staging, ^{18}F-FDG PET/CT was performed. PET/CT revealed increased FDG uptake at the edges of the tumor with a SUVmax of 15.9, while the central FDG uptake was low, indicating a large area of necrosis. These findings reflected the aggressive growth and high malignant potential of the tumor. In addition, there were no metastatic lesions with abnormal FDG uptake in other parts of the body (Figures 2D–G). Then, the patient underwent resection of the retroperitoneal tumor, retroperitoneal lymphadenectomy and nephrectomy of the left side. Postoperative pathological examination of the resected specimen also revealed a mature teratoma with no other components. Immunohistochemistry staining results demonstrated the positive expression of AE1/AE3, CK7, AFP and Ki-67 (30%), whereas the negative expression of CD30, OCT3/4, CK20 and p53. Based on pathological findings, postpubertal testicular teratoma should be considered and the final diagnosis for the patient was mature teratoma of the testis with retroperitoneal metastasis.

One month after the second operation, the patient's AFP was still higher than normal (>1,210 ng/mL), so he underwent PET/CT examination again for re-staging. There were multiple soft tissue density nodules and masses around the abdominal aorta, spleen, left psoas major, left diaphragm foot and left pelvic cavity, some of which had unclear boundaries with adjacent intestines, left adrenal gland and psoas major muscle. The FDG uptake of these lesions increased unevenly, with a SUVmax of 22.5, indicating extensive recurrent metastasis of the tumor (Figures 3A–C). Then, the patients received one cycle of combination chemotherapy with bleomycin, etoposide and cisplatin. In half a year, the patient underwent PET/CT examinations twice to monitor the effect of treatment. Three months after chemotherapy, PET/CT showed some lesions shrank or disappeared to varying degrees, and FDG uptake was lower than before with a SUVmax of 8.4. Furthermore, the PET/CT results after chemotherapy showed that most of the lesions became smaller or disappeared, and FDG uptake became normal, achieving complete metabolic response recovery and suggesting that the treatment was effective (Figures 3D–F).

Discussion

Although testicular tumors account for only about 1% of all solid tumors in men, it is the most common solid malignancy in men aged 15–35 years (10). The World Health Organization updated the classification of testicular tumors in the "Tumors of the urinary system and male genital organs "category in 2022 (1). The two main types of testicular tumors are germ cell tumors (GCTs) and sex cord-stromal tumors (SCSTs), with the former accounting for 95% of cases. GCTs can be divided into pure seminomas, which consist entirely of germ cells, and all other tumors collectively called NSGCTs. Teratomas, along with embryonal carcinomas, yolk sac tumors, and choriocarcinomas, are classified as NSGCTs. Testicular teratoma can be classified into prepubertal and postpubertal teratoma. Prepubertal teratoma usually occurs in children and is typically a pure teratoma with benign biological behavior (11). However, postpubertal testicular teratomas typically occur in adults and are rarely pure teratomas. They exhibit malignant biological behavior and 22–38% of patients develop metastases (4, 5). Only a minority of teratomas contain malignant somatic tissue components, such as squamous cell carcinoma, adenocarcinoma, immature neuroectodermal elements, or sarcoma (12, 13). Testicular teratomas are characterized by slow progression and lack of typical clinical presentation, presenting with testicular

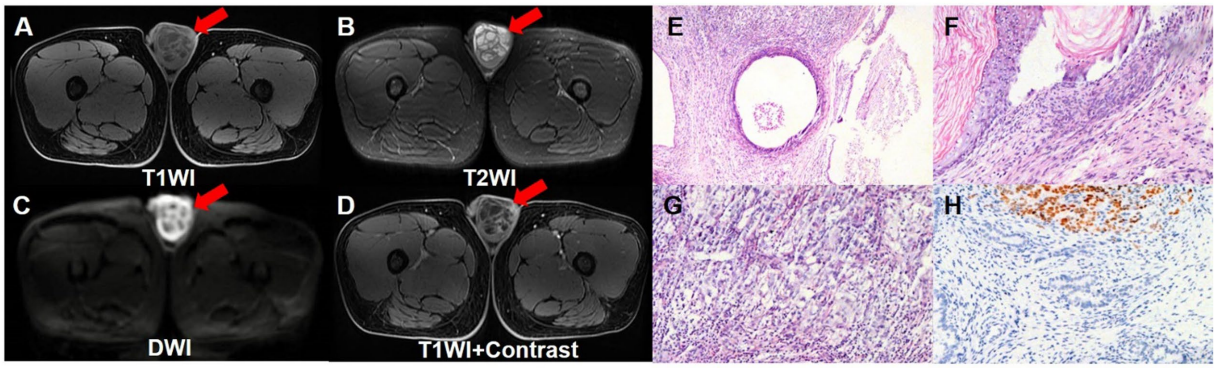

FIGURE 1
Pelvic contrast-enhanced MRI images and pathological images of the testicular teratoma. Pelvic contrast-enhanced MRI revealed that the left testicular mass contained both solid and cystic components, and it exhibited low signal intensity on T1WI transverse image **(A)**, and high signal intensity on T2WI transverse image **(B)**. There were multiple reticular structures in the mass, which exhibited low signal intensity on T1WI and T2WI, and exhibited high signal intensity on DWI transverse image **(C)**. On enhancement scan image **(D)**, the solid components showed significant enhancement. **(E–G)** The hematoxylin–eosin (HE) staining (magnification ×40 and 100) showed that the mature teratoma was infiltrated with mostly well-differentiated tissues, while focal areas showed markedly heterotypic epithelioid cells. **(H)** Immunohistochemistry showed that the tumor cells were positive for SALL4 (magnification ×100).

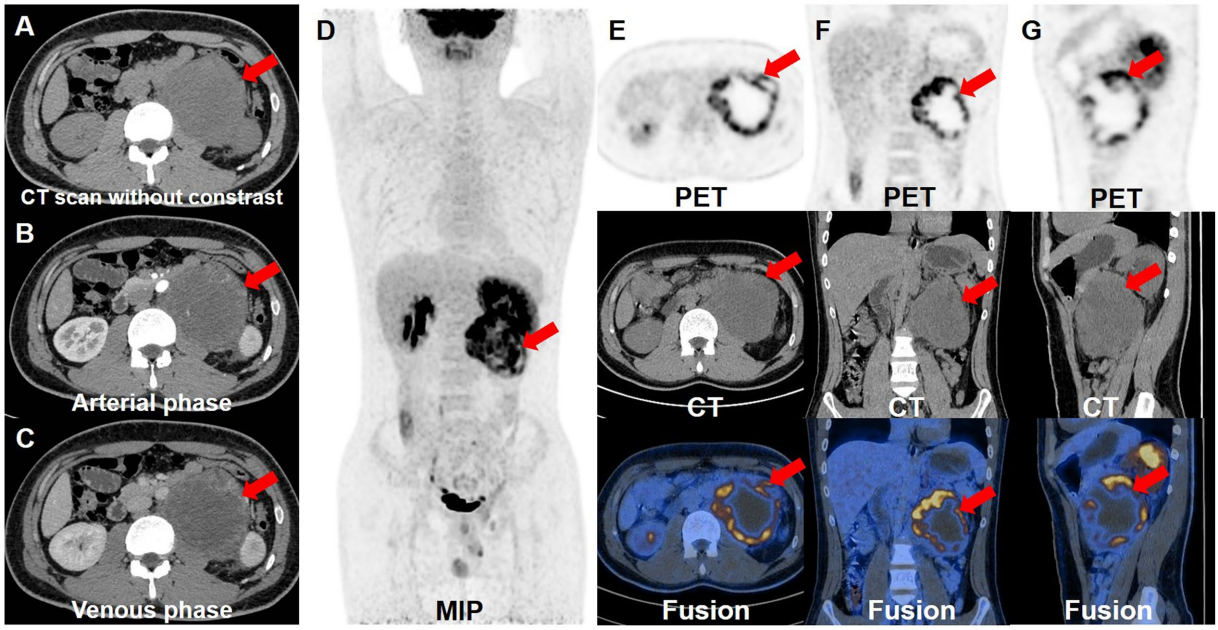

FIGURE 2
Contrast-enhanced CT and ^{18}F-FDG PET/CT images. The retroperitoneal teratoma exhibited an incomplete capsule and unclear local boundaries on the enhanced CT plain scan **(A)**, with uneven internal density. And it demonstrated uneven enhancement during the arterial **(B)** and venous **(C)** phases of the contrast-enhanced CT. **(D)** The whole-body maximum intensity projection showed the retroperitoneal lesion with hypermetabolism. The transverse **(E)**, coronal **(F)** and sagittal **(G)** images of retroperitoneal lesions showed that the tumor had high FDG uptake, with a SUVmax of 15.9.

enlargement, heaviness, discomfort, and mild pain. If a teratoma exhibits malignant biological behavior, the patient may present with rapid enlargement of the tumor, as well as systemic symptoms such as anemia and weight loss. If the tumor metastasizes, the patient may also experience other clinical symptoms such as progressive abdominal distension and disturbed bowel habits (14). Most patients with retroperitoneal teratoma are asymptomatic, and the most common symptom is nonspecific pain. Patients whose adrenals were compressed may present with vertigo and hypertension (15). In our case, the patient's testicular teratoma caused pain, while the retroperitoneal teratoma did not cause any symptoms, which was consistent with previous studies.

Various imaging modalities such as ultrasound, MRI and CT are used for evaluating testicular teratomas. Ultrasound evaluation is often the first choice of imaging modality for testicular teratoma, which typically shows a cystic or solid cystic mass with heterogeneous

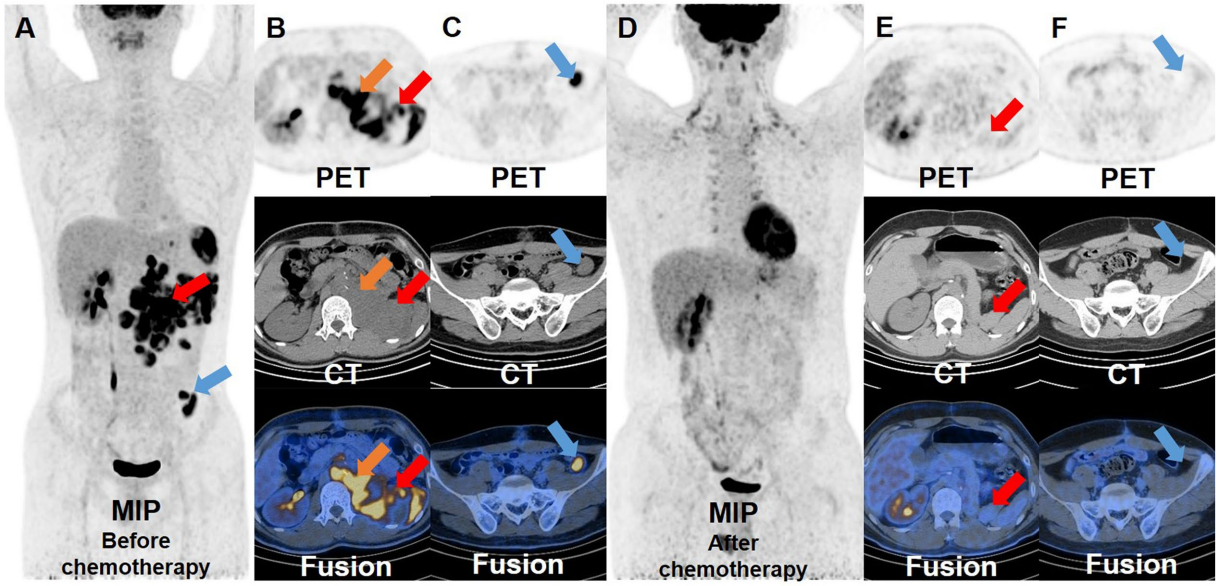

FIGURE 3
^{18}F-FDG PET/CT images before and after chemotherapy. Before the patient received chemotherapy, the whole-body maximum intensity projection **(A)** showed multiple hypermetabolic lesions around the abdominal aorta, spleen, left psoas major, left diaphragm foot and left pelvic cavity. And the transverse images **(B,C)** showed that these lesions had significantly increased FDG uptake, with a SUVmax of 22.5. After the patient received a cycle of chemotherapy, the whole-body maximum intensity projection **(D)** and the transverse images **(E,F)** showed that the pre-existing lesions shrank or disappeared, and the remaining lesions displayed a marked reduction in FDG uptake compared to before.

echogenicity. The mass may contain calcifications and other elements, such as bone and hair. Immature teratomas are richly vascularized due to their predominantly solid component, while mature teratomas are mainly cystic and lack vascularity (16, 17). When a teratoma undergoes malignant somatic transformation, it may initially present as a cystic lesion with low-level echogenicity and gradually become solid, with a heterogeneous pattern of echogenicity and rich blood flow (18). A benign teratoma typically presents as an ellipsoid mass with distinct borders on MRI. Mixed signal intensity is observed on both T1WI and T2WI, and the presence of high signal intensity fat can also be detected. Contrast-enhanced scanning shows mild and heterogeneous enhancement. Meanwhile, a malignant teratoma can present with an indistinct border and heterogeneous signal intensity, with significant and heterogeneous enhancement (19). CT has a limitation in evaluating soft tissue components, but it still widely used for patients with teratomas because it is superior to MRI in scanning time, cost and scanning coverage. The typical CT manifestation of teratoma consists of a heterogeneous cystic-solid mass composed of various components, including fat, hair, and fluid. The cyst wall can vary in thickness and may exhibit arc-shaped calcification. The density of the fat component within the cyst is negative. On contrast-enhanced scans, the solid portion and the septa of the mass show mild to moderate enhancement, while the low-density areas and the fat components remain unenhanced. Malignant teratoma is characterized by the presence of a nodular forming and enhancing soft tissue component, extracapsular tumor growth with extension into adjacent structures or metastasis, etc. (20).

The final diagnosis of testicular teratoma relies on pathological examination. Mature teratomas contain well-differentiated tissues, typically including three germ layers. Immature teratomas refer to tumors containing undifferentiated components, resembling tissues at embryonic developmental stage, characterized by immature neuroepithelial islands and varying degree of differentiation including skeletal muscle, cartilage, and stromal cells. For patients with testicular GCT, the distinction between mature and immature teratoma is not of great significance, because both are considered as malignant components and have metastatic potential. Approximately one-third of testicular GCTs are mixed, presenting with two or more different GCT types. Teratoma can coexist with embryonal carcinoma and yolk sac tumor (21, 22). A small number of teratomas exhibit somatic malignant transformation, and pathological examination can reveal that these tumors contain squamous cell carcinoma, adenocarcinoma, immature neuroectodermal components, or sarcomatous components (23).

Considering that postpubertal testicular teratomas have metastatic potential, ^{18}F-FDG PET/CT examination combined with morphological and metabolic information can be used as a favorable examination to detect metastasis. A literature search was performed on the PubMed and database from 1997 to 2022, using the keyword "retroperitoneal teratoma" and "PET/CT." There were night cases of retroperitoneal teratoma with PET/CT findings. The basic information and metabolism of retroperitoneal teratoma are summarized in Table 1 (15, 24–29). Out of these night cases, only one patient was 7 months old, while other patients were adults, ranging in age from 23 to 49 years, with more males than females. Consistent with most reports, the patient we reported was a near-adult male. Retroperitoneal teratoma generally did not cause clinical symptoms, as reported in our case, but might also presented as abdominal pain. When the tumor invaded the spine, patients might present with back pain. When the tumor was a pure mature teratoma, there was usually no increased FDG uptake or slightly increased FDG uptake, which was consistent with previous findings

TABLE 1 Literature review of retroperitoneal teratoma cases with ^{18}F-FDG PET/CT manifestations.

No.	References	Age	Sex	Clinical symptoms	Primary tumor site	AFP	Pathological type of the retroperitoneal tumor	^{18}F-FDG uptake of the retroperitoneal tumor
1	Suh et al. (24)	7 months	F	Abdominal distention	Retroperitoneum	27.17 ng/mL	Mature teratoma	Slight increase (SUVmax 4.1)
2	Ma et al. (15)	40 years	F	Asymptomatic	Retroperitoneum	Normal (<7.5 ng/mL)	Dermoid cyst (a kind of mature cystic teratoma)	Slight increase
3	Quak et al. (25)	41 years	M	Asymptomatic	Testis	Normal (<7.5 ng/mL)	Mature teratoma with malignant somatic transformation	Significant increase
4	Rodrigo et al. (26)	42 years	M	Not mentioned	Testis	Normal (<7.5 ng/mL)	Teratoma with malignant somatic transformation	Significant increase (SUVmax 14.7)
5	Rodrigo et al. (26)	47 years	M	Not mentioned	Testis	Normal (<7.5 ng/mL)	Teratoma with malignant somatic transformation	Slight increase (SUVmax 5)
6	Yousef et al. (27)	49 years	M	Not mentioned	Testis	Normal (<7.5 ng/mL)	Mature teratoma	Slight increase
7	Martin et al. (28)	23 years	M	Not mentioned	Testis	Normal (<7.5 ng/mL)	Mature teratoma	Normal
8	Daniel et al. (29)	33 years	M	Abdominal pain	Testis	Normal (<7.5 ng/mL)	Teratoma with embryonal carcinoma	Significant increase
9	Daniel et al. (29)	38 years	M	Back pain	Testis	Normal (<7.5 ng/mL)	Mature and immature teratomas with minimal viable malignant tumor	Significant increase

that mature teratomas had a very low avidity for ^{18}F-FDG, with a SUVmean of 1.38 (7, 8). However, one infant with a mature teratoma had a SUVmax of 4.1, possibly due to the abundant central nervous tissue (24). In addition to this, if mature teratomas showed increased FDG uptake, possibly due to the presence of immature teratoma, embryonal carcinoma, or malignant somatic tissue components. However, none of these components were found in the pathological examination of the patient in our case. It is also worth mentioning that among the above adult patients, patients with pure mature teratoma, or teratoma combined with embryonal carcinoma, or teratoma combined with malignant somatic transformation all had normal levels of AFP (<7.5 ng/mL), whereas the patient in our case had a significantly increased AFP level (>1,210 ng/mL). Literature reports suggested that elevated AFP or β-HCG could not be attributed to teratoma components, and an increase in these tumor markers suggested the presence of coexisting other GCT components (22, 30). For example, significant elevation of AFP indicated the presence of yolk sac tumor components in the tumor (6). The pathological examination of this case did not reveal the presence of yolk sac tumor components, possibly due to the limited sampling site. However, combining the significantly elevated AFP level and the hypermetabolism of the tumor on PET/CT images, it can be inferred with high probability that this patient had a mixed GCT, more specifically, a combination of teratoma and yolk sac tumor. SALL4 is a transcription factor and serves as a marker of yolk sac tumor (31, 32). In order to verify the presence of yolk sac tumor components in the patient's primary testicular teratoma, we reperformed immunohistochemical staining of the testicular teratoma pathology images and found that the tumor cells were positive for SALL4, suggesting that there was a high probability of the presence of yolk sac tumor components in the lesion. In terms of prognosis, it has been reported that patients had a poor prognosis if other GCT components were present in teratomas, especially in mature teratomas (9). In addition, AFP levels were correlated with disease severity (30). Therefore, the patient might have a very poor prognosis. In our case, ^{18}F-FDG PET/CT played an important role in patients with testicular teratoma and metastatic retroperitoneal teratoma, as it could compensate for the limitations of pathological sampling, clarify the diagnosis, and provide more accurate information about the prognosis.

The standard treatment for all GCTs in adults is radical orchiectomy. Patients with postpubertal testicular teratoma have a high incidence of retroperitoneal metastasis, with rates of 30% in patients with clinical stage I and 75% in patients with clinical stage II (33). Therefore, the patient underwent imaging examination of the retroperitoneum, which revealed a massive retroperitoneal metastatic teratoma. Studies have shown that even in patients with pure testicular teratoma, approximately 20% of patients may experience recurrence during surveillance (34, 35). Thus, after undergoing retroperitoneal tumor resection, the patient received regular PET/CT scans to monitor tumor recurrence. One month after surgery, PET/CT revealed extensive recurrent lesions with high FDG uptake, with a SUVmax of 22.5. The patient then underwent chemotherapy and also used PET/CT to test the efficacy of the treatment. Late relapse is rare in patients with testicular GCTs, and follow-up may not be necessary to detect recurrence after 5 years (36). However, this patient not only

presented with retroperitoneal metastasis but also had extensive recurrent lesion with hypermetabolism in the abdominal and pelvic cavity revealed by PET/CT, indicating the need for a longer follow-up period.

Conclusion

Postpubertal testicular teratoma has metastatic potential and ^{18}F-FDG PET/CT can be used as a favorable examination to detect systemic tumor metastasis. In addition, although the diagnosis of teratoma relies on pathological examination, it can be inaccurate due to sampling limitations. If AFP levels are significantly elevated and PET/CT shows lesions with high FDG uptake, the presence of yolk sac tumor component in the teratoma should be suspected. PET/CT helps to compensate for the limitations of pathological sampling, thus confirming the diagnosis. If teratoma coexists with other GCT components, the patient has a poorer prognosis, and PET/CT plays an important role in predicting patient prognosis, monitoring tumor metastasis and recurrence, and evaluating the therapeutic effect.

Data availability statement

The original contributions presented in the study are included in the article/supplementary material, further inquiries can be directed to the corresponding authors.

Ethics statement

Written informed consent was obtained from the minor(s)' legal guardian/next of kin for the publication of any potentially identifiable images or data included in this article.

Author contributions

HJ: Writing – original draft, Writing – review & editing. YQ: Writing – original draft, Writing – review & editing. WH: Writing – review & editing. YZ: Writing – review & editing. ZC: Writing – review & editing. AW: Writing – review & editing, Supervision. LK: Writing – review & editing, Supervision.

Funding

The author(s) declare financial support was received for the research, authorship, and/or publication of this article.

This work was supported by the National Natural Science Foundation of China (82171970), the Beijing Science Foundation for Distinguished Young Scholars (JQ21025), the Beijing Municipal Science & Technology Commission (Z221100007422027), National High Level Hospital Clinical Research Funding (Interdisciplinary Research Project of Peking University First Hospital, 2023IR17).

Conflict of interest

The authors declare that the research was conducted in the absence of any commercial or financial relationships that could be construed as a potential conflict of interest.

Publisher's note

All claims expressed in this article are solely those of the authors and do not necessarily represent those of their affiliated organizations, or those of the publisher, the editors and the reviewers. Any product that may be evaluated in this article, or claim that may be made by its manufacturer, is not guaranteed or endorsed by the publisher.

References

1. Moch H, Amin MB, Berney DM, Compérat EM, Gill AJ, Hartmann A, et al. The 2022 World Health Organization classification of tumours of the urinary system and male genital organs-part a: renal, penile, and testicular tumours. *Eur Urol*. (2022) 82:458–68. doi: 10.1016/j.eururo.2022.06.016

2. Moch H, Cubilla AL, Humphrey PA, Reuter VE, Ulbright TM. The 2016 who classification of tumours of the urinary system and male genital organs-part a: renal, penile, and testicular tumours. *Eur Urol*. (2016) 70:93–105. doi: 10.1016/j.eururo.2016.02.029

3. Müller J, Skakkebaek NE, Ritzén M, Plöen L, Petersen KE. Carcinoma in situ of the testis in children with 45,X/46,XY gonadal dysgenesis. *J Pediatr*. (1985) 106:431–6. doi: 10.1016/s0022-3476(85)80670-3

4. Lyn BJ, Cheng L. 2016 World Health Organization classification of tumors of the testis and the penis: an update. *Zhonghua Bing Li Xue Za Zhi*. (2016) 45:518–21. doi: 10.3760/cma.j.issn.0529-5807.2016.08.004

5. Taza F, Chovanec M, Snavely A, Hanna NH, Cary C, Masterson TA, et al. Prognostic value of Teratoma in primary tumor and Postchemotherapy retroperitoneal lymph node dissection specimens in patients with metastatic germ cell tumor. *J Clin Oncol*. (2020) 38:1338–45. doi: 10.1200/jco.19.02569

6. Peng B, Yang C, Cao YS. Tissue type analysis of 122 pediatric testicular tumors in young male players. *Int J Med Sci Phys Act Sport*. (2023) 23:261–70. doi: 10.15366/rimcafd2022.89.018

7. Aide N, Briand M, Bohn P, Dutoit S, Lasnon C, Chasle J, et al. αvβ3 imaging can accurately distinguish between mature teratoma and necrosis in ^{18}F-Fdg-negative residual masses after treatment of non-Seminomatous testicular Cancer: a preclinical study. *Eur J Nucl Med Mol Imaging*. (2011) 38:323–33. doi: 10.1007/s00259-010-1624-9

8. Sugawara Y, Zasadny KR, Grossman HB, Francis IR, Clarke MF, Wahl RL. Germ cell tumor: differentiation of viable tumor, mature Teratoma, and necrotic tissue with FDG pet and kinetic modeling. *Radiology*. (1999) 211:249–56. doi: 10.1148/radiology.211.1.r99ap16249

9. Funt SA, Patil S, Feldman DR, Motzer RJ, Bajorin DF, Sheinfeld J, et al. Impact of teratoma on the cumulative incidence of disease-related death in patients with advanced germ cell tumors. *J Clin Oncol*. (2019) 37:2329–37. doi: 10.1200/JCO.18.01608

10. Siegel RL, Miller KD, Wagle NS, Jemal A. Cancer statistics, 2023. *CA Cancer J Clin*. (2023) 73:17–48. doi: 10.3322/caac.21763

11. Brosman SA. Testicular tumors in Prepubertal children. *Urology*. (1979) 13:581–8. doi: 10.1016/0090-4295(79)90375-3

12. Cabral FC, Krajewski KM, Rosenthal MH, Hirsch MS, Howard SA. Teratoma with malignant transformation: report of three cases and review of the literature. *Clin Imag*. (2014) 38:589–93. doi: 10.1016/j.clinimag.2014.04.011

13. Yoshida M, Tanaka M, Gomi K, Ohama Y, Kigasawa H, Iwanaka T, et al. Malignant steroidogenic tumor arising from Sacrococcygeal mature Teratoma. *Hum Pathol*. (2011) 42:1568–72. doi: 10.1016/j.humpath.2010.12.022

14. Donkol RH, Monib S, Eltounsi I. Occult testicular Teratoma presenting with solid mesenteric metastasis. *J Ultrasound Med*. (2007) 26:675–8. doi: 10.7863/jum.2007.26.5.675

15. Ma X, Xiao J, Wang W. Retroperitoneal dermoid cyst mimicking a Liposarcoma based on imaging assessment: case report and literature review. *Gland Surg*. (2021) 10:2062–8. doi: 10.21037/gs-21-65

16. Epifanio M, Baldissera M, Esteban FG, Baldisserotto M. Mature testicular teratoma in children: multifaceted tumors on ultrasound. *Urology*. (2014) 83:195–7. doi: 10.1016/j.urology.2013.07.046

17. Cai X, Yang X, Li T. Comparative analysis of MRI and B-ultrasound diagnosis of testicular tumors in children. *J Clin Radiol*. (2019) 38:313–7. doi: 10.13437/j.cnki.jcr.2019.02.033

18. Guo C, Wang L, Liu W, Xu H. Ovarian malignant teratoma: ultrasound findings and misdiagnosis analysis. *Chin J Med Imag*. (2013) 21:775–9. doi: 10.3969/j.issn.1005-5185.2013.10.016

19. Qiu X-X, Xia J, Du L-X, Hu R-F, Lei Y. Diagnostic value of MRI in testicular tumor. *Natl J Androl*. (2012) 18:493–8. doi: 10.13263/j.cnki.nja.2012.06.008

20. Park SB, Cho KS, Kim JK. CT findings of mature cystic teratoma with malignant transformation: comparison with mature cystic teratoma. *Clin Imag*. (2011) 35:294–300. doi: 10.1016/j.clinimag.2010.08.016

21. Krag Jacobsen G, Barlebo H, Olsen J, Schultz HP, Starklint H, Søgaard H, et al. Testicular germ cell tumours in Denmark 1976-1980. Pathology of 1058 consecutive cases. *Acta Radiol Oncol*. (1984) 23:239–47. doi: 10.3109/02841868409136019

22. Kim BH. Pure immature Teratoma with increase of serum alpha-fetoprotein – a case report. *Korean J Pathol*. (2007) 41:63–5.

23. Motzer RJ, Amsterdam A, Prieto V, Sheinfeld J, Murty VV, Mazumdar M, et al. Teratoma with malignant transformation: diverse malignant Histologies arising in men with germ cell tumors. *J Urol*. (1998) 159:133–8. doi: 10.1016/S0022-5347(01)64035-7

24. Suh YJ, Kim MJ, Lee MJ. Increased ^{18}F-Fdg uptake by a retroperitoneal mature cystic teratoma in an infant. *Clin Nucl Med*. (2014) 39:352–4. doi: 10.1097/RLU.0b013e3182995dfd

25. Quak E, Kovacs I, Oyen WJ, van der Graaf WT. FDG-PET/CT in a patient with poor-risk non-seminoma testis with mature teratoma and secondary Gliosarcoma: multimodality imaging for guiding multimodality treatment. *Nucl Med Mol Imaging*. (2015) 49:237–40. doi: 10.1007/s13139-015-0321-9

26. Cárdenas-Perilla R. Malignant somatic transformation arising from Teratoma in metastatic testicular germ cell tumor detected on (18)F-FDG PET/CT. *Rev Esp Med Nucl Imagen Mol*. (2022) 41:S39–s41. doi: 10.1016/j.remnie.2021.07.004

27. Abu-Salha YM, Ahlschlager L, Milowsky MI, Saunders K, Rose TL, Wobker SE, et al. Vigilance is key: metastatic teratoma in an enlarging retroperitoneal mass after treatment of advanced seminoma – a case report. *J Clin Urol*. (2022). doi: 10.1177/20514158221075411

28. Reinhardt MJ, Müller-Mattheis VG, Gerharz CD, Vosberg HR, Ackermann R, Müller-Gärtner HW. FDG-PET evaluation of retroperitoneal metastases of testicular Cancer before and after chemotherapy. *J Nucl Med*. (1997) 38:99–101.

29. Green DB, La Rosa FG, Craig PG, Khani F, Lam ET. Metastatic mature teratoma and growing teratoma syndrome in patients with testicular non-Seminomatous germ cell tumors. *Korean J Radiol*. (2021) 22:1650–7. doi: 10.3348/kjr.2020.1391

30. Talerman A, Haije WG, Baggerman L. Serum Alphafetoprotein (AFP) in patients with germ cell tumors of the gonads and Extragonadal sites: correlation between endodermal sinus (yolk sac) tumor and raised serum AFP. *Cancer*. (1980) 46:380–5. doi: 10.1002/1097-0142(19800715)46:2<380::AID-CNCR2820460228>3.0.CO;2-U

31. Wu P, Luo R, Sun B, Zhao J, Xu Q, Feng S, et al. Sall4 is a useful marker for pediatric yolk sac tumors. *Pediatr Surg Int*. (2020) 36:727–34. doi: 10.1007/s00383-020-04652-w

32. Cao D, Humphrey PA, Allan RW. Sall4 is a novel sensitive and specific marker for metastatic germ cell tumors, with particular utility in detection of metastatic yolk sac tumors. *Cancer*. (2009) 115:2640–51. doi: 10.1002/cncr.24308

33. Carver BS, Al-Ahmadie H, Sheinfeld J. Adult and pediatric testicular teratoma. *Urol Clin North Am*. (2007) 34:245–51; abstract x. doi: 10.1016/j.ucl.2007.02.013

34. Simmonds PD, Lee AH, Theaker JM, Tung K, Smart CJ, Mead GM. Primary pure teratoma of the testis. *J Urol*. (1996) 155:939–42. doi: 10.1016/S0022-5347(01)66352-3

35. Read G, Stenning SP, Cullen MH, Parkinson MC, Horwich A, Kaye SB, et al. Medical research council prospective study of surveillance for stage I testicular teratoma. Medical research council testicular tumors working party. *J Clin Oncol*. (1992) 10:1762–8. doi: 10.1200/jco.1992.10.11.1762

36. Richie JP. Late recurrence in 1263 men with testicular germ cell tumors. Multivariate analysis of risk factors and implications for management. *J Urol*. (2003) 169:2419–20.

frontiers | Frontiers in Medicine

TYPE Case Report
PUBLISHED 19 September 2023
DOI 10.3389/fmed.2023.1266630

OPEN ACCESS

EDITED BY
Carmelo Caldarella,
Radioterapia Oncologica ed Ematologia,
Fondazione Policlinico Universitario A. Gemelli IRCCS, Italy

REVIEWED BY
Salvatore Annunziata,
Fondazione Policlinico Universitario A. Gemelli IRCCS, Italy
Luca Urso,
Hospital Santa Maria della Misericordia of Rovigo, Italy

*CORRESPONDENCE
Aixiang Wang
✉ wax20030826@126.com
Lei Kang
✉ kanglei@bjmu.edu.cn

RECEIVED 25 July 2023
ACCEPTED 31 August 2023
PUBLISHED 19 September 2023

CITATION
Huang W, Peng Y, Zhang Y, Qiu Y, Liu Y, Wang A and Kang L (2023) Multimodality imaging of Xp11.2 translocation/TFE3 gene fusion associated with renal cell carcinoma: a case report.
Front. Med. 10:1266630.
doi: 10.3389/fmed.2023.1266630

Multimodality imaging of Xp11.2 translocation/TFE3 gene fusion associated with renal cell carcinoma: a case report

Wenpeng Huang[1], Yushuo Peng[1], Yongbai Zhang[1], Yongkang Qiu[1], Yi Liu[2,3,4], Aixiang Wang[2,3,4]* and Lei Kang[1]*

[1]Department of Nuclear Medicine, Peking University First Hospital, Beijing, China, [2]Department of Urology, Peking University First Hospital, Beijing, China, [3]Institute of Urology, Peking University, Beijing, China, [4]National Urological Cancer Center, Beijing, China

Background: Xp11.2 translocation/TFE3 gene fusion associated with renal cell carcinoma (Xp11.2 RCC) exhibits unique biological characteristics and is associated with an increased incidence of tumor thrombosis, lymph node metastasis, and advanced disease stages. Multimodality imaging, including US, contrast-enhanced CT, multi-parametric MRI, and ^{18}F-FDG PET/CT plays a crucial role in the preoperative diagnosis and differentiation of renal tumors.

Case report: A 15-year-old female presented with lumbar pain worsened, and developed persistent painless hematuria. The CT attenuation values of the scan without contrast, corticomedullary phase, nephrographic phase, and delayed phases were 35 HU, 83 HU, 82 HU, and 75 HU, respectively. The solid component of the mass displayed heterogeneous marked enhancement. Furthermore, MRU indicated that the lesion involved the cortical medulla and infringed on the renal sinus fat. The lesion appeared isosignal in T1WI, slightly low signal in T2WI, and slightly high signal in DWI. The degree of enhancement in the three phases of enhancement scan was lower than that in the renal parenchyma, and hemorrhage and necrosis were observed within the internal part of the lesion. To further clarify the staging, the patient underwent ^{18}F-FDG PET/CT. PET/CT images showed multiple irregular occupancies in the right kidney with unclear borders, showing a heterogeneous increase in ^{18}F-FDG uptake, with SUVmax values ranging from 2.3 to 5.2 in the routine imaging phase (60 min post-injection), compared to SUVmax values ranging from 2.8 to 6.9 in the delayed imaging phase (160 min post-injection). Additionally, multiple enlarged and fused lymph nodes were observed in the medial part of the right kidney and the retroperitoneum, exhibiting a heterogeneous increase in ^{18}F-FDG uptake, with SUVmax values ranging from 4.1 to 8.7 in the routine imaging phase, compared to SUVmax values ranging from 4.4 to 9.1 in the delayed imaging phase. The postoperative pathology, immunohistochemistry, and molecular analysis of histiocytes were consistent with a diagnosis of Xp11.2 RCC. One month after surgery, enhanced-CT examination of the patient revealed lung metastasis, peritoneal metastasis, and multiple lymph node metastases throughout the body, with an overall survival of 16 months.

Conclusion: Xp11.2 RCC exhibits unique biological characteristics and is associated with an increased incidence of tumor thrombosis, lymph node metastasis, and advanced disease stages. Long-term follow-up is essential to monitor the likelihood of recurrence and metastasis. ^{18}F-FDG PET/CT examination can comprehensively visualize the lesion's location and extent, providing a basis

for clinical tumor staging and aiding in treatment monitoring and follow-up. To address the limitations of FDG, the utilization of specific tracers designed for RCC or tracers that are not excreted via the urinary system would be ideal. Further advancements in molecular imaging technologies and the development of novel tracers hold great promise in advancing the diagnosis and management of RCC, ultimately contributing to better patient outcomes and overall disease management.

KEYWORDS

translocation renal cell carcinoma, Xp11.2, ultrasound, computed tomography, magnetic resonance imaging, ^{18}F-FDG, PET/CT

Introduction

Annually, malignant kidney tumors are diagnosed in 3–15 individuals per 100,000 (1). Apart from the well-known clear cell cancers, which constitute 80–85% of all renal cell cancer (RCC) cases, the 2016 World Health Organization (WHO) classification introduced new molecular-driven histotypes. These include MiTF family translocation carcinoma, succinate dehydrogenase (SDH)-deficient RCC, and hereditary leiomyomatosis and RCC syndrome-associated RCC (2). One infrequent RCC subtype is RCC associated with Xp11.2 translocation/TFE3 gene fusion (Xp11.2 RCC) (3, 4), which has been integrated into the MiT family translocation RCC category. The significance of molecular data in enhancing kidney tumor classification was affirmed in the latest WHO classification. This new classification introduced a category of molecularly defined RCC, encompassing TFE3-rearranged RCC, TFEB-rearranged and TFEB-amplified RCC, FH-deficient RCC, SDH-deficient RCC, ALK-rearranged RCC, ELOC (formerly TCEB1)-mutated RCC, and SMARCB1 (INI1)-deficient RCC (5, 6). For TFE3-rearranged RCC, the identification of gene rearrangement through FISH assays or RNA-sequencing stands as the gold standard for confirming diagnosis (7, 8). Due to distinct translocation genes implicated, varying morphology, and notably different behavior, TFE3-rearranged RCC are currently recognized as distinct entities. Additionally, Xp11.2 RCC has been documented to display a more aggressive behavior when compared to other RCC subtypes, exhibiting a propensity for distant and lymphatic metastases, ultimately leading to a poorer prognosis (9, 10).

To enhance understanding of this rare neoplasm, we present a case study detailing the multimodal imaging manifestations of a patient with Xp11.2 RCC. Following surgical resection of the tumor, the patient experienced rapid disease progression, developing pulmonary metastases, peritoneal metastases, and multiple lymph node metastases throughout the body, ultimately resulting in an overall survival of 16 months.

Case presentation

A 15-year-old female presented with right lumbar pain, which began 2 years ago and was left untreated. Two months ago, the patient's lumbar pain worsened, and she developed persistent painless hematuria. On admission, physical examination revealed a palpable hard mass in the right upper abdomen. Laboratory tests showed elevated alpha-fetoprotein levels (18.32 ng/mL).

Abdominal ultrasound was performed, revealing a highly heterogeneous hypoechoic mass in the lower right abdomen with an irregular, lobulated morphology. The mass encroached on the renal sinus and protruded outward from the kidney. A class I blood flow signal was observed within and around the mass (Figure 1A). Additionally, multiple enlarged lymph nodes were detected adjacent to the right renal hilum, in proximity to the inferior vena cava, in the right adrenal region, and near the abdominal aorta. These lymph nodes were fused together and exhibited uneven echogenicity (Figure 1B). CT examination revealed a right renal mass measuring approximately 5.2 cm × 7.1 cm × 8.8 cm (AP × LR × SI) with multiple calcifications. The CT attenuation values of the scan without contrast, corticomedullary phase, nephrographic phase, and delayed phases were 35 HU, 83 HU, 82 HU, and 75 HU, respectively. The solid component of the mass displayed heterogeneous marked enhancement, with areas of hypodense necrosis observed within. Additionally, several fused lymph nodes were identified in the medial right kidney and retroperitoneum, showing the same density and enhancement pattern as the right intrarenal lesion (Figure 2). Furthermore, magnetic resonance urography (MRU) indicated that the lesion was located in the ventral part of the middle and lower pole of the right kidney. The lesion involved the cortical medulla and infringed on the renal sinus fat. The lesion appeared isosignal in T1WI, slightly low signal in T2WI, and slightly high signal in DWI (Figures 3A–C). The degree of enhancement in the three phases of enhancement scan was lower than that in the renal parenchyma, and hemorrhage and necrosis were observed within the internal part of the lesion. Additionally, pseudocoated membrane was observed around the lesion (Figures 3D–F).

Compression and forward displacement of the right renal vein and inferior vena cava were present, with no evidence of tumor thrombus in the vein. To further clarify the staging, the patient underwent ^{18}F-FDG PET/CT to evaluate the lesions. PET/CT images showed multiple irregular occupancies in the right kidney with unclear borders, showing a heterogeneous increase in ^{18}F-FDG uptake, with SUVmax values ranging from 2.3 to 5.2 in the routine imaging phase (60 min post-injection), compared to SUVmax values ranging from 2.8 to 6.9 in the delayed imaging phase (160 min post-injection). Additionally, multiple enlarged and fused lymph nodes were observed in the medial part of the right kidney and the retroperitoneum, exhibiting a heterogeneous increase in ^{18}F-FDG uptake, with SUVmax values ranging from 4.1 to 8.7 in the routine imaging phase, compared to SUVmax values ranging

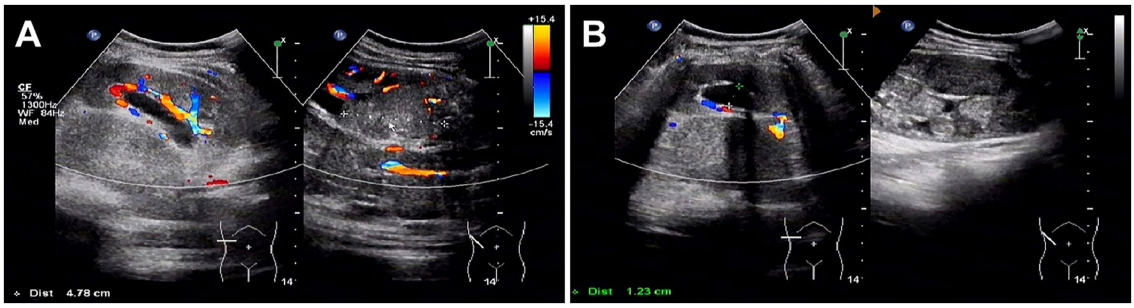

FIGURE 1
Ultrasound images of Xp11.2 translocation/TFE3 gene fusion associated with renal cell carcinoma (Xp11.2 RCC). **(A)** A highly heterogeneous hypoechoic mass in the right subrenal region with an irregular, lobulated morphology. The mass encroached on the renal sinus and protruded outward from the kidney. A class I blood flow signal was observed within and around the mass. **(B)** Multiple enlarged lymph nodes were detected adjacent to the right renal hilum, in proximity to the inferior vena cava, in the right adrenal region, and near the abdominal aorta.

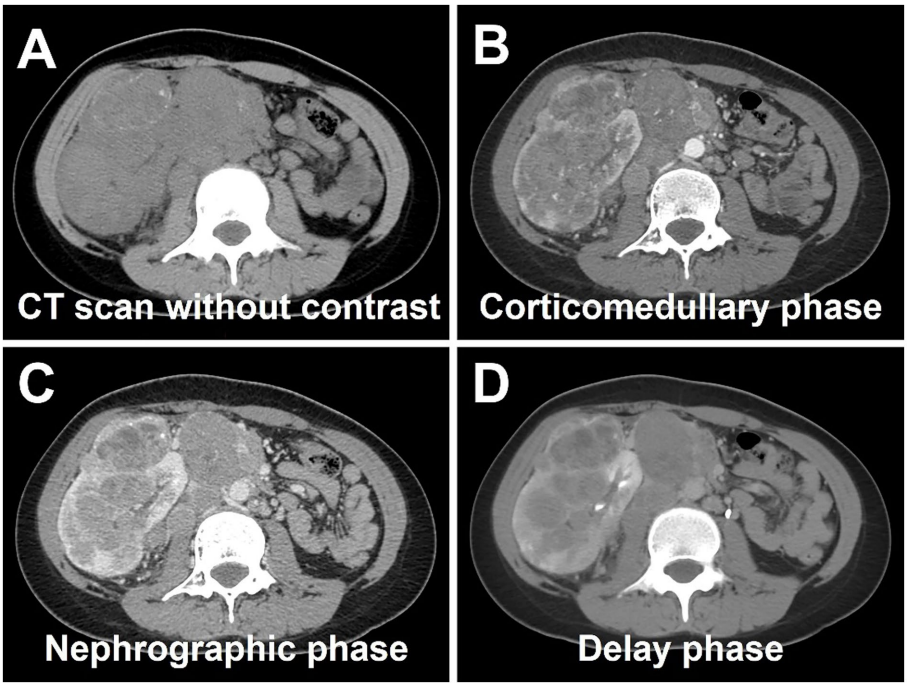

FIGURE 2
Computed tomography (CT) images of Xp11.2 RCC. **(A)** The transverse image shows a right renal mass measuring approximately 5.2 cm × 7.1 cm × 8.8 cm with multiple calcifications. **(B–D)** The CT attenuation values of corticomedullary phase, nephrographic phase, and delayed phases were 83 HU, 82 HU, and 75 HU, respectively. The solid component of the mass displayed heterogeneous marked enhancement, with areas of hypodense necrosis observed within. Several fused lymph nodes were identified in the medial right kidney and retroperitoneum, showing the same density and enhancement pattern as the right intrarenal lesion.

from 4.4 to 9.1 in the delayed imaging phase. The lesions were poorly demarcated from the right renal artery, right ureter, lower vena cava, and the head of the pancreas, and they were not well demarcated from the right renal artery. Furthermore, the lesion exhibited poor demarcation from the right kidney, right renal artery, right ureter, inferior vena cava, abdominal aorta, and the head of the pancreas, with the right kidney being displaced laterally due to compression, resulting in dilated hydronephrosis of the right renal pelvis (Figures 4A–C). In the right adrenal gland, a soft tissue density nodule measuring approximately 1.2 cm × 2.0 cm was visible, showing increased ^{18}F-FDG uptake with an SUVmax of 4.4 (Figure 4D), compared to SUVmax of 4.9 measured during delayed imaging. Based on the diagnostic imaging, the patient was considered to have nephroblastoma with concurrent retroperitoneal lymph node and right adrenal gland metastases.

The patient underwent surgical resection of the right renal lesion and lymph node dissection. Postoperative pathologic microscopy revealed papillary structures composed of epithelioid clear cells, eosinophils, and gravel bodies (Figures 5A,B). Immunohistochemistry showed positive expression of TFE-3 (Figure 5C), HMB45, P504S, CD10, Vimentin, GATA-3, and AE1/AE3. The molecular analysis of histiocytes further revealed the *TFE3* gene disruption. The above findings were consistent with the diagnosis of Xp11.2 RCC. One

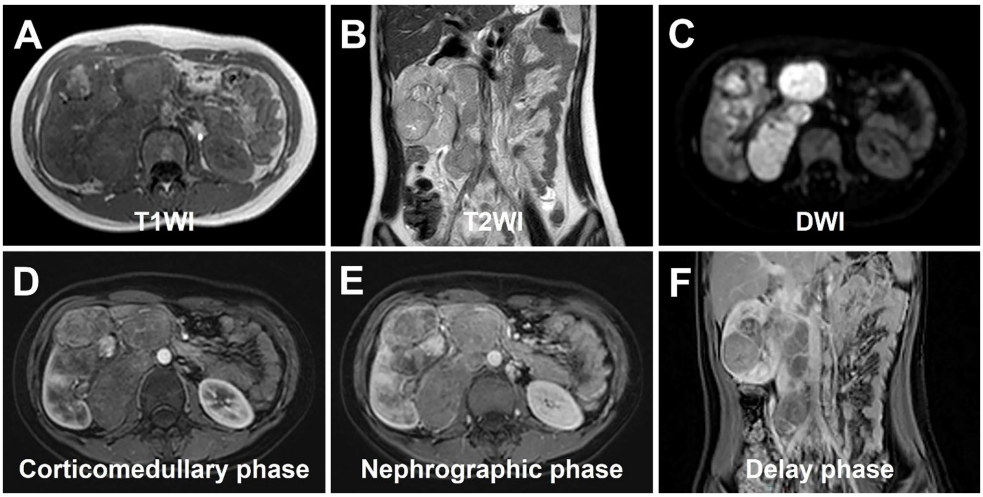

FIGURE 3
magnetic resonance urography (MRU) of Xp11.2 RCC. **(A)** T1WI transverse image shows a heterogeneous isosignal lesion. **(B)** T2WI transverse image shows a heterogeneous slightly low signal lesion. **(C)** DWI transverse image shows a slightly high signal lesion. **(D–F)** The degree of enhancement in the three phases of enhancement scan was lower than that in the renal parenchyma, and hemorrhage and necrosis were observed within the internal part of the lesion. Additionally, pseudocoated membrane was observed around the lesion.

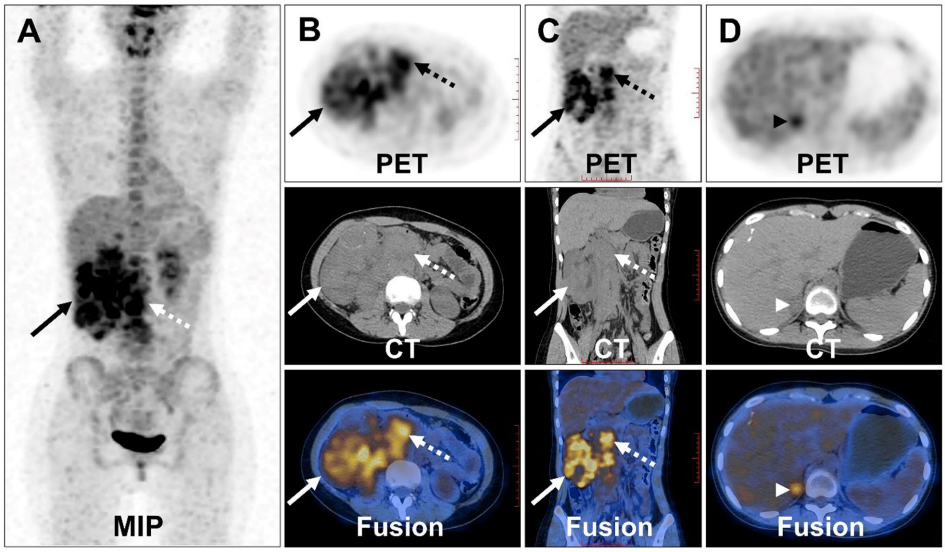

FIGURE 4
^{18}F-FDG PET/CT images of Xp11.2 RCC. **(A)** The anteroposterior 3-dimensional maximum intensity projection image (MIP) demonstrated increased metabolic activity in the right kidney (long arrows) and retroperitoneal lymph nodes (dashed arrows). **(B,C)** Transverse images and coronal images showed multiple irregular occupancies in the right kidney with unclear borders, showing a heterogeneous increase in FDG uptake, with SUVmax values ranging from 2.3 to 5.2. Multiple enlarged and fused lymph nodes were observed in the medial part of the right kidney and the retroperitoneum, exhibiting a heterogeneous increase in FDG uptake, with SUVmax values ranging from 4.1 to 8.7. **(D)** Transverse images showed a soft tissue density nodule of the right adrenal gland measuring approximately 1.2 cm × 2.0 cm (arrowheads), with increased FDG uptake (SUVmax = 4.4).

month after surgery, enhanced-CT examination of the patient revealed lung metastasis, peritoneal metastasis, and multiple lymph node metastases throughout the body, with an overall survival of 16 months.

Discussion

Xp11.2 RCC, a rare subtype of RCC, predominantly affects children rather than adults, accounting for 20–40% of pediatric RCC cases and 1–1.6% of RCC cases in adults (11). Commonly, patients with Xp11.2/TFE3 RCC present with nonspecific symptoms such as abdominal pain, flank mass, and gross hematuria (12). Despite advancements in research, the underlying mechanism of Xp11.2 RCC remains elusive. Some researchers have postulated that the abnormal upregulation of the HGF/MET pathway is closely related to the uncontrolled proliferation, metastasis, and invasion of tumor cells, which occurs when the TFE3 fusion protein binds with the MET promoter, leading to increased MET protein expression (13). Additionally, the inactivation of the FLCN tumor suppressor gene has been suggested to elevate the transcriptional activity of the TFE3 protein, contributing to tumorigenesis (14).

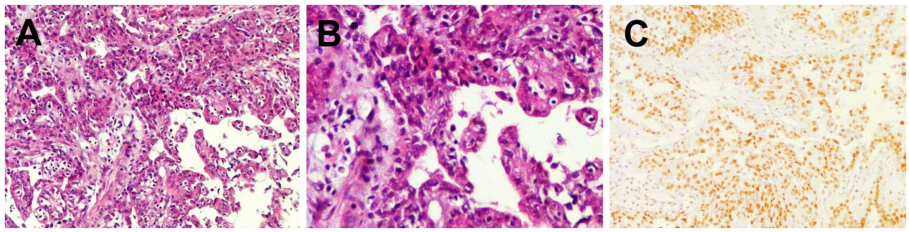

FIGURE 5
Histopathological and immunohistochemical images of Xp11.2 RCC. **(A,B)** Hematoxylin–eosin (HE) staining (magnification ×100 and 200) showed papillary structures composed of epithelioid clear cells, eosinophils, and gravel bodies. **(C)** Immunohistochemistry showed that the tumor cells were positive for TFE-3 (magnification ×100).

According to Argani et al. (15), Xp11.2-RCC results from the fusion of the TFE3 gene with one of five different genes: ASPL (17q25), PRCC (1q21), PSF (1q34), NonO (Xq12), and CLTC (17q23), characterized by chromosomal rearrangements including t(X;17)(p11.2;q25), t(X;1)(p11.2;q21), t(X;1)(p11.2;p34), t(X;17)(p11.2;q23), and inv.(X)(p11.2;q12), respectively (16).

Pathological diagnosis of Xp11.2 RCC is challenging due to its heterogeneous features, characterized by prominent eosinophilic cytoplasm and a papillary growth pattern (17–19). The overexpression of TFE3 protein resulting from translocations makes immunohistochemistry (IHC) assay the most commonly used diagnostic technique in clinical practice (20). However, false negatives and positives may occur. Currently, fluorescence *in situ* hybridization (FISH) detection is considered the most reliable method for diagnosing Xp11.2 RCC (13).

Multimodality imaging, including conventional ultrasound (US), contrast-enhanced US (CEUS), computed tomography (CT), and multi-parametric magnetic resonance imaging (MRI), plays a crucial role in the preoperative diagnosis and differentiation of renal tumors (21). While most Xp11.2 RCCs are located in the renal medullary tissue or in both the medullary and cortical tissues within the kidney's contour, some may breach the renal envelope, leading to alterations in the renal contour and manifesting as sizeable masses (22). These tumors often exhibit heterogeneity attributed to cystic degeneration, necrosis, or hemorrhage.

CEUS offers numerous advantages, including noninvasiveness, real-time imaging capabilities, and the accurate assessment of renal tumor characteristics and vascularity. In a study conducted by Ma et al. (23), fast wash-out patterns were identified as the primary features of Xp11.2 RCC. Furthermore, Wei et al. (24) investigated the differentiation between Xp11.2 RCC and clear cell type renal cell carcinoma (ccRCC) using CEUS and found that Xp11.2 RCC exhibited lower peak enhancement compared to ccRCC. CT examination offers the advantage of high spatial resolution and the ability to detect and recognize calcifications in the evaluation of RCC. Previous studies have emphasized the utility of CT characteristics and dynamic contrast-enhanced patterns in distinguishing Xp11.2 RCC from clear cell RCC (ccRCC) (25, 26). In a comparative study by He et al. (26), which included 20 cases of Xp11.2 RCC and 21 cases of renal clear cell carcinoma, the tumor-to-cortex attenuation ratio in the corticomedullary phase, with a cutoff value of less than 0.62, demonstrated a sensitivity of 90.0% and a specificity of 92.9% for differentiating Xp11.2 RCC from ccRCC. CT characteristics and dynamic contrast-enhanced patterns, along with the index, were effective in distinguishing Xp11.2 RCC from ccRCC. MRI examination plays an essential role in the evaluation of RCC, offering advantages such as superior soft tissue contrast, multi-planar imaging capabilities, and the ability to assess tumor vascularity and invasion, thereby facilitating accurate diagnosis and treatment planning. In terms of MRI signal features, Xp11.2 RCC typically appears hyper- to isointense on T1WI and heterogeneously hypointense on T2WI, with restricted diffusion observed on DWI. However, when the tumor involves hemorrhage and lipid, the signal can be hybrid in both T1WI and T2WI. Tumor necrosis and hemorrhage are frequent occurrences in advanced stage patients and represent independent characteristics unrelated to age or tumor size (4, 27). In a comparative analysis, Liu et al. (28) reported that all Xp11.2 RCCs exhibited an infiltrative growth pattern, whereas Zhu et al. (29) found that all 6 Xp11.2 RCCs appeared as well-defined masses. Altinok et al. (16) discovered that 73% of pediatric Xp11.2 RCCs were associated with thick, fibrous capsules, and Zhu et al. (29) described a capsule sign with a clear edge in all 9 cases. Within our study, Xp11.2 renal carcinoma showed invasive growth, involving both the renal medulla and cortex, presenting as a heterogeneous mass with cystic components, calcifications, and hemorrhages, and revealing a visible pseudocapsule. The density and degree of tumor enhancement may be related to the compression of vasculature by fibrous tissues (27). Following contrast administration, the lesions exhibited a mild, prolonged enhancement pattern (30, 31). In this case, Xp11.2 RCC showed heterogeneous enhancement, likely attributed to the uniform microvessel area within the tumor (32).

Studies focusing on FDG-PET for RCC are scarce, primarily due to challenges in distinguishing the radioactivity of FDG accumulated in renal tumors from the radioactivity of FDG excreted via the urinary system during physiological processes. Moreover, false-negative cases can result in low sensitivity for RCC detection. Nonetheless, evidence suggests that FDG-PET, utilizing SUV, may play a role in predicting the pathological grade of renal tumors (33). Xp11.2 RCC is associated with an increased incidence of tumor thrombosis, lymph node metastasis, and later stages of disease (26). PET/CT staging demonstrates higher sensitivity compared to other imaging modalities. The PET/CT manifestations ofXp11.2 RCC exhibit significant hypermetabolic activity and consistently present varying degrees of renal vascular invasion, lymph node involvement, or distant metastasis. Further observation of the similarities and differences between PET/CT manifestations of Xp11.2 RCC and other types of renal cancers is warranted, particularly as more cases are accumulated.

Several studies have extensively investigated and documented the potential applicability of radiotracers beyond FDG for the purpose of characterizing and staging RCC (34–37). Leveraging the marked expression of carbonic anhydrase IX (CAIX) observed in 95% of ccRCC,

the anti-CAIX monoclonal antibody girentuximab emerges as a promising candidate for ccRCC detection. In a study by Hekman et al. (37), ^{89}Zr-girentuximab PET/CT emerged as an invaluable diagnostic tool, capable of guiding clinical decision-making when faced with diagnostic uncertainties related to ccRCC suspicion. The upregulation of the receptor tyrosine kinase c-MET in RCC demonstrates a correlation with overall survival in cases of metastatic disease (38). A novel PET ligand, ^{68}Ga-EMP-100, rooted in a c-Met binding peptide, has been developed. Mittlmeier et al. (35) demonstrated the feasibility of visualizing c-MET expression using ^{68}Ga-EMP-100, enabling effective clinicopathological staging in cases of metastatic RCC. Recent case reports have showcased the efficacy of ^{68}Ga/^{18}F-PSMA PET/CT in restaging recurrent renal cancer post-nephrectomy (34, 36). However, there remains an absence of documented experiences regarding the imaging of Xp11.2 RCC with specific radiotracers within the current literature. Recent investigations have highlighted the notable therapeutic impact of vascular endothelial growth factor receptor-targeted agents and mammalian target of rapamycin inhibitors in the treatment of metastatic Xp11.2 RCC (15, 39). Notably, radionuclide-labeled vascular endothelial growth factor receptor-targeted agents hold the potential to provide insightful contributions to the characterization, staging, and assessment of treatment response for Xp11.2 RCC. Further advancements in molecular imaging technologies and the development of novel tracers hold great promise in advancing the diagnosis and management of RCC, ultimately contributing to better patient outcomes and overall disease management.

Differentiating Xp11.2 RCC from other subtypes of renal cancer is crucial. Distinguishing features of ccRCC, such as necrosis and hemorrhage, often correlate with lymph node metastasis and renal vein infiltration, similar to those found in Xp11.2 RCC (40, 41). However, ccRCC stands out as a hyper-vascular tumor, displaying significantly greater enhancement in the corticomedullary phase. In contrast, Xp11.2 RCC exhibits less enhancement than ccRCC. Notably, overlapping morphological features between Xp11.2 RCC and pRCC are observed, as pRCC also tends to appear hypo-vascular. A well-differentiated papillary RCC (pRCC) is characterized by homogeneity, small size, regular shape, low-level enhancement, and a peripheral location. On T2-weighted imaging, pRCC typically presents as a mass with homogeneous low signal intensity, likely due to cytoplasmic or interstitial histiocytic hemosiderin deposition in the tumor cells (42, 43). Additionally, pRCC is considered a low-grade malignant tumor with a low likelihood of retroperitoneal lymph node metastasis and the formation of renal vein cancer emboli. In contrast, chromophobe RCC often localize peripherally and manifest as well-defined, large, solid masses without necrosis or calcification, frequently diagnosed at an early stage (44, 45).

The treatment for Xp11.2 RCC remains ill-defined. Radical surgical excision stands as the primary therapy for early-stage cases (46–48). Regarding adjuvant treatment, there is still no research elucidating the most optimal or reliable approach for individual patients (49, 50). Chemotherapy, such as sunitinib, can also be considered (51). However, regardless of the applied treatment, Xp11.2 RCC demonstrates a poorer prognosis (19, 52). Lifelong follow-up should be implemented, incorporating medical history, physical examination, laboratory tests, and imaging data, for a more accurate assessment of the patient's prognosis. According to the study, T stage at presentation is the sole factor associated with both progression-free survival and overall survival in patients with Xp11.2 RCC (50, 53).

Conclusion

In conclusion, Xp11.2 RCC exhibits unique biological characteristics and is associated with an increased incidence of tumor thrombosis, lymph node metastasis, and advanced disease stages. Long-term follow-up is essential to monitor the likelihood of recurrence and metastasis. In this report, we present a case that may contribute to a better understanding of the disease for clinicians. ^{18}F-FDG PET/CT examination can comprehensively visualize the lesion's location and extent, providing a basis for clinical tumor staging and aiding in treatment monitoring and follow-up. To address the limitations of FDG, the utilization of specific tracers designed for RCC or tracers that are not excreted via the urinary system would be ideal. Further advancements in molecular imaging technologies and the development of novel tracers hold great promise in advancing the diagnosis and management of RCC, ultimately contributing to better patient outcomes and overall disease management.

Data availability statement

The original contributions presented in the study are included in the article/supplementary material, further inquiries can be directed to the corresponding authors.

Ethics statement

Written informed consent was obtained from the individual(s), and minor(s)' legal guardian/next of kin, for the publication of any potentially identifiable images or data included in this article.

Author contributions

WH: Writing – original draft, Writing – review & editing. YP: Writing – review & editing. YZ: Writing – review & editing. YQ: Writing – review & editing. YL: Writing – review & editing. AW: Writing – review & editing. LK: Writing – original draft, Writing – review & editing.

Funding

The author(s) declare financial support was received for the research, authorship, and/or publication of this article. This work was supported by the National Natural Science Foundation of China (82171970), the Beijing Science Foundation for Distinguished Young Scholars (JQ21025), the Beijing Municipal Science and Technology Commission (Z221100007422027), and National High Level Hospital Clinical Research Funding (Interdisciplinary Research Project of Peking University First Hospital, 2023IR17).

Conflict of interest

The authors declare that the research was conducted in the absence of any commercial or financial relationships that could be construed as a potential conflict of interest.

Publisher's note

References

1. Capitanio U, Bensalah K, Bex A, Boorjian SA, Bray F, Coleman J, et al. Epidemiology of renal cell carcinoma. *Eur Urol*. (2019) 75:74–84. doi: 10.1016/j.eururo.2018.08.036

2. Moch H, Cubilla AL, Humphrey PA, Reuter VE, Ulbright TM. The 2016 WHO classification of tumours of the urinary system and male genital organs-part a: renal, penile, and testicular tumours. *Eur Urol*. (2016) 70:93–105. doi: 10.1016/j.eururo.2016.02.029

3. Bruder E, Passera O, Harms D, Leuschner I, Ladanyi M, Argani P, et al. Morphologic and molecular characterization of renal cell carcinoma in children and young adults. *Am J Surg Pathol*. (2004) 28:1117–32. doi: 10.1097/01.pas.0000131558.32412.40

4. Gong P, Zhuang Q, Wang K, Xu R, Chen Y, Wang X, et al. Adult-onset renal cell carcinoma associated with Xp11.2 translocation/TFE3 gene fusion: 3 case reports and review of literature. *Medicine (Baltimore)*. (2018) 97:e11023. doi: 10.1097/MD.0000000000011023

5. Amin MB. (ed.). *WHO classification of tumours: Urinary and male genital tumours*. International Agency for Research on Cancer (2022).

6. Caliò A, Marletta S, Brunelli M, Martignoni G. WHO 2022 classification of kidney tumors: what is relevant? An update and future novelties for the pathologist. *Pathologica*. (2022) 115:1–9. doi: 10.32074/1591-951X-814

7. Harada S, Caliò A, Janowski KM, Morlote D, Rodriguez Pena MD, Canete-Portillo S, et al. Diagnostic utility of one-stop fusion gene panel to detect TFE3/TFEB gene rearrangement and amplification in renal cell carcinomas. *Mod Pathol*. (2021) 34:2055–63. doi: 10.1038/s41379-021-00858-y

8. Caliò A, Harada S, Brunelli M, Pedron S, Segala D, Portillo SC, et al. TFEB rearranged renal cell carcinoma. A clinicopathologic and molecular study of 13 cases. Tumors harboring MALAT1-TFEB, ACTB-TFEB, and the novel NEAT1-TFEB translocations constantly express PDL1. *Mod Pathol*. (2021) 34:842–50. doi: 10.1038/s41379-020-00713-6

9. Cheng X, Gan W, Zhang G, Li X, Guo H. Clinical characteristics of XP11.2 translocation/TFE3 gene fusion renal cell carcinoma: a systematic review and meta-analysis of observational studies. *BMC Urol*. (2016) 16:40. doi: 10.1186/s12894-016-0154-6

10. Rao Q, Guan B, Zhou X-j. Xp11.2 translocation renal cell carcinomas have a poorer prognosis than non-Xp11.2 translocation carcinomas in children and young adults: a meta-analysis. *Int J Surg Pathol*. (2010) 18:458–64. doi: 10.1177/1066896910375565

11. Kmetec A, Jeruc J. Xp 11.2 translocation renal carcinoma in young adults; recently classified distinct subtype. *Radiol Oncol*. (2014) 48:197–202. doi: 10.2478/raon-2013-0077

12. Hung C-C, Pan C-C, Lin C-C, Lin ATL, Chen K-K, Chang Y-H. XP11.2 translocation renal cell carcinoma: clinical experience of Taipei Veterans General Hospital. *J Chin Med Assoc*. (2011) 74:500–4. doi: 10.1016/j.jcma.2011.09.005

13. Hodge JC, Pearce KE, Wang X, Wiktor AE, Oliveira AM, Greipp PT. Molecular cytogenetic analysis for TFE3 rearrangement in Xp11.2 renal cell carcinoma and alveolar soft part sarcoma: validation and clinical experience with 75 cases. *Mod Pathol*. (2014) 27:113–27. doi: 10.1038/modpathol.2013.83

14. Hong S-B, Oh H, Valera VA, Baba M, Schmidt LS, Linehan WM. Inactivation of the FLCN tumor suppressor gene induces TFE3 transcriptional activity by increasing its nuclear localization. *PLoS One*. (2010) 5:e15793. doi: 10.1371/journal.pone.0015793

15. Argani P, Antonescu CR, Illei PB, Lui MY, Timmons CF, Newbury R, et al. Primary renal neoplasms with the ASPL-TFE3 gene fusion of alveolar soft part sarcoma: a distinctive tumor entity previously included among renal cell carcinomas of children and adolescents. *Am J Pathol*. (2001) 159:179–92. doi: 10.1016/S0002-9440(10)61684-7

16. Altinok G, Kattar MM, Mohamed A, Poulik J, Grignon D, Rabah R. Pediatric renal carcinoma associated with Xp11.2 translocations/TFE3 gene fusions and clinicopathologic associations. *Pediatr Dev Pathol*. (2005) 8:168–80. doi: 10.1007/s10024-004-9106-3

17. Gaillot-Durand L, Chevallier M, Colombel M, Couturier J, Pierron G, Scoazec JY, et al. Diagnosis of Xp11 translocation renal cell carcinomas in adult patients under 50 years: interest and pitfalls of automated immunohistochemical detection of TFE3 protein. *Pathol Res Pract*. (2013) 209:83–9. doi: 10.1016/j.prp.2012.10.013

18. Koo HJ, Choi HJ, Kim M, Cho K-S. Radiologic-pathologic correlation of renal cell carcinoma associated with Xp11.2 translocation. *Acta Radiol*. (2013) 54:827–34. doi: 10.1177/0284185113484019

19. Klatte T, Streubel B, Wrba F, Remzi M, Krammer B, de Martino M, et al. Renal cell carcinoma associated with transcription factor E3 expression and Xp11.2 translocation: incidence, characteristics, and prognosis. *Am J Clin Pathol*. (2012) 137:761–8. doi: 10.1309/AJCPQ6LLFMC4OXGC

20. Komai Y, Fujiwara M, Fujii Y, Mukai H, Yonese J, Kawakami S, et al. Adult Xp11 translocation renal cell carcinoma diagnosed by cytogenetics and immunohistochemistry. *Clin Cancer Res*. (2009) 15:1170–6. doi: 10.1158/1078-0432.CCR-08-1183

21. Tsili AC, Andriotis E, Gkeli MG, Krokidis M, Stasinopoulou M, Varkarakis IM, et al. The role of imaging in the management of renal masses. *Eur J Radiol*. (2021) 141:109777. doi: 10.1016/j.ejrad.2021.109777

22. Wang W, Ding J, Li Y, Wang C, Zhou L, Zhu H, et al. Magnetic resonance imaging and computed tomography characteristics of renal cell carcinoma associated with Xp11.2 translocation/TFE3 gene fusion. *PLoS One*. (2014) 9:e99990. doi: 10.1371/journal.pone.0099990

23. Ma W, Zhang F, Huang H, Wang W, Zhu Y, Lu Y, et al. Contrast-enhanced ultrasound features of adult Xp11.2 translocation renal cell carcinoma: differential diagnosis with three main renal cell carcinoma subtypes. *J Ultrasound Med*. (2022) 41:2673–85. doi: 10.1002/jum.15951

24. Wei S, Tian F, Xia Q, Huang P, Zhang Y, Xia Z, et al. Contrast-enhanced ultrasound findings of adult renal cell carcinoma associated with Xp11.2 translocation/TFE3 gene fusion: comparison with clear cell renal cell carcinoma and papillary renal cell carcinoma. *Cancer Imaging*. (2019) 20:1. doi: 10.1186/s40644-019-0268-7

25. Liu K, Xie P, Peng W, Zhou Z. Renal carcinomas associated with Xp11.2 translocations/TFE3 gene fusions: findings on MRI and computed tomography imaging. *J Magn Reson Imaging*. (2014) 40:440–7. doi: 10.1002/jmri.24349

26. He J, Gan W, Liu S, Zhou K, Zhang G, Guo H, et al. Dynamic computed tomographic features of adult renal cell carcinoma associated with Xp11.2 translocation/TFE3 gene fusions: comparison with clear cell renal cell carcinoma. *J Comput Assist Tomogr*. (2015) 39:730–6. doi: 10.1097/RCT.0000000000000263

27. Dong H, Ni Y, Liu Z, Wang Z, Hu B, Xu H, et al. Imaging findings, clinical and pathological characters of 28 patients with Xp11.2/TFE3 translocation renal cell carcinoma. *J Cancer Res Ther*. (2023) 19:132–40. doi: 10.4103/jcrt.jcrt_1505_22

28. Liu N, Qu F, Shi Q, Zhuang W, Ma W, Yang Z, et al. Nephron-sparing surgery for adult Xp11.2 translocation renal cell carcinoma at clinical T1 stage: a multicenter study in China. *Ann Surg Oncol*. (2021) 28:1238–46. doi: 10.1245/s10434-020-08813-y

29. Zhu Q-Q, Wang Z-Q, Zhu W-R, Chen W-X, Wu J-T. The multislice CT findings of renal carcinoma associated with XP11.2 translocation/TFE gene fusion and collecting duct carcinoma. *Acta Radiol*. (2013) 54:355–62. doi: 10.1258/ar.2012.120255

30. Chen X, Zhu Q, Li B, Cui W, Zhou H, Duan N, et al. Renal cell carcinoma associated with Xp11.2 translocation/TFE gene fusion: imaging findings in 21 patients. *Eur Radiol*. (2017) 27:543–52. doi: 10.1007/s00330-016-4421-4

31. Dai C, Sheng R, Ding Y, Yang M, Hou J, Zhou J. Magnetic resonance imaging findings of renal cell carcinoma associated with Xp11.2 translocation/TFE3 gene fusion in adults: a pilot study. *Abdom Radiol*. (2019) 44:209–17. doi: 10.1007/s00261-018-1703-0

32. Aziz SA, Sznol J, Adeniran A, Colberg JW, Camp RL, Kluger HM. Vascularity of primary and metastatic renal cell carcinoma specimens. *J Transl Med*. (2013) 11:15. doi: 10.1186/1479-5876-11-15

33. Takahashi M, Kume H, Koyama K, Nakagawa T, Fujimura T, Morikawa T, et al. Preoperative evaluation of renal cell carcinoma by using 18F-FDG PET/CT. *Clin Nucl Med*. (2015) 40:936–40. doi: 10.1097/RLU.0000000000000875

34. Urso L, Castello A, Rocca GC, Lancia F, Panareo S, Cittanti C, et al. Role of PSMA-ligands imaging in renal cell carcinoma management: current status and future perspectives. *J Cancer Res Clin Oncol*. (2022) 148:1299–311. doi: 10.1007/s00432-022-03958-7

35. Mittlmeier LM, Todica A, Gildehaus F-J, Unterrainer M, Beyer L, Brendel M, et al. 68Ga-EMP-100 PET/CT-a novel ligand for visualizing c-MET expression in metastatic renal cell carcinoma-first in-human biodistribution and imaging results. *Eur J Nucl Med Mol Imaging*. (2022) 49:1711–20. doi: 10.1007/s00259-021-05596-6

36. Chen E-J, Tan TH, Chew MT, Chye PC. 68Ga-PSMA PET/CT and 18F-FDG PET/CT in renal cell carcinoma. *Clin Nucl Med*. (2020) 45:e317–9. doi: 10.1097/RLU.0000000000003053

37. Hekman MCH, Rijpkema M, Aarntzen EH, Mulder SF, Langenhuijsen JF, Oosterwijk E, et al. Positron emission tomography/computed tomography with 89Zr-girentuximab can aid in diagnostic dilemmas of clear cell renal cell carcinoma suspicion. *Eur Urol*. (2018) 74:257–60. doi: 10.1016/j.eururo.2018.04.026

38. Gibney GT, Aziz SA, Camp RL, Conrad P, Schwartz BE, Chen CR, et al. C-met is a prognostic marker and potential therapeutic target in clear cell renal cell carcinoma. *Ann Oncol*. (2013) 24:343–9. doi: 10.1093/annonc/mds463

39. Caliò A, Brunelli M, Segala D, Pedron S, Remo A, Ammendola S, et al. Comprehensive analysis of 34 MiT family translocation renal cell carcinomas and review of the literature: investigating prognostic markers and therapy targets. *Pathology*. (2020) 52:297–309. doi: 10.1016/j.pathol.2019.11.006

40. Fujimoto H, Wakao F, Moriyama N, Tobisu K, Sakamoto M, Kakizoe T. Alveolar architecture of clear cell renal carcinomas (< or = 5.0 cm) show high attenuation on dynamic CT scanning. *Jpn J Clin Oncol*. (1999) 29:198–203. doi: 10.1093/jjco/29.4.198

41. Young JR, Margolis D, Sauk S, Pantuck AJ, Sayre J, Raman SS. Clear cell renal cell carcinoma: discrimination from other renal cell carcinoma subtypes and oncocytoma at multiphasic multidetector CT. *Radiology*. (2013) 267:444–53. doi: 10.1148/radiol.13112617

42. Pedrosa I, Chou MT, Ngo L, Baroni HR, Genega EM, Galaburda L, et al. MR classification of renal masses with pathologic correlation. *Eur Radiol*. (2008) 18:365–75. doi: 10.1007/s00330-007-0757-0

43. Silverman SG, Mortele KJ, Tuncali K, Jinzaki M, Cibas ES. Hyperattenuating renal masses: etiologies, pathogenesis, and imaging evaluation. *Radiographics*. (2007) 27:1131–43. doi: 10.1148/rg.274065147

44. Rini BI, Wilding G, Hudes G, Stadler WM, Kim S, Tarazi J, et al. Phase II study of axitinib in sorafenib-refractory metastatic renal cell carcinoma. *J Clin Oncol*. (2009) 27:4462–8. doi: 10.1200/JCO.2008.21.7034

45. Sasaguri K, Irie H, Kamochi N, Nakazono T, Yamaguchi K, Uozumi J, et al. Magnetic resonance imaging of large chromophobe renal cell carcinomas. *Jpn J Radiol*. (2010) 28:453–9. doi: 10.1007/s11604-010-0450-0

46. Feng R, Tao Y, Chen Y, Xu W, Zhang G, Wang H. Renal cancer associated with Xp11.2 translocation/TFE3 gene fusion: Clinicopathological analysis of 13 cases. *Ann Diagn Pathol*. (2022) 58:151908. doi: 10.1016/j.anndiagpath.2022.151908

47. Miroński I, Zaucha JM, Kowalski J, Zaucha R. Case report: TFE3 positive Xp11.2 translocation renal cell carcinoma (TRCC) - a case study and review of the literature. Front. *Oncologia*. (2021) 11:826325. doi: 10.3389/fonc.2021.826325

48. Ahluwalia P, Nair B, Kumar G. Renal cell carcinoma associated with Xp11.2 translocation/TFE3 gene fusion: a rare case report with review of the literature. *Case Rep Urol*. (2013) 2013:810590:1–4. doi: 10.1155/2013/810590

49. Song HC, Sun N, Zhang WP, He L, Fu L, Huang C. Biological characteristics of pediatric renal cell carcinoma associated with Xp11.2 translocations/TFE3 gene fusions. *J Pediatr Surg*. (2014) 49:539–42. doi: 10.1016/j.jpedsurg.2013.10.005

50. Wu Y, Chen S, Zhang M, Liu K, Jing J, Pan K, et al. Factors associated with survival from Xp11.2 translocation renal cell carcinoma diagnosis-a systematic review and pooled analysis. *Pathol Oncol Res*. (2021) 27:610360. doi: 10.3389/pore.2021.610360

51. Numakura K, Tsuchiya N, Yuasa T, Saito M, Obara T, Tsuruta H, et al. A case study of metastatic Xp11.2 translocation renal cell carcinoma effectively treated with sunitinib. *Int J Clin Oncol*. (2011) 16:577–80. doi: 10.1007/s10147-010-0154-6

52. Meyer PN, Clark JI, Flanigan RC, Picken MM. Xp11.2 translocation renal cell carcinoma with very aggressive course in five adults. *Am J Clin Pathol*. (2007) 128:70–9. doi: 10.1309/LR5G1VMXPY3G0CUK

53. Liu N, Wang Z, Gan W, Xiong L, Miao B, Chen X, et al. Renal cell carcinoma associated with Xp11.2 translocation/TFE3 gene fusions: clinical features, treatments and prognosis. *PLoS One*. (2016) 11:e0166897. doi: 10.1371/journal.pone.0166897

frontiers | Frontiers in Medicine

TYPE Case Report
PUBLISHED 23 November 2023
DOI 10.3389/fmed.2023.1256176

OPEN ACCESS

EDITED BY
Giorgio Treglia,
Ente Ospedaliero Cantonale (EOC), Switzerland

REVIEWED BY
Harun Ilhan,
LMU Munich University Hospital, Germany
Carmelo Caldarella,
Fondazione Policlinico Universitario A. Gemelli IRCCS, Italy

*CORRESPONDENCE
Hehe Li
✉ 344192253@qq.com

RECEIVED 10 July 2023
ACCEPTED 08 November 2023
PUBLISHED 23 November 2023

CITATION
Zhang Z and Li H (2023) Surgical treatment of primary hepatic neuroendocrine tumor diagnosed by Al^{18}F-NOTA-Octreotide PET/CT: a case report.
Front. Med. 10:1256176.
doi: 10.3389/fmed.2023.1256176

Surgical treatment of primary hepatic neuroendocrine tumor diagnosed by Al^{18}F-NOTA-Octreotide PET/CT: a case report

Zhongyan Zhang[1] and Hehe Li[2]*

[1]Department of Hepatobiliary Surgery, Weifang People's Hospital, Weifang, China, [2]Department of Geriatrics, Weifang People's Hospital, Weifang, China

Neuroendocrine tumors (NETs) are a heterogeneous group of tumors originating from peptide-producing neurons and neuroendocrine cells. The liver is the most common site of metastasis for NETs, while primary hepatic neuroendocrine tumors (PHNETs) are exceedingly rare. While somatostatin receptor scintigraphy (SRS) has demonstrated superior efficacy compared to [^{18}F]FDG PET imaging in the diagnosis of neuroendocrine tumors, [^{18}F]AlF-NOTA-Octreotide ([^{18}F]AlF-OC) PET/CT also exhibits specific advantages over SRS. This article presents a case study of a patient with a liver mass who underwent sequential [^{18}F]FDG and [^{18}F]AlF-OC PET/CT scans, ruling out hepatocellular carcinoma and confirming the diagnosis of PHNETs. Subsequently, the patient underwent surgical treatment. From another perspective, [^{18}F]AlF-OC exhibits distinct advantages. The postoperative pathology revealed a PHNETs, which further emphasizes its clinical rarity.

KEYWORDS

hepatic primary neuroendocrine tumor, PHNETs, [^{18}F]AlF-OC, PET/CT, diagnosis, surgical resection, case report

Introduction

Neuroendocrine tumors (NETs) are a heterogeneous group of tumors originating from peptide-producing neurons and neuroendocrine cells. They predominantly occur in the gastrointestinal tract, pancreas, and bronchopulmonary tissues. The liver is the most common site of metastasis for NETs, while primary hepatic neuroendocrine tumors (PHNETs) are exceedingly rare (1), accounting for only 0.8% of all NETs. The incidence of PHNETs is very low, accounting for only 0.46% of all primary liver tumors. These tumors typically occur in adults over 40, with a slightly higher prevalence in females than males.

PHNETs can occur as solitary or multiple lesions, and they typically present as large lesions with heterogeneous cystic and solid components. Common internal features include cystic changes and areas of necrosis, which contribute to the uneven density or signal characteristics observed. PET (Positron Emission Tomography) has the advantage of providing comprehensive information about the systemic tumor burden and the metabolic activity of the tumor. However, its diagnostic value for cystic lesions is limited. Numerous studies have demonstrated that Ga68 SSA-PET([^{68}Ga]Ga-DOTANOC, [^{68}Ga]Ga-DOTATOC, [^{68}Ga]Ga-DOTATATE) imaging offers higher diagnostic accuracy for NETs (2–5). While 68Ga labeling has the advantage of eluting isotopes from a generator, fluorine labeling offers benefits like longer half-life, improved spatial resolution, higher production yield, and consistent advantages in imaging and logistics. [^{18}F]

AlF-OC demonstrates its advantages in certain aspects, particularly in diagnosing PHNETs.

Hepatic lobectomy is considered the most effective treatment for PHNETs. In some cases, a complete cure can be achieved through surgical intervention, leading to a favorable prognosis.

This article presents a case study of a patient with a liver mass who underwent sequential [^{18}F]FDG and [^{18}F]AlF-OC PET/CT scans, ruling out hepatocellular carcinoma and confirming the diagnosis of PHNETs. Subsequently, the patient underwent surgical treatment. In addition, a literature review was conducted to provide insights and guidance regarding treatment strategies for patients with PHNETs.

Case description

A 56-year-old female patient was found to have a liver mass during a physical examination on August 3, 2022. There is no previous history of chronic liver disease. Six years ago, she underwent a hysterectomy for uterine fibroids at a local hospital. On admission, no significant positive physical signs were detected during the examination. The results of the blood tests are as follows: Complete Blood Count (CBC), liver function, kidney function, electrolytes, and coagulation function are generally within normal ranges. The C-reactive protein (CRP) level is elevated at 25.7 mg/L. The hepatitis B panel shows positive results for anti-HBc, while the remaining parameters are negative. The testing for hepatitis C antibodies does not show any abnormalities. HIV and syphilis testing results are negative. On August 13, 2022, the patient underwent a contrast-enhanced abdomen CT, which revealed that the left lobe of the liver shows a clustered low-density mass with relatively clear borders. Within the mass, there are multiple rounded cystic areas with unclear boundaries. On the contrast-enhanced scan, the lesion demonstrates continuous enhancement. Additionally, the abdominal cavity has enlarged lymph nodes (Figure 1). A metastatic malignant tumor cannot be ruled out. On August 16, 2022, the patient underwent an [^{18}F]FDG PET/CT scan, revealing a malignant tumor in the liver. Multiple clustered low-density lesions with heterogeneous enhancement are seen in the left lobe of the liver. The radioactive distribution is uneven with the maximum standardized uptake value (SUVmax) of 15.1, the mean standardized uptake value (SUVmean) of 9.3, and the tumor-to-normal (T/N) ratio of 2.9. The borders of the lesions are slightly indistinct. The largest lesion measures approximately 6.7 cm × 5.1 cm in cross-section. Multiple enlarged lymph nodes are observed in the hepatogastric ligament, showing increased radioactive distribution with an SUVmax of 16.9. The largest lymph node measures approximately 1.3 cm × 1.1 cm in cross-section (Figures 2A1–A8). According to the Barcelona Clinic Liver Cancer (BCLC) staging system, the patient is classified as stage B, which suggests treatment options such as transarterial chemoembolization (TACE), systemic therapy, or liver transplantation. However, since the patient's A-fetoprotein (AFP) levels are not elevated, a diagnosis of hepatocellular carcinoma (HCC) cannot be confirmed. The possibility of a neuroendocrine tumor cannot be ruled out. So, on August 26, 2022, the patient underwent an [^{18}F]AlF-OC PET/CT scan, which indicated a PHNET with abdominal lymph node metastasis. Multiple clustered and heterogeneous low-density lesions are observed in the left lobe of the liver, with SUVmax = 36.6, SUVmean = 16.3, and T/N = 4.0. The largest lesion measures approximately 8.3 cm × 6.6 cm in cross-section. Enlarged lymph nodes are visible in the hepatogastric ligament, showing increased radiotracer uptake with SUVmax = 37.9. The largest lymph node measures approximately 1.3 cm × 1.1 cm in cross-section (Figures 2B1–B8). The patient has been ultimately ruled out for hepatocellular carcinoma and metastatic liver neuroendocrine tumor, and the diagnosis is confirmed as PHNETs.

On August 30, 2022, the patient underwent a left hepatectomy, cholecystectomy, adhesiolysis for intestinal obstruction, partial gastrectomy, and intra-abdominal lymph node dissection under general anesthesia with endotracheal intubation. A firm mass was observed in the left liver lobe. Multiple enlarged lymph nodes were palpated along the lesser curvature of the stomach, showing a close relationship with the gastric wall, suggesting invasion into the gastric wall. Gastric wall resection and lymph node excision were performed. The surgery lasted approximately 310 min, with an estimated blood loss of about 200 mL. No blood transfusion was required.

Postoperative pathology report: The left hemi-liver specimen reveals a malignant tumor (Figure 3A). Immunohistochemical analysis confirms it is a neuroendocrine tumor (NET, G3). The immunohistochemical markers show positive staining for Synaptophysin (Syn), CD56, CK19, and partially positive staining for Chromogranin A (CgA) and CK7. The markers HepPar-1, Glypican-3, CD10 are negative. Blood vessel staining with CD34 is positive. The Ki-67 proliferation index is 30% (Figures 3B–I).

Discussion

NETs are a diverse group of tumors originating from neuroendocrine cells that can uptake and decarboxylate amine precursors. While commonly found in the stomach, intestines, and pancreas, the pancreas remains the most frequent site of occurrence. PHNETs, on the other hand, are relatively uncommon (1). PHNETs present a challenge regarding their non-specific clinical symptoms and limited diagnostic specificity through imaging examinations. Furthermore, the homogeneous nature of NETs poses challenges in differentiating between PHNETs and metastatic NETs in the liver.

Due to the limitations of conventional anatomical imaging techniques, the specific endocrine features of PHNETs cannot be easily visualized. As a result, distinguishing PHNETs from HCC can be challenging (6, 7). The overexpression of somatostatin receptors (SSTR) is a prominent feature of NETs. This provides a crucial target for diagnosing NETs and peptide receptor radionuclide therapy (PRRT), which utilizes peptide-receptor interactions for targeted treatment (8). PET imaging offers advantages such as high sensitivity and spatial resolution. Conventional [^{18}F]FDG glucose metabolism PET/CT imaging plays a crucial role in clinically diagnosing and treating tumors. Furthermore, PET/CT targeted imaging using radiolabeled tumor-specific markers is vital for precise tumor diagnosis, staging, and personalized treatment planning. Commonly used radiolabels include [^{18}F]F, [^{68}Ga]Ga, and [^{11}C]C.

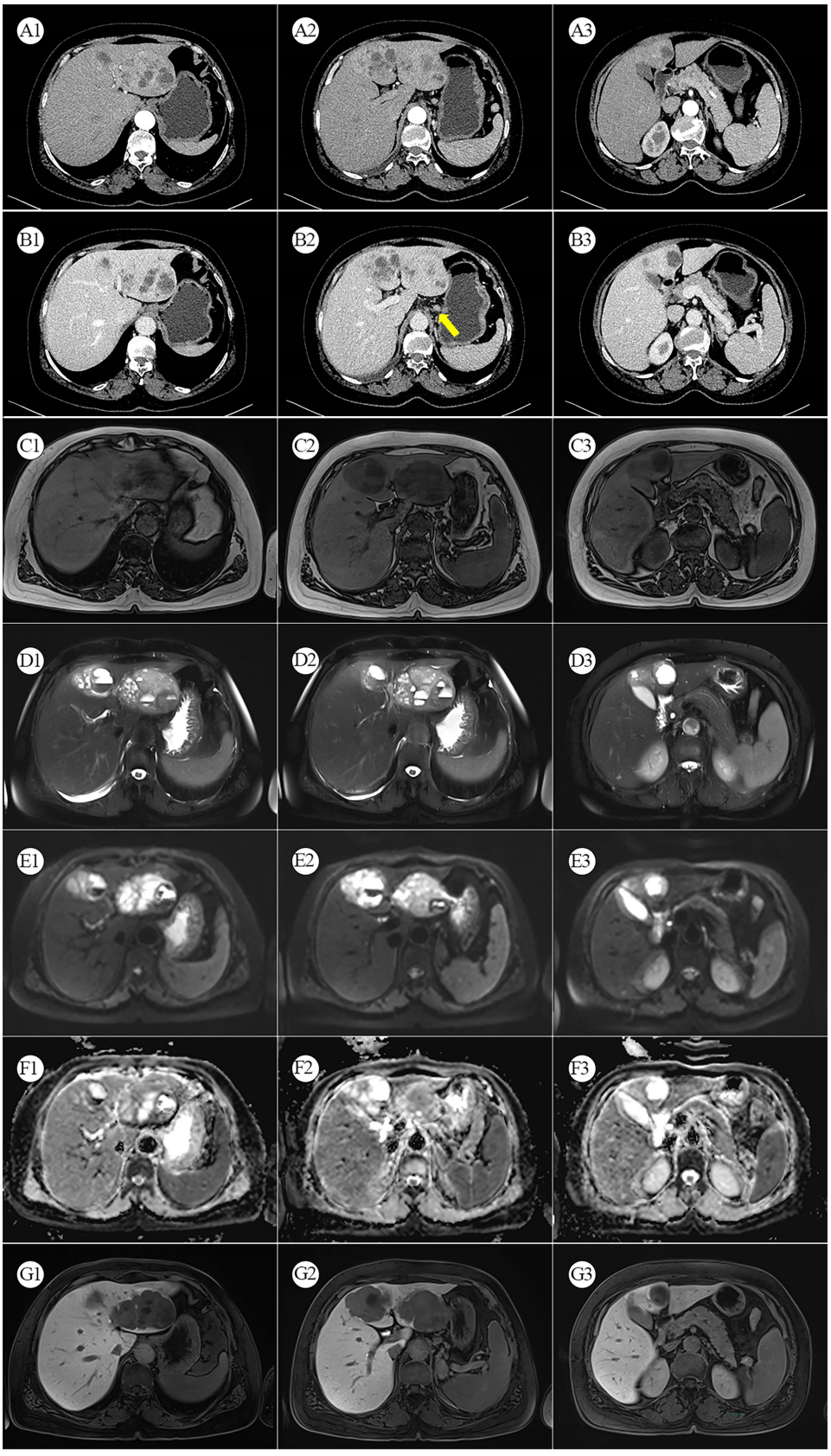

FIGURE 1
(A1–A3) Arterial phase CT. **(B1–B3)** Venous phase CT: The yellow arrows indicate enhanced and enlarged lymph nodes between the liver and stomach. **(C1–C3)** MRI T1-weighted image. **(D1–D3)** MRI T2-weighted image. **(E1–E3)** Diffusion-weighted MRI. **(F1–F3)** MRI ADC map. **(G1–G3)** Gadoxetic Acid-enhanced (Primovist) MRI.

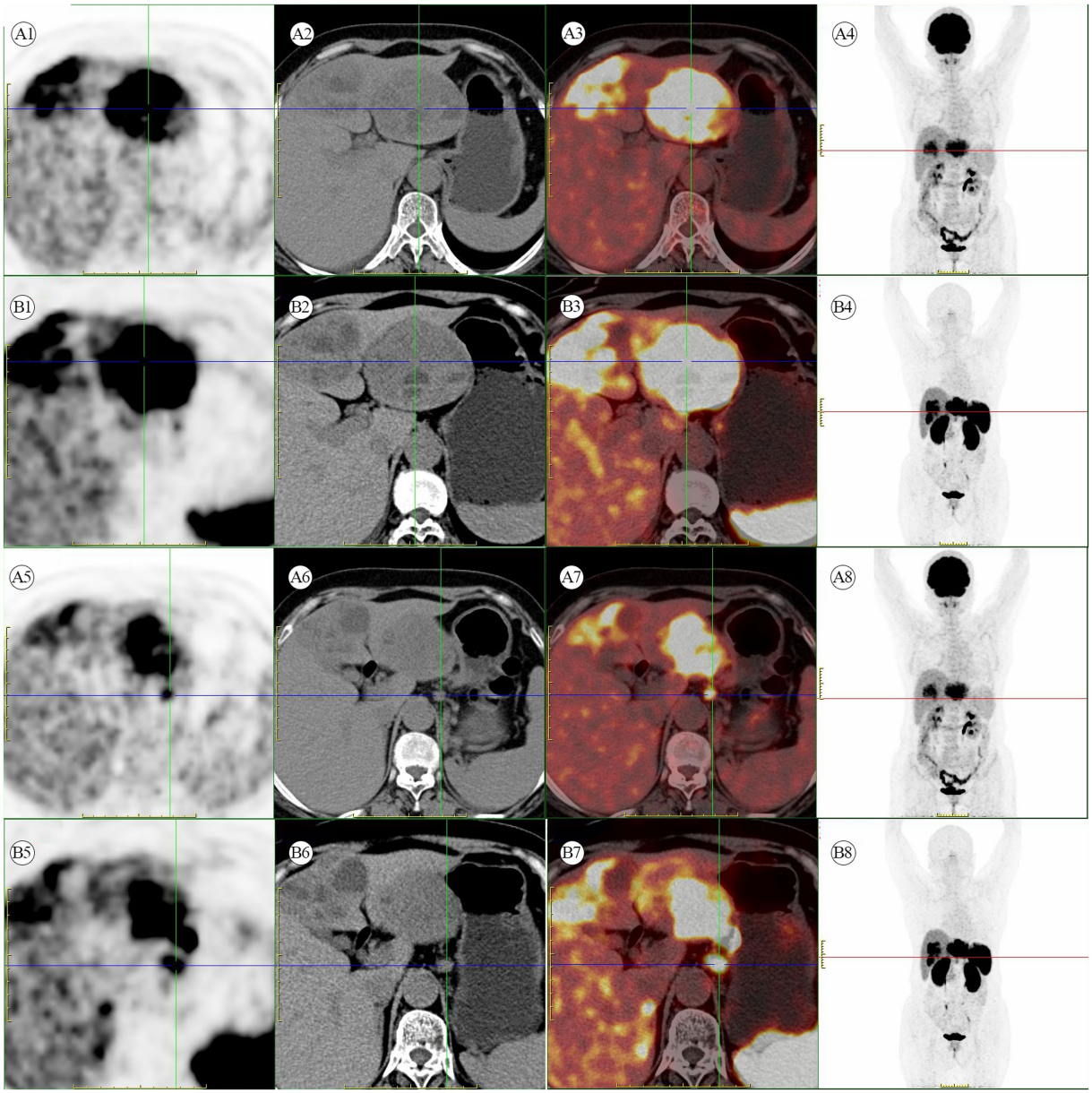

FIGURE 2
(A1–A8) [^{18}F]FDG PET/CT scan. Multiple hypermetabolic heterogeneous lesions are present in the left lobe of the liver, indicating possible malignant lesions. Additionally, multiple hypermetabolic enlarged lymph nodes are seen in the space between the liver and stomach, suggesting metastasis. **(B1–B8)** [^{18}F]AlF-OC PET/CT scan. A liver mass with multiple enlarged lymph nodes in the hepatogastric ligament shows high somatostatin receptor expression.

In recent years, [^{68}Ga]Ga-labeled somatostatin analogs (SSAs) for diagnosis and treatment have been increasingly widespread in clinical practice. Currently, commonly used in clinical practice are [^{68}Ga]Ga SSA-PET, such as [^{68}Ga]Ga-DOTATATE, [^{68}Ga]Ga-DOTATOC, and [^{68}Ga]Ga-DOTANOC, which have become the gold standard for the diagnosis of NETs (9, 10). However, [^{68}Ga]Ga SSA-PET have their limitations, such as the higher positron energy of ^{68}Ga, which can lead to inferior image quality compared to ^{18}F. The advantages of [^{18}F] AlF-OC include its shorter synthesis time, strong affinity to SSTR, good stability, and excellent imaging performance in neuroendocrine tumors (11). It significantly improves the tumor-to-background ratio, making the lesions more clearly visible.

In this article, despite the utilization of [^{18}F]FDG PET/CT examination, the specific type of liver tumor remained indeterminate. However, the diagnosis was ultimately established using [^{18}F]AlF-OC, enabling the development of a treatment plan primarily centered around surgical resection. This approach prevented misdiagnosis and ensured appropriate action (12).

Surgical resection remains the primary approach for treating primary lesions of NET G1 and G2. Preoperative evaluation should encompass various aspects, including tumor size, non-specific symptoms, endocrine function, the location of the primary lesion, and the extent of local invasion. Hepatic lobectomy is considered the most effective treatment for PHNETs, and in some cases, surgical

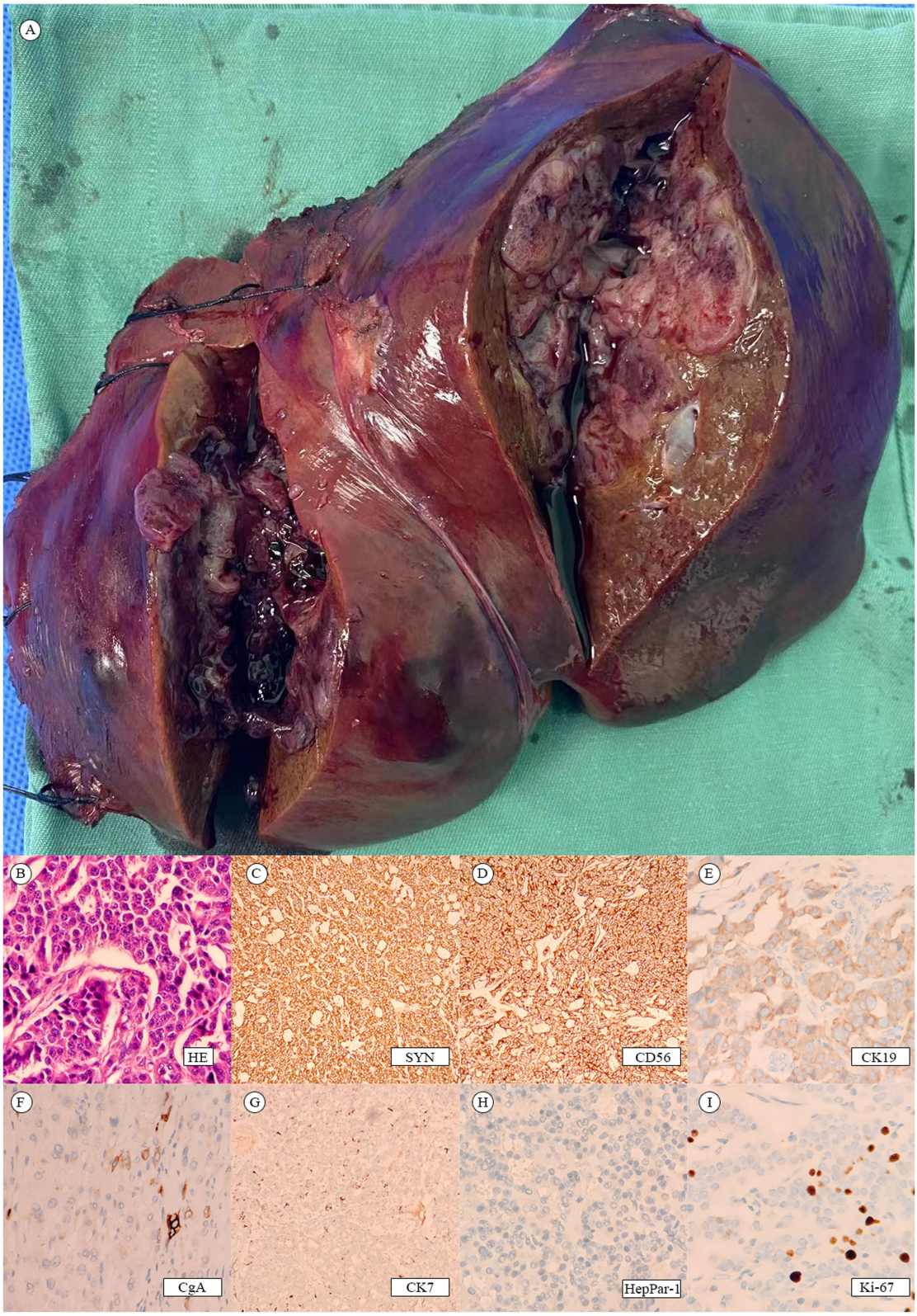

FIGURE 3
(A) Postoperative liver tumor. **(B–I)** Tumor pathology.

intervention can lead to a complete cure with a favorable prognosis (13). Additionally, liver transplantation can be a viable option for select patients with PHNETs. Patients meeting certain criteria, such as well-differentiated NETs (Ki-67 < 10%), age < 55 years, absence of extrahepatic disease, complete resection of the primary tumor before transplantation, at least 6 months of disease stability before

transplantation, and liver involvement <50%, can benefit from liver transplantation. Moreover, for unresectable PHNETs, TACE has shown promising therapeutic efficacy due to the rich vascularity and ischemia sensitivity of neuroendocrine tumors.

Conclusion

In conclusion, PET/CT imaging, particularly with [^{18}F]AlF-OC, plays a crucial role in diagnosing and managing PHNETs. The advantages of [^{18}F]AlF-OC, including its shorter synthesis time, strong affinity to somatostatin receptors, and excellent imaging performance, contribute to improved visualization and accurate assessment of PHNETs. [^{18}F]AlF-OC has significantly enhanced the tumor-to-background ratio, leading to a clearer identification of lesions. This imaging modality has proven valuable in guiding treatment decisions and avoiding misdiagnosis in challenging cases. Continued research and development in PET/CT imaging techniques, including using radiolabeled tracers, will further advance the field and improve patient outcomes in the management of PHNETs.

Data availability statement

The original contributions presented in the study are included in the article/supplementary material, further inquiries can be directed to the corresponding author.

Ethics statement

Written informed consent was obtained from the individual(s) for the publication of any potentially identifiable images or data included in this article.

Author contributions

ZZ: Formal analysis, Visualization, Writing – original draft, Writing – review & editing. HL: Data curation, Formal analysis, Supervision, Writing – original draft, Writing – review & editing.

Funding

The author(s) declare that no financial support was received for the research, authorship, and/or publication of this article.

Acknowledgments

We would like to express my gratitude to all those who helped me during the writing of this manuscript and their efforts in the management of this patient.

Conflict of interest

The authors declare that the research was conducted in the absence of any commercial or financial relationships that could be construed as a potential conflict of interest.

Publisher's note

References

1. Strosberg JR, Halfdanarson TR, Bellizzi AM, Chan JA, Dillon JS, Heaney AP, et al. The north American neuroendocrine tumor society consensus guidelines for surveillance and medical management of midgut neuroendocrine tumors. *Pancreas*. (2017) 46:707–14. doi: 10.1097/MPA.0000000000000850

2. Hu X, Li D, Wang R, Wang P, Cai J. Comparison of the application of 18f-fdg and 68ga-dotatate pet/ct in neuroendocrine tumors: a retrospective study. *Medicine (Baltimore)*. (2023) 102:e33726. doi: 10.1097/MD.0000000000033726

3. Singh S, Bergsland EK, Card CM, Hope TA, Kunz PL, Laidley DT, et al. Commonwealth neuroendocrine tumour research collaboration and the north american neuroendocrine tumor society guidelines for the diagnosis and management of patients with lung neuroendocrine tumors: an international collaborative endorsement and update of the 2015 european neuroendocrine tumor society expert consensus guidelines. *J Thorac Oncol*. (2020) 15:1577–98. doi: 10.1016/j.jtho.2020.06.021

4. Sadowski SM, Neychev V, Millo C, Shih J, Nilubol N, Herscovitch P, et al. Prospective study of 68ga-dotatate positron emission tomography/computed tomography for detecting gastro-entero-pancreatic neuroendocrine tumors and unknown primary sites. *J Clin Oncol*. (2016) 34:588–96. doi: 10.1200/JCO.2015.64.0987

5. Singh S, Poon R, Wong R, Metser U. 68ga pet imaging in patients with neuroendocrine tumors: a systematic review and meta-analysis. *Clin Nucl Med*. (2018) 43:802–10. doi: 10.1097/RLU.0000000000002276

6. Li R, Tang CL, Yang D, Zhang XH, Cai P, Ma KS, et al. Primary hepatic neuroendocrine tumors: clinical characteristics and imaging features on contrast-enhanced ultrasound and computed tomography. *Abdom Radiol (Ny)*. (2016) 41:1767–75. doi: 10.1007/s00261-016-0770-3

7. Mottaghy FM, Reske SN. Functional imaging of neuroendocrine tumours with pet. *Pituitary*. (2006) 9:237–42. doi: 10.1007/s11102-006-0269-y

8. Theodoropoulou M, Stalla GK. Somatostatin receptors: from signaling to clinical practice. *Front Neuroendocrinol*. (2013) 34:228–52. doi: 10.1016/j.yfrne.2013.07.005

9. Bozkurt MF, Virgolini I, Balogova S, Beheshti M, Rubello D, Decristoforo C, et al. Guideline for pet/ct imaging of neuroendocrine neoplasms with (68)ga-dota-conjugated somatostatin receptor targeting peptides and (18)f-dopa. *Eur J Nucl Med Mol Imaging*. (2017) 44:1588–601. doi: 10.1007/s00259-017-3728-y

10. Ambrosini V, Morigi JJ, Nanni C, Castellucci P, Fanti S. Current status of pet imaging of neuroendocrine tumours ([18f]fdopa, [68ga]tracers, [11c]/[18f]-htp). *Q J Nucl Med Mol Imaging*. (2015) 59:58–69.

11. Long T, Yang N, Zhou M, Chen D, Li Y, Li J, et al. Clinical application of 18f-alf-nota-octreotide pet/ct in combination with 18f-fdg pet/ct for imaging neuroendocrine neoplasms. *Clin Nucl Med*. (2019) 44:452–8. doi: 10.1097/RLU.0000000000002578

12. Yalav O, Ulku A, Akcam TA, Demiryurek H, Doran F. Primary hepatic neuroendocrine tumor: five cases with different preoperative diagnoses. *Turk J Gastroenterol*. (2012) 23:272–8. doi: 10.4318/tjg.2012.0465

13. Shi C, Zhao Q, Dai B, Xie F, Yang J. Primary hepatic neuroendocrine neoplasm: long-time surgical outcome and prognosis. *Medicine (Baltimore)*. (2018) 97:e11764. doi: 10.1097/MD.0000000000011764

frontiers | Frontiers in Medicine

TYPE Case Report
PUBLISHED 28 November 2023
DOI 10.3389/fmed.2023.1330341

OPEN ACCESS

EDITED BY
Carmelo Caldarella,
Fondazione Policlinico Universitario A. Gemelli IRCCS, Italy

REVIEWED BY
Corinna Altini,
Azienda Ospedaliero Universitaria Consorziale Policlinico di Bari, Italy
Masatoshi Hotta,
University of California, Los Angeles, United States

*CORRESPONDENCE
Lei Kang
kanglei@bjmu.edu.cn

RECEIVED 30 October 2023
ACCEPTED 15 November 2023
PUBLISHED 28 November 2023

CITATION
Huang W, Xiao X, Zhang Y, Peng Y, Song L, Li L, Gao J and Kang L (2023) Case Report: A rare case multicentric angiosarcomas of bone mimicking multiple myeloma on ^{18}F-FDG PET/CT. *Front. Med.* 10:1330341.
doi: 10.3389/fmed.2023.1330341

Case Report: A rare case multicentric angiosarcomas of bone mimicking multiple myeloma on ^{18}F-FDG PET/CT

Wenpeng Huang[1], Xiaoyan Xiao[2], Yongbai Zhang[1], Yushuo Peng[1], Lele Song[1], Liming Li[2], Jianbo Gao[2] and Lei Kang[1]*

[1]Department of Nuclear Medicine, Peking University First Hospital, Beijing, China, [2]Department of Radiology, The First Affiliated Hospital of Zhengzhou University, Zhengzhou, Henan Province, China

Background: Angiosarcoma, a rare endothelial-origin tumor, can develop throughout the body, with the head and neck skin being the most commonly affected areas. It can also originate in other sites such as the breast, iliac artery, and visceral organs including the liver, spleen, and kidneys. Angiosarcoma of the bone is remarkably rare, presenting as either unifocal or multifocal bone lesions and often leading to a grim prognosis. Diagnosing bone angiosarcoma poses a significant challenge. ^{18}F-FDG PET/CT serves as a reliable and indispensable imaging modality for evaluating distant metastases and clinically staging angiosarcomas.

Case report: A 57-year-old woman presented with a 10-day history of dizziness and headaches. Cranial CT scan revealed bone destruction of the parietal bone, accompanied by soft tissue lesions, protruding into the epidural space. MRI examination demonstrated lesions with slightly elevated signal intensity on T2FLAIR, showing moderate enhancement. Furthermore, multiple foci were observed within the T_{12}, $L_{1\text{-}5}$, and $S_{1\text{-}2}$ vertebrae, as well as in the bilateral iliac bones. For staging, ^{18}F-FDG PET/CT was performed. The MIP PET showed multifocal FDG-avid lesions in the sternum, bilateral clavicles, bilateral scapulae, multiple ribs, and pelvic bones. Heterogeneous FDG uptake was observed in multiple bone lesions, including intracranial (SUVmax = 11.3), right transverse process of the T10 vertebra (SUVmax = 5.8), ilium (SUVmax = 3.3), and pubis (SUVmax = 4.7). The patient underwent surgical resection of the cranial lesion. The pathological diagnosis was made with a highly differentiated angiosarcoma.

Conclusion: Angiosarcoma of bone on FDG PET/CT scans is characterized by abnormal FDG uptake along with osteolytic destruction. This case highlights that angiosarcoma of bone can manifest as multicentric FDG uptake, resembling the pattern seen in multiple myeloma. FDG PET/CT can be a useful tool for staging this rare malignant tumor, offering the potential to guide biopsy procedures toward the most metabolically active site. And it should be considered in the differential diagnosis of multiple osteolytic lesions, including metastatic carcinoma, multiple myeloma, and lymphoma of bone.

KEYWORDS

bone, angiosarcoma, magnetic resonance imaging, computed tomography, ^{18}F-FDG PET/CT, case report

Introduction

Angiosarcoma is a rare endothelial-origin tumor that can develop in the whole body (1). The most commonly affected areas are the head and neck skin. Other sites where may originate include the breast, iliac artery, and visceral organs such as the liver, spleen and kidneys (2–7). Angiosarcoma of the bone is remarkably rare, constituting less than 1% of all primary bone sarcomas, predominantly occurring between the ages of 50 and 70 (8, 9). It can manifest as either unifocal or multifocal bone lesions and typically heralds a bleak prognosis (10, 11). Diagnosing angiosarcoma of the bone poses a considerable challenge and represents the malignant end of the CD31/ERG positive vascular tumors spectrum, encompassing hemangiomas, hemangioendotheliomas, as well as well-differentiated and poorly differentiated angiosarcomas (12).

Fluorine-18 fluorodeoxyglucose positron emission tomography/computed tomography (^{18}F-FDG PET/CT) stands as a dependable and indispensable imaging modality for assessing distant metastases and clinically staging angiosarcomas (13). In an effort to enrich comprehension of this rare neoplasm, we present a case study delineating the ^{18}F-FDG PET/CT imaging manifestations in a patient afflicted by multicentric angiosarcomas of the bone, marked by a challenging clinical diagnosis.

Case presentation

A 57-year-old woman presented with a 10-day history of dizziness and headaches. Cranial CT scan revealed bone destruction of the parietal bone, accompanied by soft tissue lesions, with the largest measuring approximately 3.6 × 2.7 × 2.0 cm, protruding into the epidural space (Figures 1A,B). MRI examination demonstrated lesions with slightly elevated signal intensity on T2FLAIR (Figure 1C), showing moderate enhancement (Figure 1D). Furthermore, multiple foci were observed within the T_{12}, $L_{1\text{-}5}$, and $S_{1\text{-}2}$ vertebrae, as well as in the bilateral iliac bones. These exhibited irregular signal patterns on fat-suppressed T2WI and mild enhancement (Figures 1E,F).

For staging, ^{18}F-FDG PET/CT was performed (Figures 2A–J). The MIP PET showed multifocal FDG-avid lesions in the sternum, bilateral clavicles, bilateral scapulae, multiple ribs, and pelvic bones. Sagittal images of the spine revealed the presence of multiple bone-destroying lesions, with the highest FDG uptake detected in the T6 vertebra (SUVmax = 7.6). Heterogeneous FDG uptake was observed in multiple bone lesions, including intracranial (SUVmax = 11.3), right transverse process of the T10 vertebra (SUVmax = 5.8), ilium (SUVmax = 3.3), and pubis (SUVmax = 4.7).

The patient underwent a bone marrow aspiration biopsy, which showed active proliferation of bone marrow tissue and the presence of granulocyte lineage, thereby ruling out the diagnosis of multiple myeloma. Subsequently, the patient underwent surgical resection of the cranial lesion. Hematoxylin and eosin staining revealed irregular vascular channels and hyperplasia of atypical cells arranged in a diffuse sheet-like growth pattern (Figure 3A). Immunohistochemical staining showed positive expression of CD31 (Figure 3B), CD34 (Figure 3C), ERG, FLI-1 (Figure 3D), and SMA. The pathological diagnosis was made with a highly differentiated angiosarcoma.

Discussion

Angiosarcomas, highly aggressive and exceptionally rare within the spectrum of sarcomas, represent less than 1% of all sarcomas (4).

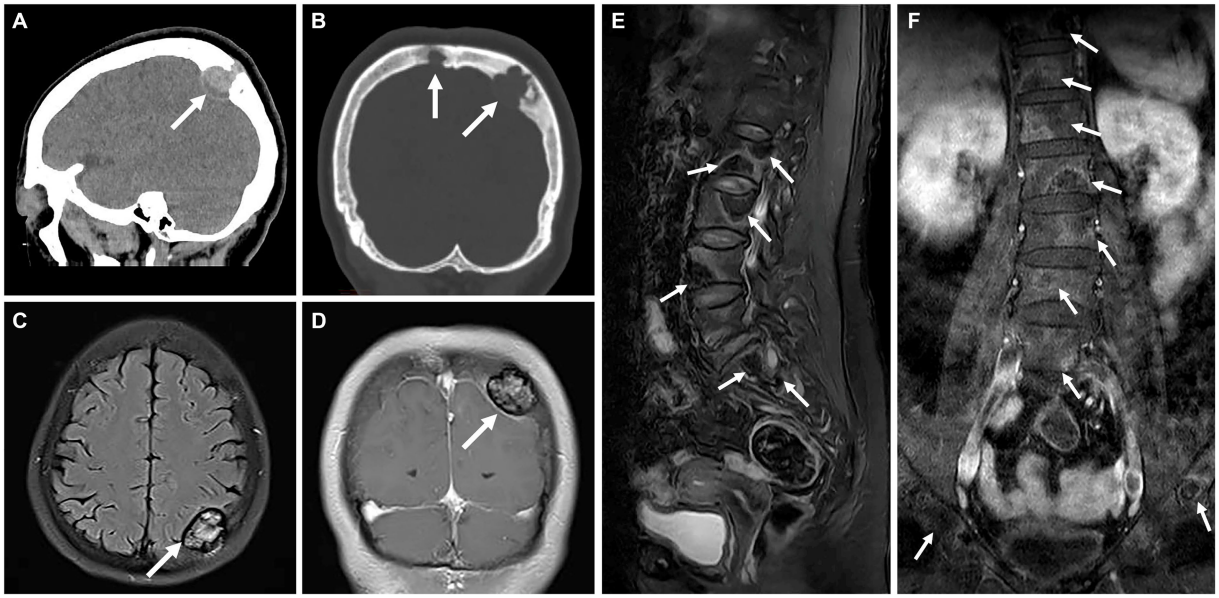

FIGURE 1
Computed tomography (CT) and magnetic resonance (MR) images of multicentric angiosarcomas of bone. Sagittal and coronal CT image revealed bone destruction of the parietal bone **(A)**, accompanied by soft tissue lesions (long arrows), with the largest measuring approximately 3.6 × 2.7 × 2.0 cm, protruding into the epidural space **(B)**. MRI examination demonstrated lesions with slightly elevated signal intensity on T2FLAIR **(C,** long arrows**)**, showing moderate enhancement on Fat-sat Gd-T1WI **(D)**. Multiple foci were observed within the T12, L1-5, and S1-2 vertebrae, as well as in the bilateral iliac bones. These exhibited irregular signal patterns on fat-suppressed T2WI **(E,** long arrows**)** and mild enhancement on Fat-sat Gd-T1WI **(F)**.

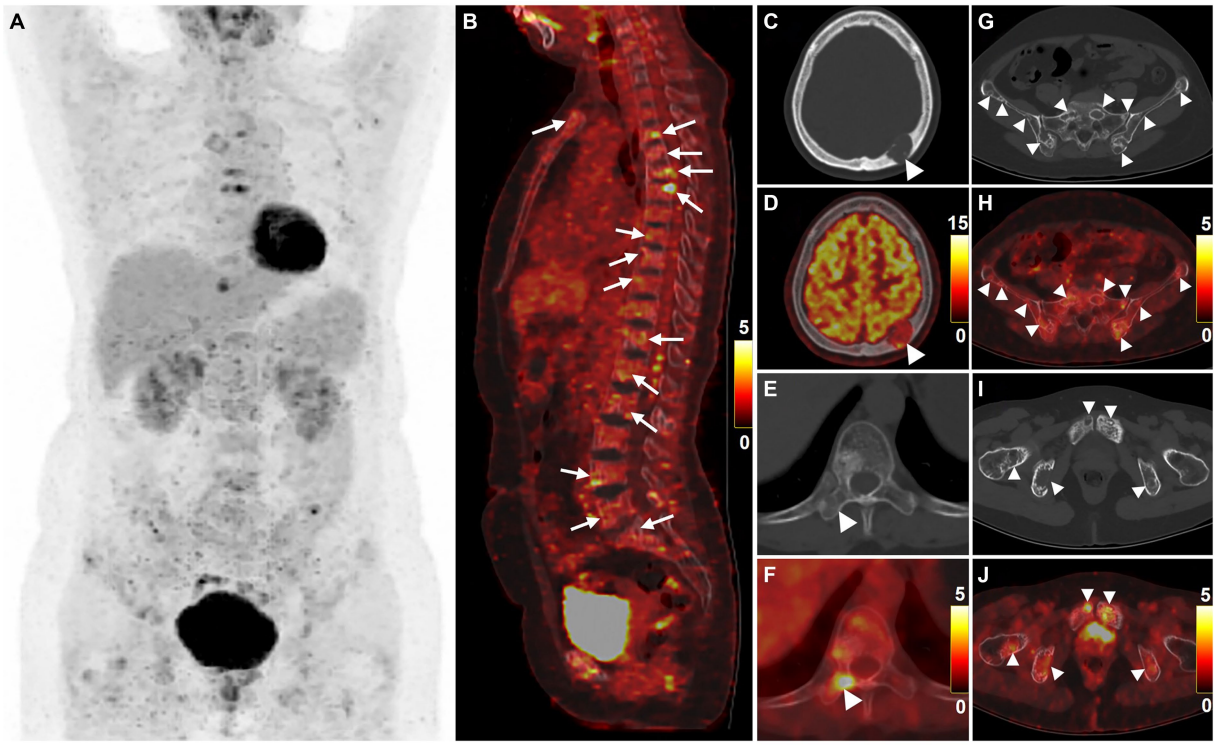

FIGURE 2
^{18}F-FDG PET/CT images of multicentric angiosarcomas of bone. The anteroposterior 3-dimensional maximum intensity projection image (MIP) revealed multifocal FDG-avid lesions in the sternum, bilateral clavicles, bilateral scapulae, multiple ribs, and pelvic bones **(A)**. Sagittal images of the spine revealed the presence of multiple bone-destroying lesions (long arrows), with the highest FDG uptake detected in the T6 vertebra (**B**, SUVmax = 7.6). Heterogeneous FDG uptake was observed in multiple bone lesions (arrowheads), including intracranial (**C,D**, SUVmax = 11.3), right transverse process of the T10 vertebra (**E,F**, SUVmax = 5.8), ilium (**G,H**, SUVmax = 3.3), and pubis (**I,J**, SUVmax = 4.7).

These sarcomas predominantly afflict elderly men, with over 50% of cases manifesting in the cutaneous and soft tissues of the head and neck. The remaining occurrences of angiosarcomas may emerge from various sites, including the breast, soft tissues, bones, and visceral organs such as the liver and spleen (1, 4, 14, 15). Long-term sun exposure, radiation exposure, genetic predispositions, environmental factors, and trauma have been implicated in the development of angiosarcoma (16).

Vascular bone tumors encompass a spectrum of clinicopathological entities, ranging from benign hemangiomas at one end to angiosarcomas at the other (8, 17). Compared to hemangiomas, recognized as benign tumors, epithelioid hemangioendothelioma represents a low-grade malignancy, and hemangioendothelioma occupies the intermediate category, while angiosarcoma emerges as a high-grade malignancy (18). Angiosarcoma of bone may present as unifocal or multifocal disease, potentially affecting any bone. In the majority of cases, angiosarcoma of bone occurs in long bones and short tubular bones, most frequently observed in the femur, tibia, and humerus, followed by the pelvis, ribs, and vertebrae (8, 17). It can consist of multiple lesions within a single bone, affecting the same extremity, or spreading throughout the skeleton (8, 10, 11, 19). Clinical manifestations typically involve bone pain, pathologic fractures, and hypercalcemia. In our case, the sternum, bilateral clavicles, bilateral scapulae, multiple ribs, and pelvic bones demonstrated multicentricity of the tumor.

The diagnosis of angiosarcoma heavily relies on biopsy findings, with neoplastic cells demonstrating endothelial differentiation of vascular or lymphatic origin. Angiosarcomas exhibit varying histologic presentations, ranging from well-differentiated to poorly differentiated tumors. Histologic characteristics span from abnormal endothelial cells retaining some degree of well-differentiated vascular architecture to poorly differentiated sheets of abnormal cells with substantial hemorrhage and necrosis (16, 20). The most prevalent histological feature observed was the presence of intracytoplasmic vacuoles, either containing erythrocytes or empty. Additionally, the identification of three or more mitoses per 10 high-power fields (HPF), the presence of a macronucleolus, and fewer than five eosinophilic granulocytes per 10 HPF serve as prognostic risk factors. The presence of all three risk factors in a single lesion decreases the 5-year survival rate to 0% (8). Immunohistochemistry plays a vital role in identifying poorly differentiated tumors. Positive staining for the ERG endothelial marker, factor VIII, CD31, FLI-1, CD99, S-100 protein, STAT6, SMA, and the Ki-67 proliferation marker is characteristic for angiosarcomas. Expression of these markers confirms the endothelial phenotype of malignant vascular tumors. Definitive identification relies on immunohistochemistry demonstrating vascular and endothelial markers, such as CD31, CD34, FLI-1, and ERG. Our patient's tumor displayed positivity for all these markers, with CD31 often considered the most specific marker for vascular bone tumors (8, 21, 22).

The integrated ^{18}F-FDG PET/CT stands as the foremost functional and metabolic imaging technique, delivering clinicians

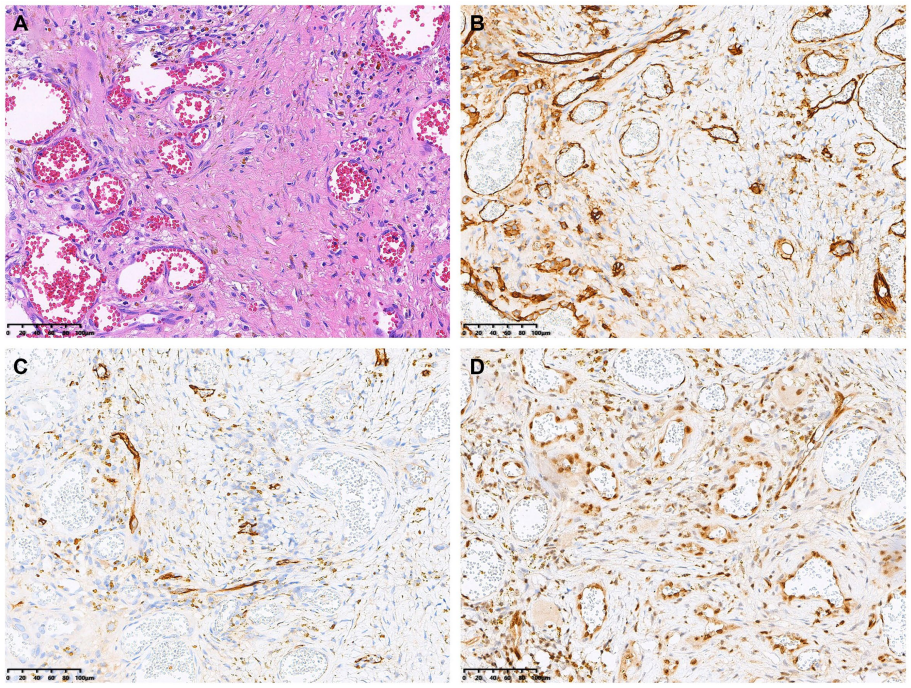

FIGURE 3
Histopathological and immunohistochemical images. Hematoxylin–eosin (HE) staining (magnification × 200) revealed irregular vascular channels and hyperplasia of atypical cells arranged in a diffuse sheet-like growth pattern **(A)**. Immunohistochemistry showed that the positive expression of CD31 **(B)**, CD34 **(C)** and FLI-1 **(D)** of the tumor cells (magnification × 200).

with comprehensive and precise information at present (23, 24). On FDG PET scans, angiosarcoma typically exhibits increased FDG uptake, and PET/CT is a valuable tool for staging angiosarcoma and assessing distant metastases (5–7, 10, 25–29). Chen et al. (30) conducted a retrospective study involving 19 pathologically diagnosed angiosarcoma cases before treatment, examining the relationship among clinical characteristics, laboratory examinations, ^{18}F-FDG PET/CT parameters, and the prognosis of angiosarcoma. In comparison to conventional imaging, systemic ^{18}F-FDG PET/CT, with its high sensitivity and specificity, presents significant advantages in the evaluation of angiosarcoma, particularly in the detection of occult metastases like those in bone marrow, subcutaneous tissue, liver, and even hydrothorax and ascitic fluid. The SUVmax of angiosarcoma correlates with histopathological tumor grade (27). An increasing SUVmax is associated with a worse prognosis, can be a valuable noninvasive prognostic marker (6). Lee et al. (28) observed that the degree of FDG uptake, as reflected by SUVmax, served as a prognostic indicator for patients with vascular tumors. Using a cutoff SUVmax of 3.0, the 2-year progression-free survival rate was notably higher in the 14 patients with a tumor SUVmax <3.0 (75.0%) compared to the 12 patients with a tumor SUVmax ≥3.0 (0%) ($p = 0.0053$). In a study of 16 angiosarcoma cases by Kato et al. (27), higher SUVmax, MTV, whole-body TLG, TBR, and whole-body TLG ratio significantly correlated with poorer overall survival in patients evaluated by ^{18}F-FDG PET/CT before treatment. Umemura et al. (29) conducted an early prognosis assessment of 18 cases of cutaneous angiosarcoma using PET/CT, noting that those with higher SUVmax at the initial diagnosis experienced a markedly poorer prognosis compared to those with a lower SUVmax.

The prognosis of angiosarcomas is notably poor (19), with frequent occurrences of both local recurrence and distant metastasis (31, 32), typically resulting in a reported 5-year survival rate of approximately 31–33% (8, 33). Angiosarcoma manifesting in bone exhibits a significantly bleaker prognosis compared to general angiosarcoma, with a 5-year survival rate of 20% and an approximate median survival time of 10 months (34, 35). Wang et al. (11) observed that the prognosis of malignant bone angiosarcoma was notably worse than that of malignant vascular tumors, with a median overall survival (OS) of merely 9 months. Age, stage, and the utilization of surgery stand as independent prognostic factors for patients with bone angiosarcoma (11, 36, 37). Managing angiosarcoma poses a considerable clinical challenge due to both the aggressive nature of the tumor and the limited evidence guiding treatment modalities and agents. Treatment strategies for angiosarcomas are contingent on the stage and location. Surgical resection remains the primary therapeutic approach for localized disease, although achieving negative margins can be challenging due to the infiltrative nature of the ailment. A multidisciplinary approach, involving surgery, radiation, chemotherapy, and potentially recent immune-oncology agents, can yield positive outcomes (38). Studies have suggested that bone angiosarcoma treated with surgery alone or in combination with radiotherapy exhibits better outcomes compared to cases treated with radiotherapy alone or without therapy. Due to the endothelial origin of angiosarcomas, there is a growing interest in employing antiangiogenic agents for this tumor.

Research has explored various agents, including bevacizumab, a monoclonal antibody targeting vascular endothelial growth factor-A; TRC105, a monoclonal antibody against endoglin; trebananib, a neutralizing peptibody to angiopoietin-1/2; and vascular endothelial growth factor receptor inhibitors such as pazopanib, sorafenib, and axitinib (16).

Conclusion

In conclusion, we offer a case study detailing the ^{18}F-FDG PET/CT imaging manifestations in a patient affected by multicentric angiosarcomas of the bone. Angiosarcoma of bone on FDG PET/CT scans is characterized by abnormal FDG uptake along with osteolytic destruction. This case highlights that angiosarcoma of bone can manifest as multicentric FDG uptake, resembling the pattern seen in multiple myeloma. FDG PET/CT can be a useful tool for staging this rare malignant tumor, offering the potential to guide biopsy procedures toward the most metabolically active site. And it should be considered in the differential diagnosis of multiple osteolytic lesions, including metastatic carcinoma, multiple myeloma, and lymphoma of bone.

Data availability statement

The original contributions presented in the study are included in the article/supplementary material, further inquiries can be directed to the corresponding author.

Ethics statement

Written informed consent was obtained from the minor(s)' legal guardian/next of kin for the publication of any potentially identifiable images or data included in this article.

Author contributions

WH: Writing – original draft, Writing – review & editing. XX: Data curation, Writing – review & editing. YZ: Supervision, Writing – original draft. YP: Data curation, Formal analysis, Writing – original draft. LS: Data curation, Writing – original draft. LL: Data curation, Writing – review & editing. JG: Supervision, Writing – review & editing. LK: Funding acquisition, Writing – review & editing.

Funding

The author(s) declare financial support was received for the research, authorship, and/or publication of this article. This work was supported by the National Natural Science Foundation of China (82171970), the Beijing Science Foundation for Distinguished Young Scholars (JQ21025), the Beijing Municipal Science & Technology Commission (Z221100007422027), National High Level Hospital Clinical Research Funding (Interdisciplinary Research Project of Peking University First Hospital, 2023IR17).

Conflict of interest

The authors declare that the research was conducted in the absence of any commercial or financial relationships that could be construed as a potential conflict of interest.

Publisher's note

References

1. Lahat G, Dhuka AR, Hallevi H, Xiao L, Zou C, Smith KD, et al. Angiosarcoma: clinical and molecular insights. *Ann Surg.* (2010) 251:1098–106. doi: 10.1097/SLA.0b013e3181dbb75a

2. Wang R, Wang X, Ji B, Guan Q, Chen B. Primary common iliac artery Angiosarcoma with multiple bone metastases revealed by dual-time point FDG PET/CT imaging. *Clin Nucl Med.* (2019) 44:232–3. doi: 10.1097/RLU.0000000000002435

3. Cheng J, Ou X. Prominent bone marrow metastases without concurrent intra-chest metastasis in a case of cardiac Angiosarcoma. *Clin Nucl Med.* (2020) 45:638–9. doi: 10.1097/RLU.0000000000003130

4. Florou V, Wilky BA. Current Management of Angiosarcoma: recent advances and lessons from the past. *Curr Treat Options in Oncol.* (2021) 22:61. doi: 10.1007/s11864-021-00858-9

5. Zheng K, Liu Y, Cui R, Li F. Primary spleen Angiosarcoma with concomitant hepatic hemangiomas on 18F-FDG PET/CT. *Clin Nucl Med.* (2018) 43:222–3. doi: 10.1097/RLU.0000000000001982

6. Cassou-Mounat T, Champion L, Bozec L, Laurence V, Huchet V, Luporsi M, et al. Primary and secondary breast Angiosarcoma: FDG PET/CT series. *Clin Nucl Med.* (2019) 44:e33–5. doi: 10.1097/RLU.0000000000002334

7. Yang J, Dong A, Nian S, Peng Y, Zuo C. FDG PET/CT in a case of primary Angiosarcoma of the kidney. *Clin Nucl Med.* (2023) 48:370–2. doi: 10.1097/RLU.0000000000004586

8. Verbeke SLJ, Bertoni F, Bacchini P, Sciot R, Fletcher CDM, Kroon HM, et al. Distinct histological features characterize primary angiosarcoma of bone. *Histopathology.* (2011) 58:254–64. doi: 10.1111/j.1365-2559.2011.03750.x

9. Matti A, Farolfi A, Frisoni T, Fanti S, Nanni C. FDG-PET/CT guided biopsy in Angiosarcoma of bone: diagnosis. *Staging and Beyond Clin Nucl Med.* (2018) 43:e48–9. doi: 10.1097/RLU.0000000000001918

10. Li F, Ou X. A low-grade bone angiosarcoma presented as low to mild 18F-FDG uptake mimicking multiple myeloma. *Hell J Nucl Med.* (2020) 23:360–1. doi: 10.1967/s002449912217

11. Wang B, Chen L-J, Wang X-Y. A clinical model of bone Angiosarcoma patients: a population-based analysis of epidemiology, prognosis, and treatment. *Orthop Surg.* (2020) 12:1652–62. doi: 10.1111/os.12803

12. Palmerini E, Leithner A, Windhager R, Gosheger G, Boye K, Laitinen M, et al. Angiosarcoma of bone: a retrospective study of the European musculoskeletal oncology society (EMSOS). *Sci Rep.* (2020) 10:10853. doi: 10.1038/s41598-020-66579-5

13. Ariga A, Matsumoto S, Tanizawa T, Hayakawa K, Minami Y, Saito M, et al. Bone metastases with "false negative" findings on 18F-FDG PET/CT in patients with angiosarcoma: a case series with literature review. *Medicine (Baltimore).* (2023) 102:e34196. doi: 10.1097/MD.0000000000034196

14. Scholsem M, Raket D, Flandroy P, Sciot R, Deprez M. Primary temporal bone angiosarcoma: a case report. *J Neuro-Oncol.* (2005) 75:121–5. doi: 10.1007/s11060-005-0375-0

15. Conic RRZ, Damiani G, Frigerio A, Tsai S, Bragazzi NL, Chu TW, et al. Incidence and outcomes of cutaneous angiosarcoma: a SEER population-based study. *J Am Acad Dermatol.* (2020) 83:809–16. doi: 10.1016/j.jaad.2019.07.024

16. Bernstock JD, Shafaat O, Hardigan A, Fox BM, Moore LS, Chagoya G, et al. Angiosarcoma of the temporal bone: case report and review of the literature. *World Neurosurg.* (2019) 130:351–7. doi: 10.1016/j.wneu.2019.07.107

17. Baliaka A, Balis G, Michalopoulou-Manoloutsiou E, Papanikolaou A, Nikolaidou A. Primary angiosarcoma of bone. A case report. *Hippokratia*. (2013) 17:180–2.

18. Boriani S, Cecchinato R, Righi A, Bandiera S, Dei Tos AP, Ghermandi R, et al. Primary vascular bone tumors in the spine: a challenge for pathologists and spine oncology surgeons. *Eur Spine J*. (2019) 28:1502–11. doi: 10.1007/s00586-019-05930-5

19. Marthya A, Patinharayil G, Puthezeth K, Sreedharan S, Kumar A, Kumaran CM. Multicentric epithelioid angiosarcoma of the spine: a case report of a rare bone tumor. *Spine J*. (2007) 7:716–9. doi: 10.1016/j.spinee.2006.08.013

20. Hammon RJ, Lin HW, Sadow PM, Lin DT, Rocco JW. Pathology quiz case 1. Angiosarcoma. *Arch Otolaryngol Head Neck Surg*. (2011) 137:198–201. doi: 10.1001/archoto.2010.247-a

21. Young RJ, Brown NJ, Reed MW, Hughes D, Woll PJ. Angiosarcoma. *Lancet Oncol*. (2010) 11:983–91. doi: 10.1016/S1470-2045(10)70023-1

22. O'Neill JP, Bilsky MH, Kraus D. Head and neck sarcomas: epidemiology, pathology, and management. *Neurosurg Clin N Am*. (2013) 24:67–78. doi: 10.1016/j.nec.2012.08.010

23. Donnelly SC. 18F-FDG-PET/CT scanning-clinical usefulness beyond cancer. *QJM*. (2018) 111:593. doi: 10.1093/qjmed/hcy184

24. Dammacco F, Rubini G, Ferrari C, Vacca A, Racanelli V. ^{18}F-FDG PET/CT: a review of diagnostic and prognostic features in multiple myeloma and related disorders. *Clin Exp Med*. (2015) 15:1–18. doi: 10.1007/s10238-014-0308-3

25. Yang Z, Tao H, Ye Z, Yang D. Multicentric epithelioid angiosarcoma of bone. *Orthopedics*. (2012) 35:e1293–6. doi: 10.3928/01477447-20120725-39

26. Takahashi H, Hara T, Suzuki H, Hashimoto R, Minami M. FDG-PET/CT demonstrates splenic Angiosarcoma bone marrow metastasis. *Clin Nucl Med*. (2020) 45:e20–3. doi: 10.1097/RLU.0000000000002717

27. Kato A, Nakamoto Y, Ishimori T, Saga T, Togashi K. Prognostic value of quantitative parameters of 18F-FDG PET/CT for patients with Angiosarcoma. *AJR Am J Roentgenol*. (2020) 214:649–57. doi: 10.2214/AJR.19.21635

28. Lee WW, So Y, Kang SY, So M-K, Kim H, Chung HW, et al. F-18 fluorodeoxyglucose positron emission tomography for differential diagnosis and prognosis prediction of vascular tumors. *Oncol Lett*. (2017) 14:665–72. doi: 10.3892/ol.2017.6192

29. Umemura H, Yamasaki O, Kaji T, Hamada T, Otsuka M, Asagoe K, et al. Prognostic value of 18 F-fluorodeoxyglucose positron emission tomography/computed tomography in patients with cutaneous angiosarcoma: a retrospective study of 18 cases. *J Dermatol*. (2017) 44:1046–9. doi: 10.1111/1346-8138.13839

30. Chen D, Tang M, Lv S, Wang H, Du W, Zhao X, et al. Prognostic usefulness of clinical features and pretreatment 18F-FDG PET/CT metabolic parameters in patients with angiosarcoma. *Quant Imaging Med Surg*. (2022) 12:2792–804. doi: 10.21037/qims-21-563

31. Germans SK, Weinberg OK. Metastatic angiosarcoma in a bone marrow biopsy. *Blood*. (2022) 140:2001. doi: 10.1182/blood.2022018036

32. Wang C, Rabah R, Blackstein M, Riddell RH. Bone marrow metastasis of angiosarcoma. *Pathol Res Pract*. (2004) 200:551–5. doi: 10.1016/j.prp.2004.05.003

33. Fury MG, Antonescu CR, Van Zee KJ, Brennan MF, Maki RG. A 14-year retrospective review of angiosarcoma: clinical characteristics, prognostic factors, and treatment outcomes with surgery and chemotherapy. *Cancer J*. (2005) 11:241–7. doi: 10.1097/00130404-200505000-00011

34. Palmerini E, Maki RG, Staals EL, Alberghini M, Antonescu CR, Ferrari C, et al. Primary angiosarcoma of bone: a retrospective analysis of 60 patients from 2 institutions. *Am J Clin Oncol*. (2014) 37:528–34. doi: 10.1097/COC.0b013e31827defa1

35. Righi A, Sbaraglia M, Gambarotti M, Gibertoni D, Rovira MP, Benini S, et al. Primary vascular tumors of bone: a Monoinstitutional morphologic and molecular analysis of 427 cases with emphasis on epithelioid variants. *Am J Surg Pathol*. (2020) 44:1192–203. doi: 10.1097/PAS.0000000000001487

36. Lee KC, Chuang S-K, Philipone EM, Peters SM. Characteristics and prognosis of primary head and neck Angiosarcomas: a surveillance, epidemiology, and end results program (SEER) analysis of 1250 cases. *Head Neck Pathol*. (2019) 13:378–85. doi: 10.1007/s12105-018-0978-3

37. Wang W, Hong J, Meng J, Wu H, Shi M, Yan S, et al. Survival analysis of patients with osseous malignant vascular tumors: results of the surveillance, epidemiology, and end results (SEER) database from 1973 to 2015. *Med Sci Monit*. (2019) 25:5525–35. doi: 10.12659/MSM.914950

38. Sturm EC, Marasco IS, Katz SC. Multidisciplinary Management of Angiosarcoma – a review. *J Surg Res*. (2021) 257:213–20. doi: 10.1016/j.jss.2020.07.026

frontiers | Frontiers in Immunology

TYPE Case Report
PUBLISHED 04 December 2023
DOI 10.3389/fimmu.2023.1243208

OPEN ACCESS

EDITED BY
Carmelo Caldarella,
Fondazione Policlinico Universitario A. Gemelli IRCCS, Italy

REVIEWED BY
Romain-David Seban,
Institut Curie, France
Lars Ny,
University of Gothenburg, Sweden

*CORRESPONDENCE
Karim Amrane
kamrane@ch-morlaix.fr

†These authors have contributed equally to this work

RECEIVED 20 June 2023
ACCEPTED 13 November 2023
PUBLISHED 04 December 2023

CITATION
Amrane K, Le Meur C, Thuillier P, Dzuko Kamga J, Alemany P, Chauvelot F, Niel C, Bellange A and Abgral R (2023) Case Report: Long-term metabolic response of metastatic uveal melanoma to pembrolizumab on FDG-PET/CT despite a serial pseudoprogressions phenomenon. *Front. Immunol.* 14:1243208. doi: 10.3389/fimmu.2023.1243208

Case Report: Long-term metabolic response of metastatic uveal melanoma to pembrolizumab on FDG-PET/CT despite a serial pseudoprogressions phenomenon

Karim Amrane[1,2*†], Coline Le Meur[3†], Philippe Thuillier[2,4], Jacques Dzuko Kamga[5], Pierre Alemany[6], Frederic Chauvelot[7], Clémence Niel[1], Alex Bellange[1] and Ronan Abgral[5,8†]

[1]Department of Oncology, Centre Hospitalier des Pays de Morlaix, Morlaix, France, [2]Inserm, UMR1227, Lymphocytes B et Autoimmunité, Univ Brest, Inserm, LabEx Immunotherapy-Graft-Oncology (IGO), Brest, France, [3]Department of Radiotherapy, University Hospital of Brest, Brest, France, [4]Department of Endocrinology, University Hospital of Brest, Brest, France, [5]Department of Nuclear Medicine, University Hospital of Brest, Brest, France, [6]Department of Pathology, Ouestpathology Brest, Brest, France, [7]Department of Onco-pharmacy, Centre Hospitalier des Pays de Morlaix, Morlaix, France, [8]Unité Mixte de Recherche (UMR) Inserm 1304 Groupe d'étude de la thrombose de Bretagne-Occidentale (GETBO), Institut Federatif de Recherche (IFR) 148, University of Western Brittany, Brest, France

Uveal melanoma (UV) is a rare and aggressive melanoma with poor 1-year survival. up to 50% of UV patients develop metastases, mainly to the liver. Here, the authors present a 2-deoxy-2-[^{18}F] fluoro-D-glucose positron emission tomography (^{18}F-FDG-PET) study of a very rare case of secondarily metastatic UV in an 81-year-old Caucasian with a dramatic response to pembrolizumab associated with serial pseudogression. ^{18}F-FDG-PET associated with clinical status and peripheral blood derived neutrophil-to-lymphocyte ratio (dNLR) were performed to guide therapeutic strategy due to an atypical pseudoprogression phenomenon.

KEYWORDS

uveal melanoma, pembrolizumab, FDG-PET, immune checkpoint inhibition, pseudoprogression

Introduction

Uveal melanoma (UV) accounts for less than 5% of all melanomas (1). Although UV arises from uveal melanocytes, it differs from cutaneous melanoma (CM) in its oncogenic drivers, development, and tumor microenvironment, with different molecular drivers and a cold tumor microenvironment compared to CM (2, 3). These differences likely contribute to a poor clinical response to systemic therapy, including immune checkpoint inhibition (ICI), which rarely induces durable remissions in patients with metastatic UV (4–6). Up to 50% of patients with UV develop metastases, primarily to the liver (7, 8), which affects prognosis with a median overall survival of approximately 1 year (9).

Case description

We present the case of an 81-year-old Caucasian man with a previous medical history of non-mutated right eye UV (BRAF/NRAS/c-Kit wild-type), treated by surgery 16 years ago and in complete remission since then. He was referred to our oncology department because of a histologically proven unresectable liver recurrence, which was detected by ultrasound as part of the surveillance performed since surgery.

A 2-deoxy-2-[^{18}F] fluoro-D-glucose positron emission tomography (FDG-PET/CT) scan was performed for stating and showed pathological hypermetabolism (SUVmax 5.7) in a large isolated right hepatic hypodense area with no other lesions, particularly locoregional lymph nodes. A complementary magnetic resonance imaging (MRI) scan of the brain showed no metastasis. A pre-therapeutic work-up including lactate dehydrogenase (LDH) assay (assessed as 165 u/l, i.e. within the norm) (10–12) and peripheral blood derived neutrophil-to-lymphocyte ratio (dNLR) was calculated with a favorable score of 2.15 (<3) (13), classifying the disease as having a favorable immune prognostic index (IPI) (14). Anti PD-1 immune checkpoint inhibitor (ICI) therapy with pembrolizumab every 3 weeks was initiated (15).

After 3 cycles of pembrolizumab, FDG-PET/CT (Figure 1B FDG-PET MIP, Figure 1E Axial FDG-PET/CT: assessment after cycle 3 of pembrolizumab) was in favor of unconfirmed progressive metabolic disease (uPMD) according to iPERCIST criteria (16, 17) with an increase of 34% in lean body mass corrected SUV peak (SULpeak) (>30%) compared to baseline (Figure 1A FDG-PET MIP, Figure 1D Axial FDG-PET/CT: initial staging), without new hypermetabolism. After 2 new cycles of pembrolizumab, a close evaluation was performed in order not to confirm or not a proven progression. The result showed a decrease in SULpeak of more than 15%, confirming a pseudoprogression (PsPD) (Figure 1C FDG-PET MIP, Figure 1F Axial FDG-PET/CT: assessement after cycle 5 of pembrolizumab). In parallel with this episode of PsPD, the patient developed rheumatoid arthritis grade 2 according to the Common Terminology Criteria for Adverse Events (CTCAE - version 5.0) classification (18), which resolved rapidly with short-term corticosteroid therapy.

The disease remained stable for more than 1 year with excellent clinical tolerability (Figure 2A FDG-PET MIP, Figure 2D Axial FDG-PET/CT). After 21 cycles of pembrolizumab, a PET scan showed a 28% increase in SULpeak of the main lesion and the appearance of 2 new lesions (Figure 2B FDG-PET MIP, Figure 2E Axial FDG-PET/CT, arrows SUVmax 6,7 and 6,9), consistent with progression according to PERCIST criteria (19). Given the good general condition and excellent tolerability of the patient, it was decided to continue treatment until cycle 23. At the same time, a liver biopsy was performed, which revealed the presence of disease without specific lymphocytic infiltrate. The early re-assessment (Figure 2C FDG-PET MIP, Figure 2F Axial FDG PET-CT) showed a further 15% decrease in SULpeak with the disappearance of the 2 new hypermetabolisms seen on the previous scan thus corresponding to a uPMD according to iPERCIST criteria (16, 17).

The disease remained stable for more than 3 months with excellent clinical tolerability (Figure 3A FDG-PET MIP, Figure 3D Axial FDG-PET/CT). After 34 cycles of pembrolizumab, a PET scan showed a 27% increase in SULpeak

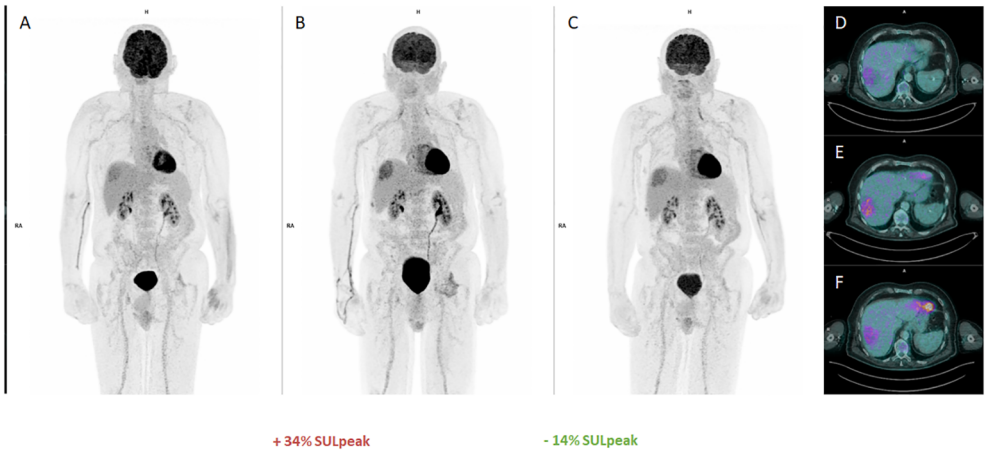

FIGURE 1
FDG-PET first pseudoprogression : (**A, D**: MIP and Axial baseline), (**B, E** : MIP and Axial unconfirmed progressive metabolic disease (uPMD) with 28% increase in SULpeak of the main lesion, (**C, F**: MIP and Axial confirming a pseudoprogression (PsPD).

10.3389/fimmu.2023.1243208

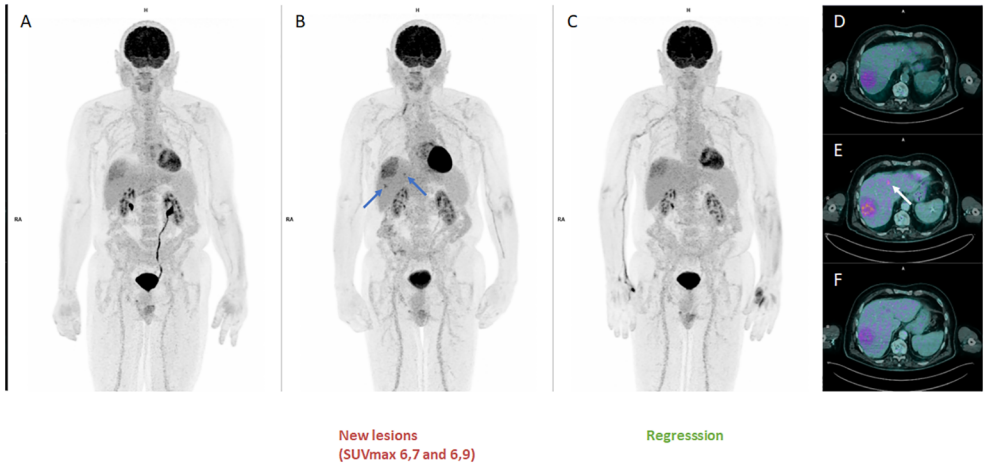

FIGURE 2
FDG-PET second pseudoprogression : (**A, D**: MIP and Axial disease stable before progression), (**B, E** : MIP and Axial disease progression according to PERCIST criteria with 28% increase in SULpeak of the main lesion and the appearance of 2 new lesions), (**C, F**: MIP and Axial confirming a pseudoprogression (PsPD) with 15% decrease in SULpeak with the disappearance of the 2 new hypermetabolisms corresponding to a uPMD according to iPERCIST criteria.

of the main lesion and the recurrence of the 2 previous lesions (Figure 3B FDG-PET MIP, Figure 3E Axial FDG-PET/CT, arrows SUVmax 5,1 and 5,8) described in Figure 2, consistent with progression (19). Once again, it was decided to continue treatment until cycle 38. The early re-assessment showed a stable SULpeak with renewed disappearance of the 2 hypermetabolisms seen on the previous scan (Figure 3C FDG-PET MIP, Figure 3F Axial FDG-PET/CT).

Finally, 3 months after cycle 38 of ICI treatment, the patient presented confirmed disease progression, with an unequivocal metabolic increase in the main lesion of the hepatic dome and the appearance of multiple other FDG-avid liver metastasis. A new line of treatment was proposed with tebentafusp (20). Disease control with pembrolizumab lasted a total of 28months in this patient.

Discussion

This case showed a dramatic response to anti PD1 (28 months) but also a series of PsPD (3 times), which is exceptional because it is the first reported in UV and the second reported in melanoma (21). However, the first published report concerned a 2 times PsPD in a metastatic (liver and bone) CM, treated with nivolumab. Indeed, they found a 118% increase in the size of liver lesion after 3 months starting nivolumab followed by regression; then the appearance of a peritoneal nodule at 8 months, which decreased at 12 months.

ICI immunotherapy has revolutionized cancer management, but it soon became apparent that a subset of patients treated with ICI had an atypical tumor response profile, either after an increase in tumor burden or after the appearance of new lesions, a

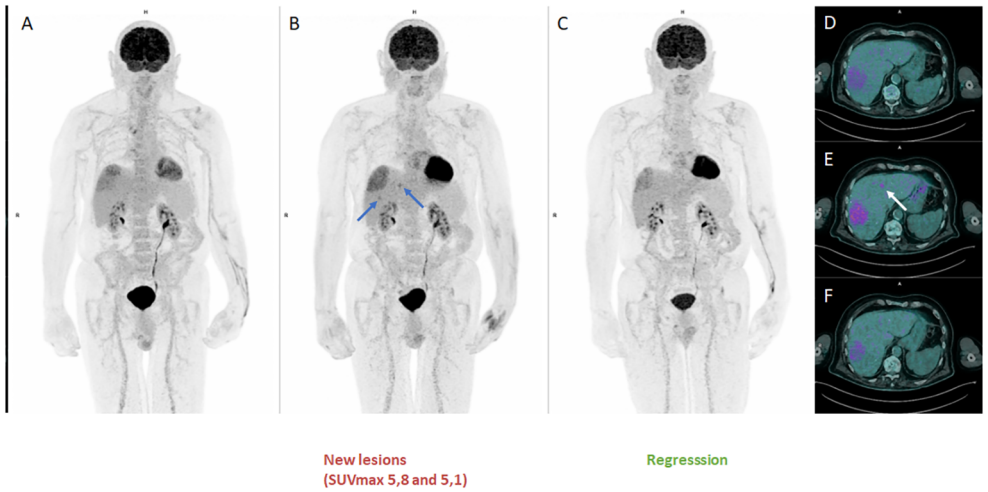

FIGURE 3
FDG-PET MIP third pseudoprogression (**A, D**: MIP and Axial disease stable before progression), (**B, E** : MIP and Axial disease progression according to PERCIST criteria with 27% increase in SULpeak of the main lesion and the recurrence of the 2 previous lesions), (**C, F**: MIP and Axial confirming a pseudoprogression (PsPD) with a stable SULpeak with renewed disappearance of the 2 hypermetabolisms seen on the previous scan.

phenomenon known as pseudoprogression disease (PsPD), which is classified as progressive disease by conventional response criteria (RECIST in CT and PERCIST in PET) (22). Several teams have developed different criteria to take into account this specificity associated with the immune response, such as in conventional imaging the immune-related response criteria (irRC) (23), the immune-related solid tumor response evaluation criteria (irRECIST) (24, 25) and iRECIST (26); and in PET imaging the iPERCIST and imPERCIST criteria (16, 17, 27).

Park et al. reported in a meta-analysis that the incidence of PsPD in clinical trials assessing immunotherapy was 6.0%. PsPD is defined as progressive disease followed by stable disease or partial or complete response (28). The incidence of PsPD by tumor type was 6.4% for melanoma, 5.0% for non-small cell lung cancer and 7.0% for genitourinary cancer. The incidence of PsPD with PD-1/PD-L1 inhibitors alone was 5.7% (95% CI: 4.8%, 6.6%), while it was estimated at 9.7% with anti-CTLA-4 (28).

In an analysis of 32 patients with a variety of tumors, Monch et al. studied the characteristics of PsPD, relatively concordant with our case report. They found that PsPD occurs in 81% of cases after the first treatment response assessment as immune unconfirmed progressive disease (iUPD), with a tumor burden growth regularly below +100%. PsPD was associated with a significant increase in progression of both targeted and non-targeted lesions. LDH levels in PsPD patients were normal in most cases and 40% of patients with PsPD had adverse events (29).

The CD3+, CD4+, CD8+, TIA1+ and granzyme B+ lymphoid infiltrate found in the tumor biopsy could be a strong argument in favor of PsPD (30, 31). In our case, we did not perform a biopsy at the time of the first PsPD because we believed that this phenomenon was well known in literature and that an early re-assessment could spare the patient an invasive procedure. Nevertheless, a biopsy was performed at the time of the second PsPD episode, a rare situation as above mentioned. But it did not show a particularly large lymphoid infiltrate, which could be explained by the fact that the specimen was not infiltrated by lymphocytes.

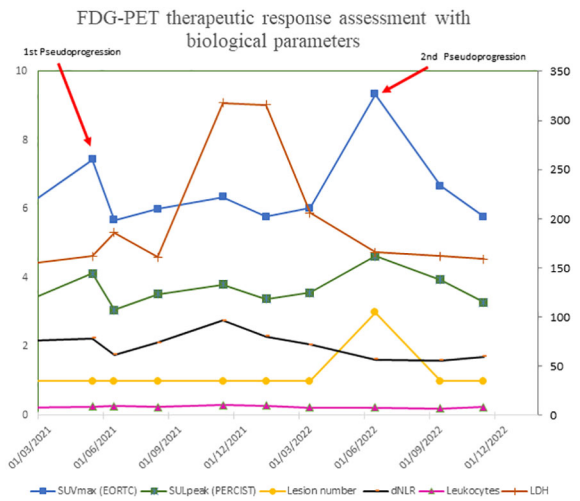

FIGURE 4
FDG-PET therapeutic response assessment with biological parameters.

In contrast, we had performed biological monitoring based on the number of leukocytes and neutrophils in peripheral blood during treatment to calculate dNLR (32) and LDH (10–12). As shown in Figure 4, normal LDH levels, dNLR <3 and IPI score were associated with maintenance of good overall clinical status throughout treatment, suggesting ongoing activation of antitumor immune responses that may lead to this phenomenon of serial PsPD. However, this biological monitoring does not appear to be as robust as measuring circulating ctDNA to distinguish PsPD from proven progression. Indeed, Lee et al. demonstrate that ctDNA profiles can accurately differentiate PsPD from true disease progression in melanoma patients treated with anti PD-1 therapy, with a sensitivity of 90% (95% CI, 68%-99%) and a specificity of 100% (95% CI, 60%-100%) for predicting PsPD (33).

Finally, the choice of interpretation criteria in the context of ICI immunotherapy is critical. Although the RECIST V.1.1 criteria are the gold standard for assessing treatment response, progression or stable disease in patients with solid tumors following cancer therapy (22), they do not take into account unconventional response patterns, such as PsPD in ICI therapy.

To date, the two main RECIST1.1-derived and immunotherapy-adapted assessment criteria used in clinical practice for morphological imaging are irRECIST and iRECIST. Nishino et al. proposed the irRECIST criteria, a system based on unidimensional assessment and a lower number of target lesions than the RECIST 1.1 criteria (24). The main difference between irRECIST and RECIST 1.1 is how new lesions are included in response assessment. In contrast to RECIST 1.1, where new lesions are immediately equated with PD, irRECIST includes new lesions in the total measured tumor burden (TMTB). This method ensures that potentially effective treatment is not interrupted when new lesions appear (34). In addition, a comparison of the 2 criteria for evaluating immunotherapy showed a discrepancy of 8.3% (35). Confirmation of progression is recommended for patients with a minimal increase in TMTB of more than 20%, particularly during the first 12 weeks of treatment, in order to distinguish PsPD from progression (24, 25).

The iRECIST criteria are similar to RECIST 1.1 and irRECIST in terms of recommended imaging modalities, definitions of measurable lesions and target lesions. However, target and non-target lesions are not counted together. Therefore, unlike irRECIST, they are not added to the largest dimension of all target lesions (26). Once iUPD has been identified, re-assessment should be carried out 4 to 8 weeks later to allow for continuity of treatment, but also for salvage therapy, if necessary (34).

In this case, we used FDG-PET/CT to assess treatment response, as recommended by French and European guidelines (36, 37). As with functional imaging, PERCIST-based criteria adapted to immunotherapy have been developed, the most recent being iPERCIST and imPERCIST (16, 27). It has been shown that while imPERCIST reduces the overdiagnosis of progressive disease, new lesions in patients with partial metabolic response or stable metabolic disease were ultimately found to be metastases in 55% of cases. Thus, the prognosis for patients whose target lesions are

shrinking or stable but who develop new lesions appears indeterminate. Therefore, histological confirmation by biopsy should be considered before changing treatment (27).

This case highlights the usefulness of a combined clinical-biological and FDG-PET/CT approach in assessing response to ICI and also suggests that the appearance of a new hypermetabolic lesion should not routinely be equated with ICI treatment failure.

Data availability statement

The original contributions presented in the study are included in the article/supplementary material. Further inquiries can be directed to the corresponding author.

Ethics statement

Written informed consent was obtained from the individual(s) for the publication of any potentially identifiable images or data included in this article.

Author contributions

KA and RA drafted an initial version of the manuscript and are the guarantors of the case report. KA, CL, FC, CN, and AB provided the patient details. PT, JD, and RA provided image analysis. PA provided histological analysis. All authors contributed to the article and approved the version submitted for publication.

Conflict of interest

The authors declare that the research was conducted in the absence of any commercial or financial relationships that could be construed as a potential conflict of interest.

Publisher's note

All claims expressed in this article are solely those of the authors and do not necessarily represent those of their affiliated organizations, or those of the publisher, the editors and the reviewers. Any product that may be evaluated in this article, or claim that may be made by its manufacturer, is not guaranteed or endorsed by the publisher.

References

1. Chattopadhyay C, Kim DW, Gombos DS, Oba J, Qin Y, Williams MD, et al. Uveal melanoma: From diagnosis to treatment and the science in between. *Cancer* (2016) 122:2299–312. doi: 10.1002/cncr.29727

2. van der Kooij MK, Speetjens FM, van der Burg SH, van der Burg SH, Kapiteijn E. Uveal versus cutaneous melanoma; same origin, very distinct tumor types. *Cancers* (2019) 11:845. doi: 10.3390/cancers11060845

3. Coupland SE, Lake SL, Zeschnigk M, Damato BE. Molecular pathology of uveal melanoma. *Eye Lond Engl* (2013) 27:230–42. doi: 10.1038/eye.2012.255

4. Algazi AP, Tsai KK, Shoushtari AN, Munhoz RR, Eroglu Z, Piulats JM, et al. Clinical outcomes in metastatic uveal melanoma treated with PD-1 and PD-L1 antibodies. *Cancer* (2016) 122:3344–53. doi: 10.1002/cncr.30258

5. Pelster MS, Gruschkus SK, Bassett R, Gombos DS, Shephard M, Posada L, et al. Nivolumab and ipilimumab in metastatic uveal melanoma: results from a single-arm phase II study. *J Clin Oncol* (2021) 39:599–607. doi: 10.1200/JCO.20.00605

6. Piulats JM, Espinosa E, de la Cruz Merino L, Varela M, Alonso Carrión L, Martín-Algarra S, et al. Nivolumab plus ipilimumab for treatment-naïve metastatic uveal melanoma: an open-label, multicenter, phase II trial by the Spanish multidisciplinary melanoma group (GEM-1402). *J Clin Oncol Off J Am Soc Clin Oncol* (2021) 39:586–98. doi: 10.1200/JCO.20.00550

7. Bustamante P, Piquet L, Landreville S, Burnier JV. Uveal melanoma pathobiology: Metastasis to the liver. *Semin Cancer Biol* (2021) 71:65–85. doi: 10.1016/j.semcancer.2020.05.003

8. Lorenzo D, Piulats JM, Ochoa M, Arias L, Gutiérrez C, Català J, et al. Clinical predictors of survival in metastatic uveal melanoma. *Jpn J Ophthalmol* (2019) 63:197–209. doi: 10.1007/s10384-019-00656-9

9. Khoja L, Atenafu EG, Suciu S, Leyvraz S, Sato T, Marshall E, et al. Meta-analysis in metastatic uveal melanoma to determine progression free and overall survival benchmarks: an international rare cancers initiative (IRCI) ocular melanoma study. *Ann Oncol Off J Eur Soc Med Oncol* (2019) 30:1370–80. doi: 10.1093/annonc/mdz176

10. Knispel S, Gassenmaier M, Menzies AM, Loquai C, Johnson DB, Franklin C, et al. Outcome of melanoma patients with elevated LDH treated with first-line targeted therapy or PD-1-based immune checkpoint inhibition. *Eur J Cancer Oxf Engl* (1990) 2021:148:61–75. doi: 10.1016/j.ejca.2021.01.034

11. Xu J, Zhao J, Wang J, Sun C, Zhu X. Prognostic value of lactate dehydrogenase for melanoma patients receiving anti-PD-1/PD-L1 therapy. *Med (Baltimore)* (2021) 100:e25318. doi: 10.1097/MD.0000000000025318

12. Waninger JJ, Ma VT, Journey S, Skvarce J, Chopra Z, Tezel A, et al. Validation of the American joint committee on cancer eighth edition staging of patients with metastatic cutaneous melanoma treated with immune checkpoint inhibitors. *JAMA Netw Open* (2021) 4:e210980. doi: 10.1001/jamanetworkopen.2021.0980

13. Capone M, Giannarelli D, Mallardo D, Madonna G, Festino L, Grimaldi AM, et al. Baseline neutrophil-to-lymphocyte ratio (NLR) and derived NLR could predict overall survival in patients with advanced melanoma treated with nivolumab. *J Immunother Cancer* (2018) 6:74. doi: 10.1186/s40425-018-0383-1

14. Sander MS, Stukalin I, Vallerand IA, Goutam S, Ewanchuk BW, Meyers DE, et al. Evaluation of the modified immune prognostic index to prognosticate outcomes in metastatic uveal melanoma patients treated with immune checkpoint inhibitors. *Cancer Med* (2021) 10:2618–26. doi: 10.1002/cam4.3784

15. Rossi E, Pagliara MM, Orteschi D, Dosa T, Sammarco MG, Caputo CG, et al. Pembrolizumab as first-line treatment for metastatic uveal melanoma. *Cancer Immunol Immunother CII* (2019) 68:1179–85. doi: 10.1007/s00262-019-02352-6

16. Goldfarb L, Duchemann B, Chouahnia K, Zelek L, Soussan M. Monitoring anti-PD-1-based immunotherapy in non-small cell lung cancer with FDG PET: introduction of iPERCIST. *EJNMMI Res* (2019) 9:8. doi: 10.1186/s13550-019-0473-1

17. Lopci E. Immunotherapy monitoring with immune checkpoint inhibitors based on [18F]FDG PET/CT in metastatic melanomas and lung cancer. *J Clin Med* (2021) 10:5160. doi: 10.3390/jcm10215160

18. *CTCAE files* . Available at: https://evs.nci.nih.gov/ftp1/CTCAE/About.html.

19. JH O, Lodge MA, Wahl RL. Practical PERCIST: A simplified guide to PET response criteria in solid tumors 1.0. *Radiology* (2016) 280:576–84. doi: 10.1148/radiol.2016142043

20. Hassel JC, Piperno-Neumann S, Rutkowski P, Baurain J-F, Schlaak M, Butler MO, et al. Three-year overall survival with tebentafusp in metastatic uveal melanoma. *N Engl J Med* (2023). doi: 10.1056/NEJMoa2304753

21. Ozaki Y, Shindoh J, Miura Y, Nakajima H, Oki R, Uchiyama M, et al. Serial pseudoprogression of metastatic Malignant melanoma in a patient treated with nivolumab: a case report. *BMC Cancer* (2017) 17:778. doi: 10.1186/s12885-017-3785-4

22. Schwartz LH, Litière S, de Vries E, Ford R, Gwyther S, Mandrekar S, et al. RECIST 1.1 – update and clarification: from the RECIST committee. *Eur J Cancer Oxf Engl* (1990) 2016:62:132–137. doi: 10.1016/j.ejca.2016.03.081

23. Wolchok JD, Hoos A, O'Day S, Weber JS, Hamid O, Lebbe C, et al. Guidelines for the evaluation of immune therapy activity in solid tumors: immune-related response criteria. *Clin Cancer Res* (2009) 15:7412–20. doi: 10.1158/1078-0432.CCR-09-1624

24. Nishino M, Giobbie-Hurder A, Gargano M, Suda M, Ramaiya NH, Hodi FS. Developing a common language for tumor response to immunotherapy: immune-related response criteria using unidimensional measurements. *Clin Cancer Res Off J Am Assoc Cancer Res* (2013) 19:3936–43. doi: 10.1158/1078-0432.CCR-13-0895

25. Nishino M. Immune-related response evaluations during immune-checkpoint inhibitor therapy: establishing a "common language" for the new arena of cancer treatment. *J Immunother Cancer* (2016) 4:30. doi: 10.1186/s40425-016-0134-0

26. Seymour L, Bogaerts J, Perrone A, Ford R, Schwartz LH, Mandrekar S, et al. iRECIST: guidelines for response criteria for use in trials testing immunotherapeutics. *Lancet Oncol* (2017) 18:e143–52. doi: 10.1016/S1470-2045(17)30074-8

27. Ito K, Teng R, Schöder H, Humm JL, Ni A, Michaud L, et al. 18F-FDG PET/CT for monitoring of ipilimumab therapy in patients with metastatic melanoma. *J Nucl Med Off Publ Soc Nucl Med* (2019) 60:335–41. doi: 10.2967/jnumed.118.213652

28. Park HJ, Kim KW, Pyo J, Suh CH, Yoon S, Hatabu H, et al. Incidence of pseudoprogression during immune checkpoint inhibitor therapy for solid tumors: A systematic review and meta-analysis. *Radiology* (2020) 297:87–96. doi: 10.1148/radiol.2020200443

29. Mönch S, Heimer MM, Winkelmann M, Guertler A, Schlaak M, Tufman A, et al. Patterns of pseudoprogression across different cancer entities treated with immune checkpoint inhibitors. *Cancer Imaging Off Publ Int Cancer Imaging Soc* (2023) 23:58. doi: 10.1186/s40644-023-00580-9

30. Ma Y, Wang Q, Dong Q, Zhan L, Zhang J. How to differentiate pseudoprogression from true progression in cancer patients treated with immunotherapy. *Am J Cancer Res* (2019) 9:1546–53.

31. Jia W, Gao Q, Han A, Zhu H, Yu J. The potential mechanism, recognition and clinical significance of tumor pseudoprogression after immunotherapy. *Cancer Biol Med* (2019) 16:655–70. doi: 10.20892/j.issn.2095-3941.2019.0144

32. Ding Y, Zhang S, Qiao J. Prognostic value of neutrophil-to-lymphocyte ratio in melanoma: Evidence from a PRISMA-compliant meta-analysis. *Med (Baltimore)* (2018) 97:e11446. doi: 10.1097/MD.0000000000011446

33. Lee JH, Long GV, Menzies AM, Lo S, Guminski A, Whitbourne K, et al. Association between circulating tumor DNA and pseudoprogression in patients with metastatic melanoma treated with anti-programmed cell death 1 antibodies. *JAMA Oncol* (2018) 4:717–21. doi: 10.1001/jamaoncol.2017.5332

34. Calandri M, Solitro F, Angelino V, Moretti F, Veltri A. The role of radiology in the evaluation of the immunotherapy efficacy. *J Thorac Dis* (2018) 10:S1438–46. doi: 10.21037/jtd.2018.05.130

35. Manitz J, D'Angelo SP, Apolo AB, Eggleton SP, Bajars M, Bohnsack O, et al. Comparison of tumor assessments using RECIST 1.1 and irRECIST, and association with overall survival. *J Immunother Cancer* (2022) 10:e003302. doi: 10.1136/jitc-2021-003302

36. Salaün P-Y, Abgral R, Malard O, Querellou-Lefranc S, Quere G, Wartski M, et al. [Update of the recommendations of good clinical practice for the use of PET in oncology]. *Bull Cancer (Paris)* (2019) 106:262–74. doi: 10.1016/j.bulcan.2019.01.002

37. Salaün P-Y, Abgral R, Malard O, Querellou-Lefranc S, Quere G, Wartski M, et al. Good clinical practice recommendations for the use of PET/CT in oncology. *Eur J Nucl Med Mol Imaging* (2020) 47:28–50. doi: 10.1007/s00259-019-04553-8fimmu.2023.1243208

frontiers | Frontiers in Medicine

TYPE Case Report
PUBLISHED 07 December 2023
DOI 10.3389/fmed.2023.1322048

OPEN ACCESS

EDITED BY
Carmelo Caldarella,
Fondazione Policlinico Universitario A. Gemelli IRCCS, Italy

REVIEWED BY
Giorgio Treglia,
Ente Ospedaliero Cantonale (EOC), Switzerland
Federico Selvaggi,
University of Studies G. d'Annunzio Chieti and Pescara, Italy

*CORRESPONDENCE
Xianwen Hu
✉ 541757091@qq.com

RECEIVED 15 October 2023
ACCEPTED 27 November 2023
PUBLISHED 07 December 2023

CITATION
Yang W, Sun Q, Shang M, Li S, Hu X and Hu X (2023) Multimodal imaging study of hepatic perivascular epithelioid cell tumors: a case report.
Front. Med. 10:1322048.
doi: 10.3389/fmed.2023.1322048

Multimodal imaging study of hepatic perivascular epithelioid cell tumors: a case report

Wenbi Yang, Quanlin Sun, Maocai Shang, Song Li, Xiao Hu and Xianwen Hu*

Department of Nuclear Medicine, Affiliated Hospital of Zunyi Medical University, Zunyi, China

Hepatic perivascular epithelioid cell tumors (PEComas) are rare interstitial tumors that are often misdiagnosed as hepatocellular carcinomas due to their unique vascular enhancement patterns. Herein, we present a case of a 61-year-old man who was incidentally found to have a lesion in the left medial segment of the liver during a chest computed tomography (CT) examination performed 4 days prior to his presentation for chest discomfort. Imaging revealed solid components with density similar to that of normal liver tissue and areas of low-density adipose tissue within the lesion. The solid components exhibited increased uptake of fluorine-18 fluorodeoxyglucose on positron emission tomography/CT. Magnetic resonance imaging demonstrated areas with unevenly high signal intensity in both T1-weighted imaging (T1WI) in-phase and T2-weighted imaging (T2WI) sequences, while T2WI in the opposite phase displayed areas with unevenly low signal intensity, indicating the presence of fatty components. Contrast-enhanced T1WI displayed a "fast in and fast out" enhancement pattern. These distinct imaging features contribute to the diagnosis of hepatic PEComas and distinguish it from hepatocellular carcinoma.

KEYWORDS

hepatic, perivascular epithelioid cell tumors, computed tomography, magnetic resonance imaging, positron emission tomography

Introduction

Perivascular epithelioid cell tumors (PEComas) are a group of mesenchymal tumors with histological and immunohistochemical features characterized by the coexpression of perivascular epithelioid myoid cells and melanocyte markers (1). PEComas are a family of tumors that includes angiomyolipomas, lymphangiomyomatosis, lung clear-cell glycomas, clear-cell myomelanocyte tumors, and clear-cell tumors that occur rarely in the pancreas, rectum, bone, and soft tissue (2). PEComas can occur in various parts of the body, especially in the genitourinary system, which accounts for approximately 40% of cases, followed by lung, pancreas and so on (2). In recent years, reports of hepatic PEComas have increased with increasing attention to the disease (3, 4). The incidence of PEComas in the liver is approximately six times higher in women than in men, with a wide age range and a peak incidence in young and middle-aged individuals (5). Patients typically do not exhibit obvious clinical symptoms, and most of them seek medical attention due to incidental findings from routine physical examinations or discomfort caused by the compression effect of large masses (6). Herein, we present the diagnosis and treatment of a patient with hepatic PEComa, focusing on the imaging features and differential diagnosis, with the hope of raising awareness regarding this rare disease.

Case presentation

A 61-year-old man was admitted to the hospital following the discovery of liver lesions during a chest computed tomography (CT) examination, which had been performed due to chest discomfort 4 days prior. He had no history of hypertension, diabetes, hepatitis, tumors, trauma, or prior surgery. His family also denied any history of tumors or genetic problems; physical examination revealed no positive signs. Laboratory examination showed that except for a slight elevation of total bilirubin (37.5 μmol/L, normal: 5–21 μmol/L) and direct bilirubin (7.9 μmol/L, normal: 0–3.4 μmol/L), other laboratory indicators including blood routine and serum tumor markers of digestive system were within the normal reference value range. CT examination revealed a mixed density nodule approximately 2.0 cm × 1.8 cm in size in the medial segment of the left hepatic lobe. On magnetic resonance imaging (MRI as shown in Figure 1), the lesion presented uneven short T1 and long T2 signals, with a clear "fast in and fast out" appearance on contrast-enhanced scans. Based on these imaging findings, the patient was initially suspected of hepatocellular carcinoma. To determine the best course of treatment, the patient underwent a positron emission tomography (PET)/CT examination (PET/CT imaging presented in Figure 2), which revealed increased fluorine-18 fluorodeoxyglucose (^{18}F-FDG) uptake in the lesion, while no significant abnormal radioactive uptake was observed throughout the rest of the body. Subsequently, the patient underwent surgical resection of the lesion under general anesthesia. The excised tumor tissue was sent for histopathological examination; under a microscope, it showed a grayish-red color. The tumor cells as shown in Figure 3 were composed of epithelioid cells rich in transparent cytoplasm and eosinophilic granules. Immunohistochemistry showed that the tumor cells positively expressed HMB45, melan-A, smooth muscle actin (SMA), and calponin. However, they were negative for hepatocyte, microphthalmia-associated transcription factor (MITF), anaplastic lymphoma kinase (ALK), S100, and Ki-67, with a positive index of approximately 10%. Based on the pathological and immunohistochemical results, the patient was diagnosed with hepatic PEComa. The patient was discharged 5 days after receiving antiinflammatory treatment following surgery. To date, the patient has been followed-up for 14 months, and showed no evidence of recurrence.

Discussion

Hepatic PEComas are usually solitary, with only 5–15% occurring as part of the tuberous sclerosis complex (5). Hepatic PEComas are mainly angiomyolipomas, often characterized by a prominent epithelioid morphology and may lack mature adipose tissue or thick-walled blood vessels, typically presenting as a single phenotype (7). Therefore, it can histomorphologically mimic some hepatocyte-derived tumors, such as hepatocellular adenomas and hepatocellular carcinoma (HCC), leading to an incorrect diagnosis. Patients with liver PEComas do not have specific symptoms and most seek medical attention because of physical examination findings or compression symptoms due to excessive tumor volume. A few patients may experience symptoms such as upper abdominal pain, nausea, indigestion, and loss of appetite. There is also a reported case in literature of one patient presenting with chills and fever (8). In our case, a chest CT examination was performed due to chest discomfort, incidentally revealing a liver lesion.

The preoperative diagnosis of PEComa relies mainly on imaging methods. On CT, PEComas in the liver appear mainly as circular or lobulated mixed-density masses with clear boundaries. The solid components of the tumor appear to be of equal or slightly lower density than the liver parenchyma, and the lesion may contain low-density cystic necrotic areas or fatty components (9). On contrast-enhanced scanning, the enhancement mode of the tumor is related to the proportion of various components in the tumor tissue, mainly presenting as obvious enhancement in the arterial phase accompanied by rapid regression, arterial phase enhancement accompanied by slow regression, arterial phase enhancement accompanied by late continuous enhancement, or uneven enhancement (10). On MRI, the main findings of the tumor are a low signal on T1-weighted imaging (T1WI) and a slightly high signal on T2-weighted imaging (T2WI); in typical cases, large tortuous vascular flow empty signal shadows can be seen inside the visible lesions, which has a certain specificity for the diagnosis of PEComas (11). Moreover, the isoinverse phase of T1WI can determine whether there is fat concomitancy inside the lesion, and cystic necrosis inside the lesion is more clearly visible (12). There are only a few literature reports on PET/CT of liver PEComas, and according to the composition of the epithelioid tissue contained in the tumor, its presentation can range from no ^{18}F-FDG uptake to obviously increased ^{18}F-FDG uptake (13–15). Our patient showed equal and low mixed densities on CT, with slightly high signal intensity on T1WI in the same phase and low signal intensity in the opposite phase, indicating the presence of fatty components in the lesion. T2WI showed slightly higher signal intensity, and diffusion-weighted imaging showed limited tumor spread. On contrast-enhanced T1WI, the lesion was significantly enhanced in the arterial phase, and rapidly subsided in the portal phase, presenting as a "fast in and fast out" appearance. On PET/CT, the solid components of the tumor showed increased ^{18}F-FDG uptake, while the surrounding fat components did not show any uptake. These findings are consistent with the imaging features of hepatic PEComas reported in the aforementioned literature.

The clinical and imaging-based differential diagnosis of hepatic PEComas includes HCC, focal nodular hyperplasia of the liver, hepatic adenoma, liposarcoma, and hemangioma. HCC also presents with a "fast in and fast out" enhancement mode on contrast-enhanced CT and MRI, and cystic necrosis may be associated with large masses. However, patients with HCC usually have a history of hepatitis B or C viral infection and cirrhosis, and serum alpha-fetoprotein is often elevated (16); while hepatic PEComas do not have such characteristics. Focal nodular hyperplasia of the liver appears on CT as an equal-or slightly lower-density mass with a typical star scar in the middle and less fatty components. The contrast-enhanced scan showed that the lesions were significantly enhanced in the arterial stage and gradually decreased in the venous and delayed stages, and the central scar in the delayed stage exhibited delayed enhancement and gradually filled with isodense material compared to the liver parenchyma, thus providing specificity (17). Typical liver adenomas also exhibit "fast in and slow out" in contrast enhancement, and they are more likely to merge with bleeding and are more common in women, with a history of taking contraceptives and steroids (18). Liposarcomas of the liver are relatively rare and contain fat. However, the tumor volume is mostly large, and cystic necrosis is relatively rare. Contrast-Enhanced

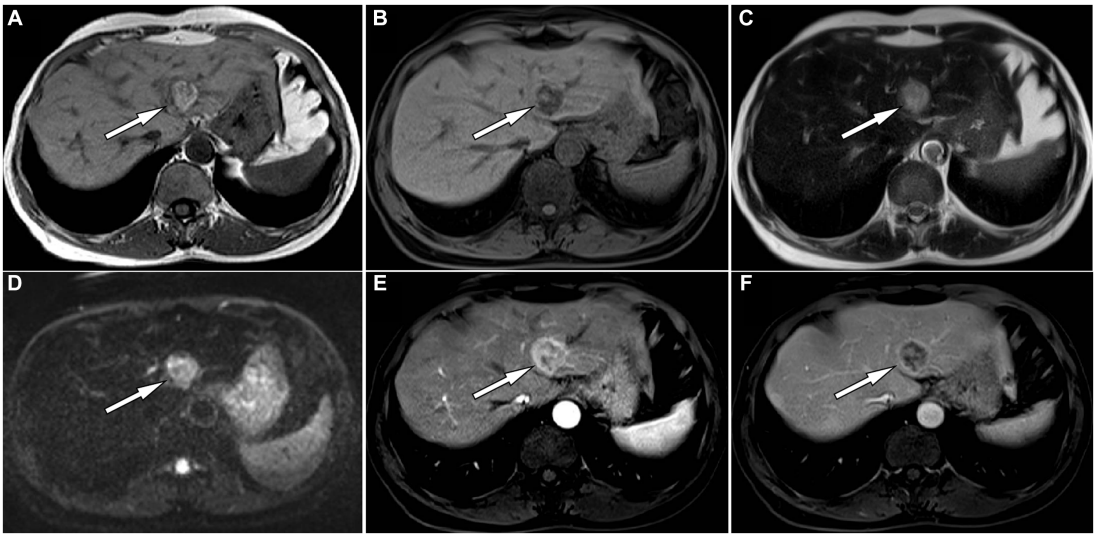

FIGURE 1
The in-phase T1-weighted imaging (T1WI) of abdominal magnetic resonance imaging (MRI) reveals a high and low mixed signal nodule about 2.0 cm × 1.8 cm in size in the medial segment of the left lobe of liver (**A**, arrow); The reverse phase of T1WI shows that the signal of the high signal part of the original nodules has become low (**B**, arrow), indicating fat composition; The nodule shows slightly high signal on T2-weighted imaging (T2WI) **(C)** and diffusion weighted imaging **(D)**. On contrast-enhanced T1WI, the lesion shows significant enhancement in the arterial phase **(E)** and rapid resolution in the venous phase **(F)**, presenting a typical "fast in and fast out" enhancement pattern.

scanning shows uneven enhancement in all stages, which is different from the "fast in and fast out" feature of liver PEComas (19). Hepatic hemangiomas appear as a slightly low-density mass on CT; the dynamic enhanced scan shows nodular enhancement at the edge of the lesion at the arterial stage, and the lesion gradually fills to the center at the portal and delayed stages, showing a "fast in and slow out" enhancement mode, which distinguishes them from hepatic PEComas (20). The detailed differentiation between hepatic PEComas and other liver lesions is shown in Table 1.

Histopathology is the gold standard for the diagnosis of PEComas, and epithelial cell morphology and clear eosinophilic cytoplasm can be observed under a microscope with abundant glycogen, premelanin bodies, and half-desmosomes (21). Immunohistochemical staining for PEComas can positively express both muscle cell (SMA, muscle-specific actin, calponin, etc.) and melanocyte (HMB 45, melan A, tyrosinase) markers (1). The tumor cells in this patient were composed of epithelioid cells rich in transparent cytoplasm and eosinophilic granules. Immunohistochemistry showed positive expression of HMB45, melan-A, SMA, and calponin in the tumor cells, which is consistent with the diagnosis of PEComa.

Due to the low incidence of hepatic PEComas, there is no unified standard for related treatment strategies, and surgical resection remains the primary approach for their management. Some studies suggest that for lesions >5 cm, if there is progressive enlargement, presence of clinical symptoms, or an indication of malignant tendency on fine-needle biopsy, more active methods should be used for treatment, and that mTOR inhibitors such as rapamycin have a certain effect on the treatment of malignant PEComas (22, 23). As the biological behavior of most hepatic PEComas is benign, their prognosis is good (24). Our patient underwent surgical resection of the mass without further treatment, was followed up for 14 months, and is still healthy and alive, which is consistent with literature reports.

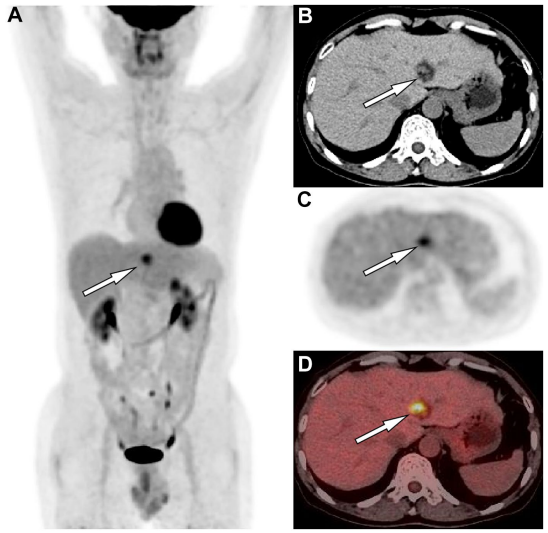

FIGURE 2
(A) The maximum intensity projection of the positron emission tomography (PET)/computed tomography (CT) shows a nodule (arrow) on the left side of the spine with increased uptake of fluorine-18 fluorodeoxyglucose (^{18}F-FDG), with a maximum standardized uptake value (SUVmax) of 5.4. Axial images CT **(B)** showed the corresponding nodule at the medial segment of the left lobe of liver, with solid components of equal hepatic parenchymal density and low-density adipose tissue (arrow). Axial PET **(C)** and PET/CT fusion image **(D)** showed an increased ^{18}F-FDG uptake of the solid component of the nodule (arrows).

Conclusion

Hepatic PEComas are rare interstitial tumors that are often misdiagnosed as hepatocellular carcinoma on imaging due to their

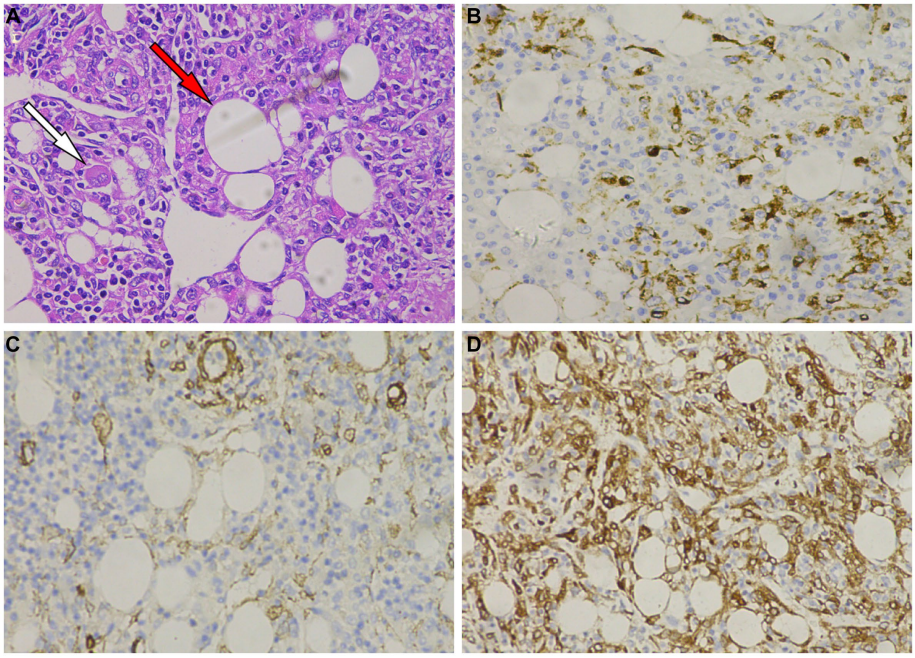

FIGURE 3
(A) Hematoxylin–Eosin staining shows that tumor cells are composed of epithelioid cells, with smooth muscle (white arrow) and adipose tissue (red arrow) visible within the tumor tissue. Immunohistochemistry shows that tumor cells positively express HMB45 **(B)**, melan-A **(C)**, smooth muscle actin (SMA) **(D)**.

TABLE 1 The clinical features and imaging findings of hepatic PEComas and other liver masses.

Indexs	Clinical features	Epidemicity	Imaging findings			
			CT	MRI	CEM	PET
PEComas	Usually has no symptoms and found by accident	Preference for young and middle-aged women	Low density, typically containing fat	Long T1 and long T2 signals, but fat components showed short T1 and long T2 signals	Most are "fast in and fast out", and a few are continuous enhancement	Different levels of ^{18}F-FDG uptake increased
Hepatocellular carcinoma	Signs of cachexia such as abdominal pain and emaciation; Serum alpha-fetoprotein increased	More common in patients with previous hepatitis or cirrhosis.	Equal or low-density mass, usually accompanied by necrosis	Uneven long T1 and long T2 signals	"fast in and fast out"	Different levels of ^{18}F-FDG uptake increased
Focal nodular hyperplasia	Usually has no symptoms and found by accident	More common in middle-aged and elderly patients	Equal or slightly lower density masses	T1WI shows equal or slightly lower signal, T2WI shows equal or slightly higher signal	"Fast in and slow out", with star shaped scars visible in the center	Moderate uptake of ^{18}F-FDG increased, with no uptake in the central stellate scar.
Hepatic adenoma	Usually has no symptoms and found by accident	More common in women with a history of taking birth control pills or steroids	Equal density mass, easily accompanied by high-density bleeding	T1WI shows equal or slightly lower signal, T2WI shows equal or slightly higher signal	"Fast in and slow out"	Mildly increased ^{18}F-FDG uptake
Liposarcoma	May manifest as abdominal pain and bloating	More common in adults	Uneven isodense, low-density mass	Both T1WI and T2WI showed uneven signals	Uneven enhancement in all phases	Obviously increased ^{18}F-FDG uptake
Hemangioma	Usually has no symptoms and found by accident	More common in middle-aged and elderly people, with more females than males	Uniformly equal or slightly lower density	Long T1 and long T2 signals	More show "Fast in and slow out" while a few show "fast in and fast out"	No or mild increase in ^{18}F-FDG uptake

CEM, contrast enhancement model; CT, computed tomography; MRI, magnetic resonance imaging; PET, positron emission tomography; T1WI, T1 weighted imaging; T2WI, T2 weighted imaging.

unique rich blood supply enhancement pattern. However, the imaging findings did possess a certain degree of specificity. The presence of solid components with density similar to that of hepatic parenchyma and adjacent low-density adipose tissue within the lesion, along with increased uptake of ^{18}F-FDG, is characteristic. Contrast enhancement typically exhibits a "fast in and fast out" pattern. In cases of hepatic lesions with these features, considering the possibility of PEComas is crucial for an accurate diagnosis.

Data availability statement

The original contributions presented in the study are included in the article/supplementary material, further inquiries can be directed to the corresponding author.

Ethics statement

Written informed consent was obtained from the individual(s) for the publication of any potentially identifiable images or data included in this article.

Author contributions

WY: Conceptualization, Formal analysis, Methodology, Writing – original draft. QS: Investigation, Project administration, Supervision, Writing – original draft. MS: Conceptualization, Data curation, Project administration, Writing – original draft. SL: Data curation, Software, Validation, Writing – original draft. XiaoH: Data curation, Project administration, Software, Writing – original draft. XianH: Conceptualization, Formal analysis, Methodology, Resources, Writing – review & editing.

Funding

The author(s) declare that no financial support was received for the research, authorship, and/or publication of this article.

Conflict of interest

The authors declare that the research was conducted in the absence of any commercial or financial relationships that could be construed as a potential conflict of interest.

Publisher's note

All claims expressed in this article are solely those of the authors and do not necessarily represent those of their affiliated organizations, or those of the publisher, the editors and the reviewers. Any product that may be evaluated in this article, or claim that may be made by its manufacturer, is not guaranteed or endorsed by the publisher.

References

1. Folpe AL, Kwiatkowski DJ. Perivascular epithelioid cell neoplasms: pathology and pathogenesis. *Hum Pathol*. (2010) 41:1–15. doi: 10.1016/j.humpath.2009.05.011

2. Martignoni G, Pea M, Reghellin D, Zamboni G, Bonetti F. PEComas: the past, the present and the future. *Virchows Arch*. (2008) 452:119–32. doi: 10.1007/S00428-007-0509-1

3. Gao X, Tang H, Wang J, Yao Q, Wang H, Wang Y, et al. Specific imaging features indicate the clinical features of patients with hepatic perivascular epithelioid cell tumor by comparative analysis of CT and ultrasound imaging. *Front Oncol*. (2022) 12:908189. doi: 10.3389/Fonc.2022.908189

4. Matrood S, Görg C, Safai Zadeh E, Alhyari A. Hepatic perivascular epithelioid cell tumor (PEComa): contrast-enhanced ultrasound (CEUS) characteristics-a case report and literature review. *Clin J Gastroenterol*. (2023) 16:444–9. doi: 10.1007/S12328-023-01779-W

5. Son HJ, Kang DW, Kim JH, Han HY, Lee MK. Hepatic perivascular epithelioid cell tumor (PEComa): a case report with a review of literatures. *Clin Mol Hepatol*. (2017) 23:80–6. doi: 10.3350/Cmh.2016.0034

6. Ameurtesse H, Chbani L, Bennani A, Toughrai I, Beggui N, Kamaoui I, et al. Primary perivascular epithelioid cell tumor of the liver: new case report and literature review. *Diagn Pathol*. (2014) 9:149. doi: 10.1186/1746-1596-9-149

7. Jia J, Luo J, Pan CG, Ge G, Feng M, Zou B, et al. Single-center experience in the diagnosis and treatment of hepatic perivascular epithelioid cell neoplasm. *J Clin Transl Hepatol*. (2022) 10:72–9. doi: 10.14218/Jcth.2020.00170

8. Song Z, Xu F, Dai C. Chills and fever as the first presentation of hepatic perivascular epithelioid cell tumor. *Hepatobiliary Surg Nutr*. (2019) 8:436–8. doi: 10.21037/Hbsn.2019.07.03

9. O'malley ME, Chawla TP, Lavelle LP, Cleary S, Fischer S. Primary perivascular epithelioid cell tumors of the liver: CT/MRI findings and clinical outcomes. *Abdom Radiol*. (2017) 42:1705–12. doi: 10.1007/S00261-017-1074-Y

10. Nie P, Wu J, Wang H, Zhou R, Sun L, Chen J, et al. Primary hepatic perivascular epithelioid cell tumors: imaging findings with histopathological correlation. *Cancer Imaging*. (2019) 19:32. doi: 10.1186/S40644-019-0212-X

11. Tan Y, Xiao EH. Hepatic perivascular epithelioid cell tumor (PEComa): dynamic CT, MRI, ultrasonography, and pathologic features—analysis of 7 cases and review of the literature. *Abdom Imaging*. (2012) 37:781–7. doi: 10.1007/S00261-012-9850-1

12. Cardoso H, Silva M, Vilas-Boas F, Cunha R, Lopes J, Maia JC, et al. Hepatic perivascular epithelioid tumor (PEcoma). a case report. *Clin Res Hepatol Gastroenterol*. (2017) 41:E43–6. doi: 10.1016/J.Clinre.2017.02.003

13. Wang X, Wang J, Cheng X, Li F, Huo L. Hepatic angiomyolipoma having FDG uptake at the similar level of the normal liver parenchyma. *Clin Nucl Med*. (2019) 44:599–601. doi: 10.1097/Rlu.0000000000002551

14. Wang S, Xia H, Liu X, Liu Y, Lou C. Hepatic epithelioid angiomyolipoma mimicking hepatocellular carcinoma on MR and (18)F-FDG PET/CT imaging: a case report and literature review. *Hell J Nucl Med*. (2022) 25:205–9. doi: 10.1967/S002449912480

15. Zhang Y, Li B, Hou J, Yu H, Shi H. Hepatic epithelioid angiomyolipoma and 18f-FDG PET/CT. *Clin Nucl Med*. (2018) 43:422–4. doi: 10.1097/Rlu.0000000000002048

16. Forner A, Reig M, Bruix J. Hepatocellular carcinoma. *Lancet*. (2018) 391:1301–14. doi: 10.1016/S0140-6736(18)30010-2

17. Legout JD, Bolan CW, Bowman AW, Caserta MP, Chen FK, Cox KL, et al. Focal nodular hyperplasia and focal nodular hyperplasia-like lesions. *Radiographics*. (2022) 42:1043–61. doi: 10.1148/Rg.210156

18. Aziz H, Brown ZJ, Eskander MF, Aquina CT, Baghdadi A, Kamel IR, et al. A scoping review of the classification, diagnosis, and management of hepatic adenomas. *J Gastrointest Surg*. (2022) 26:965–78. doi: 10.1007/S11605-022-05246-8

19. Terunuma Y, Takahashi K, Doi M, Shimomura O, Miyazaki Y, Furuya K, et al. Primary pleomorphic liposarcoma of the liver: a case report and literature review. *Surg Case Rep*. (2021) 7:244. doi: 10.1186/S40792-021-01322-4

20. Liu Z, Yi L, Chen J, Li R, Liang K, Chen X, et al. Comparison of the clinical and MRI features of patients with hepatic hemangioma, epithelioid hemangioendothelioma, or angiosarcoma. *BMC Med Imaging*. (2020) 20:71. doi: 10.1186/S12880-020-00465-4

21. Tan Y, Zhang H, Xiao EH. Perivascular epithelioid cell tumour: dynamic CT, MRI and clinicopathological characteristics--analysis of 32 cases and review of the literature. *Clin Radiol*. (2013) 68:555–61. doi: 10.1016/J.Crad.2012.10.021

22. Nguyen TT, Gorman B, Shields D, Goodman Z. Malignant hepatic angiomyolipoma: report of a case and review of literature. *Am J Surg Pathol*. (2008) 32:793–8. doi: 10.1097/Pas.0b013e3181607349

23. Dickson MA, Schwartz GK, Antonescu CR, Kwiatkowski DJ, Malinowska IA. Extrarenal perivascular epithelioid cell tumors (Pecomas) respond to Mtor inhibition: clinical and molecular correlates. *Int J Cancer*. (2013) 132:1711–7. doi: 10.1002/Ijc.27800

24. Perán Fernández C, De Paco Navaro Á, Castañer Ramón-Llin J, Bertelli Puche J, Sánchez Espinosa A. Perivascular epithelioid cell tumor (PEComa) of the liver. An extremely rare diagnosis. *Rev Esp Enferm Dig*. (2023) 117:348–9. doi: 10.17235/Reed.2023.9558/2023

frontiers | Frontiers in Medicine

TYPE Case Report
PUBLISHED 04 January 2024
DOI 10.3389/fmed.2023.1347791

OPEN ACCESS

EDITED BY
Carmelo Caldarella,
Fondazione Policlinico Universitario A. Gemelli IRCCS, Italy

REVIEWED BY
Domenico Albano,
University of Brescia, Italy
Giorgio Treglia,
Ente Ospedaliero Cantonale (EOC), Switzerland

*CORRESPONDENCE
J. H. van Snick
✉ j.h.van.snick@umcg.nl

RECEIVED 01 December 2023
ACCEPTED 06 December 2023
PUBLISHED 04 January 2024

CITATION
van Snick JH, van Leer B, Nijsten MWN, Pillay J, Slart RHJA, Glaudemans AWJM and van Rijsewijk ND (2024) Long axial field of view PET/CT in critically ill patients: lessons from a case report.
Front. Med. 10:1347791.
doi: 10.3389/fmed.2023.1347791

Long axial field of view PET/CT in critically ill patients: lessons from a case report

J. H. van Snick[1]*, B. van Leer[1,2], M. W. N. Nijsten[2], J. Pillay[2,3], R. H. J. A. Slart[1,4], A. W. J. M. Glaudemans[1] and N. D. van Rijsewijk[1]

[1]Department of Nuclear Medicine and Molecular Imaging, University Medical Center Groningen, University of Groningen, Groningen, Netherlands, [2]Department of Critical Care, University Medical Center Groningen, University of Groningen, Groningen, Netherlands, [3]Groningen Research Institute for Asthma and COPD (GRIAC), University Medical Center Groningen, University of Groningen, Groningen, Netherlands, [4]Biomedical Photonic Imaging Group, Faculty of Science and Technology, University of Twente, Enschede, Netherlands

The introduction of new long axial field of view (LAFOV) scanners is a major milestone in positron emission tomography/computed tomography (PET/CT) imaging. With these new systems a revolutionary reduction in scan time can be achieved, concurrently lowering tracer dose. Therefore, PET/CT has come within reach for groups of patients in whom PET/CT previously was undesirable. In this case report we discuss the procedure of a continuous bed motion (CBM) total-body [^{18}F]FDG PET/CT scan in an intensive care patient. We emphasize the clinical and technical possibilities with this new camera system, a matched clinical protocol, and the added value of a dedicated team.

KEYWORDS

CT, ICU patient, critically ill, imaging procedure, nuclear medicine, PET, FDG

Introduction

The use of ^{18}F-fluoro-deoxy-D-glucose ([^{18}F]FDG) positron emission tomography computed tomography (PET/CT) in infection and inflammation imaging has increased over the last decade. Inflammatory cells and bacteria involved in infectious and inflammatory processes have a high glycolytic rate and therefore result in [^{18}F]FDG accumulation This allows PET/CT to show areas of ongoing infection and inflammation (1, 2).

[^{18}F]FDG PET/CT is of added value for a broad range of infectious and inflammatory causes, such as vasculitis, endocarditis, osteomyelitis and especially when the infection or inflammation is of unknown origin (3, 4). The latter patient category suffers from fever and elevated inflammatory markers while the location of the infection or inflammation remains unknown (5). [^{18}F]FDG PET/CT imaging allows for the determination of foci of infection and/or inflammation, thereby guiding therapy (6, 7).

Although [^{18}F]FDG PET/CT has become an established diagnostic tool in the clinic it is seldomly used within the intensive care setting (8). This is surprising as both infection and inflammation have a high prevalence in this patient population. The two major syndromes defined by infection and inflammation respectively, sepsis and the acute respiratory distress syndrome, comprise 30% of ICU (intensive care unit) admissions

(9–11). Furthermore, nosocomial infections occur frequently in critically ill patients contributing to prolonged organ dysfunction and mortality (12–14). In patients with persistent critical illness (i.e., ≥ 10 days of ICU admission) more than 50% develop a new septic episode, frequently with an unknown focus (15–18). The fact that PET/CT is not widely used in ICU patients is due to the perceived complexity of patients, the comprehensive patient preparation and extensive scanning time (8, 19).

Recent advances in PET/CT technology, such as ultra-high sensitivity mode in long axial field of view (LAFOV) PET/CT systems, have led to a dramatic reduction in acquisition time and administered activity (20–23). These technological improvements remove a perceived barrier to more routine use of PET/CT in ICU patients.

In this case report, we demonstrate the use of the new LAFOV PET/CT system in an ICU patient. The technical and clinical aspects and benefits will be discussed.

Case

A 67-year-old female was admitted to the ICU due to a Hemophilus influenza sepsis complicated by a heart tamponade, caused by a pericarditis, resulting in an in-hospital cardiac arrest. Successful resuscitation was achieved by pericardiocentesis and placement of pericardial drains. An arthroscopy with rinsing was performed for a bacterial arthritis of the right knee, from which Hemophilus influenza was cultured. Antibiotic therapy with ceftriaxone was started. Subsequently a contrast enhanced CT scan of the thorax was performed showing a bilateral pleural effusion. After an initial phase of recovery, the patient relapsed with an inflammatory profile including fever and a CRP of 128 mg/L, despite continued antibiotic treatment. To identify possible secondary foci, a request for [^{18}F]FDG PET/CT examination was made with emphasis on the upper airway since all problems had started with a painful throat. Previously no imaging focusing on this area had been performed.

In the nuclear medicine department, a dedicated physician assistant (PA) is available for ICU patients to manage logistics and patient preparation. The patient was prepared following international standards, including 4 h fasting period and discontinuation of glucose infusion (24, 25).

The patient was scheduled with priority the next day on a LAFOV (106 cm) Biograph Vision Quadra PET/CT scanner (Siemens Healthineers, Knoxville, TN, United States). A total of 145 MBq (2 MBq/kg) of [^{18}F]FDG was intravenously administered at the ICU department after checking the blood glucose (6.4 mmol/L). After 30 min, the patient was transferred to nuclear medicine department according to our in-house protocol for transfer of critically ill patients. For transfer from the bed to the scanning table, a hoist mechanism is used. During the scan, the patient was fully sedated, required mechanical ventilation and vasopressor support through multiple intravenous lines. The tubing for the intravenous lines was extended to 2.5 m (26). Prior to the start of the scan, a scan-table movement test was conducted to confirm the placement and unhindered movement of the patient with the lines and tube. Once these checks were confirmed, the PET/CT scan was started 60 min post injection (27).

In order to take full advantage of the new features of the Quadra system, the scan was performed in 12 min continuous bed mode (CBM) and in ultra-high sensitivity (UHS) mode (23). Continuous bed mode facilitates the slow and gentle movement of the scan bed through the gantry, permitting 195 cm to be scanned in one pass without limitation of the 106 cm FOV. In this case, it was crucial to focus not only on the primary area of concern (the throat), but also on the known foci in the knee that required examination. The data were reconstructed with our clinical standard protocol: Ordinary-Poisson Ordered-Subsets Expectation–Maximization and TrueX+TOF (UltraHD-PET) 4 iterations, 5 subsets, matrix 440 × 440 voxel 1.65 × 1.65 mm, no filter, and Ultra High Sensitivity. Images were reviewed by a nuclear medicine specialist in Syngo.Via VB60 using MM-oncology (Siemens Healthineers, Erlangen, Germany) (28).

The [^{18}F]FDG PET/CT did not show an infectious focus in the head and neck area besides some reactive lymph nodes. Furthermore, persisting pericardial fluid without [^{18}F]FDG uptake was seen despite continuous drainage (Figures 1B–D). [^{18}F]FDG enhancement was seen in the pericardial layers, mainly around the right atrium, most likely due to some remaining pericarditis (Figures 1A,B,D). Bilateral pleural effusion did not show [^{18}F]FDG uptake, which was in line with negative cultures of this fluid obtained directly after the PET/CT. However, some increased uptake in the pleural sheets could indicate pleuritis. [^{18}F]FDG uptake was seen in the right cephalic vein indicating a possible thrombophlebitis (Figure 1A). In the synovial space of the right knee clear [^{18}F]FDG enhancement was visible, indicating the earlier diagnosed synovitis (Figures 1A,E,G).

Concurrently with the PET/CT scan, blood cultures were taken, later showing *Enterococcus faecium*. The central line was removed shortly before the PET/CT, which later showed to be the source, and vancomycin therapy was started. The [^{18}F]FDG uptake pattern was classified as a reactive remainder of the initial infection. Together with the negative pleural punction and the central line infection as a cause for the deterioration, ceftriaxone and vancomycin treatment was stopped. The patient rapidly recovered.

Discussion

This case illustrates the challenges of performing a PET/CT scan in ICU patients due to the complexity of mechanical ventilation and vasopressor support required by the patient, presence of intravenous lines and the necessary planning, logistics and transport. The added value of performing a [^{18}F]FDG PET/CT scan in ICU patients was demonstrated. Thanks to the PET/CT scan another localization of the *Hemophilus influenza* could be excluded facilitating safe tapering of antibiotic treatment. However, more importantly, we showed that, with the recent advancement in technology, a PET/CT can be performed relatively easily in ICU patients using a LAFOV PET/CT camera, which is mainly achieved by reduction of the scan time (up to 2 min for one bed position) (29).

Another advantage of the newest function of the LAFOV PET/CT system is the added value of scanning in CBM mode, allowing to scan a total body while the table moves gently and remains comfortable for the patient, with also less risk for lines and tubes to get stuck or tangled compared to scanning total body using the

Abbreviations: [^{18}F]FDG, 2-18F-fluoro-deoxy-D-glucose; CT, Computed Tomography; LAFOV, Long Axial Field of View; PET, Positron Emission Tomography; ICU, Intensive Care Unit.

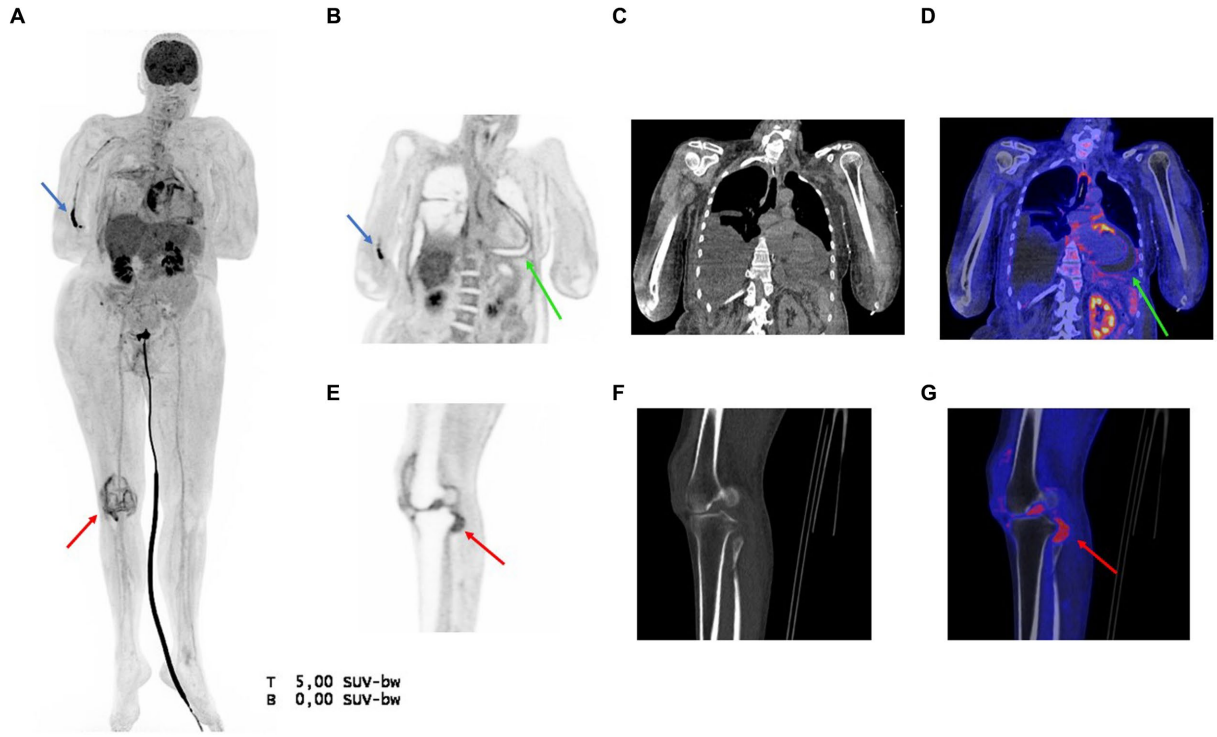

FIGURE 1
(A) Maximum Intensity Projection (MIP) showing pathological [^{18}F]FDG uptake in the pericardial cavity and right knee (red arrow) and [^{18}F]FDG enhancement in the cephalic vein, possibly caused by a thrombophlebitis (blue arrow). Furthermore, physiological uptake can be seen in the liver, kidneys, and urinary catheter tract. **(B–D)** Coronal PET, low-dose CT, and PET/CT fusion image of the thorax, respectively, showing clear pericardial effusion (green arrow) with slightly elevated [^{18}F]FDG uptake in the pericardial layers. The pleural effusion showed no tracer uptake. **(E–G)** Sagittal PET, low-dose CT, and PET/CT fusion image of the right knee (red arrow), respectively, showing increased [^{18}F]FDG uptake in the synovial space due to the Hemophilus Influenza infection.

multiple bed positions method. This bed position method is used in older type of scanners, statically scanning one bed position before moving to the next, resulting in relatively sudden movements between positions. Besides, it needs large overlap in bed positions for sufficient fusion between the low dose CT and PET scan, demanding more acquisition time.

In this case, a total acquisition time of 12 min was used since this was the first time an ICU patient was scanned using the LAFOV PET/CT system in CBM mode. By further adapting the procedure, a total of 6–7 min acquisition time seems to be feasible in this patient group, without compromising image quality and diagnostic value. In comparison, the acquisition time would have been approximately 30 min on a conventional PET/CT system. Furthermore, due to the limited sensitivity of conventional PET/CT's, a higher radioactivity dose must be administered with these types of camera systems. This results not only in a higher radiation dose for the patient but also for the ICU staff (30, 31). A dose reduction as low as 1 MBq/kg for a LAFOV PET/CT has already been suggested (20).

The successful execution of an [^{18}F]FDG PET/CT procedure for critically ill patients requires a specialized team with sufficient experience and expertise. Key members of this team include an ICU physician, an ICU nurse and competent PET/CT technologists. Furthermore, it is crucial to have a dedicated facilitator to ensure smooth communication and coordination between the two departments. This role is fulfilled in our institution using a physician assistant of the nuclear medicine department. Furthermore, a standard operating procedure should be available for both departments.

In conclusion, the utilization of LAFOV PET/CT yields a nearly similar duration for transport and scanning when compared with an ordinary CT scan. Therefore, using this system, PET/CT has become more accessible for use in critically ill patients. However, before implementation, perceived barriers in scanning complex ICU patients need to be addressed by research into safety, patient preparation, and logistics. Eventually, this may result in international practice guidelines.

Data availability statement

The datasets presented in this article are not readily available because the raw data is protected by privacy laws. Fully anonymized data is available on reasonable request. Requests to access the datasets should be directed to the corresponding author.

Ethics statement

The requirement of ethical approval was waived by Medical ethical committee UMCG for the studies involving humans. The studies were conducted in accordance with the local legislation and institutional requirements. The participants provided their written informed consent to participate in this study. Written informed consent was

obtained from the individual(s) for the publication of any potentially identifiable images or data included in this article.

Author contributions

JS: Conceptualization, Methodology, Writing – original draft. BL: Conceptualization, Supervision, Writing – review & editing. MN: Writing – review & editing. JP: Writing – review & editing. RS: Writing – review & editing. AG: Supervision, Writing – review & editing. NR: Conceptualization, Supervision, Writing – review & editing.

Funding

The author(s) declare that financial support was received for the research, authorship, and/or publication of this article. JP is supported by a research grant from the Netherlands Organization for Health Research and Development, the Netherlands (ZonMw Clinical Fellowship grant 09032212110044).

Conflict of interest

The authors declare that the research was conducted in the absence of any commercial or financial relationships that could be construed as a potential conflict of interest.

The author(s) declared that they were an editorial board member of Frontiers, at the time of submission. This had no impact on the peer review process and the final decision.

Partnership of UMCG-Siemens for building the future of Health (PUSH). Siemens was not involved in the imaging process nor in the writing phase of this case.

Publisher's note

References

1. Annunziata S, Treglia G, Jamar F, Lauri C, Palestro CJ, Gheysens O, et al. Nuclear medicine practice in the field of infection and inflammation imaging: a pragmatical survey. *Eur J Nucl Med Mol Imaging*. (2022) 49:2113–9. doi: 10.1007/s00259-022-05725-9

2. Lawal IO, Gheysens O, Sathekge MM, Glaudemans AWJM. Editorial: functional imaging of inflammation and infection. *Front Med (Lausanne)*. (2022) 9:925635. doi: 10.3389/fmed.2022.925635

3. Slart RHJA, Glaudemans AWJM, Gheysens O, Lubberink M, Kero T, Dweck MR, et al. Procedural recommendations of cardiac PET/CT imaging: standardization in inflammatory-, infective-, infiltrative-, and innervation (4Is)-related cardiovascular diseases: a joint collaboration of the EACVI and the EANM. *Eur J Nucl Med Mol Imaging*. (2021) 48:1016–39. doi: 10.1007/s00259-020-05066-5

4. ten Hove D, Slart RHJA, Sinha B, Glaudemans AWJM, Budde RPJ. 18F-FDG PET/CT in infective endocarditis: indications and approaches for standardization. *Curr Cardiol Rep*. (2021) 23:130. doi: 10.1007/s11886-021-01542-y

5. van Rijsewijk ND, IJpma FFA, Wouthuyzen-Bakker M, Glaudemans AWJM. Molecular imaging of fever of unknown origin: an update. *Semin Nucl Med*. (2023) 53:4–17. doi: 10.1053/j.semnuclmed.2022.07.002

6. Ropers FG, van Mossevelde RMP, Bleeker-Rovers CP, van Velden FHP, van Assema DME, Adam JA, et al. Evaluation of FDG-PET/CT use in children with suspected infection or inflammation. *Diagnostics*. (2020) 10:715. doi: 10.3390/diagnostics10090715

7. Medvedeva N, Radcliffe C, Malinis M, Chen M-K, Azar MM. Real-world assessment of the clinical utility of whole body 18F-FDG PET/CT in the diagnosis of infection. *PLoS One*. (2022) 17:e0277403. doi: 10.1371/journal.pone.0277403

8. van Leer B, van Rijsewijk ND, Nijsten MWN, Slart RHJA, Pillay J, Glaudemans AWJM. Practice of 18F-FDG-PET/CT in ICU patients: a systematic review. *Semin Nucl Med*. (2023) 53:809–19. doi: 10.1053/j.semnuclmed.2023.05.003

9. Sakr Y, Jaschinski U, Wittebole X, Szakmany T, Lipman J, Ñamendys-Silva SA, et al. Sepsis in intensive care unit patients: worldwide data from the intensive care over nations audit. *Open Forum Infect Dis*. (2018) 5:ofy313. doi: 10.1093/ofid/ofy313

10. Bellani G, Laffey JG, Pham T, Fan E, Brochard L, Esteban A, et al. Epidemiology, patterns of care, and mortality for patients with acute respiratory distress syndrome in intensive care units in 50 countries. *JAMA*. (2016) 315:788–800. doi: 10.1001/jama.2016.0291

11. Hendrickson KW, Peltan ID, Brown SM. The epidemiology of acute respiratory distress syndrome before and after coronavirus disease 2019. *Crit Care Clin*. (2021) 37:703–16. doi: 10.1016/j.ccc.2021.05.001

12. Blot S, Ruppé E, Harbarth S, Asehnoune K, Poulakou G, Luyt CE, et al. Healthcare-associated infections in adult intensive care unit patients: changes in epidemiology, diagnosis, prevention and contributions of new technologies. *Intensive Crit Care Nurs*. (2022) 70:103227. doi: 10.1016/j.iccn.2022.103227

13. Prowle JR, Echeverri JE, Ligabo EV, Sherry N, Taori GC, Crozier TM, et al. Acquired bloodstream infection in the intensive care unit: incidence and attributable mortality. *Crit Care*. (2011) 15:R100. doi: 10.1186/cc10114

14. Talmor M. Relationship of systemic inflammatory response syndrome to organ dysfunction, length of stay, and mortality in critical surgical illness. *Arch Surg*. (1999) 134:81–7. doi: 10.1001/archsurg.134.1.81

15. Kalb TH, Lorin S. Infection in the chronically critically ill: unique risk profile in a newly defined population. *Crit Care Clin*. (2002) 18:529–52. doi: 10.1016/S0749-0704(02)00009-X

16. Iwashyna TJ, Hodgson CL, Pilcher D, Bailey M, van Lint A, Chavan S, et al. Timing of onset and burden of persistent critical illness in Australia and New Zealand: a retrospective, population-based, observational study. *Lancet Respir Med*. (2016) 4:566–73. doi: 10.1016/S2213-2600(16)30098-4

17. Nedeva C, Menassa J, Puthalakath H. Sepsis: inflammation is a necessary evil. *Front Cell Dev Biol*. (2019) 7:108. doi: 10.3389/fcell.2019.00108

18. Van Vught LAV, Klein Klouwenberg PM, Spitoni C, Scicluna BP, Wiewel MA, Horn J, et al. Incidence, risk factors, and attributable mortality of secondary infections in the intensive care unit after admission for sepsis. *JAMA*. (2016) 315:1469–79. doi: 10.1001/jama.2016.2691

19. Van Hulst A., Van Hulst A. M., Van Rijk M. C., Bavelaar-Croon C. D. L., Tjan D. H. T., "The value of F-18-fluorodeoxyglucose positron emission tomography (FDG-PET/CT) in the intensive care unit: a review Netherlands journal of critical care the value of F-18-fluorodeoxyglucose positron emission tomography (FDG-PET/CT) in the intensive care unit: A review," (2019). [Online]. Available at: https://www.researchgate.net/publication/362134916

20. Calderón E, Schmidt FP, Lan W, Castaneda-Vega S, Brendlin AS, Trautwein NF, et al. Image quality and quantitative PET parameters of low-dose [18F]FDG PET in a long axial field-of-view PET/CT scanner. *Diagnostics*. (2023) 13:3240. doi: 10.3390/diagnostics13203240

21. Alberts I, Sari H, Mingels C, Afshar-Oromieh A, Pyka T, Shi K, et al. Long-axial field-of-view PET/CT: perspectives and review of a revolutionary development in nuclear medicine based on clinical experience in over 7000 patients. *Cancer Imaging*. (2023) 23:28. doi: 10.1186/s40644-023-00540-3

22. Sachpekidis C, Pan L, Kopp-Schneider A, Weru V, Hassel JC, Dimitrakopoulou-Strauss A. Application of the long axial field-of-view PET/CT with low-dose [18F]FDG in melanoma. *Eur J Nucl Med Mol Imaging*. (2023) 50:1158–67. doi: 10.1007/s00259-022-06070-7

23. Mingels C, Weidner S, Sari H, Buesser D, Zeimpekis K, Shi K, et al. Impact of the new ultra-high sensitivity mode in a long axial field-of-view PET/CT. *Ann Nucl Med*. (2023) 37:310–5. doi: 10.1007/s12149-023-01827-y

24. Nakatani K, Nakamoto Y, Togashi K. Risk factors for extensive skeletal muscle uptake in oncologic FDG-PET/CT for patients undergoing a 4-h fast. *Nucl Med Commun*. (2012) 33:648–55. doi: 10.1097/MNM.0b013e328352290f

25. Kaneta T, Hakamatsuka T, Takanami K, Yamada T, Takase K, Sato A, et al. Evaluation of the relationship between physiological FDG uptake in the heart and age, blood glucose level, fasting period, and hospitalization. *Ann Nucl Med*. (2006) 20:203–8. doi: 10.1007/BF03027431

26. "Biograph Vision Quadra PET/CT Scanner-Siemens Healthineers-Siemens Healthineers." [Online]. Available: https://www.siemens-healthineers.com/molecular-imaging/pet-ct/biograph-vision-quadra (Accessed November 23, 2023)

27. Boellaard R, Delgado-Bolton R, Oyen WJ, Giammarile F, Tatsch K, Eschner W, et al. FDG PET/CT: EANM procedure guidelines for tumour imaging: version 2.0. *Eur J Nucl Med Mol Imaging*. (2015) 42:328–54. doi: 10.1007/s00259-014-2961-x

28. "syngo.via imaging software for advanced visualization by Siemens Healthineers | Open Inventor 3D SDK." [Online]. Available at: https://www.openinventor.com/en/about/user-testimonials/detail/syngo-via-imaging-software-for-advanced-visualization-by-siemens-healthineers (Accessed November 23, 2023)

29. He Y, Gu Y, Yu H, Wu B, Wang S, Tan H, et al. Optimizing acquisition times for total-body positron emission tomography/computed tomography with half-dose 18F-fluorodeoxyglucose in oncology patients. *EJNMMI Phys*. (2022) 9:45. doi: 10.1186/s40658-022-00474-y

30. Leide-Svegborn S. Radiation exposure of patients and personnel from a PET/CT procedure with 18F-FDG. *Radiat Prot Dosim*. (2010) 139:208–13. doi: 10.1093/rpd/ncq026

31. Studenski MT. Effective dose to patients and staff when using a mobile PET/SPECT system. *J Appl Clin Med Phys*. (2013) 14:215–25. doi: 10.1120/jacmp.v14i3.4250

frontiers | Frontiers in Medicine

TYPE Original Research
PUBLISHED 02 February 2024
DOI 10.3389/fmed.2024.1353466

OPEN ACCESS

EDITED BY
Carmelo Caldarella,
Fondazione Policlinico Universitario A. Gemelli IRCCS, Rome, Italy

REVIEWED BY
Andor W. J. M. Glaudemans,
University of Groningen, Netherlands
Akram Al-ibraheem,
King Hussein Cancer Center, Jordan
Ryogo Minamimoto,
National Center for Global Health and Medicine, Japan

*CORRESPONDENCE
Fengxiang Liao
✉ 30923363@qq.com
Wuping Ai
✉ awp226@163.com

†These authors have contributed equally to this work and share first authorship

RECEIVED 10 December 2023
ACCEPTED 08 January 2024
PUBLISHED 02 February 2024

CITATION
Huang Z, Zou S, Liu Q, Qi W, Sharma A, Wang Y, Jin A, Schmidt-Wolf IGH, Lu P, Ai W and Liao F (2024) Inferring the diagnostic potential of 18F-FDG-PET/CT in post-renal transplantation from a unique case harboring multiple rare complications. *Front. Med.* 11:1353466. doi: 10.3389/fmed.2024.1353466

Inferring the diagnostic potential of 18F-FDG-PET/CT in post-renal transplantation from a unique case harboring multiple rare complications

Zizhen Huang[1†], Shiwei Zou[2†], Qian Liu[3], Wanling Qi[4], Amit Sharma[5,6], Yulu Wang[7], Aifang Jin[4], Ingo G. H. Schmidt-Wolf[5], Ping Lu[4], Wuping Ai[8*] and Fengxiang Liao[4*]

[1]Sterilization and Supply Center, Jiangxi Provincial People's Hospital, The First Affiliated Hospital of Nanchang Medical College, Nanchang, China, [2]Department of Ultrasound Medicine, Dongxiang District Hospital of Traditional Chinese Medicine, Fuzhou, China, [3]Department of Pathology, Jiangxi Provincial People's Hospital, The First Affiliated Hospital of Nanchang Medical College, Nanchang, China, [4]Department of Nuclear Medicine, Jiangxi Provincial People's Hospital, The First Affiliated Hospital of Nanchang Medical College, Nanchang, China, [5]Department of Integrated Oncology, Center for Integrated Oncology (CIO), University Hospital of Bonn, Bonn, Germany, [6]Department of Stereotactic and Functional Neurosurgery, University Hospital of Bonn, Bonn, Germany, [7]Department of Hematology, The First Affiliated Hospital of Nanchang University, Nanchang, China, [8]Department of Orthopaedics, Dongxiang District Hospital of Traditional Chinese Medicine, Fuzhou, China

Renal transplantation is undoubtedly an effective treatment for patients with end-stage renal disease, but it is certainly not a cure. Patients require lifelong immunosuppression to maintain optimal allograft function, and post-operative risk complications such as cancer in the transplant recipient cannot be ignored. Besides, infection is a silent complication that follows transplantation. Relatedly, herein, we present a report of a 40-year-old patient who underwent renal transplantation and promptly developed a diffuse large B-cell tumor in the liver and Aspergillus infection in the trachea. In addition, an inflammatory necrotizing granuloma was also observed in the muscles. Of importance, we also described the potential of 18F-FDG-PET/CT, which was instrumental in monitoring and evaluating these relevant post-operative complications in this rare case.

KEYWORDS

post-renal transplant, 18F-FDG, Aspergillus tracheobronchitis, necrotizing granulomatous inflammation, complications

Introduction

Organ transplantation has long been considered the standard treatment for patients with end-stage organ failure. In particular, renal transplantation has had high success rates ever since the first successful attempt by Dr Joseph Murray in 1954. However, concerns about cancer risk and infections are common consequences of immunosuppressive drugs, which are required to prevent organ rejection and contribute to the highest mortality rates among renal transplant recipients. This can be evident from the studies showing that

the risk of malignant tumors in patients after renal transplantation was 2.19−6.7% (1). Likewise, the pulmonary fungal infections, a common post-operative complication of renal transplant patients, also complicate the clinical scenario as 30% of patients with pulmonary fungal infections usually die due to lack of timely treatment (1–3). More than 20% of renal transplant recipients experience at least one case of infection in the first year after transplantation (4).

Given the emerging field of molecular predictive medicine, several molecular biomarkers for pre/post-renal transplantation monitoring have been discussed (5). However, their complete success in improving transplant success and defining the causes of long-term complications remains to be seen. Undeniably, imaging examination continues to be the reliable standard and clinical decisions for kidney transplantation rely heavily on imaging techniques, including ultrasound, computed tomography, magnetic resonance imaging, and nuclear medicine examinations (6, 7).

It is worth mentioning that conventional imaging inevitably misses lesions in recipients due to local scanning, whereas 18F-FDG-PET/CT imaging offers obvious advantages in imaging lesions throughout the body due to whole-body scanning. Nevertheless, a detailed knowledge of post-transplant complications (malignancies, infections, etc.) can help improve patient survival and facilitate the development of an optimal monitoring plan for addressing post-transplant challenges. Considering this, herein, we reported a 40-year-old male patient who underwent renal transplantation after hemodialysis treatment for renal failure and developed rare post-operative tumor (diffuse large B-cell lymphoma) and infectious (fungal Aspergillus, necrotizing granulomatosis) complications. Importantly, 18F-FDG-PET/CT greatly assisted in the monitoring and evaluation of certain complications of the patients that might have been missed with other conventional imaging approaches.

Case description

In 2008, the patient was diagnosed with chronic nephritis after proteinuria was noticed. Thereafter, a symptomatic treatment was initiated.

In March 2014, the examination of renal function revealed a creatinine value of more than 2,000°μmol/L and glomerular filtration rate(GFR) less than 15 ml/min. then the patient was diagnosed as "stage 5 of chronic kidney disease." While undergoing hemodialysis five times every two weeks through the arteriovenous fistula, the patient's condition was getting more stable.

Since June 2016, due to the increase in creatinine again, hemodialysis has gradually increased to three times a week, resulting in poor compliance of the patient to dialysis. In November 2018, based on the appropriate lab results, patient was admitted for kidney allotransplantation. As the donor was being treated in the Intensive Care Unit (ICU), ceftazidime and caspofungin were administered to avoid the potential risk of infection after the transplant. Also, immunosuppressants such as tacrolimus (2.5 mg, bid), mycophenolate mofetil (500 mg, bid), and ponisone acetate tablets (10 mg, qd) were given to prevent rejection. However, on the second day after surgery, an increased blood flow resistance index and impaired renal graft artery function were observed on Color Doppler ultrasound, suggesting delayed recovery of renal graft function. And Urine volume decreased to only 63°ml, serum creatinine was found to be 1558°μmol/L, indicating acute rejection. As a result, Hemodialysis was arranged intermittently, and Mycophenolate Mofetil Capsules, tacrolimus, mebonilone and ATG immunosuppressants were given to prevent rejection. When urine output approaches 2,100°ml and creatinine has decreased to 143°μmol/L, approximately 20 days after treatment, regular anti-rejection medication was prescribed. Following renal transplantation, liver and kidney function, blood and urine levels, electrolytes, tacrolimus drug concentration and color Doppler ultrasound were routinely monitored. Importantly, there were normal leukocytes numbers and serum creatinine-141.3 ± 9.2°μmol/L, β2-microglobulin-6.3 ± 0.5°mg/L, fructosamine-2.6 ± 0.3°mmol/L, albumin-37.8 ± 2.3°g/L.

In October 2021, the patient was checked concerning occlusion of an arteriovenous fistula in the left forearm. A routine CT scan of the lungs incidentally revealed a low-density intrahepatic shadow. Subsequently, an upper abdominal enhanced CT scan showed multiple low-density circular shadows in the liver (**Figures 1A–C**), leading to suspicion of metastasis. Gastroenteroscopy was performed to rule out the origin of the primary lesion from the gastrointestinal tract, but no abnormalities were found. A color ultrasound-guided needle biopsy of the liver lesion was performed, and the pathological diagnosis was noticed as diffuse large B-cell lymphoma (DLBCL, IE stage, IPI0) (**Figure 1H**). To clarify the systemic condition, an 18F-FDG-PET/CT scan was performed, and FDG uptake was found to be markedly elevated in the three lesions in the liver with the SUVmax of 22.8 in the most prominent lesion (**Figures 1D–G**). Promptly, R-CHOP chemotherapy (reduced dose, q3w) was administered: rituximab 700°mg, cyclophosphamide 1,100°mg, vincristine 2°mg, epirubicin 110°mg, prednisone 100°mg, combined with ibrutinib. Also, the patient was recommended a continuation of immunosuppressive therapy with an adjusted drug regimen, specifically the tacrolimus dose was reduced to 0.5 mg per day and sirolimus (0.3 tablets per day) was added as anti-tumor treatment. The clinical laboratory tests (creatinine -149°μmol/L, tacrolimus-11.0°ng/ml, CA199-56.5°U/ml (0−27), AFP and CEA) were normal, also the levels of T lymphocytes-89.9% (62.60−76.80%) and CD4 + T cells-52.9% (30−46%) were determined. Also, T inhibitory cells were 42.05% (15−33%), lactate dehydrogenase was normal, and α-hydroxybutyrate dehydrogenase was 186°U/L.

In November 2021, the patient was admitted for second chemotherapy and continued to receive R-CHOP chemotherapy (conventional dose). During this period, herpes zoster was diagnosed in the right groin. To prevent herpes virus, acyclovir was administered, and calamine was used for external treatment.

In April 2022, the patient was admitted to the hospital for the sixth chemotherapy and had symptoms of fever, cough and sputum, with the highest temperature of 38.4°C, which starts appearing about a month ago. The leukocyte

Abbreviations: 18F-FDG-PET/CT:18F-fluoro-2-deoxy-D-glucose positron emission tomography/computed tomography; MIP, maximum intensity projection; CT, computed tomography; PTLD, Post-transplant lymphoproliferative disorder; HLA, human leukocyte antigen; IA, invasive aspergillosis; IPA, invasive pulmonary aspergillosis; IATB, Isolated invasive Aspergillus tracheobronchitis; NGI, necrotizing granulomatous inflammation.

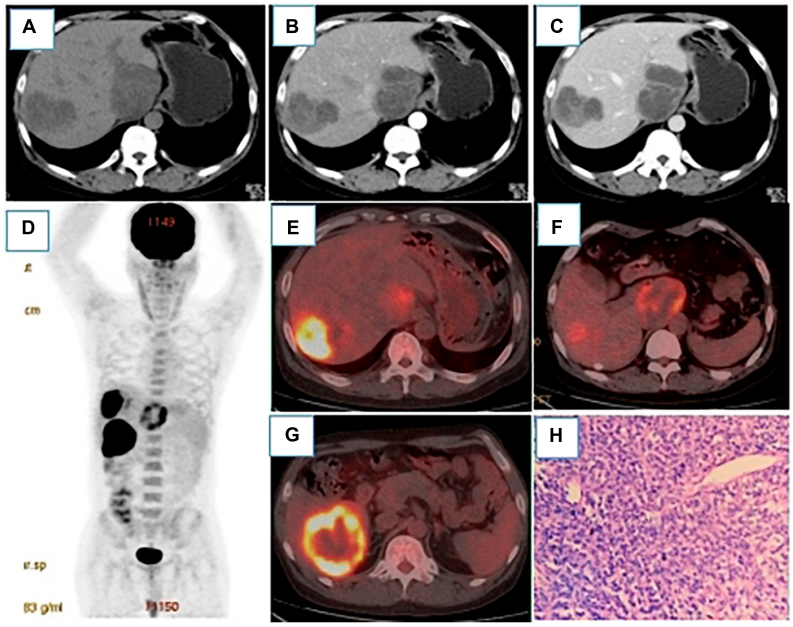

FIGURE 1
(A–C) were plain CT scans, arterial phase and venous phase of CT enhancement, respectively. After renal transplantation, round low-density lesions were observed in the liver with uneven density, the largest of which was about 79 × 68°mm. The fiber partition was slightly increased in the arterial phase, and further enhanced in the venous phase, but no clear enhancement was showed in the low-density shadow.18 F-FDG PET/CT MIP **(D)** showed three hypermetabolic lesions in the liver, which located in the Segment VI, with the size of 54 × 50°mm and SUVmax of 15.9 **(E)**, segment I, with the size of 61 × 50°mm and SUVmax of 8.1 **(F)**, and segment VIII, with the size of 69 × 58°mm and SUVmax of 22.8 **(G)**. Pathology [**(H)**, HE400 ×] showed a large number of tumor cells and a small number of lymphocytes in the necrotic tissue. Immunohistochemistry showed CD20(+), CD79a(+) and Ki-67 (60% positive).

count (16.10 × 109/L), procalcitonin level (0.13°ng/ml) and C-reactive protein levels (97.5°mg/L) indicated possible infection. Therefore, symptomatic treatment, such as anti-infection and relieving cough, was adopted. To assess the efficacy of the chemotherapy, an 18F-FDG-PET/CT scan was performed, which showed that the liver lesions were reduced in size and metabolism was markedly decreased (Figures 2A–D). Strikingly, the proximal wall of the left main bronchus and upper lobe bronchus was markedly thickened, and the metabolic was markedly elevated with the SUVmax of 12.8, suggesting the possibility of bronchial lung carcinoma (Figures 2E–G). But fiberoptic bronchoscopy showed fungal infection with inflammatory granulation tissue, abscess and necrosis in the left main bronchus (Figures 2H, I). The bronchoalveolar lavage fluid was galactomannan(GM) positive and Aspergillus flavus/Aspergillus oryzae was detected by NGS(Next Generation Sequencing) (Figures 2J, K). Considering the obvious drug interaction between sirolimus, tacrolimus and voriconazole, caspofungin was given as an antifungal infection. The antirejection regimen was subsequently adjusted: Cellception (was discontinued), Prednisone (oral 5°mg/d), and Sirolimus and Tacrolimus (5°ng/ml) were maintained. It took 5 days for the body temperature and the inflammatory indicators to return as normal. The chemotherapy with R-CHOP plus zebrutinib was continued, and the antifungal therapy was maintained with voriconazole. The laboratory tests were: Tacrolimus-11.30°ng/ml, Sirolimus-3.41°ng/ml, virus related tests (Cytomegalovirus DNA, Epstein-Barr virus nucleic acid, BK virus DNA, JC virus DNA, Cryptococcal capsular polysaccharide, T-SPOT) were negative and acid fast stain showed no acid fast bacilli. There were also values measured for galactomannan antigen (GM-3.30°ug/L(positive > 0.95), and 1-3-β-D-glucan < 10°pg/mL(60—100).

In July 2022, an 18F-FDG-PET/CT scan was performed to evaluate the treatment effect of PHL and Invasive Aspergillus Tracheobronchitis (IAT), and a residual lesion was found in the liver with no obvious metabolic activity (Figures 3A–D). There was also no obvious thickening or hypermetabolic lesion in the left main bronchus wall (Figure 3E). However, hypermetabolic nodules was observed in the right vastus lateralis muscle (Figure 3F). The pathology of the ultrasound-guided biopsy showed necrotizing granulomatous inflammation (Figure 3G). Noticeably, fluorescent staining of fungi, silver hexamine staining, Gram staining, and acid-fast staining were all negative. The laboratory tests revealed the presence of angiotensin convertase -64°U/L (5—52), creatine kinase- 16I°U/L (50—310), β2-microglobulin- 6.35°mg/L (1.0—3.00), and tacrolimus-1.70°ng/mL. The lesion of the muscle, surprisingly, disappeared spontaneously after one month without any treatment. Timeline of complications after renal transplantation in this patient was showed in Figure 4.

Discussion

While renal transplantation can significantly improve survival, the risk of delayed recovery of graft function, post-transplant rejection, malignancy and infection cannot be ruled out (8). Herein,

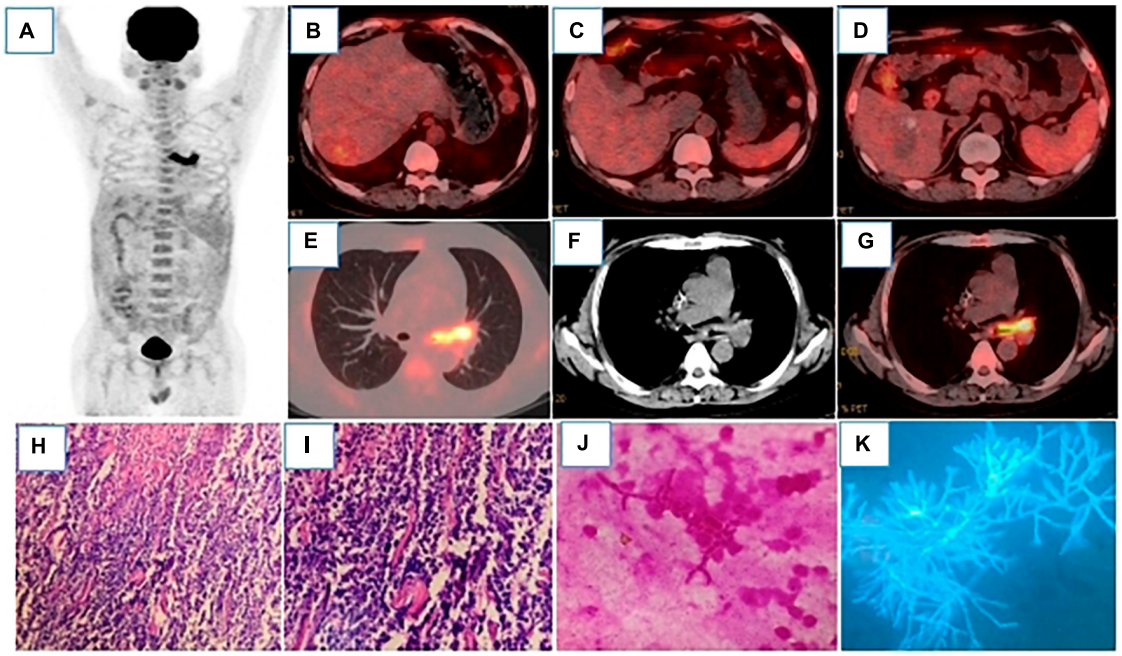

FIGURE 2
18F-FDG-PET/CT MIP **(A)** showed hypermetabolic lesions in the left main bronchus. After 4 cycles of chemotherapy, the intrahepatic lesions were all reduced, and FDG uptake was significantly decreased, which were as follows: Segment VI, with the size of 31 × 26°mm and SUVmax of 3.2 **(B)**; segment I, with the size of 45 × 32°mm and SUVmax of 1.7 **(C)**; segment VIII, with the size of 50 × 33°mm and SUVmax of 1.9 **(D)**, liver SUVmax was 1.8. **(E–G)** showed that the wall of the left main bronchus was significantly thickened, the lumen was narrow, and FDG uptake was significantly increased with the SUVmax of 12.8. Bone marrow reactive hyperplasia after chemotherapy resulted in increased diffuse FDG uptake. Pathology [**(H)**, HE200 × ; **(I)**, HE400 ×] showed that a large number of cells were apoptotic and infiltrated by inflammatory cells. **(J)** (Gram staining) and **(K)** (Silver staining) showed Gram-negative or non-staining, with parallel hyphal walls, septum, acute Angle branching, and "bamboo."

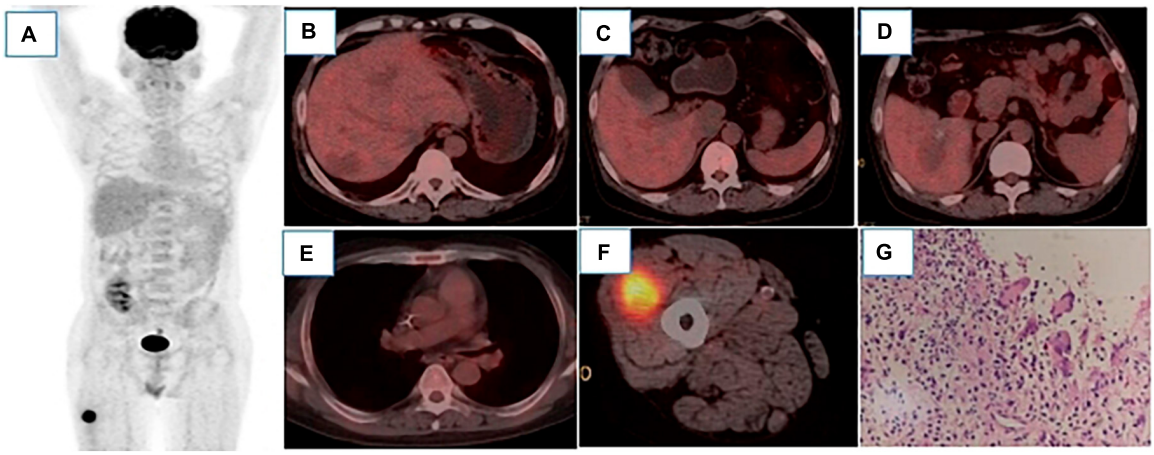

FIGURE 3
18 F-FDG PET/CT MIP image **(A)** showed only hypermetabolic lesions on the right thigh. After 6 cycles of chemotherapy, there were still low-density lesions in the liver, but there was no increase in FDG uptake, which were as follows: Segment VI, with the size of 27 × 22°mm and SUVmax 2.2 **(B)**, segment I, with the size of 38 × 29°mm and SUVmax of 1.8 **(C)**, segment VIII, with the size of 42 × 30°mm and SUVmax of 2.2 **(D)**, liver SUVmax was 2.3. The left main bronchus wall was slightly thickened without significant FDG uptake **(E)**. In the vastus lateralis muscle of the right thigh, nodular slightly low-density shadow was observed with the size of 32 × 28°mm, FDG uptake was increased with the SUVmax of 8.8. **(F)** Pathology [**(G)**, HE400 ×] showed fibrous hyperplasia around necrotic tissue, accompanied by inflammatory cells and multinucleated giant cells reaction, which was considered as necrotizing granulomatous inflammation.

we also report a unique case of multiple rare complications after renal transplantation where delayed recovery of graft function and acute rejection occurred immediately after renal transplantation. Though most complications normalized after 20 days of active treatment, however, from the third year post-surgery, patient developed (*de novo*) diffuse large B-cell lymphoma of the liver,

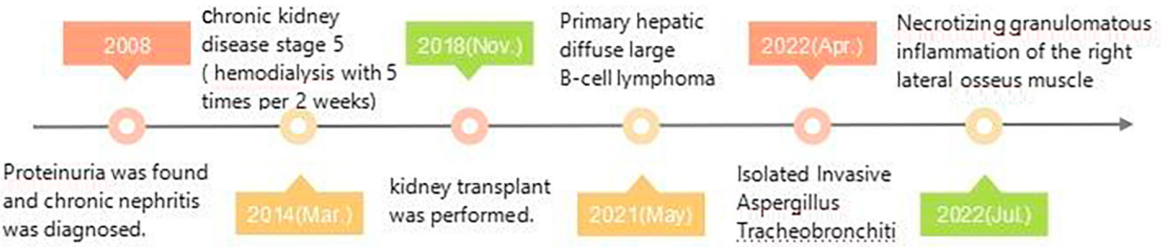

FIGURE 4
Timeline of complications after renal transplantation in this patient.

Aspergillus infection of the trachea and necrotizing inflammatory granuloma of the muscles.

Nonetheless, recipients of solid organ transplants are at high risk of developing Post-transplant lymphoproliferative disorders (PTLD), more than half of which were diffuse large B-cell lymphoma (DLBCL)(9, 10). However, the occurrence of DLBCL in the liver as primary hepatic lymphoma (PHL) remains obscure, especially after renal transplantation, accounting for about 0.016% of non-Hodgkin lymphoma (NHL), 0.4% of extranodal lymphoma, and 0.1% of liver malignant tumors (11). Certainly, owing to its heterogeneity DLBCL poses a major clinical challenge toward achieving successful therapeutic goals (12).

Since the recipients take immunosuppressive drugs, the impairment of the function of the innate immune cells is expected. The occurrence of PHL was affected by many factors, such as high blood drug concentration, high Treg expression, human leukocyte antigen (HLA) mismatch, hemodialysis time, older age at transplantation, etc. (1, 13, 14). Some studies have reported that drug concentrations in the blood of patients with lymphoma were higher after renal transplantation (15). In our case, the concentration of tacrolimus was significantly elevated, reaching 11.0°ng/mL, which was higher than the previous maximum value of 8.9°ng/ml. It was also presumed that long-term hemodialysis might increase the risk of malignant tumors and viral infections, which may favor the occurrence of liver cancer and lymphoma (16). This might fit well with the patient enrolled in our study, who was relatively young (40 years) at the time of transplantation, but had chronic nephritis for almost 10 years prior to kidney transplantation, and had been haemodialysed for more than 4 years. PHL differs from common systemic lymphomas involving the liver, and is related to hepatitis, cirrhosis, administration of immunosuppressive agents (17) and viral infections (mainly HCV, HBV, HIV, EBV infections) (16, 18). In the present case, there was a history of chronic hepatitis B with HBV positive, hepatitis B core antibody (HBcAb) was much higher and it had the features of liver cirrhosis like hepatosplenomegaly and portal hypertension. In some studies, EBV infection has been found to be more closely associated with the occurrence and development of DLBCL, accounting for approximately 9−20% of cases, while accounting for 8−30% of negative cases (19, 20). The onset time of PTLD in EBV negative patients was delayed, usually 3−5 years after SOT (20). In our case, EBV was negative, and the onset of the tumor was late, PHL was detected in the third year after transplantation, which is consistent with literature reports.

It should be mentioned that single or multiple hypodensities of PHL may be seen on the CT scan, and the larger of these may be lobular with central necrosis. What's more, it was a poorly perfused tumor with little or no enhancement in the arterial phase and mild or marginal enhancement in the portal phase and delayed phase. 18F-FDG-PET/CT usually showed high FDG uptake and obvious hypermetabolism (21, 22). The degree of FDG uptake of PHL depended on the pathological type of lymphoma, indolent lymphomas had lower FDG uptake, while diffuse large B-cell lymphatics tumor, Burkitt lymphoma, and T-cell lymphoma had relatively high uptake. The 18F-FDG PET-CT findings of PHL could be divided into multiple nodules type, single mass type and diffuse infiltration type. In this case, PHL was multiple inodular with high FDG uptake. Reducing the level of immunosuppression (rRIS) has always been the main treatment for lymphoma (23). The R-CHOP regimen in combination with rituximab has been shown to have a better chemotherapy effect than the CHOP regimen. As a result, the 3-year OS increased from 30 to 50% before rituximab to more than 60% (24). In the study, immediately after the diagnosis of PHL, the dosage of immunosuppressant tacrolimus was greatly reduced, and sirolimus was increased as an adjuvant antitumor agent. Moreover, 6-cycle R-CHOP combined with zebrutinib chemotherapy regimen was adopted, which achieved unexpected therapeutic effect and achieved complete remission.

Taking immunosuppressants post-transplantation not only leads to a disturbance of immune function, but can also lead to viral infections (6, 25). In particular, pulmonary infection became the most common infectious complication after renal transplantation, with fungal infections accounting for approximately 20% (26). The most serious pathogenic bacterium appeared to be Aspergillus infection, which had a high mortality rate of 40−100%, with a cure rate of only 18−67% (27, 28). Isolated invasive Aspergillus tracheobronchitis (IATB), i.e., fungal infection confined to the bronchus, has been relatively rare, accounting for less than 7% of invasive pulmonary aspergillosis (IPA). We detected fungal infection (Aspergillus flavus/Aspergillus oryzae) with inflammatory granulation tissue in this study.

Some studies found that the factors responsible for the increased risk of IATB after renal transplantation included: Immunosuppressants, glucocorticoids, antibiotics, and chemical drugs administered at high doses over a long period of time (29, 30). In addition, renal donor status, age at transplantation (≥60 years), delayed recovery of graft function, acute rejection, underlying diseases (such as diabetes, hypertension, hyperlipidemia, chronic lung disease, etc.), duration of hemodialysis treatment, leukopenia

(WBC < 3.5 × 109/L), hypoproteinemia (ALB < 40 g/L) served also as important factors.

Linares et al. (6) studied 156 patients with IATB after renal transplantation. Of them, 86.5% were immunosuppressed, 71.8% of them had received glucocorticoid treatment, and 25% of them had received chemotherapy. Most patients required hemodialysis as a transitional treatment, but hemodialysis would generate oxidative stress, leading to ischemia-reperfusion injury of the kidneys and increasing the incidence of DGF and acute rejection (31). Such patients had to receive high-dose corticosteroid or lymphocyte antibody shock therapy (32), which induces more aggression against lymphocytes and further inhibits and damages the patients' immune function. Patients in the study had been treated with immunosuppressants and glucocorticoids for a long time; in particular, for PHL, it received 5 cycles of chemotherapy. Besides, the kidney donor patient had been admitted to the ICU, there might be a risk of pathogenic bacteria recessive infection or donor infection was not effectively controlled. Though the patient was young at the time of transplantation, he had many underlying diseases, including hypertension, hyperglycemia, and hyperlipidemia, DGF and acute rejection occurred immediately after transplantation, in addition he received corticosteroid shock treatment. Notably, white blood cell counts were in the normal range, but albumin was below 40 g/L for a long time, which affected the patients' immune response. Imaging examination of IATB did not reveal typical features that could manifest as thickening of the trachea or bronchial wall, atoptasis, or obstructive pneumonia due to lumen stenosis and poor drainage, and the coexistence of multiple images, such as multiple exudates, consolidation, and cavities in multiple lobar sections of both lungs. It has also been reported that some patients even have normal images (33).

In this study, 18F-FDG-PET/CT showed thickening of the left main bronchial wall, stenosis of the lumen, and significantly increased FDG uptake, but no lesions were found in the lungs. The detection of 1, 3-β-D-glucan (G test) and galactomannan antigen (GM test) in blood or alveolar lavage fluid could serve as the basis for the microbiological diagnosis of invasive aspergillosis (IA), and the GM test of bronchoalveolar lavage fluid remained the preferred detection method (34). Recently, voriconazole has been recommended as the primary treatment for Aspergillus (34). Kramer et al. (35) reported that oral itraconazole treatment for 6–12 months was effective in IA after lung transplantation. In this case, sirolimus, tacrolimus and voriconazole were considered to have obvious drug interaction, so caspofungin was first given as anti-fungal infection. Following significant improvement, voriconazole was used as maintenance treatment, which achieved a good effect. After 3 months, the lesion had completely disappeared, and the drug was immediately discontinued.

Necrotizing granulomatous inflammation (NGI) is usually caused by tuberculosis, which usually occurs in the lung. The extrapulmonary sites commonly include lymph node, pleura, and joints, although any organ may be affected (36). Despite a complete histological evaluation with clinical, microbiological and serological correlation, nearly 20–40% of necrotizing granulomas remain undetermined (37). Ulbright and Katzenstein suggested that the cases involved infectious granulomas where the microorganisms were killed and/or removed by the inflammatory process, leading most patients to receive no treatment rather have a good prognosis (38). A very similar scenario occurred in the current patient, where fungal staining, silver hexamine, Gram stain, and acid fast stain were all negative, and the lesion spontaneously disappeared without any medical treatment.

The diagnosis of PHL required the exclusion of extra-hepatic infiltrating lesions. Similarly, the diagnosis of iIAT required confirmation that Aspergillus infection was confined to the tracheobronchus. With 18F-FDG-PET/CT imaging, whole-body images can be obtained in a single scan, providing complete information about the anatomy and metabolic activity of the lesion and reflecting the distribution of systemic lesions with high sensitivity and specificity (39). Also, 18F-FDG-PET/CT is superior to purely anatomical imaging in detecting additional extra-nodal lesions, with good diagnostic performance particularly in adults (40). It is the possibility for metabolic quantification, implemented through semi-quantitative measurements. In immunocompetent lymphoma patients, a high maximum standardized uptake value (SUVmax) has been shown to predict aggressive B-cell lymphomas, as well as being a significant prognostic factor for progression-free survival and overall survival (41). In this study, extrahepatic infiltrating lesions of lymphoma were excluded and Aspergillus infection confined to the left main bronchus was verified by 18F-FDG-PET/CT. Of interest, 18F-FDG-PET/CT also detected an inflammatory granulomatous lesion in the patient's right medial thigh muscle that might have been missed with other conventional imaging modalities. 18F-FDG-PET/CT has been shown to be very useful in monitoring response to therapy (42). In this case, serial 18F-FDG-PET/CT scans showed a higher value in the evaluation and follow-up of the multi-rare and distinct complications. The 18F-FDG-PET/CT scan during chemotherapy (4th cycle) provided important information on intrahepatic lesion size (reduced only about 30%) and metabolism (reduced over 80%), indicating that the ongoing treatment was effective, yet there remained tumor activity and no complete remission. The metabolism of the lesion did not decrease to a normal level by the end of the sixth chemotherapy in the 18F-FDG-PET/CT examination, but there was still a large residual lesion. With traditional imaging depending only on the size change, this was obviously not feasible to assess the activity of the similar residual lesion. Also, 18F-FDG-PET/CT after antifungal treatment with iIAT showed that the left main bronchus was morphologically and metabolically normal, which also enabled clinical efficacy to be reliably evaluated.

Overall, we provide evidence in support of a possible association between post-renal transplant odds with cancers and infections. In a rare case reported here, the patient developed a diffuse large B-cell lymphoma in the liver, an Aspergillus infection in the trachea and necrotizing granulomatosis in the right medial thigh muscle following a renal transplant. Of importance, 18F-FDG-PET/CT greatly assisted in the monitoring and evaluation of certain complications that might have been missed with other conventional imaging approaches. Concerning these risks, we also recommend post-transplant cancer screening for individual recipients.

Data availability statement

The original contributions presented in this study are included in this article/supplementary material, further inquiries can be directed to the corresponding authors.

Ethics statement

The studies involving humans were approved by the Medical Ethics Committee of Jiangxi Provincial People's Hospital. The studies were conducted in accordance with the local legislation and institutional requirements. Written informed consent for participation in this study was provided by the participants' legal guardians/next of kin. Written informed consent was obtained from the individual(s), and minor(s)' legal guardian/next of kin, for the publication of any potentially identifiable images or data included in this article.

Author contributions

FL: Writing – review & editing. ZH: Writing – original draft. SZ: Writing – original draft. QL: Writing – review & editing. WQ: Data curation, Writing – review & editing. AS: Formal Analysis, Writing – original draft. YW: Investigation, Writing – original draft. AJ: Methodology, Writing – review & editing. IS-W: Project administration, Writing – review & editing. PL: Resources, Writing – review & editing. WA: Writing – review & editing.

Funding

The author(s) declare that no financial support was received for the research, authorship, and/or publication of this article.

Conflict of interest

The authors declare that the research was conducted in the absence of any commercial or financial relationships that could be construed as a potential conflict of interest.

Publisher's note

References

1. Sprangers B, Nair V, Launay-Vacher V, Riella LV, Jhaveri KD. Risk factors associated with post-kidney transplant malignancies: an article from the cancer-kidney international network. *Clin Kidney J.* (2018) 11:315–29. doi: 10.1093/ckj/sfx122

2. Campoli C, Ferraro S, Salfi N, Coladonato S, Morelli MC, Giannella M, et al. Diffuse primary cutaneous infection by Alternaria alternata in a liver transplant recipient with pulmonary nocardiosis: importance of prompt identification for clinical resolution. *Med Mycol Case Rep.* (2020) 28:42–5. doi: 10.1016/j.mmcr.2020.04.007

3. Yu Z, Gu Q, Zhang B, Chen X, Tang J, Hou Y, et al. Clinical features of fatal pandemic influenza A/H1N1 infection complicated by invasive pulmonary fungal infection. *Mycopathologia.* (2020) 185:319–29. doi: 10.1007/s11046-019-00421-z

4. Kupeli E, Ulubay G, Colak T, Ozdemirel TS, Ozyurek BA, Akcay S, et al. Pulmonary complications in renal recipients after transplantation. *Transplant Proc.* (2011) 43:551–553.

5. Lepoittevin M, Kerforne T, Pellerin L, Hauet T, Thuillier R. Molecular markers of kidney transplantation outcome: current omics tools and future developments. *Int J Mol Sci.* (2022) 23:6318. doi: 10.3390/ijms23116318

6. Wang J, Zu Q, Wang W. Analysis of factors of pulmonary fungal infection in mice in respiratory medicine department based on logistic regression analysis model and Progranulin. *Saudi J Biol Sci.* (2020) 27:629–35. doi: 10.1016/j.sjbs.2019.12.001

7. Linares L, Cofán F, Cervera C, Ricart M, Oppenheimer F, Campistol J, et al. Infection-related mortality in a large cohort of renal transplant recipients. *Transplant Proc.* (2007) 39:2225–7. doi: 10.1016/j.transproceed.2007.07.047

8. Dobrzycka M, Proczko-Stepaniak M, Kaska Ł, Wilczyński M, Dębska-Ślizień A, Kobiela J. Weight loss after bariatric surgery in morbidly obese end-stage kidney disease patients as preparation for kidney transplantation. Matched pair analysis in a high-volume bariatric and transplant center. *Obes Surg.* (2020) 30:2708–14. doi: 10.1007/s11695-020-04555-8

9. Kumar R, Khosla D, Kapoor R, Bharti S. Small intestinal lymphoma in a post-renal transplant patient: a rare case with late presentation. *J Gastrointest Cancer.* (2014) 45 (Suppl. 1):2–5. doi: 10.1007/s12029-013-9517-32

10. Vaglio A, Manenti L, Mancini C, Chierici E, Cobelli R, Bacci F, et al. EBV-associated Ieukoencephalopathy with late onset of central nervous system Lymphoma in a kidney transplant recipient. *Am J Transplant.* (2010) 10:947–51. /j.1600-6143.2009.02999.X doi: 10.1111

11. Noronha V, Shafi N, Obando JA, Kummar S. Primary non-Hodgkin's lymphoma of the liver. *Crit Rev Oncol Hematol.* (2005) 53:199–207. doi: 10.1016/j.critrevonc.2004.10.010

12. Li Y, Sharma A, Bloemendal M, Schmidt-Wolf R, Kornek M, Schmidt-Wolf I. PD-1 blockade enhances cytokine-induced killer cell-mediated cytotoxicity in B-cell non-Hodgkin lymphoma cell lines. *Oncol Lett.* (2021) 22:613. doi: 10.3892/ol.2021.12874

13. Elserwy N, Lotfy E, Fouda M, Mahmoud M, Donia A, Mashaly M, et al. Postrenal transplant malignancy: incidence, risk factors, and prognosis. *Saudi J Kidney Dis Transpl.* (2017) 28:579–88. doi: 10.4103/1319-2442.206456

14. Baker R, Mark P, Patel R, Stevens K, Palmer N. Renal association clinical practice guideline in post-operative care in the kidney transplant recipient. *BMC Nephrol.* (2017) 18:174. doi: 10.1186/s12882-017-0553-2

15. Axelrad J, Lichtiger S, Yajnik V. Inflammatory bowel disease and cancer: the role of inflammation,immunosuppression,and cancer treatment. *World J Gastroenterol.* (2016) 22:4794–801. doi: 10.3748/wjg.v22.i20.4794

16. Ma Y, Chen E, Chen X, Wang J, Tang H. Primary hepatic diffuse large B cell lymphoma: a case report: primary hepatic diffuse large B cell lymphoma. *Hepat Mon.* (2011) 11:203–5.

17. De Renzo A, Perna F, Persico M, Notaro R, Mainolfi C, de Sio I, et al. Excellent prognosis and prevalence of HCV infection of primary hepatic and splenic non-Hodgkin's lymphoma. *Eur J Haematol.* (2008) 81:51–7. doi: 10.1111/j.1600-0609.2008.01081.x

18. Ng A. Diffuse large B-cell lymphoma. *Semin Radiat Oncol.* (2007) 17:169–75. doi: 10.1016/j.semradonc.2007.02.002

19. Gibson S, Hsi E. Epstein-Barr virus-positive B-cell lymphoma of the elderly at a United States tertiary medical center: an uncommon aggressive lymphoma with a nongerminal center B-cell phenotype. *Hum Pathol.* (2009) 40:653–61. doi: 10.1016/j.humpath.2008.10.007

20. Nael A, Wu WW, Siddiqi I, Zhao X, Kahlon KS, Rezk SA. Epstein - Barr virus association with plasma cell neoplasms. *Histol Histopathol.* (2019) 34:655-662. doi: 10.14670/HH-18-066

21. Pan B, Wang C, Han J, Zhan L, Ni M, Xu S. ^{18}F-fluorodeoxyglucose PET/CT findings of a solitary primary hepatic lymphoma: a case report. *World J Gastroenterol.* (2012) 18:7409–12. doi: 10.3748/wjg.v18.i48.7409

22. Seshadri N, Ananthasivan R, Kavindran R, Srikanth G, Chandra S. Primary hepatic (extranodal) lymphoma: utility of [(18)F]fluorodeoxyglucose-PET/CT. *Cancer Imaging.* (2010) 10:194–7. doi: 10.1102/1470-7330.2010.0028

23. Sun X, Peterson L, Gong Y, Traynor A, Nelson B. The sun post-transplant plasma cell myeloma and polymorphic lymphoproliferative disorder with monoclonal serum protein occurring in solid organ transplant recipients. *Mod Pathol.* (2004) 17:389–94. doi: 10.1038/modpathol.3800080

24. Elstrom RL, Andreadis C, Aqui NA, Ahya VN, Bloom RD, Brozena SC, et al. Treatment of PTLD with rituximab or chemotherapy. *Am J Transplant.* (2006) 6:569–76.

25. Clark NM. Pulmonary and invasive fungal infections. *Semin Respir Crit Care Med.* (2020) 41:1–2.

26. Israel E, Hirschwerk D, Jhaveri K. Acremonium skin and soft tissue infection in a kidney transplant recipient. *Transplantation.* (2013) 95:e20. doi: 10.1097/TP.0b013e31827eefb4

27. Trabelsi H, Néji S, Sellami H, Yaich S, Cheikhrouhou F, Guidara R, et al. Invasive fungal infections in renal transplant recipients: about 11 cases. *J Mycol Med.* (2013) 23:255–60. doi: 10.1016/j.mycmed.2013.07.052

28. Santos T, Aguiar B, Santos L, Romaozinho C, Tome R, Macario F, et al. Invasive fungal infections after kidney transplantation: a single-center experience. *Transplant Proc.* (2015) 47:971–5. doi: 10.1016/j.transproceed.2015.03.040

29. Wijesuriya T, Weerasekera M, Kottahachchi J, Ranasinghe K, Dissanayake M, Prathapan S, et al. Proportion of lower limb fungal foot infections in patients with type 2 diabetes at a tertiary care hospital in Sri Lanka. *Indian J Endocrinol Metab.* (2014) 18:63–9. doi: 10.4103/2230-8210.126556

30. Oner-Eyüboğlu F, Karacan O, Akçay S, Arslan H, Demirhan B, Haberal M. Invasive pulmonary fungal infections in solid organ transplant recipients: a four-year review. *Transplant Proc.* (2003) 35:2689–91. doi: 10.1016/j.transproceed.2003.08.070

31. Pieringer H, Biesenbach G. Risk factors for delayed kidney function and impact of delayed function on patient and graft survival in adult graft recipients. *Clin Transplant.* (2005) 19:391–8. doi: 10.1111/j.1399-0012.2005.00360.x

32. Mange K, Joffe M, Feldman H. Dialysis prior to living donor kidney transplantation and rates of acute rejection. *Nephrol Dial Transplant.* (2003) 18:172–7. doi: 10.1093/ndt/18.1.172

33. Tunniciliffe G, Schomberg L, Walsh S, Tinwell B, Harrison T, Chua F, et al. Airway and parenchymal manifestations of pulmonary aspergillosis. *Respir Med.* (2013) 107:1113–23.

34. Kousha M, Tadi R, Soubani AO. Pulmonary aspergillosis: a clinical review. *Eur Respir Rev.* (2011) 20:156–74.

35. Kramer MR, Denning DW, Marshall SE, Ross DJ, Berry G, Lewiston NJ, et al. Ulcerative tracheobronchitis after lung transplantation. A new form of invasive aspergillosis. *Am Rev Respir Dis.* (1991) 144(3 Pt. 1):552–6. doi: 10.1164/ajrccm/144.3_Pt_1.552

36. Alves F, Baptista A, Brito H, Mendonca I. Necrotizing granulomatous lymphadenitis. *BMJ Case Rep.* (2011) 2011:bcr1120103548.

37. Aubry MC. Necrotizing granulomatous inflammation: what does it mean if your special stains are negative? *Mod Pathol.* (2012) 25:31e8. doi: 10.1038/modpathol.2011.155

38. Silverstein A, Siltzbach LE. Muscle involvement in sarcoidosis. Asymptomatic, myositis, and myopathy. *Arch Neurol.* (1969) 21:235–41.

39. Scott JA. PET in lymphoma: making a difference in patients' lives. *Radiology.* (2019) 290:496–7. doi: 10.1148/radiol.2018182517

40. Montes de Jesus FM, Kwee TC, Kahle XU, Nijland M, van Meerten T, Huls G, et al. Diagnostic performance of FDG-PET/CT of post-transplant lymphoproliferative disorder and factors affecting diagnostic yield. *Eur J Nucl Med Mol Imaging.* (2020) 47:529–36. doi: 10.1007/s00259-019-04481-7

41. Chihara D, Oki Y, Onoda H, Taji H, Yamamoto K, Tamaki T, et al. High maximum standard uptake value (SUVmax) on PET scan is associated with shorter survival in patients with diffuse large B cell lymphoma. *Int J Hematol.* (2011) 93:502–8.

42. Metser U, Prica A, Hodgson D, Mozuraitis M, Eberg M, Mak V, et al. Effect of PET/CT on the management and outcomes of participants with hodgkin and aggressive non-hodgkin lymphoma: a multicenter registry. *Radiology.* (2019) 290:488–95. doi: 10.1148/radiol.2018181519

frontiers | Frontiers in Medicine

TYPE Case Report
PUBLISHED 20 March 2024
DOI 10.3389/fmed.2024.1382672

OPEN ACCESS

EDITED BY
Carmelo Caldarella,
Fondazione Policlinico Universitario A. Gemelli IRCCS, Roma, Italy

REVIEWED BY
Mahboubeh Nabavinia,
The Research Institute at Nationwide Children's Hospital, United States
Tanyaluck Thientunyakit,
Mahidol University, Thailand
Priscilla Guglielmo,
Veneto Institute of Oncology (IRCCS), Italy

*CORRESPONDENCE
Lei Kang
✉ kanglei@bjmu.edu.cn
Zhaonan Sun
✉ zhaonan_sun@163.com

†These authors have contributed equally to this work

RECEIVED 06 February 2024
ACCEPTED 08 March 2024
PUBLISHED 20 March 2024

CITATION
Huang W, Zheng Z, Bao Z, Xiao X, Li L, Sun Z and Kang L (2024) A poor prognostic male choriocarcinoma with multiple systemic metastases: a case report and the literature review.
Front. Med. 11:1382672.
doi: 10.3389/fmed.2024.1382672

A poor prognostic male choriocarcinoma with multiple systemic metastases: a case report and the literature review

Wenpeng Huang[1†], Zuohuan Zheng[2†], Zheng Bao[1], Xiaoyan Xiao[3], Liming Li[3], Zhaonan Sun[4*] and Lei Kang[1*]

[1]Department of Nuclear Medicine, Peking University First Hospital, Beijing, China, [2]Department of Traditional Chinese Medicine, The Seventh People's Hospital of Chongqing, Chongqing, China, [3]Department of Radiology, The First Affiliated Hospital of Zhengzhou University, Zhengzhou, Henan Province, China, [4]Department of Medical Imaging, Peking University First Hospital, Beijing, China

Background: Non-gestational choriocarcinoma, also known as primary choriocarcinoma, is extremely rare in men, manifesting with specific signs such as breast feminization, testicular atrophy, and loss of libido. The presentation typically includes elevated serum β-hCG levels, widespread metastatic disease, and a rapid progression of the condition.

Case report: We present a rare case of a 41-year-old man diagnosed with choriocarcinoma, exhibiting a unique combination of multiple metastases, including lung, brain, bone, and retroperitoneal lymph node metastases, as confirmed by ^{18}F-FDG PET/CT imaging. The patient was treated with aggressive chemotherapy and pembrolizumab, and the prognosis remained poor. The patient's overall survival was a mere 5 months following diagnosis.

Conclusion: Non-gestational choriocarcinoma represents a rare entity in clinical practice and should be considered in young men presenting with gynaecomastia and elevated β-hCG levels alongside normal gonads. Thus, we advocate for a more comprehensive inquiry into medical history and a systematic examination. The ^{18}F-FDG PET/CT examination not only visually delineates the lesion's location and extent but also serves as a cornerstone for clinical tumor staging, providing valuable support for treatment monitoring and subsequent follow-up.

KEYWORDS

male, primary choriocarcinoma, prognosis, computed tomography, ^{18}F-FDG, PET/CT

Introduction

Choriocarcinoma, a rare trophoblastic tumor, exhibits high invasiveness and is characterized by the proliferation and interstitial transformation of abnormal chorionic trophoblast cells. It is distinguished by the absence of a chorionic structure, accompanied by hemorrhage and necrosis, and has the capability to secrete beta-human chorionic gonadotropin (β-hCG). The condition can be classified into two main categories: gestational choriocarcinoma and non-gestational choriocarcinoma (primary choriocarcinoma) (1–5). Gestational choriocarcinoma originates from the trophoblast of various gestational events, such as hydatidiform mole, spontaneous abortion, and normal pregnancy. On the other hand, non-gestational choriocarcinoma, also

known as primary choriocarcinoma, is extremely rare in men, manifesting with specific signs such as breast feminization, testicular atrophy, and loss of libido (2, 6, 7). This type of choriocarcinoma can be further categorized into gonadal choriocarcinoma (testis) and extragonadal choriocarcinoma (such as mediastinum and retroperitoneum) based on its origin and primary site (8, 9). The presentation typically includes elevated serum β-hCG levels, widespread metastatic disease, and a rapid progression of the condition (10, 11).

In this report, we present a rare case of a 41-year-old man diagnosed with choriocarcinoma, exhibiting a unique combination of multiple metastases, including lung, brain, bone, and retroperitoneal lymph node metastases, as confirmed by 2-Deoxy-2-[fluorine-18]-fluoro-D-glucose (^{18}F-FDG) positron emission tomography combined with computed tomography (PET/CT) imaging. Through an extensive literature search on the PubMed database, covering the period from 1996 to 2023 and utilizing keywords related to choriocarcinoma and CT, the search was carried out with and without the addition of filters, such as English language only, type of article, and subjects, excluding duplicate papers. We identified a total of 53 relevant publications. The summarized findings are presented in Table 1 (12–64). Previous studies have overwhelmingly reported cases of choriocarcinoma in pregnant females. The current case of primary choriocarcinoma occurring in a male is exceptionally rare.

Case presentation

A 41-year-old man presented with diminished appetite symptoms a year ago, but he did not undergo an examination. His condition deteriorated 2 months ago, marked by malaise, night sweats, and lower back pain, leading to a weight loss of 10.5 kg over 1 year. The patient was hospitalized for a physical examination, revealing bilateral breast development and a palpable mass measuring approximately 12 cm × 10 cm with poor mobility in the right abdomen. Laboratory tests indicated a white blood cell count of 12.00 × 109/L (normal range 3.5–9.5 × 109/L), D-dimer of 5.94 mg/L (normal range 0–0.5 mg/L), fibrinogen of 5.10 g/L (normal range 2–4 g/L), C-reactive protein of 99.90 mg/L (normal range 0–10 mg/L), and CA-reactive protein of 99.90 mg/L (normal range 0–10 mg/L). Additionally, CA-199 was elevated at 47.76 U/mL (normal range 0–37 U/mL), non-small cell lung cancer antigen 21–1 was elevated at 28.16 ng/mL (normal range 0–3 ng/mL), neuron-specific enolase was elevated at 67.66 ng/mL (normal range 0–16.3 ng/mL), prolactin was elevated at 35.62 ng/mL (normal range 2.1–17.7 ng/mL), estradiol was lower than normal at 26.33 pg./mL (normal range 35–245 pg./mL), testosterone was elevated at 179.32 ng/mL (normal range 1.75–7.81 ng/mL), beta-human chorionic gonadotropin (β-hCG) was markedly elevated at 937,268.00 mIU/mL (normal range 0–5 mIU/mL), and EBV antibody IgG was 4.06 (positively expressed).

The patient underwent an enhanced CT examination, revealing bilateral enlarged breasts (Figure 1A), empty scrotums bilaterally, with the testes not visualized (Figure 1B). A roundish mass with heterogeneous density was observed in the pelvis, post-enhancement, the mass exhibited heterogeneous mild enhancement (Figures 1C,D). Multiple enlarged lymph nodes were identified in the retroperitoneum, merging with one another, encircling the abdominal aorta and vessels, resulting in displacement of surrounding organs (Figure 1E). Additionally, multiple hypodense foci, characterized by ring-shaped and mild enhancement, were detected in the liver (Figure 1F). Furthermore, multiple rounded hyperdense nodules were observed in both lungs (Figure 1G). Following a thorough physical examination, laboratory tests, and CT imaging, the clinician initially suspected the presence of seminomas and metastases.

For staging, the patient underwent further ^{18}F-FDG PET/CT (Figures 2A,B). The ^{18}F-FDG PET/CT scan, performed utilizing Siemens Biograph Truepoint 64 PET/CT machine, was conducted 60 min after the intravenous administration of ^{18}F-FDG (6.1 mCi), revealing multiple soft tissue nodules in both lungs with significantly increased ^{18}F-FDG uptake (SUVmax = 12.7, Figure 2C). The liver exhibited multiple slightly hypodense nodules and masses, characterized by markedly increased ^{18}F-FDG uptake (SUVmax = 38.6). The larger liver mass measured approximately 3.6 cm × 2.1 cm (Figure 2D). In the retroperitoneum, numerous intermingled soft tissue masses with markedly increased ^{18}F-FDG uptake (SUVmax = 13.1) were observed, with the largest dimension measuring about 16.2 cm × 16.3 cm. Additionally, patchy calcifications were evident within this area (Figure 2E). A soft tissue mass of irregular shape was identified in the right pelvis, displaying unevenly increased ^{18}F-FDG uptake (SUVmax = 19.5). The maximum dimensions of this mass were approximately 12.0 cm × 15.2 cm, with areas of cystic necrosis and calcifications noted (Figure 2F). Markedly increased ^{18}F-FDG uptake (SUVmax = 11.8) was detected at the thoracic 11 vertebral attachments (Figure 2G). Notably, no testes were visualized in the bilateral scrotum. The bilateral breast glands exhibited thickening with a slight increase in ^{18}F-FDG uptake (SUVmax = 1.2, Figure 2H).

The patient underwent CT-guided puncture biopsy of a lesion on the liver, extensive hemorrhage was seen microscopically with typical features of choriocarcinoma. The tumor consists of mononuclear cytotrophoblasts and multinucleated syncytiotrophoblasts (Figures 3A,B). Immunohistochemistry showed positive expression of HPL (Figure 3C), β-HCG (Figure 3D), CD34 (vascular), CK7, CK19 and SALL-4. In addition, Ki-67 was observed to be positive in 90% of the tumor cells. The pathologic diagnosis confirmed choriocarcinoma metastasis.

After confirming the absence of contraindications to chemotherapy, the patient underwent treatment with an eight-cycle regimen consisting of etoposide (200 mg/d1–4), cisplatin (40 mg/d1–3), and bleomycin (30 U/d1,5). According to RECIST guidelines, subsequent CT examinations indicated stable disease (SD) in the patient's status. Considering the patient's chemotherapy tolerance, a collaborative decision was made to initiate a four-cycle course of anti-tumor therapy using the PD-1 antibody (pembrolizumab). Unfortunately, the patient experienced adverse effects of diarrhoea during this treatment phase. At the conclusion of the Avelumab treatment, follow-up CT scans revealed an increase in size of metastatic lesions in both lungs and liver, accompanied by the emergence of multiple metastases in the vertebral body (Figure 4A). Due to an inadequate response to pembrolizumab, the patient was subsequently treated with the regimen of "methotrexate (1.5 g) + actinomycin (0.4 mg)." Two weeks post-treatment initiation, the patient presented with dizziness and headache. A cranial MRI disclosed a rounded lesion in the left frontal lobe with high signal on T2WI (Figure 4B), measuring approximately 1.7 cm in diameter, and exhibiting inhomogeneous annular enhancement (Figure 4C). Nine days later, the patient's secondary epileptic symptoms exacerbated, with a repeat MRI showing an enlarged frontal lobe lesion surpassing its previous size (Figure 4D). Additionally, new bilateral occipital lobe metastases were evident (Figure 4E). Despite medical recommendations, the patient declined further treatment and succumbed to the illness

TABLE 1 ^{18}F-FDG PET/CT and CT manifestations of primary choriocarcinoma.

Case	Authors	Gender	Age	Obstetric history	Medical history	Clinical symptoms	Max β-hCG, mIU/mL	Primary sites	Invasion and metastasis	Max diameter/cm	SUVmax	Management	Outcome
1	Lowe et al. (12)	M	18	None	Microcytic anemia	Black stools, lethargy, and dizziness	32,219	Testicles	Stomach, brain and kidney lungs	NA	NA	Surgery + chemotherapy	Alive
2	Maruoka et al. (13)	F	26 y	Molar pregnancy history at 20 y and spontaneous abortion history at 26 y.	NA	NA	233.8	Negative	Pulmonary metastasis	3.0	2.0	Surgery	Alive at 1 mo
3	Dose et al. (14)	F	37 y	Abortion at 34 y	Leiomyoma of the uterus, Cystic lesion of the right ovary	Irregular bleedings, and secondary sterility	8,000	Uterus	None	5	NA	Surgery + chemotherapy	Alive at 13 mo
4	Gazzilli et al. (15)	F	36 y	History of 4 spontaneous abortion	NA	Repeated epistaxis	3,839	Nasal and ethmoid	Sphenoidal and maxillary sinuses; cervical lymph node	NA	NA	Surgery + chemotherapy	Complete remission
5	Numnum et al. (16)	F	22 y	Molar pregnancy history at 16 and a term delivery at 19 y	GTD (gestational trophoblastic disease)	Vaginal bleeding and abdominal cramping	1,341	Left pelvis	None	NA	5.0	Surgery + chemotherapy	Alive at 8 mo
6	Hebart et al. (17)	F	32 y	NA	Irregular menstruation	Irregular periods, intermittent pleuritic chest pains and nonproductive cough	127,429	None	Left lung artery and right lung	NA	NA	Chemotherapy	Died within few hours
7	Hebart et al. (17)	F	29 y	Term delivery 4 mo ago.	NA	NA	400	None	Left and right lung	NA	NA	Surgery + chemotherapy	Alive at 1 y

(Continued)

10.3389/fmed.2024.1382672

TABLE 1 (Continued)

Case	Authors	Gender	Age	Obstetric history	Medical history	Clinical symptoms	Max β-hCG, mIU/mL	Primary sites	Invasion and metastasis	Max diameter/cm	SUVmax	Management	Outcome
8	Huang et al. (18)	F	40 y	Term delivery 10 y ago	Pseudoaneurysms, GTD	Headache	4,154	None	Left frontal lobe in brain and left lung	1.5	NA	Chemotherapy	Alive at 3 y
9	Tripathi et al. (19)	F	38 y	Term delivery 4 y ago	NA	NA	33,000	NA	Right atrium and lung	NA	NA	Chemotherapy + surgery	Alive after 5 cycles
10	Rao et al. (20)	F	28 y	Term delivery 4 y ago	NA	Irregular vaginal bleeding	1,004.69	Pancreas	None	5.4	3.9	Surgery + chemotherapy	Alive at 2 y
11	Huang et al. (21)	F	46 y	NA	NA	Right upper abdominal pain	59,283	Pancreas	Liver and inferior vena cava lymph nodes	7.4	17.7	Surgery +125I-seed implantation	Died at 10 mo
12	Trübenbach et al. (22)	F	33 y	Abortion 10 months ago	Pulmonary embolism, pleural effusion and pulmonary hypertension	Recurrent episodes of exertional dyspnoea and pleuritic chest pain	129,500	None	Left pulmonary artery	NA	NA	Methotrexate	Died at 1 d
13	Zhang et al. (23)	F	29 y	NA	Recurrent right-sided pneumothoraces	Recurrent right-sided pneumothoraces and episodic menorrhagia	NA	Left lung	NA	NA	7.2	Surgery	NA
14	FCimarelli et al. (24)	M	23	None	GCT (germ cell tumors)	Gynecomastia and abdomen pain	425,000	Retroperitoneal	Liver, lung and lomboaortic lymph nodes	14	NA	Surgery + chemotherapy	NA
15	Joshua et al. (25)	F	31 y	Term delivery	Dult polycystic kidney disease and mild hypertension	Pulmonary vein bleeding	91,348	Uterus	Lung and liver	NA	NA	Chemotherapy	Alive at 8 mo
16	Sone et al. (26)	F	31 y	NA	NA	NA	NA	NA	Lung	NA	7.3	Chemotherapy	Died
17	Kidd et al. (27)	M	48 y	None	NA	Blurred vision and headache	NA	NA	Brain and lung and	NA	NA	Supportive therapy	Died at 10 d

(Continued)

10.3389/fmed.2024.1382672

TABLE 1 (Continued)

Case	Authors	Gender	Age	Obstetric history	Medical history	Clinical symptoms	Max β-hCG, mIU/mL	Primary sites	Invasion and metastasis	Max diameter/cm	SUVmax	Management	Outcome
18	Aleem et al. (28)	F	30 y	NA	NA	A lump in right breast and right axilla	NA	Uterus	Right breast	7	5.9	Surgery + chemotherapy	alive
19	Goldfarb et al. (29)	F	50 y	Gravida 3, para 2, abortus 1	NA	An intra-uterine mass and hemorrhaged during an office endometrial biopsy	28,725	Uterus	Lungs	NA	NA	Surgery + chemotherapy + targeted therapy	Disease progression at 2 y
20	Du et al. (30)	F	37 y	One term delivery and two miscarriages	Irregular menstruation	Hemoptysis	279,064	NA	Lung, renal and brain	5.8	18.3	Surgery + chemotherapy	Died at 1 y
21	Wang et al. (31)	F	21 y	Miscarriage at 20 y.	NA	Chest pain and fever	>10,000	NA	Lung	NA	27.5	Chemotherapy	Alive at 1 y
22	Sekine et al. (32)	M	49 y	None	Diabetes mellitus and hepatitis C	Abdominal pain and fever	5,3,000	Liver	Lung	NA	NA	None	Died at 60 d
23	Sironi et al. (33)	F	38 y	No obstetric history in the past 10 y	NA	NA	210	NA	Lung	NA	NA	Surgery + chemotherapy	Alive at 12 mo
24	Sironi et al. (33)	F	29 y	Recent molar pregnancy history	NA	NA	3,471	NA	Lung	0.5	Poor FDG avidity	Surgery	Alive at 6 mo
25	Sironi et al. (33)	F	49 y	Molar pregnancy 6 y ago	NA	NA	>10,000	NA	Left lung and liver	13	7.98	Surgery + chemotherapy	Alive
26	Gasparri et al. (34)	F	37 y	Term delivery 1 y ago	Enhancement of beta-human chorionic gonadotropin levels	Period suspension	NA	NA	Lung	1.1	NA	Surgery + chemotherapy	Alive at 2 y

(Continued)

10.3389/fmed.2024.1382672

TABLE 1 (Continued)

Case	Authors	Gender	Age	Obstetric history	Medical history	Clinical symptoms	Max β-hCG, mIU/mL	Primary sites	Invasion and metastasis	Max diameter/cm	SUVmax	Management	Outcome
27	Gvinianidze et al. (35)	F	42 y	Term delivery 6 mo ago	NA	Cough, shortness of breath on physical exertion and haemoptysis	3,200	NA	Lung and brain	NA	NA	Surgery + chemotherapy	Alive at 8 mo
28	Snoj et al. (36)	F	35	Three spontaneous abortions in the past year	NA	Right chest pain	169,396	Lung	Brain	6.4	2.7	Surgery + chemotherapy + radiotherapy	Alive at 1 y
29	Göksel et al. (37)	M	27	None	Anemia and melena	Anemia and melena	NA	Testicles	Stomach	NA	NA	NA	NA
30	Francischetti et al. (38)	M	41	None	Transient ischemic attack and stroke	Recurrent numbness of right finger and arm, left facial weakness and language difficulty	12,118	Mediastinum	Brain	9	NA	NA	NA
31	Pakkala et al. (39)	F	23	At 28 weeks of gestation	NA	Right hypochondrium pain	11,875	NA	Liver and pulmonary, presacral, rectal, and iliac nodal metastasis	11.6	NA	Termination of pregnancy + surgery + chemotherapy	Alive at 7 mo
32	Su et al. (40)	F	31	NA	Right ovarian dermoid cyst and bilateral polycystic ovaries	NA	790,000	Uterus	Lung	0.4	Poor FDG avidity	Surgery + chemotherapy	NA
33	Lee et al. (41)	F	15	None	NA	Uterine bleeding	76,600	Right ovary	None	8.5	NA	Surgery + chemotherapy	Alive at 6 y
34	Lehmann et al. (42)	F	32	Term delivery 5 mo ago	Gestational choriocarcinoma	Uterine bleeding	13,575	Uterus	Lung and brain	NA	NA	Surgery + chemotherapy	Alive at 2 y

(Continued)

10.3389/fmed.2024.1382672

TABLE 1 (Continued)

Case	Authors	Gender	Age	Obstetric history	Medical history	Clinical symptoms	Max β-hCG, mIU/mL	Primary sites	Invasion and metastasis	Max diameter/cm	SUVmax	Management	Outcome
35	Usta et al. (43)	F	28	Term delivery 4 y ago	NA	Lower pelvic pain, flank pain, vaginal bleeding and a delayed menstrual period	70,373	Renal artery	NA	NA	NA	Surgery + chemotherapy	Alive at 1 y
36	Clair et al. (44)	F	30	A 15-week twin pregnancy consisting of a normal fetus and a suspected molar gestation	NA	NA	96,952	Uterus	Lungs	3.2	NA	Surgery + chemotherapy + radiotherapy + targeted therapy	Alive at 5 y
37	Dance et al. (45)	M	37 d	None	Anemia and thrombocytopenia	A pedunculated, friable red glabellar mass	NA	NA	Cutaneous, liver, and lung	6.8	10.3	Surgery + liver transplant + chemotherapy	Alive at 3 mo
38	Shaw et al. (46)	F	38 y	An abortion 11 mo ago	Pulmonary tuberculosis	Oliguria and leg edema	382	Uterus	Stomach	NA	3.63	Surgery	Alive at 15 mo
39	Hyun et al. (47)	F	38	Molar pregnancy history 4 y ago	Hydatidiform mole and asymptomatic recurrent pneumothorax	NA	NA	Uterus	Lung	NA	Poor FDG avidity	Surgery + chemotherapy	Alive at 22 mo
40	Pessanha et al. (48)	M	14	None	Tyrosinemia type I, HCC, Budd-Chiari Syndrome with partial occlusion of the hepatic veins and micronodular hepatic cirrhosis	Weight loss, minor edema of the lower limbs, moderate gynecomastia, and morning nausea	1,984	Liver	Lung	6.7	Poor FDG avidity	Surgery + chemotherapy	Alive at 11 y

(Continued)

10.3389/fmed.2024.1382672

TABLE 1 (Continued)

Case	Authors	Gender	Age	Obstetric history	Medical history	Clinical symptoms	Max β-hCG, mIU/mL	Primary sites	Invasion and metastasis	Max diameter/cm	SUVmax	Management	Outcome
41	Chen et al. (49)	F	43	Term delivery 3 y ago	Ectopic pregnancy	Low abdomen pain	5,241	NA	Liver, lungs, marrow cavity, thoracic vertebra and brain	5.8	6.4	Surgery + chemotherapy	Alive at 32 mo
42	Kohler et al. (50)	M	64 y	None	NA	Abdomen pain and intra-abdominal bleeding	>5,000	Liver	Lungs and iliacal lymph nodes	14.5	NA	Surgery + chemotherapy	Died at 6 mo
43	Dlewati et al. (51)	F	54	NA	Hypertension and ischemic stroke	Dyspnea, cough, and intermittent hemoptysis	98,138	Lung	Right breast and brain	4.8	3.1	Surgery + chemotherapy + radiotherapy	NA
44	Dasgupta et al. (52)	M	29	None	NA	A lump on the neck	18	Testicle	Cervical lymph node	4.8	NA	Surgery	NA
45	Huang et al. (53)	F	32	Molar pregnancy 7 mo ago	Hydatidiform mole and GTD	NA	17,094	Uterus	Anterior pelvic peritoneal wall	NA	4.7	Surgery + chemotherapy	Alive at 30 mo
46	Chatterjee et al. (54)	F	41	Molar pregnancy history	NA	Headache and left eye pain	7,062	NA	Endocranium	3.5	Poor FDG avidity	Surgery + chemotherapy	Alive at 3 y
47	Zhou et al. (55)	F	66	NA	NA	Abdominal discomfort	795.14	Stomach	Liver	2.0	NA	Surgery + chemotherapy + radiotherapy	Died at 8 mo
48	Matsuo et al. (56)	F	46	Term delivery 5 y ago	NA	Hemoptysis	132	NA	Lung	4	NA	Surgery + chemotherapy	Alive at 8 mo
49	Røge et al. (57)	M	71	None	Concurrent goserelin-treated metastasized prostate adenocarcinoma	Back pain	NA	Mediastinum	Lungs	5.5	NA	Surgery	Died

(Continued)

10.3389/fmed.2024.1382672

TABLE 1 (Continued)

Case	Authors	Gender	Age	Obstetric history	Medical history	Clinical symptoms	Max β-hCG, mIU/mL	Primary sites	Invasion and metastasis	Max diameter/cm	SUVmax	Management	Outcome
50	Kazemi et al. (58)	F	49	Gravida 2, para 2	Asthma, pulmonary edema, and hyperlipidemia	Cough and right upper quadrant pain	79,000	NA	Liver and lungs	NA	NA	Chemotherapy + target therapy	Died
51	Pan et al. (59)	M	19	None	NA	Chest pain and occasional cough	>200,000	Mediastinum	Lungs, brain, liver, spleen, kidney, and skeletal	8.8	NA	Surgery + chemotherapy	Died at 4 mo
52	Kamata et al. (60)	M	70	None	NA	Cough	NA	Lung	NA	3.8	6.5	Surgery	Alive at 2 y
53	Iijima et al. (61)	F	45	Molar pregnancy history 6 y ago	Hydatidiform mole	Irregular vaginal bleeding	482.8	Uterus	Lung	NA	9.57	Surgery + chemotherapy	Alive at 7 y
54	Horotsu et al. (62)	M	78	None	NA	NA	120	Stomach	Liver	3	5.4	Surgery + chemotherapy	Died at 10 mo
55	Rehman et al. (63)	M	50	None	NA	Painful bilateral gynaecomastia	3,756	Mediastinum	Lung	NA	NA	Surgery + chemotherapy	Alive at 3 y
56	Guo et al. (64)	F	61	Term delivery at 31 y	NA	Vaginal bleeding	9273.9	Vagina	Lung	3	Poor FDG avidity	Surgery + chemotherapy	Alive at 4 y

10.3389/fmed.2024.1382672

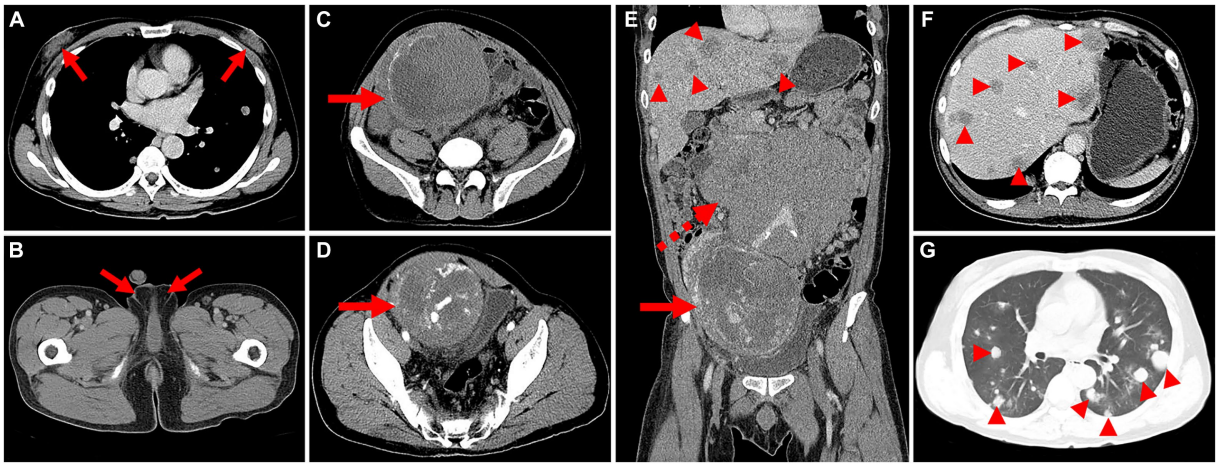

FIGURE 1
Computed tomography (CT) images of male choriocarcinoma with multiple systemic metastases (December 15, 2018). **(A)** The transverse image reveals bilaterally enlarged breasts (long arrows). **(B)** The transverse image displays empty scrotums bilaterally, with the testes not visualized (long arrows). **(C)** A roundish mass with heterogeneous density is observed in the pelvis, featuring eggshell-like calcifications at its margins (long arrows). **(D)** The transverse image in the arterial phase shows heterogeneous mild enhancement of the lesion, with evident thickening of blood-supplying arteries, areas of necrotic cystic degeneration in the interior, and tortuous, dilated veins in the surrounding area (long arrows). **(E)** The coronal image in the venous phase reveals multiple enlarged lymph nodes in the retroperitoneum, merging with one another (dashed arrows). **(F)** The transverse image in the venous phase exhibits multiple hypodense foci in the liver, characterized by ring-shaped and mild enhancement (arrowheads). **(G)** The transverse image depicts multiple rounded hyperdense nodules in both lungs (arrowheads).

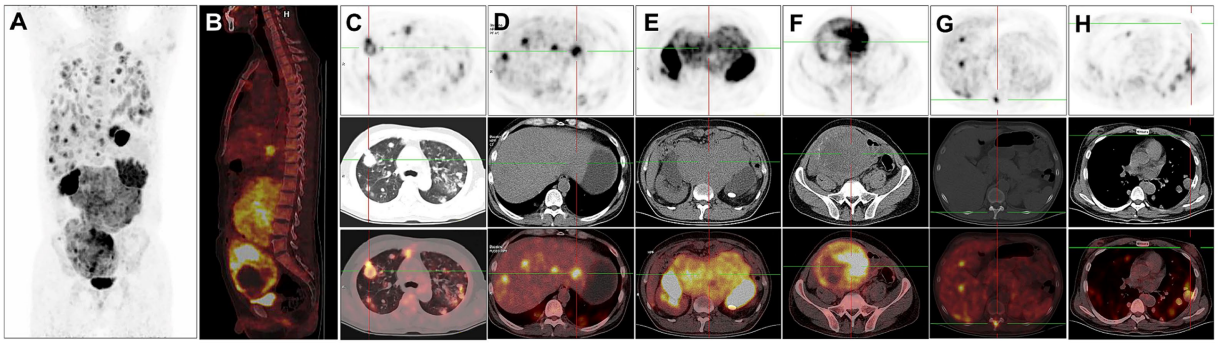

FIGURE 2
^{18}F-FDG PET/CT images of male choriocarcinoma with multiple systemic metastases (December 20, 2018). **(A)** The anteroposterior 3-dimensional maximum intensity projection (MIP) image demonstrates increased metabolic activity in the both lungs, abdominal cavity, and pelvic cavity. **(B)** The sagittal fusion image demonstrates increased metabolic activity in the liver, retroperitoneum and pelvis. **(C)** Transverse images reveal multiple soft tissue nodules in both lungs with significantly increased ^{18}F-FDG uptake (SUVmax = 12.7). **(D)** Transverse images reveal the liver exhibiting multiple slightly hypodense nodules and masses, characterized by markedly increased ^{18}F-FDG uptake (SUVmax = 38.6). **(E)** Transverse images depict, in the retroperitoneum, numerous intermingled soft tissue masses with markedly increased ^{18}F-FDG uptake (SUVmax = 13.1). **(F)** Transverse images identify a soft tissue mass of irregular shape in the right pelvis, displaying unevenly increased ^{18}F-FDG uptake (SUVmax = 19.5). The maximum dimensions of this mass are approximately 12.0 cm × 15.2 cm, with areas of cystic necrosis and calcifications noted. **(G)** Transverse images reveal markedly increased ^{18}F-FDG uptake at the thoracic 11 vertebral attachments (SUVmax = 11.8). **(H)** Transverse images show the bilateral breast glands exhibiting thickening with a slight increase in ^{18}F-FDG uptake (SUVmax = 1.2).

2 weeks later. The patient's overall survival was a mere 5 months following diagnosis.

Discussion

Germ cell tumors encompass various cell types, broadly categorized into seminoma and non-seminoma. Non-seminomatous germ cell tumors (NSGCTs) exhibit four subtypes: embryonal carcinoma, yolk sac tumor, teratoma, and choriocarcinoma, often displaying a combination of seminomatous and non-seminomatous components. Choriocarcinoma, the rarest subtype, lacks a clear etiology in males, potentially associated with various risk factors such as Klinefelter syndrome, cryptorchidism, exposure to radiation, and more. Cryptorchidism may be one of the significant factors contributing to testicular choriocarcinoma. It has been reported that the likelihood of choriocarcinoma in cryptorchidism patients is 20–40 times higher compared to individuals with normal testes (65, 66). The absence of the testicle in this particular case may be a significant factor contributing to the development of testicular choriocarcinoma.

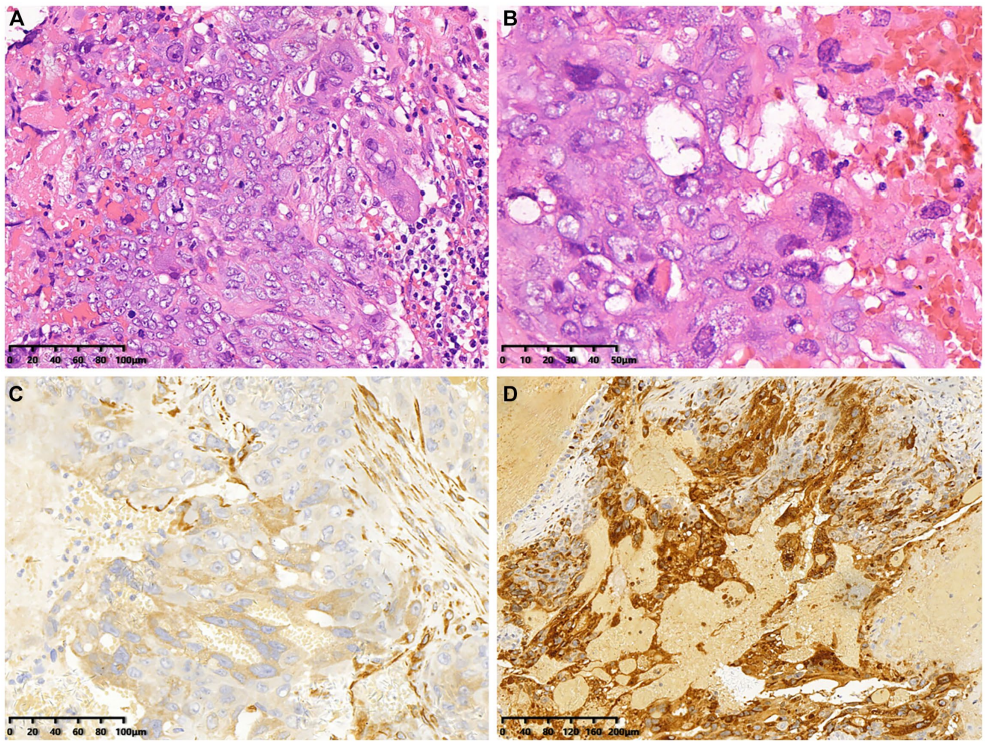

FIGURE 3
Histopathological and immunohistochemical images of choriocarcinoma (December 22, 2018). **(A,B)** Hematoxylin–eosin (HE) staining (magnification ×200 and 400) showed extensive hemorrhage and characteristic features indicative of choriocarcinoma. **(C,D)** Immunohistochemistry showed that the tumor cells were positive for HPL and β-HCG (magnification ×200).

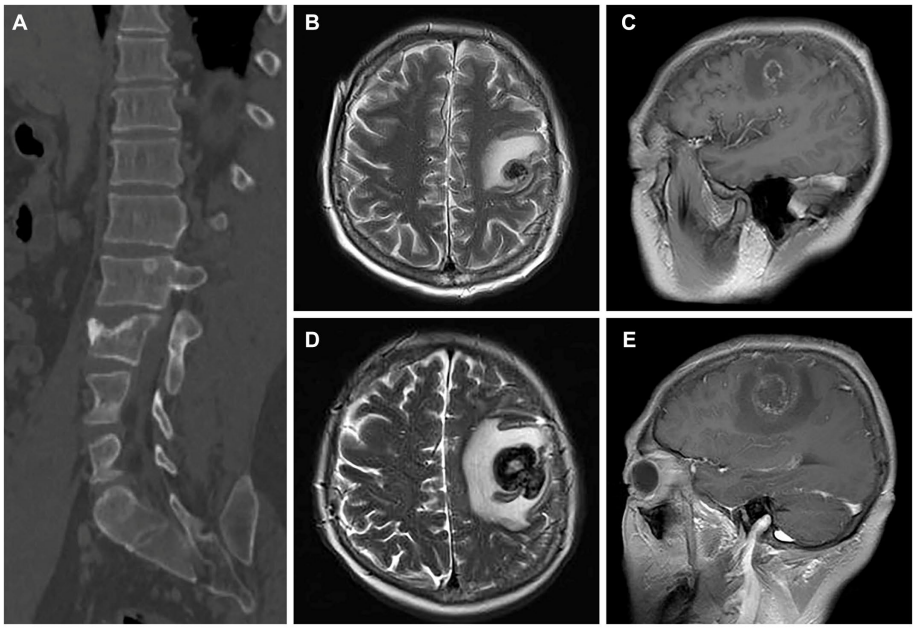

FIGURE 4
CT images and magnetic resonance images after treatment for choriocarcinoma (May 5 & 14, 2020). **(A)** The sagittal bone window CT image reveals multiple metastases in the vertebral body. **(B,C)** The T2-weighted imaging (T2WI) and enhanced images indicate the development of brain metastases in the patient. **(D,E)** Subsequent scans after 9 days demonstrate an enlargement and increased size of the patient's brain metastatic lesions compared to the previous images in both T2WI and enhanced sequences.

Due to its pronounced invasiveness into blood vessels and tissues, extensive hemorrhage, necrosis, and lymphovascular invasion are common findings (67). Choriocarcinoma primarily metastasizes hematogenously, resulting in early and extensive dissemination to sites such as the lungs, liver, skin, retroperitoneal lymph nodes, gastrointestinal tract, and central nervous system (37, 68–71). In this case, the diagnosis of choriocarcinoma was established at an advanced stage, with multiple metastases already present throughout the body. A thorough medical history and examination are necessary to detect the primary lesion. Characteristics of the typical choriocarcinoma patient history include pregnancy-relatedness, elevated β-hCG levels, abnormal uterine bleeding, and vaginal bleeding. Patients with choriocarcinoma usually have a history of multiple pregnancies. Primary choriocarcinoma is extremely rare in men, manifesting with specific signs such as breast feminization, testicular atrophy, and loss of libido.

The determination of serum tumor markers, specifically serum β-hCG and AFP, proves beneficial in choriocarcinoma diagnosis as they are elevated in approximately 80% of cases. Our case report demonstrates markedly elevated serum β-hCG, produced by syncytiotrophoblasts, indicating its diagnostic relevance. Monitoring the serum concentration of β-hCG also aids in assessing treatment response. According to the International Cooperative Organization for Germ Cell Cancer, a β-hCG level exceeding 50,000 mIU/mL signifies a poor prognosis. Some patients may manifest hyperthyroidism or bilateral gynecomastia, attributed to markedly elevated serum β-hCG levels, often exceeding 50,000 mIU/mL (66, 72). In our case, elevated β-hCG levels stimulated supraphysiological testosterone secretion, subsequently aromatized to estradiol, resulting in gynecomastia. Following chemotherapy, a substantial decrease in β-hCG levels was observed, aligning with existing literature. In addition to the abnormal laboratory results, elevated white blood cell count may indicate an underlying infection or inflammation. Elevated levels of D-dimer, C-reactive protein, and fibrinogen may suggest a hypercoagulable state, which could be related to the patient's malignancy. Elevated tumor markers and neuron-specific enolase levels may indicate an underlying malignancy. Elevated prolactin and testosterone levels and a low estradiol level may suggest an endocrine disorder, potentially related to the patient's breast development and gynecomastia. Furthermore, positive EBV antibody IgG suggests a previous Epstein–Barr virus infection, which may have contributed to the patient's condition.

The pathogenesis of extragonadal choriocarcinoma has been a subject of prolonged debate, currently revolving around three hypotheses (73). First, the tumor is postulated to arise from retained primordial germ cells that undergo abnormal migration during embryogenesis (74). Second, it is proposed that the lesion originates from the transformation of a nontrophoblastic neoplasm (75). The third hypothesis suggests that the tumor results from the metastasis of choriocarcinoma from the gonads, accompanied by the spontaneous regression of the primary choriocarcinoma in the gonads.

Histologically, choriocarcinoma is distinguished by a biphasic pattern featuring mononucleated cytotrophoblast cells (including intermediate trophoblast cells) alongside multinucleated syncytiotrophoblasts, with an absence of chorionic villi. The former cells organize lamellarily to form a villous structure, while the latter secrete β-hCG and human placental lactogen (HPL), observable at the tumor progression margin (76–78). Immunohistochemistry plays a crucial role in the differential diagnosis of relevant diseases (79). GATA binding protein 3 (GATA-3), Spalt-like transcription factor 4 (SALL-4), Cytokeratin (CK) AE1/AE3, and 3-beta-hydroxysteroid dehydrogenase type 1 (HSD3B1) have been identified as potential immunohistochemical markers for gestational choriocarcinoma (80, 81). A high Ki-67 proliferation index is noted in over 90% of choriocarcinoma cases (1). Immunohistochemistry holds significance in the differential diagnosis of relevant diseases.

The imaging characteristics of choriocarcinoma lack distinctive features that differentiate it from other types of germ cell tumors, making its initial diagnosis challenging. However, a comprehensive pre-operative workup, including clinical imaging assessments, remains crucial. There is a scarcity of studies reporting imaging features of retroperitoneal choriocarcinoma in men (82). On CT scans, the lesion typically exhibits a large central necrosis with common occurrences of bleeding and ring enhancement of solid components at the tumor margins. MRI findings include a mixed high signal on T1WI and T2WI associated with combined hemorrhage. Striped hypointensity on both T1WI and T2WI at the tumor margin suggests the possibility of old hemorrhage. In our presented case, CT revealed a cystic solid tumor with eggshell-like calcification at the margin, and an enhancement scan displayed circumferential enhancement, with patchy non-enhanced necrotic areas within the lesion. Due to the rapid growth of choriocarcinoma, histologically, the lesion lacks interstitial blood vessels, relying on the invasion of blood vessels for nutrition, leading to frequent internal necrosis. While CT served as the initial diagnostic modality in our case study, it proved insufficient in revealing metastatic details.

^{18}F-FDG PET/CT emerges as a noninvasive tool, showcasing its exceptional utility in discerning the metabolic activity of tumors. It proves particularly advantageous in delineating the staging of choriocarcinoma, tracking relapse, and assessing therapeutic response (18, 24, 33, 47). PET/CT effectively identifies occult choriocarcinoma lesions that may elude detection through conventional imaging methods such as MRI or CT (30). In the case under scrutiny, ^{18}F-FDG PET/CT provided comprehensive insights into the extent of systemic involvement of the tumor. Another pivotal role of ^{18}F-FDG PET/CT in choriocarcinoma management lies in its ability to monitor treatment response. Radiological assessment using ^{18}F-FDG PET/CT should be incorporated at the end of treatment and annually during follow-up. The existing literature on choriocarcinoma is predominantly comprised of case reports, highlighting its heightened metabolic state with significant ^{18}F-FDG uptake, indicative of robust trophoblastic proliferation and the tumor's highly aggressive nature (13). However, a subset of cases has demonstrated low ^{18}F-FDG accumulation in metastatic nodules from choriocarcinoma, potentially influenced by hemorrhagic and/or necrotic components affecting ^{18}F-FDG avidity (83). The reported SUVmax range for choriocarcinoma spans from 2.0 to 27.5, encompassing various studies (13, 16, 20, 21, 23, 26, 28, 30, 31, 33, 36, 45–47, 49, 51, 53, 54, 60–62, 64, 83).

The treatment approach for choriocarcinoma is contingent upon the disease's stage (66). Non-gestational choriocarcinomas often receive a diagnosis in advanced or metastatic stages. Inaba et al. propose neoadjuvant chemotherapy to reduce tumor volume or high-dose chemotherapy before cytoreductive surgery (84). Currently, there is no standardized chemotherapy regimen for primary choriocarcinoma in males, with high-intensity chemotherapy regimens commonly employed, similar to those used for female choriocarcinoma. Frequently utilized chemotherapy protocols include EMA/CO (etoposide, methotrexate, actinomycin D, cyclophosphamide, and vincristine) and TP (paclitaxel and cisplatin). It is acknowledged that male patients often develop resistance to cytotoxic chemotherapy, leading to a grim

prognosis. Factors such as poor response to chemotherapy, high disease burden, brain metastasis, and hemoptysis at the time of diagnosis correlate with shorter survival times in male primary choriocarcinoma patients, with a median overall survival of approximately 6 months and a 1-month mortality rate of 23.8% (85–90). In this study, the patient received treatment with etoposide, cisplatin, and bleomycin; however, metastases remained uncontrolled, resulting in the patient's demise due to increased intracranial pressure and secondary epilepsy exacerbated by enlarged brain metastases. The overall survival was only 5 months. A consistent phenomenon observed in patients with poor prognoses was a rapid decrease in β-hCG to a lower level during treatment, followed by a sharp rise during disease relapse (91). Liu et al. suggest that, for advanced patients, a combination of adjuvant chemoradiotherapy with palliative surgery is recommended. If serum β-hCG drops to a normal level and residual lesions persist, salvage surgery to achieve an R0 status is considered worthwhile (76).

As the medical field advances, ongoing exploration and application of new treatment modalities persist. In a pre-clinical model, PD-L1 overexpression was identified in gestational trophoblastic specimens, suggesting the potential role of this ligand in tumor-immune evasion (92). Veras et al. (93) reported PD-L1 expression in human placentas and gestational trophoblastic diseases, including choriocarcinoma. Ghorani et al. (92) documented four cases of drug-resistant gestational trophoblastic neoplasia treated with pembrolizumab. Among these cases, all displayed PD-L1 overexpression, and three out of four patients achieved remission. The lack of response in one patient was attributed to the absence of tumor-infiltrating lymphocytes. In a recent phase II, single-arm, prospective trial (CAP 01), the efficacy and safety of camrelizumab (PD-1 inhibitor) combined with apatinib (vascular endothelial growth factor (VEGF) receptor inhibitor) were evaluated in patients with high-risk chemo-refractory or relapsed gestational trophoblastic neoplasia. The study included 20 patients (19 with gestational choriocarcinoma and one with placental site trophoblastic tumor). Notably, 50% of enrolled patients achieved a complete response with the combination of the two drugs, and none of the patients with a complete response experienced disease recurrence after discontinuation of the treatment (94). Contrastingly, in a study by Adra et al. (95), only one of three male patients with choriocarcinoma exhibited PD-L1 overexpression, and none of the three patients achieved an objective response to pembrolizumab treatment. These findings suggest that PD-1/PD-L1 blockade therapy may not be universally effective in all male patients. It is posited that the therapeutic efficacy of PD-1/PDL1 blockade varies based on clinicopathological features such as PD-L1 overexpression and the presence of tumor-infiltrating lymphocytes.

Conclusion

In conclusion, non-gestational choriocarcinoma represents a rare entity in clinical practice and should be considered in young men presenting with gynaecomastia and elevated β-hCG levels alongside normal gonads. Thus, we advocate for a more comprehensive inquiry into medical history and a systematic examination. Male primary choriocarcinoma is often associated with widespread metastatic disease, rapid disease progression, and a poor prognosis. Early diagnosis is paramount for formulating an optimal management strategy and minimizing widespread metastasis to achieve the best clinical outcome. The case elucidated in this report contributes to a deeper understanding of the disease for clinicians. The ^{18}F-FDG PET/CT examination not only visually delineates the lesion's location and extent but also serves as a cornerstone for clinical tumor staging, providing valuable support for treatment monitoring and subsequent follow-up.

Data availability statement

The original contributions presented in the study are included in the article/supplementary material, further inquiries can be directed to the corresponding authors.

Ethics statement

Written informed consent was obtained from the individual(s) for the publication of any potentially identifiable images or data included in this article.

Author contributions

WH: Conceptualization, Data curation, Writing – original draft, Writing – review & editing. ZZ: Conceptualization, Writing – review & editing. ZB: Formal analysis, Supervision, Writing – review & editing. XX: Conceptualization, Data curation, Writing – review & editing. LL: Data curation, Formal analysis, Writing – review & editing. ZS: Conceptualization, Data curation, Writing – review & editing. LK: Data curation, Formal analysis, Funding acquisition, Investigation, Supervision, Writing – original draft, Writing – review & editing.

Funding

The author(s) declare that no financial support was received for the research, authorship, and/or publication of this article.

Conflict of interest

The authors declare that the research was conducted in the absence of any commercial or financial relationships that could be construed as a potential conflict of interest.

Publisher's note

References

1. Bogani G, Ray-Coquard I, Mutch D, Vergote I, Ramirez PT, Prat J, et al. Gestational choriocarcinoma. *Int J Gynecol Cancer*. (2023) 33:1504–14. doi: 10.1136/ijgc-2023-004704

2. Han C, Zhou Y, Ma J-A, Liu J, Jiang Y-N, Zhang H-X. A promising treatment option for refractory male primary choriocarcinoma: report of two cases. *Transl Cancer Res*. (2020) 9:3054–60. doi: 10.21037/tcr.2020.02.05

3. Wang Y, Wang Z, Zhu X, Wan Q, Han P, Ying J, et al. Intestinal metastasis from choriocarcinoma: a case series and literature review. *World J Surg Oncol*. (2022) 20:173. doi: 10.1186/s12957-022-02623-0

4. Rejlekova K, Cursano MC, De Giorgi U, Mego M. Severe complications in testicular germ cell Tumors: the Choriocarcinoma syndrome. *Front Endocrinol (Lausanne)*. (2019) 10:218. doi: 10.3389/fendo.2019.00218

5. Xu S, Song X, Jin C, Li Y. Tubal choriocarcinoma presented as ruptured ectopic pregnancy: a case report and review of the literature. *World J Surg Oncol*. (2020) 18:245. doi: 10.1186/s12957-020-02021-4

6. Murshed KA, Kanbour A, Akhtar M, Al HS. Primary mediastinal choriocarcinoma presenting as cutaneous metastasis with resistance to chemotherapy: case report and literature review. *J Cutan Pathol*. (2021) 48:81–5. doi: 10.1111/cup.13777

7. Vegh GL, Szigetvári I, Soltesz I, Major K, Batorfi J, Dancso J, et al. Primary pulmonary choriocarcinoma: a case report. *J Reprod Med*. (2008) 53:369–72.

8. Jiang F, Xiang Y, Feng F-Z, Ren T, Cui Z-M, Wan X-R. Clinical analysis of 13 males with primary choriocarcinoma and review of the literature. *Onco Targets Ther*. (2014) 7:1135–41. doi: 10.2147/OTT.S62561

9. Seckl MJ, Fisher RA, Salerno G, Rees H, Paradinas FJ, Foskett M, et al. Choriocarcinoma and partial hydatidiform moles. *Lancet*. (2000) 356:36–9. doi: 10.1016/S0140-6736(00)02432-6

10. Massie RJ, Shaw PJ, Burgess M. Intracranial choriocarcinoma causing precocious puberty and cured with combined modality therapy. *J Paediatr Child Health*. (1993) 29:464–7. doi: 10.1111/j.1440-1754.1993.tb03022.x

11. Reilley MJ, Pagliaro LC. Testicular choriocarcinoma: a rare variant that requires a unique treatment approach. *Curr Oncol Rep*. (2015) 17:2. doi: 10.1007/s11912-014-0430-0

12. Lowe K, Paterson J, Armstrong S, Walsh S, Groome M, Mowat C. Metastatic testicular Choriocarcinoma: a rare cause of upper GI bleeding. *ACG Case Rep J*. (2016) 3:36–8. doi: 10.14309/crj.2015.94

13. Maruoka Y, Abe K, Baba S, Isoda T, Matsuo Y, Kubo Y, et al. A case of pulmonary choriocarcinoma metastasis with unusual FDG-PET and CT findings: correlation with pathology. *Ann Nucl Med*. (2012) 26:835–9. doi: 10.1007/s12149-012-0644-x

14. Dose J, Bohuslavizki K, Hüneke B, Lindner C, Jänicke F. Detection of intramural Choriocarcinoma of the uterus with 18F-FDG-PET. *Mol Imaging Biol*. (2000) 3:37–40. doi: 10.1016/s1095-0397(00)00036-4

15. Gazzilli M, Albano D, Ardighieri L, Bertagna F, Giubbini R. Primary nasal-ethmoid choriocarcinoma detected by 18F-FDG PET/CT: a rare tumor with complete remission. *Nucl Med Rev Cent East Eur*. (2020) 23:105–7. doi: 10.5603/NMR.a2020.0012

16. Numnum TM, Leath CA, Straughn JM, Conner MG, Barnes MN. Occult choriocarcinoma discovered by positron emission tomography/computed tomography imaging following a successful pregnancy. *Gynecol Oncol*. (2005) 97:713–5. doi: 10.1016/j.ygyno.2005.01.049

17. Hebart H, Erley C, Kaskas B, Mayer R, König M, Einsele H, et al. Positron emission tomography helps to diagnose tumor emboli and residual disease in choriocarcinoma. *Ann Oncol*. (1996) 7:416–8. doi: 10.1093/oxfordjournals.annonc.a010611

18. Huang C-Y, Chen C-A, Hsieh C-Y, Cheng W-F. Intracerebral hemorrhage as initial presentation of gestational choriocarcinoma: a case report and literature review. *Int J Gynecol Cancer*. (2007) 17:1166–71. doi: 10.1111/j.1525-1438.2007.00934.x

19. Tripathi M, D'Souza MM, Jain J, Srivastava M, Jaimini A, Jain N, et al. Metastatic choriocarcinoma with tumor thrombus in the right atrium and pulmonary vessels: diagnosis and therapy monitoring with F-18 flurodeoxyglucose PET/CT. *Clin Nucl Med*. (2009) 34:381–5. doi: 10.1097/RLU.0b013e3181a3461f

20. Rao M, Chen Y, Zhu Y, Huang Z, Zhang L. Primary pancreatic choriocarcinoma revealed on FDG PET/CT. *Clin Nucl Med*. (2015) 40:76–8. doi: 10.1097/RLU.0000000000000584

21. Huang W, Qiu Y, Zhou Y, Yang Q, Kang L. Primary pancreatic Choriocarcinoma with hepatic metastases on 18 F-FDG PET/CT. *Clin Nucl Med*. (2023) 48:553–6. doi: 10.1097/RLU.0000000000004666

22. Trübenbach J, Pereira PL, Huppert PE, Farnsworth C, Mayer R, Feine U, et al. Primary choriocarcinoma of the pulmonary artery mimicking pulmonary embolism. *Br J Radiol*. (1997) 70:843–5. doi: 10.1259/bjr.70.836.9486052

23. Zhuang H, Yamamoto AJ, Ghesani N, Alavi A. Detection of choriocarcinoma in the lung by FDG positron emission tomography. *Clin Nucl Med*. (2001) 26:723. doi: 10.1097/00003072-200108000-00020

24. Cimarelli S, Deshayes E, Mognetti T, Biron P, Desuzinges C, Rivoire M, et al. F-18 FDG PET/CT imaging in a case of primary choriocarcinoma in the retroperitoneum. *Clin Nucl Med*. (2009) 34:449–51. doi: 10.1097/RLU.0b013e3181a7d0cd

25. Joshua AM, Carter JR, Beale P. The use of taxanes in choriocarcinoma; a case report and review of the literature. *Gynecol Oncol*. (2004) 94:581–3. doi: 10.1016/j.ygyno.2004.05.036

26. Sone T, Yoshikawa K, Fukunaga M. Pulmonary tumor embolism from choriocarcinoma: detection with F-18 FDG positron emission tomography. *Clin Nucl Med*. (2008) 33:773–4. doi: 10.1097/RLU.0b013e318187f0d7

27. Kidd D, Plant GT, Scaravilli F, McCartney AC, Stanford M, Graham EM. Metastatic choriocarcinoma presenting as multiple intracerebral haemorrhages: the role of imaging in the elucidation of the pathology. *J Neurol Neurosurg Psychiatry*. (1998) 65:939–41. doi: 10.1136/jnnp.65.6.939

28. Aleem J, Qureshi PAAA, Babar N, Sultan A, Rehman AU. Metastatic Choriocarcinoma of the breast: a rare entity. *Cureus*. (2022) 14:e22417. doi: 10.7759/cureus.22417

29. Goldfarb JA, Dinoi G, Mariani A, Langstraat CL. A case of multi-agent drug resistant choriocarcinoma treated with Pembrolizumab. *Gynecol Oncol Rep*. (2020) 32:100574. doi: 10.1016/j.gore.2020.100574

30. Du Y, Zhang X, Sun S, Sun M, Yang D, Yu X, et al. Case report: 18F-FDG PET/CT and laparoscopic nephron sparing surgery in the Management of Bleeding from Renal Metastases of Choriocarcinoma. *Front Oncol*. (2022) 12:829190. doi: 10.3389/fonc.2022.829190

31. Wang P, Ren D, Guo C, Ding X, Cao Y, Zhao P, et al. A rare case of pulmonary artery embolism with choriocarcinoma: a case report and literature review. *Oncol Lett*. (2023) 26:490. doi: 10.3892/ol.2023.14077

32. Sekine R, Hyodo M, Kojima M, Meguro Y, Suzuki A, Yokoyama T, et al. Primary hepatic choriocarcinoma in a 49-year-old man: report of a case. *World J Gastroenterol*. (2013) 19:9485–9. doi: 10.3748/wjg.v19.i48.9485

33. Sironi S, Picchio M, Mangili G, Garavaglia E, Zangheri B, Messa C, et al. [18F] fluorodeoxyglucose positron emission tomography as a useful indicator of metastatic gestational trophoblastic tumor: preliminary results in three patients. *Gynecol Oncol*. (2003) 91:226–30. doi: 10.1016/s0090-8258(03)00437-2

34. Gasparri R, Sedda G, Brambilla D, Girelli L, Diotti C, Spaggiari L. When a differential diagnosis is fundamental: Choriocarcinoma mimicking lung carcinoma. *J Clin Med*. (2019) 8:2018. doi: 10.3390/jcm8112018

35. Gvinianidze L, Panagiotopoulos N, Woo WL, Borg E, Lawrence D. The challenging management of lung choriocarcinoma. *J Thorac Dis*. (2014) 6:E220–2. doi: 10.3978/j.issn.2072-1439.2014.09.18

36. Snoj Z, Kocijancic I, Skof E. Primary pulmonary choriocarcinoma. *Radiol Iugoslavica*. (2017) 51:1–7. doi: 10.1515/raon-2016-0038

37. Göksel S, Akın S, Akdoğan RA, Rakıcı S, Abdioğlu GY, Ayvaz MA. 18F-FDG PET/CT imaging of metastatic testicular Choriocarcinoma mimicking gastric cancer which initial symptom is melena. *Mol Imaging Radionucl Ther*. (2021) 30:47–9. doi: 10.4274/mirt.galenos.2020.65668

38. Francischetti IMB, Cajigas A, Suhrland M, Farinhas JM, Khader S. Incidental primary mediastinal choriocarcinoma diagnosed by endobronchial ultrasound-guided fine needle aspiration in a patient presenting with transient ischemic attack and stroke. *Diagn Cytopathol*. (2017) 45:738–43. doi: 10.1002/dc.23719

39. Pakkala AK, Nekarakanti PK, Nagari B, Bansal AK, Shroff G, Uppin MS. Primary hepatic Choriocarcinoma with pregnancy: a diagnostic and therapeutic challenge. *Korean J Gastroenterol*. (2023) 81:91–4. doi: 10.4166/kjg.2022.116

40. Su H-M, Hu C, Wu C-S, Du W-N, Tsay D-G, Peng N-J. Poor FDG avidity in a case of metastatic pulmonary choriocarcinoma. *Clin Nucl Med*. (2011) 36:826–7. doi: 10.1097/RLU.0b013e31821a289e

41. Lee AJ, Im YJ, Shim S-H, Lee SJ, Kim TJ, So KA. Successful treatment of nongestational Choriocarcinoma in a 15-year-old girl: a case report. *J Pediatr Adolesc Gynecol*. (2021) 34:231–3. doi: 10.1016/j.jpag.2020.11.004

42. Lehmann M, Hosa H, Bartl T, Tsibulak I, Polterauer S, Pötsch N, et al. Combined chemotherapy and pembrolizumab salvages multi-chemotherapy agent and avelumab resistant choriocarcinoma: a case report. *Gynecol Oncol Rep*. (2023) 49:101259. doi: 10.1016/j.gore.2023.101259

43. Usta TA, Karacan T, Ozyurek E, Naki MM, Omeroglu SN, Demirkiran F. Primary renal artery choriocarcinoma causing secondary renovascular hypertension. *Int J Surg Case Rep*. (2014) 5:1197–9. doi: 10.1016/j.ijscr.2014.11.056

44. Clair KH, Gallegos N, Bristow RE. Successful treatment of metastatic refractory gestational choriocarcinoma with pembrolizumab: a case for immune checkpoint salvage therapy in trophoblastic tumors. *Gynecol Oncol Rep*. (2020) 34:100625. doi: 10.1016/j.gore.2020.100625

45. Logan D, Apurvi P, Mittun P, Alexander J T, Richard T. *Infantile choriocarcinoma with cutaneous, liver, and lung metastases*. Available at: https://appliedradiology.com/articles/infantile-choriocarcinoma-with-cutaneous-liver-and-lung-metastases (Accessed December 4, 2023).

46. Shaw S-W, Wang C-W, Ma S-Y, Ng K-K, Chang T-C. Exclusion of lung metastases in placental site trophoblastic tumor using [18F] fluorodeoxyglucose positron emission tomography: a case report. *Gynecol Oncol*. (2005) 99:239–42. doi: 10.1016/j.ygyno.2005.06.037

47. Hyun K, Jeon HW, Kim KS, Choi KB, Park JK, Park HJ, et al. Bullae-forming pulmonary metastasis from Choriocarcinoma presenting as pneumothorax. *Korean J Thorac Cardiovasc Surg*. (2015) 48:435–8. doi: 10.5090/kjtcs.2015.48.6.435

48. Pessanha I, Heitor F, Furtado E, Campos AP, Gonçalves I. Long-term survival after choriocarcinoma transmitted by liver graft: a successful report in pediatric transplantation. *Pediatr Transplant*. (2022) 26:e14135. doi: 10.1111/petr.14135

49. Chen Y, Liu L, Zheng W, Zhang X. Successful treatment of choriocarcinoma with multiple organ metastases after term delivery: a case report. *Int J Clin Exp*. (2017) 10:5468–74.

50. Kohler A, Welsch T, Sturm A-K, Baretton GB, Reissfelder C, Weitz J, et al. Primary choriocarcinoma of the liver: a rare, but important differential diagnosis of liver lesions. *J Surg Case Rep*. (2018) 2018, 2018:rjy 068. doi: 10.1093/jscr/rjy068

51. Dlewati MM, Gonzalez T, Razi SS, Hussain SF, Bennett J. Primary pulmonary Choriocarcinoma treated with neoadjuvant chemotherapy and lobectomy: a case report. *Cureus*. (2022) 14:e21931. doi: 10.7759/cureus.21931

52. Dasgupta S, Mohapatra D. Histological conversion of seminoma of testis to metastatic choriocarcinoma in left cervical lymph node: an unusual phenomenon. *J Dr. NTR Univ Health Sciences*. (2021) 10:200–4. doi: 10.4103/jdrntruhs.jdrntruhs_18_21

53. Huang K-G, Abdullah NA, Adlan A-S, Ueng S-H, Ho T-Y, Lee C-L. Successful surgical treatment of recurrent choriocarcinoma with laparoscopic resection of intraperitoneal pelvic tumor. *Taiwan J Obstet Gynecol*. (2013) 52:290–3. doi: 10.1016/j.tjog.2013.04.027

54. Chatterjee T, Martial A, Settypalli S, Lindahl L. A rare case of combined Choriocarcinoma and placental site trophoblastic tumor presenting as skin lesion: a case report. *Am J Case Rep*. (2022) 23:e936451. doi: 10.12659/AJCR.936451

55. Zhou Q, Zhou Y, Ouyang Y, Chen W, Zhou X. Hepatoid adenocarcinoma of the stomach with metastatic choriocarcinoma of the liver: a case report of a rare subtype of gastric cancer with a complex treatment course. *Front Surg*. (2022) 9:968891. doi: 10.3389/fsurg.2022.968891

56. Matsuo S, Tomita E, Fukuhara K, Kasuda S, Suzuki K, Tsukamoto Y. Metastatic gestational choriocarcinoma in lung incidentally found by hemoptysis and confirmed by DNA genotyping, highly suggesting the index antecedent pregnancy of a girl. *Human Pathology: Case Reports*. (2019) 18:200345. doi: 10.1016/j.ehpc.2019.200345

57. Røge R, Simonsen C, Petersen AC. Primary mediastinal Choriocarcinoma in an elderly patient with concurrent Goserelin-treated prostate adenocarcinoma. *Case Rep Pathol*. (2019) 2019:1–3. doi: 10.1155/2019/2734815

58. Kazemi NY, Langstraat C, John WS. Non-gestational choriocarcinoma with hyperprogression on pembrolizumab: a case report and review of the literature. *Gynecol Oncol Rep*. (2022) 39:100923. doi: 10.1016/j.gore.2022.100923

59. Pan W, Hou J. Pembrolizumab for treatment of a male with primary mediastinal choriocarcinoma: a case report. *Transl Cancer Res*. (2022) 11:3416–20. doi: 10.21037/tcr-22-766

60. Kamata S, Sakurada A, Sato N, Noda M, Okada Y. A case of primary pulmonary choriocarcinoma successfully treated by surgery. *Gen Thorac Cardiovasc Surg*. (2017) 65:361–4. doi: 10.1007/s11748-016-0666-8

61. Iijima Y, Akiyama H, Nakajima Y, Kinoshita H, Mikami I, Uramoto H, et al. Solitary lung metastasis from gestational choriocarcinoma resected six years after hydatidiform mole: a case report. *Int J Surg Case Rep*. (2016) 28:231–3. doi: 10.1016/j.ijscr.2016.09.048

62. Hirotsu A, Hiramatsu Y, Kawata S, Matsumoto T, Ozaki Y, Kikuchi H, et al. Rapid recurrence of primary gastric choriocarcinoma after complete resection. *Int J Surg Case Rep*. (2019) 57:138–41. doi: 10.1016/j.ijscr.2019.03.045

63. Rehman T, Hameed A, Beharry N, Du Parcq J, Bano G. An unusual cause of gynaecomastia in a male. *Endocrinol Diabetes Metab Case Rep*. (2019) 2019:19–0060. doi: 10.1530/EDM-19-0060

64. Guo N, Yin R, Li Q, Song L, Wang D. Postmenopausal choriocarcinoma: a rare case report and review of the literature. *Menopause*. (2018) 25:239–41. doi: 10.1097/GME.0000000000000968

65. Richie JP. Re: a meta-analysis of the risk of boys with isolated cryptorchidism developing testicular cancer in later life. *J Urol*. (2013) 190:1045. doi: 10.1016/j.juro.2013.05.078

66. Zhang P, Wang Y, Xiong L. Gastrointestinal bleeding caused by metastatic testicular choriocarcinoma: a case report and literature review. *World J Surg Oncol*. (2022) 20:205. doi: 10.1186/s12957-022-02670-7

67. Smith ZL, Werntz RP, Eggener SE. Testicular cancer: epidemiology, diagnosis, and management. *Med Clin North Am*. (2018) 102:251–64. doi: 10.1016/j.mcna.2017.10.003

68. Ma Y, Wang C, Sun P-L, Zhu Y, Huang Z-K, Jin S-X. A case of male primary pulmonary Choriocarcinoma. *Chin Med J*. (2018) 131:3001–3. doi: 10.4103/0366-6999.247205

69. Marka A, Hoyt BS, LeBlanc RE. Cutaneous metastasis of Choriocarcinoma in 2 male patients: a rare presentation of an aggressive malignancy that Dermatopathologists must recognize. *Am J Dermatopathol*. (2019) 41:50–4. doi: 10.1097/DAD.0000000000001209

70. Berkowitz RS, Goldstein DP. Current management of gestational trophoblastic diseases. *Gynecol Oncol*. (2009) 112:654–62. doi: 10.1016/j.ygyno.2008.09.005

71. Shabani S, Pritchard N, Padhya TA, Mifsud M. Head and neck cutaneous metastasis of testicular choriocarcinoma. *BMJ Case Rep*. (2020) 13:e233337. doi: 10.1136/bcr-2019-233337

72. Chen X, Xu L, Chen X, Teng X, Zheng S. Testicular choriocarcinoma metastatic to skin and multiple organs. Two case reports and review of literature. *J Cutan Pathol*. (2010) 37:486–90. doi: 10.1111/j.1600-0560.2009.01296.x

73. Zhang J, Wang Z-J, Yang B, Wei Y-Y, Yang L, Hu Y, et al. Biochemical remission by chemoradiotherapy in male mediastinal choriocarcinoma with diffuse lung metastasis: a case report. *Oncol Lett*. (2016) 11:2615–8. doi: 10.3892/ol.2016.4248

74. Fine G, Smith RW, Pachter MR. Primary extragenital choriocarcinoma in the male subject. Case report and review of the literature. *Am J Med*. (1962) 32:776–94. doi: 10.1016/0002-9343(62)90167-5

75. Deshpande JR, Kinare SG. Choriocarcinomatous transformation in metastases of an anaplastic lung carcinoma--a case report. *Indian J Cancer*. (1987) 24:161–6.

76. Liu X, Zhang X, Pang Y, Ma Y, Zhang X, Liu P. Clinicopathological factors and prognosis analysis of 39 cases of non-gestational ovarian choriocarcinoma. *Arch Gynecol Obstet*. (2020) 301:901–12. doi: 10.1007/s00404-020-05502-9

77. Nishino K, Yamamoto E, Ikeda Y, Niimi K, Yamamoto T, Kajiyama H. A poor prognostic metastatic nongestational choriocarcinoma of the ovary: a case report and the literature review. *J Ovarian Res*. (2021) 14:56. doi: 10.1186/s13048-021-00810-3

78. Wang Q, Guo C, Zou L, Wang Y, Song X, Ma Y, et al. Clinicopathological analysis of non-gestational ovarian choriocarcinoma: report of two cases and review of the literature. *Oncol Lett*. (2016) 11:2599–604. doi: 10.3892/ol.2016.4257

79. Han SN, Amant F, Leunen K, Devi UK, Neven P, Vergote I. EP-EMA regimen (etoposide and cisplatin with etoposide, methotrexate, and dactinomycin) in a series of 18 women with gestational trophoblastic neoplasia. *Int J Gynecol Cancer*. (2012) 22:875–80. doi: 10.1097/IGC.0b013e31824d834d

80. Stichelbout M, Devisme L, Franquet-Ansart H, Massardier J, Vinatier D, Renaud F, et al. SALL4 expression in gestational trophoblastic tumors: a useful tool to distinguish choriocarcinoma from placental site trophoblastic tumor and epithelioid trophoblastic tumor. *Hum Pathol*. (2016) 54:121–6. doi: 10.1016/j.humpath.2016.03.012

81. Hui P. Gestational trophoblastic Tumors: a timely review of diagnostic pathology. *Arch Pathol Lab Med*. (2019) 143:65–74. doi: 10.5858/arpa.2018-0234-RA

82. Sha L, Ma Y, Zheng Y, Zhao X. Imaging manifestations of primary retroperitoneal choriocarcinoma in a male. *Asian J Surg*. (2023) 46:1500–1. doi: 10.1016/j.asjsur.2022.09.071

83. Chang TC, Yen TC, Li YT, Wu YC, Chang YC, Ng KK, et al. The role of 18F-fluorodeoxyglucose positron emission tomography in gestational trophoblastic tumours: a pilot study. *Eur J Nucl Med Mol Imaging*. (2006) 33:156–63. doi: 10.1007/s00259-005-1873-1

84. Inaba H, Kawasaki H, Hamazaki M, Okugawa T, Uchida K, Honzumi M, et al. A case of metastatic ovarian non-gestational choriocarcinoma: successful treatment with conservative type surgery and myeloablative chemotherapy. *Pediatr Int*. (2000) 42:383–5. doi: 10.1046/j.1442-200x.2000.01236.x

85. Winter CC, Trepashko DW. Rare solitary metastasis to subcutaneous tissue from choriocarcinoma of testis. *Urology*. (1989) 33:320–1. doi: 10.1016/0090-4295(89)90276-8

86. Yokoi K, Tanaka N, Furukawa K, Ishikawa N, Seya T, Horiba K, et al. Male choriocarcinoma with metastasis to the jejunum: a case report and review of the literature. *J Nippon Med Sch*. (2008) 75:116–21. doi: 10.1272/jnms.75.116

87. Ji YS, Park SH. Clinical experience of male primary Choriocarcinoma at the Samsung medical Center. *Cancer Res Treat*. (2021) 53:874–80. doi: 10.4143/crt.2020.1066

88. Lu W-G, Ye F, Shen Y-M, Fu Y-F, Chen H-Z, Wan X-Y, et al. EMA-CO chemotherapy for high-risk gestational trophoblastic neoplasia: a clinical analysis of 54 patients. *Int J Gynecol Cancer*. (2008) 18:357–62. doi: 10.1111/j.1525-1438.2007.00999.x

89. Amikura T, Aoki Y, Banzai C, Yokoo T, Nishikawa N, Sekine M, et al. Metastatic choriocarcinoma successfully treated with paclitaxel and carboplatin after interstitial lung disease induced by EMA-CO. *Gynecol Oncol*. (2006) 102:573–5. doi: 10.1016/j.ygyno.2006.02.031

90. Zhao J, Lv WG, Feng FZ, Wan XR, Liu JH, Yi XF, et al. Placental site trophoblastic tumor: a review of 108 cases and their implications for prognosis and treatment. *Gynecol Oncol*. (2016) 142:102–8. doi: 10.1016/j.ygyno.2016.05.006

91. Belliveau RE, Wiernik PH, Sickles EA. Blood carcinoembryonic antigen, Regan isoenzyme, and human chorionic gonadotrophin in a man with primary mediastinal choriocarcinoma. *Lancet*. (1973) 1:22–4. doi: 10.1016/s0140-6736(73)91227-0

92. Ghorani E, Kaur B, Fisher RA, Short D, Joneborg U, Carlson JW, et al. Pembrolizumab is effective for drug-resistant gestational trophoblastic neoplasia. *Lancet*. (2017) 390:2343–5. doi: 10.1016/S0140-6736(17)32894-5

93. Veras E, Kurman RJ, Wang T-L, Shih I-M. PD-L1 expression in human placentas and gestational trophoblastic diseases. *Int J Gynecol Pathol*. (2017) 36:146–53. doi: 10.1097/PGP.0000000000000305

94. Huang M, Pinto A, Castillo RP, Slomovitz BM. Complete serologic response to Pembrolizumab in a woman with Chemoresistant metastatic Choriocarcinoma. *J Clin Oncol*. (2017) 35:3172–4. doi: 10.1200/JCO.2017.74.4052

95. Adra N, Einhorn LH, Althouse SK, Ammakkanavar NR, Musapatika D, Albany C, et al. Phase II trial of pembrolizumab in patients with platinum refractory germ-cell tumors: a Hoosier cancer research network study GU14-206. *Ann Oncol*. (2018) 29:209–14. doi: 10.1093/annonc/mdx680

frontiers | Frontiers in Medicine

TYPE Case Report
PUBLISHED 20 March 2024
DOI 10.3389/fmed.2024.1346647

OPEN ACCESS

EDITED BY
Ramin Sadeghi,
Mashhad University of Medical Sciences, Iran

REVIEWED BY
Damodara Naidu Kommi,
University of Virginia, United States
Yi Yi,
Longyan First Hospital Affiliated to Fujian Medical University, China
Aziz Gültekin,
Pamukkale University, Türkiye

*CORRESPONDENCE
Jiong Cai
jiong_cai@163.com

†These authors have contributed equally to this work

RECEIVED 29 November 2023
ACCEPTED 05 March 2024
PUBLISHED 20 March 2024

CITATION
Li X, Hu X, Wang P and Cai J (2024) ^{18}F-FDG PET/CT revealed sporadic schwannomatosis involving the lumbar spinal canal and both lower limbs: a case report.
Front. Med. 11:1346647.
doi: 10.3389/fmed.2024.1346647

^{18}F-FDG PET/CT revealed sporadic schwannomatosis involving the lumbar spinal canal and both lower limbs: a case report

Xiaotian Li[1,2†], Xianwen Hu[1†], Pan Wang[1] and Jiong Cai[1*]

[1]Department of Nuclear Medicine, Affiliated Hospital of Zunyi Medical University, Zunyi, China, [2]Department of Nuclear Medicine, People's Hospital of Qianxinan Buyi and Miao Minority Autonomous Prefecture, Xingyi, China

Schwannomatosis is a rare autosomal dominant hereditary syndrome disease characterized by multiple schwannomas throughout the body, without bilateral vestibular schwannoma or dermal schwannoma. The most common location of schwannomatosis is the head and neck, as well as the limbs, while multiple schwannomas in the lumbosacral canal and lower extremities are relatively rare. In this study, we report a 79-year-old woman diagnosed with schwannomatosis. MRI and contrast-enhanced imaging revealed multiple schwannomas in both lower extremities. An ^{18}F-FDG PET/CT examination revealed that in addition to multiple tumors with increased ^{18}F-FDG uptake in both lower extremities, there was also an increased ^{18}F-FDG uptake in a mass in the lumbosacral canal. These masses were confirmed to be schwannomas by pathology after surgery or biopsy. ^{18}F-FDG PET/CT findings of schwannomas were correlated with MRI and pathological components. Antoni A area rich in tumor cells showed significant enhancement on contrast-enhanced T1WI, and PET/CT showed increased uptake of ^{18}F-FDG in the corresponding area, while Antoni B region rich in mucus showed low enhancement on contrast-enhanced T1WI, accompanied by a mildly increased ^{18}F-FDG uptake.

KEYWORDS

schwannomatosis, ^{18}F-FDG, PET/CT, neurofibromatosis, schwannoma

Introduction

Schwannomatosis is a very rare disease with an incidence of 0.58 cases per 1 million people per year (1, 2), which was officially named in 1973 by Niimura (3). In 1997, the National Institutes of Health classified schwannomatosis as the third subtype of neurofibromatosis, namely NF3 (4, 5). It differs from types 1 and 2 neurofibromatosis in genetics, pathology, and clinical features, but due to insufficient understanding of the disease, it is often misdiagnosed clinically as one of the two subtypes (6). NF1 is mainly characterized by multiple café-au-lait spots on the skin, retinal iris patches, subcutaneous, or fascicular neurofibromas, and its occurrence is related to the loss of the NF1 tumor suppressor gene mutation (7, 8). NF2 is mainly characterized by bilateral vestibular schwannomas and can be accompanied by cataracts and tumors in other parts such as the brain, spinal cord, and periphery, and its occurrence is mainly caused by germline or somatic mutations and deletions of the NF2 gene

(9, 10). Schwannomatosis (NF3) is characterized by having multiple schwannomas throughout the body without bilateral vestibular schwannomas or dermal schwannomas, and according to whether the tumors have a genetic basis, which can be divided into sporadic and familial forms (11). Among them, familial cases account for 13–25% of schwannomatosis, most of which are characterized by multiple peripheral nerve or spinal nerve root schwannomas (2, 12). Sporadic cases account for the majority of schwannomatosis, and there is no familial clustering or genetic susceptibility (13). In this study, we report a rare sporadic case of schwannomatosis with pathologic and genetic diagnostic support. The aim is to share our experience in the clinical diagnosis and treatment of schwannomatosis to better understand the rare entity of sporadic schwannomatosis.

Case description

A 79-year-old woman presented with painless masses on both lower limbs in May 2012. In the past 3 months, the patient found that some of these lumps were gradually increasing, and she came to the Affiliated Hospital of Zunyi Medical University for medical help in May 2021. Both the patient and her family had no history of cancer or genetic diseases. Physical examination found multiple soft tissue masses approximately 1 cm above the skin surface in both lower limbs, no ulceration or purulent secretions, and no positive signs in other parts of the body. Laboratory tests and serum tumor markers were all within the normal reference range upon admission. Low-limb magnetic resonance imaging (MRI) showed fusiform low-signal soft tissue swelling at the proximal and distal ends of the right tibia subcutaneously, with clear boundaries and significant enhancement after the injection of contrast agent, showing increased signals in lower limb lesions (Figure 1). Subsequently, the patient underwent fluorine-18-fluorodeoxyglucose positron emission tomography/computed tomography (^{18}F-FDG PET/CT) to evaluate the systemic condition. The results showed that multiple ^{18}F-FDG uptake nodules increased in the first lumbar vertebra, the lateral side of the right ischial tuberosity, the upper part of the thigh, the lower part of the left thigh, and the right calf (Figure 2). Moreover, additional multiple high-metabolic non-specific lymph nodes were observed in the mediastinum. Subsequently, the patient underwent bilateral resection of the lower extremity tumor and an intraspinal tumor biopsy at the level of the first lumbar spine under anesthesia. The histopathological results showed that these tumors had the same pathological properties and were all schwannomas (Figure 3). Genetic testing indicated that the patient had an SMARCB1 gene mutation in the blood. The patient received anti-inflammatory treatment for 7 days postoperatively and was discharged with a good general condition. Up to now, the patient has been followed up for 30 months, and there are no signs of tumor recurrence in the surgical area of both lower limb tumors, nor have any nerve compression symptoms such as numbness or pain in either lower limb been found.

Discussion

Schwannomatosis is rare clinically and can occur in any age group, with the most common occurrence being between 30 and 60 years old, without significant differences in incidence rates between male and female patients (14, 15). Its characteristic feature is multiple schwannomas throughout the body without bilateral vestibular schwannomas or cutaneous neurofibromas, which belong to autosomal incomplete penetrance inheritance disease (16). The mechanism of this disease has not been thoroughly studied yet and may be related to abnormal expression of gene mutations. According to literature records, the abnormal expression of genes such as SMARCB1 (INI1), the LZTR1 gene, and the NF2 gene has been reported more frequently as possible causes of neurofibromatosis patients' onset, among which the SMARCB1 gene is considered the susceptibility gene for neurofibromatosis (17, 18). The clinical manifestations of this disease are atypical. Symptoms of nerve compression vary depending on the location of the tumor, with neuropathic pain resulting from compression of adjacent tissues being the primary symptom. The patient we reported was a 79-year-old woman, whose primary clinical symptoms were multiple painless masses in her lower limbs that had been present for years. There are slight differences in the age of onset and clinical symptoms compared to those reported for schwannomatosis in the literature.

Schwannoma is a tumor composed of mixed Schwann cells, perineurial-like cells, and fibroblasts, with scattered nerve fibers, linear collagen bands, and mucoid matrix (19). It is mostly round or

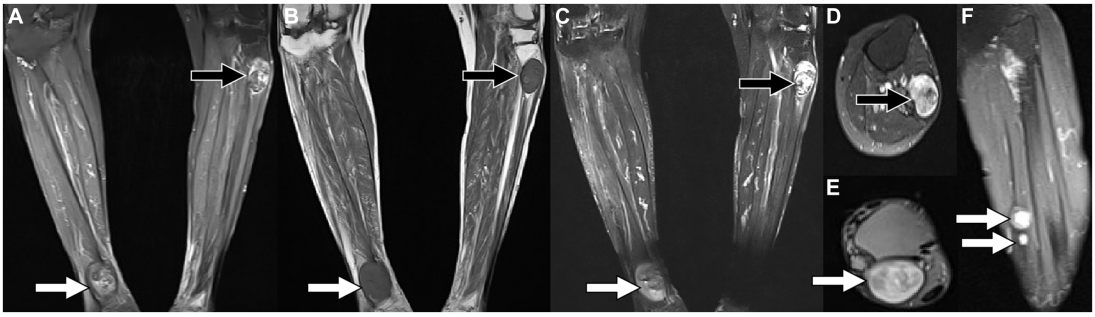

FIGURE 1
Magnetic resonance imaging [MRI; **(A)** T_2-weighted imaging (T_2WI); **(B)** T_1-weighted imaging (T_2WI)] reveals that there are fusiform soft tissue masses with low signal on T_1WI and high signal on T_2WI under the skin of the proximal tibia on the left and the distal tibia on the right, of which boundaries are clear. Contrast-enhanced T1WI sequence scan after contrast agent injection [**(C)** Coronal; **(D,E)** Axial; **(F)** Sagittal view shows small nodules of markedly enhanced soft tissue in the middle of the left calf (arrows)] revealed significant enhancement in both lower extremity lesions.

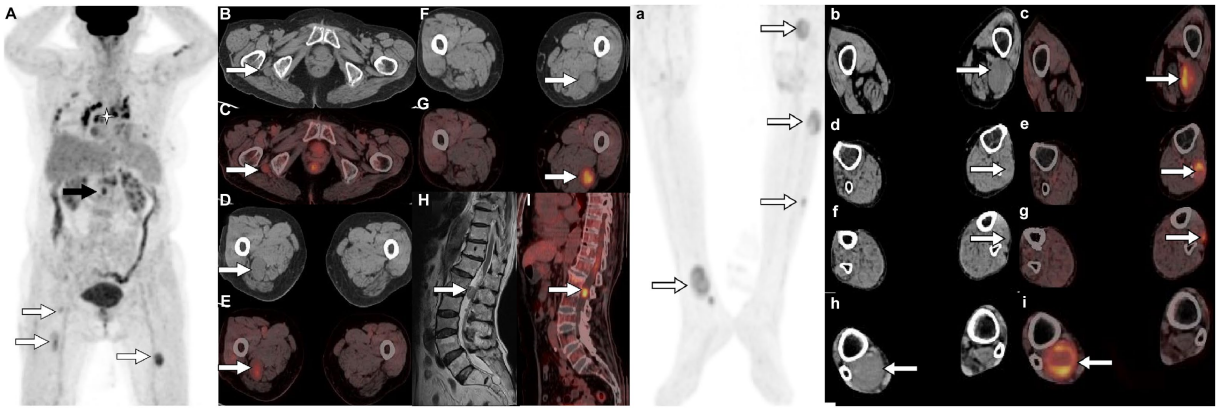

FIGURE 2
^{18}F-FDG PET/CT [**(A,a)** Maximum intensity projection (MIP)] was subsequently performed to further evaluate the patient's whole-body condition and revealed multiple nodules of hypermetabolic uptake in the lumbar spinal canal (black arrow) and lower limbs (white arrows). Besides, multiple high metabolic nonspecific lymph node uptakes were observed in the mediastinum (asterisk arrow). Tomographic images show multiple soft tissue density nodules with high FDG uptake on the lateral side of the right ischial tuberosity [**(B)** CT; **(C)** PET/CT fusion; arrows], upper thigh [**(D)** CT; **(E)** PET/CT fusion; arrows], middle [**(F)** CT; **(G)** PET/CT fusion; arrows] and lower left thigh [**(b)** CT; **(c)** PET/CT fusion; arrows], upper [**(d)** CT; **(e)** PET/CT fusion; arrows] and middle leg [**(f)** CT; **(g)** PET/CT fusion; arrows; SUVmax 7.5], and lower right leg [**(h)** CT; **(i)** PET/CT fusion; arrows]. In addition, isomuscular signal on T1WI (**H**, arrow) and high metabolic uptake nodule on PET/CT (**I**, arrow) were also observed in the posterior spinal canal of the first lumbar spine.

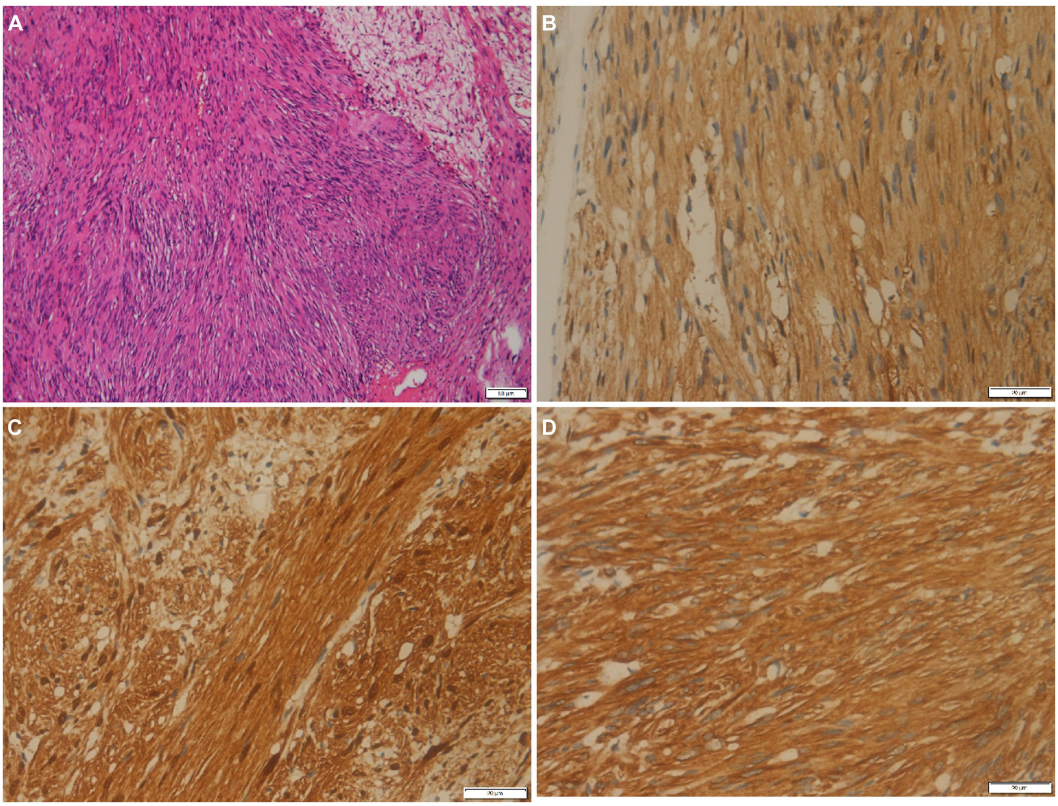

FIGURE 3
(A) Histological examination shows tumor cells are spindle-shaped, bundle-shaped, and focal fence-shaped (hematoxylin–eosin stain, original magnification ×100). Immunohistochemistry shows that tumor cells positively express PGP9.5 **(B)**, S100 **(C)**, and vimentin **(D)**.

lobulated, well-defined, encapsulated, of moderate hardness or elasticity, without fluctuation, and when the larger tumor appears to have mucoid degeneration, a puncture can draw out non-coagulating bloody fluid (20). Microscopically, schwannomas show spindle-shaped tumor cells arranged in two phases: some cells are closely adjacent to nuclear palisade-like arrangements (with Verocay bodies

in the Antoni A area), while other areas only see loose aggregation of cells on a mucoid background (Antoni B area) (21, 22). The lesion often exhibits prominent thick-walled blood vessels, along with frequent occurrences of mucoid degeneration, hemorrhage, and calcification within the tumor. Immunohistochemically, there was diffuse strong positive expression of S100 and SOX10 (23–25), focal positive expression of glial fibrillary acidic protein (GFAP) in some cases, focal keratin positivity in a few cases, while negative for melanocyte-specific markers HMB45 and melan-A (24, 26). The patient underwent bilateral lower limb tumor resection and intraspinal tumor biopsy at the level of the first lumbar spine, which microscopically showed that these tumors were composed of Antoni A areas rich in spindle cells and Antoni B areas rich in mucoid substance. Immunohistochemical results showed that PGP9.5, S100, and vimentin were all positive, consistent with the histopathological features of schwannoma.

The presentation of schwannomatosis frequently manifests as imaging features characteristic of schwannoma. The CT scan typically reveals a round or oval density with a well-defined boundary and a low-density shadow in some areas with cystic degeneration (27). The MRI findings of this condition are characterized by equal or low signals on T1WI and slightly high or high signals on T2WI (28, 29). Multifocal schwannoma in ^{18}F-FDG PET/CT is rarely described in the literature and occurs more frequently in the head and neck, spinal canal, and upper limb (30–33). The cases we reported were located in the pelvis, lower limb, and lumbar spinal canal, which are rarely reported in the literature. These tumors have a certain correlation between ^{18}F-FDG PET/CT and contrast-enhanced T1WI. The Antoni A region rich in tumor cells showed significant enhancement on contrast-enhanced T1WI, and the corresponding region presented increased ^{18}F-FDG uptake on PET/CT. While Antoni B areas rich in mucoid substances show low enhancement on contrast-enhanced T1WI, accompanied by mildly increased ^{18}F-FDG uptake. The comprehension of these findings is crucial for the exploration and elucidation of multifocal enhancements in ^{18}F-FDG activity within schwannomas. The ^{18}F-FDG uptake of schwannomas varies greatly with the components of the tumor. Moreover, our case showed that ^{18}F-FDG PET/CT can also accurately locate each tumor in schwannomatosis, and more hidden lesions can be found. In addition, the diagnosis of schwannomatosis should exclude the presence of vestibular schwannoma, requiring an MRI examination for confirmation.

According to the diagnostic criteria for schwannomatosis developed by Mac Collin et al. (34), which include: (1) A confirmed diagnosis is defined as (a) age over 30 years and presence of at least two non-cutaneous neurofibromas, with at least one confirmed by pathological examination; absence of vestibular schwannoma confirmed by high-resolution MRI, and no constitutive mutation in the NF2 gene. (b) A pathologically proven schwannoma or meningioma and a first-degree relative with schwannomatosis. (2) Possible diagnoses: (a) age below 30 years or above 45 years and two or more non-intradermal schwannomas confirmed by pathological examination as schwannoma, without abnormal symptoms of the eighth cranial nerve function, and without constitutive mutations in the NF2 gene. (b) Imaging confirms non-vestibular schwannoma and one first-degree relative meeting the diagnostic criteria. The diagnosis of segmental schwannomatosis requires meeting definite or possible schwannomatosis diagnostic criteria limited to one limb or five adjacent spinal segments. Based on these diagnostic criteria, the patient we reported is consistent with the diagnosis of schwannomatosis.

The clinical manifestations and signs of this disease are very similar to NF1 and NF2, and consequently, they need to be distinguished from them. NF1 is characterized by coffee-au-Lait plaques, subcutaneous nodules, and Lisch nodules, while NF2 is characterized by bilateral vestibular schwannomas, which can be differentiated from schwannomatosis (35). High-resolution MRI (internal auditory canal thickness below 3 mm) confirmed the absence of bilateral vestibular schwannomas in the patient, so we highly suspected the diagnosis of schwannomatosis. Schwannomatosis is generally easier to distinguish from NF1 and simple NF2, but it is difficult to differentiate from mosaic NF2. Therefore, additional genetic testing was conducted on the excised tumors, revealing a mutation in the SMARCB1 (blood) gene, which validated our diagnosis.

The SMARCB1 gene (also known as INI1) is a tumor suppressor gene, whose mutation is associated with neurofibromatosis type 2 and schwannomatosis (36). The SMARCB1 gene is located at 22q11.23 and contains nine exons that encode the SMARCB1 protein, which has a tumor-suppressive function (37). Currently, more commonly reported genes that may lead to the development of schwannomatosis include the SMARCB1 (INI1) gene (38), the LZTR1 gene (39), and the NF2 gene (40). Among them, the SMARCB1 gene was first reported by scholars to be a susceptibility gene for schwannomatosis (5), and it was found that mutations in the SMARCB1 gene play a more prominent role in the pathogenesis of schwannomatosis (2). Moreover, many scholars believe that germline mutations in the SMARCB1 gene leading to abnormalities in the structure and functional expression of the protein may be the main cause of the development of schwannomatosis (41). Current studies show that mutations in this gene occur in 8–10% of sporadic schwannomatosis patients and 40–50% of familial schwannomatosis patients (11, 42).

The main treatment for schwannomatosis is surgical resection (43, 44). However, not all schwannomas necessitate surgery; it is typically reserved for patients with symptoms such as bleeding, pain, neurological dysfunction, and a tendency to malignant transformation (45–47). The main problem facing neurosurgeons today is to achieve complete tumor resection and prevent recurrence while maximizing the protection of neurological function under the premise of protecting nerve function (47). The surgical treatment of schwannomas depends on the size, location, and complexity of the tumor and should comprehensively consider the individual situation of the patient and implement the most appropriate personalized surgical plan for the patient. The majority of schwannomatosis cases are benign, thus indicating a favorable prognosis. Due to the small volume of the tumor in our patient's lumbar spinal canal and the absence of corresponding clinical manifestations, further resection of the tumor in the lumbar spinal canal was not performed following bilateral lower limb tumor resection and lumbar spinal canal tumor puncture biopsy. The patient has a good prognosis, and no disease progression was observed during the follow-up period.

Conclusion

^{18}F-FDG PET/CT contributes to the accurate localization of schwannomatosis and has certain imaging characteristics; namely, the Antoni A area rich in tumor cells showed increased uptake of ^{18}F-FDG, while the Antoni B region rich in mucus only showed a mildly increased ^{18}F-FDG uptake.

Data availability statement

The original contributions presented in the study are included in the article/supplementary material, further inquiries can be directed to the corresponding author.

Ethics statement

Written informed consent was obtained from the individual(s) for the publication of any potentially identifiable images or data included in this article.

Author contributions

XL: Writing – original draft, Resources, Methodology, Investigation, Project administration. XH: Formal analysis, Data curation, Conceptualization, Writing – original draft, Resources, Methodology. PW: Writing – review & editing, Visualization, Validation, Supervision, Software. JC: Project administration, Data curation, Conceptualization, Writing – review & editing, Visualization.

Funding

The author(s) declare that no financial support was received for the research, authorship, and/or publication of this article.

Conflict of interest

The authors declare that the research was conducted in the absence of any commercial or financial relationships that could be construed as a potential conflict of interest.

Publisher's note

All claims expressed in this article are solely those of the authors and do not necessarily represent those of their affiliated organizations, or those of the publisher, the editors and the reviewers. Any product that may be evaluated in this article, or claim that may be made by its manufacturer, is not guaranteed or endorsed by the publisher.

References

1. Wang C, Chai Y, Zhao X, Li Q, Chen C, Kong X (2021). A novel variant of SMARCB1 in rare familial Schwannomatosis identified by whole-exome sequencing and genotype-phenotype correlation analysis. Research Square [Preprint]. doi: 10.21203/rs.3.rs-1157679/v1

2. Schraepen C, Donkersloot P, Duyvendak W, Plazier M, Put E, Roosen G, et al. What to know about schwannomatosis: a literature review. *Br J Neurosurg*. (2022) 36:171–4. doi: 10.1080/02688697.2020.1836323

3. Loh J, Ong PY, Goh DLM, Puhaindran ME, Vellayappan BA, Ow SGW, et al. Clinical characteristics and genetic testing outcome of suspected hereditary peripheral nerve sheath tumours in a tertiary cancer institution in Singapore. *Heredit Cancer Clin Pract*. (2022) 20:23. doi: 10.1186/s13053-022-00230-4

4. Plotkin SR, Messiaen L, Legius E, Pancza P, Avery RA, Blakeley JO, et al. Updated diagnostic criteria and nomenclature for neurofibromatosis type 2 and schwannomatosis: an international consensus recommendation. *Genet Med*. (2022) 98:1967–77. doi: 10.1212/WNL.98.18_supplement.3996

5. Ding Y, Rong H, Wang Y, Liu T, Zhang J, Li S, et al. Detection of germline mutations of the SMARCB1 gene in a Chinese family with intraspinal schwannomatosis. *World Neurosurg*. (2019) 123:318–22. doi: 10.1016/j.wneu.2018.11.254

6. Blakeley JO, Plotkin SR. Therapeutic advances for the tumors associated with neurofibromatosis type 1, type 2, and schwannomatosis. *Neuro-Oncology*. (2016) 18:624–38. doi: 10.1093/neuonc/nov200

7. Wang MX, Dillman JR, Guccione J, Habiba A, Maher M, Kamel S, et al. Neurofibromatosis from head to toe: what the radiologist needs to know. *Radiographics*. (2022) 42:1123–44. doi: 10.1148/rg.210235

8. Ferner RE. The neurofibromatoses and related disorders In: *Neurogenetics: A Guide for Clinicians*. Eds. A. Adil, T. Koritala, S. Munakomi and AK. Singh. A Guide for Clinicians: Cambridge University Press, Neurogenetics. *vol.* 18 (2012). 212.

9. Adil A, Koritala T, Munakomi S, Singh AK. Neurofibromatosis Type 1 In: *Stat Pearls*. Eds. A. Adil, T. Koritala, S. Munakomi and AK. Singh. Stat Pearls Publishing. (2023). Available at: http://www.ncbi.nlm.nih.gov/books/NBK459358.

10. Guarnizo A, Erripa JI, Rugilo C. A bicarotid trunk with associated right retroesophageal subclavian artery in a child with neurofibromatosis type 1 complicated by a left hemispheric stroke. *Surg Radiol Anat*. (2023) 45:1599–602. doi: 10.1007/s00276-023-03253-1

11. Tamura R. Current understanding of neurofibromatosis type 1, 2, and schwannomatosis. *Int J Mol Sci*. (2021) 22:5850. doi: 10.3390/ijms22115850

12. Stemmer-R-achamimov A, Wiestler O, Louis D. Neurofibromatosis type 2 In: *WHO Classification of Tumours of the Central Nervous System*. Eds. A. O. Stemmer-Rachamimov, O. D. Wiestler and D. N. Louis. Lyon: IARC (2007). 210–4.

13. Merker VL, Slobogean B, Jordan JT, Langmead S, Meterko M, Charns MP, et al. Understanding barriers to diagnosis in a rare, genetic disease: delays and errors in diagnosing schwannomatosis. *Am J Med Genet A*. (2022) 188:2672–83. doi: 10.1002/ajmg.a.62860

14. Chen S-L, Liu C, Liu B, Yi C-J, Wang Z-X, Rong Y-B, et al. Schwannomatosis: a new member of neurofibromatosis family. *Chin Med J*. (2013) 126:2656–60.

15. Merker VL, Esparza S, Smith MJ, Stemmer-Rachamimov A, Plotkin SR. Clinical features of schwannomatosis: a retrospective analysis of 87 patients. *Oncologist*. (2012) 17:1317–22. doi: 10.1634/theoncologist.2012-0162

16. Wimmer K, Kehrer-Sawatzki H, Legius E. Neurofibromatosis In: *Hereditary Tumors: From Genes to Clinical Consequences*. Eds. K. Wimmer, H. Kehrer-Sawatzki and E. Legius (2008). 127–45. doi: 10.1002/9783527627523.ch6

17. Fang J, Singh S, Cheng C, Natarajan S, Sheppard H, Abu-Zaid A, et al. Genome-wide mapping of cancer dependency genes and genetic modifiers of chemotherapy in high-risk hepatoblastoma. *Nat Commun*. (2023) 14:1–4003. doi: 10.1038/s41467-023-39717-6

18. Panteliadis CP, Benjamin R, Hagel C. *Neurocutaneous Disorders: A Clinical, Diagnostic and Therapeutic Approach*. Anshan Uk: Springer Nature (2022). 2010:239–284.

19. Mendoza PR, Grossniklaus HE. Pathology of the uveal tract: neoplasms In: *Albert and Jakobiec's Principles and Practice of Ophthalmology*. Eds. P. R. Mendoza and H. E. Grossniklaus. Springer: Springer International Publishing. (2022). 6223–90.

20. Wang L, Wang Q, Yang L, Ma C, Shi G. Computed tomographic imaging features to differentiate gastric schwannomas from gastrointestinal stromal tumours: a matched case–control study. *Sci Rep*. (2023) 13:1–17568. doi: 10.1038/s41598-023-43902-4

21. Fackelmayer OJ, Rodriguez ED, Sisk AE Jr, Livhits MJ. Adrenal schwannoma can be FDG-avid on PET/CT: case report and review of historic institutional pathology. *Diagn Pathol*. (2023) 18:1–112. doi: 10.1186/s13000-023-01399-5

22. Flucke UE, Hiemcke-Jiwa LS, Wesseling P (2023). *Unraveling Schwannomas*. US: Oxford University Press, Neuro-oncology, 25, 2237–2238. doi: 10.1093/neuonc/noad171

23. Doddrell RD, Dun X-P, Shivane A, Feltri ML, Wrabetz L, Wegner M, et al. Loss of SOX10 function contributes to the phenotype of human Merlin-null schwannoma cells. *Brain*. (2013) 136:549–63. doi: 10.1093/brain/aws353

24. Li Z, Niu Y. Malignant Melanotic nerve sheath tumor of the parotid gland: a case report and literature review. *Ear Nose Throat J*. (2023):014556132211458. doi: 10.1177/01455613221145803

25. Chen C, Cao J, Song L, Wang W, Guo D, Shi Q, et al. Primary lipoblastic nerve sheath tumor in an inguinal lymph node mimicking metastatic tumor: a case report and literature review. *Front Oncol*. (2023) 13:1258769. doi: 10.3389/fonc.2023.1258769

26. Li X-L, Dai S-D. Melanotic schwannoma: two cases of rare lesions. *Pathol Oncol Res*. (2019) 25:1667–70. doi: 10.1007/s12253-018-0417-5

27. Hu S, Chen Y, Wang Y, Chen KM, Song Q. Clinical and CT manifestation of pleural schwannoma. *Acta Radiol*. (2012) 53:1137–41. doi: 10.1258/ar.2012.120306

28. Ahmed A, Watanabe H, Aoki J, Shinozaki T, Takagishi K. Schwannoma of the extremities: the role of PET in preoperative planning. *Eur J Nucl Med*. (2001) 28:1541–51. doi: 10.1007/s002590100584

29. Lefebvre G, Le Corroller T. Ultrasound and MR imaging of peripheral nerve tumors: the state of the art. *Skeletal Radiol*. (2023) 52:405–19. doi: 10.1007/s00256-022-04087-5

30. Wippold FJ, Lubner M, Perrin R, Lämmle M, Perry A. Neuropathology for the neuroradiologist: Antoni a and Antoni B tissue patterns. *Am J Neuroradiol*. (2007) 28:1633–8. doi: 10.3174/ajnr.A0682

31. Miyake KK, Nakamoto Y, Kataoka TR, Ueshima C, Higashi T, Terashima T, et al. Clinical, morphologic, and pathologic features associated with increased FDG uptake in schwannoma. *Am J Roentgenol*. (2016) 207:1288–96. doi: 10.2214/AJR.15.14964

32. Knight D, Birch R, Pringle J. Benign solitary schwannomas: a review of 234 cases. *J Bone Joint Surg Am Br Volulmes*. (2007) 89:382–7. doi: 10.1302/0301-620X.89B3.18123

33. Wang S-y, Liu J-h, Yao S, Wang S-x, Shao D. PET/CT and contrast-enhanced CT imaging findings in benign solitary schwannomas. *Eur J Radiol*. (2021) 141:109820. doi: 10.1016/j.ejrad.2021.109820

34. Mac Collin M, Chiocca E, Evans D, Friedman J, Horvitz R, Jaramillo D, et al. Diagnostic criteria for schwannomatosis. *Neurology*. (2005) 64:1838–45. doi: 10.1212/01.WNL.0000163982.78900.AD

35. Smith MJ, Bowers NL, Bulman M, Gokhale C, Wallace AJ, King AT, et al. Revisiting neurofibromatosis type 2 diagnostic criteria to exclude LZTR1-related schwannomatosis. *Neurology*. (2017) 88:87–92. doi: 10.1212/WNL.0000000000003418

36. Cai C. *SWI/SNF Deficient Central Nervous System Neoplasms. Seminars in Diagnostic Pathology*. WB Saunders: Elsevier (2021). 38:167–174. doi: 10.1053/j.semdp.2021.03.003

37. Kalimuthu SN, Chetty R. Gene of the month: SMARCB1. *J Clin Pathol*. (2016) 69:484–9. doi: 10.1136/jclinpath-2016-203650

38. Sestini R, Bacci C, Provenzano A, Genuardi M, Papi L. Evidence of a four-hit mechanism involving SMARCB1 and NF2 in schwannomatosis-associated schwannomas. *Hum Mutat*. (2008) 29:227–31. doi: 10.1002/humu.20679

39. Piotrowski A, Xie J, Liu YF, Poplawski AB, Gomes AR, Madanecki P, et al. Germline loss-of-function mutations in LZTR1 predispose to an inherited disorder of multiple schwannomas. *Nat Genet*. (2014) 46:182–7. doi: 10.1038/ng.2855

40. Montgomery BK, Alimchandani M, Mehta GU, Dewan R, Nesvick CL, Miettinen M, et al. Tumors displaying hybrid schwannoma and neurofibroma features in patients with neurofibromatosis type 2. *Clin Neuropathol*. (2016) 35:78–83. doi: 10.5414/NP300895

41. Belakhoua SM, Rodriguez FJ. Diagnostic pathology of tumors of peripheral nerve. *Neurosurgery*. (2021) 88:443–56. doi: 10.1093/neuros/nyab021

42. Smith MJ, Wallace AJ, Bowers NL, Rustad CF, Woods CG, Leschziner GD, et al. Frequency of SMARCB1 mutations in familial and sporadic schwannomatosis. *Neurogenetics*. (2012) 13:141–5. doi: 10.1007/s10048-012-0319-8

43. Halliday J, Rutherford SA, McCabe MG, Evans DG. An update on the diagnosis and treatment of vestibular schwannoma. *Expert Rev Neurother*. (2018) 18:29–39. doi: 10.1080/14737175.2018.1399795

44. Dhamija R, Plotkin S, Asthagiri A, Messiaen L, Babovic-Vuksanovic D (2018). Schwannomatosis. Gene Reviews®.

45. Palmisciano P, Ferini G, Watanabe G, Conching A, Ogasawara C, Scalia G, et al. Surgical management of craniovertebral junction schwannomas: a systematic review. *Curr Oncol*. (2022) 29:4842–55. doi: 10.3390/curroncol29070384

46. Brooks DG. The neurofibromatoses: hereditary predisposition to multiple peripheral nerve tumors. Neurosurgery. *Clinics*. (2004) 15:145–55. doi: 10.1016/j.nec.2004.02.008

47. Tiel R, Kline D. Peripheral nerve tumors: surgical principles, approaches, and techniques. Neurosurgery. *Clinics*. (2004) 15:167. doi: 10.1016/j.nec.2004.02.003

frontiers | Frontiers in Medicine

TYPE Case Report
PUBLISHED 21 March 2024
DOI 10.3389/fmed.2024.1373773

OPEN ACCESS

EDITED BY
Carmelo Caldarella,
Fondazione Policlinico Universitario A. Gemelli IRCCS, Italy

REVIEWED BY
Andor W. J. M. Glaudemans,
University of Groningen, Netherlands
Priscilla Guglielmo,
Veneto Institute of Oncology (IRCCS), Italy

*CORRESPONDENCE
Lei Kang
✉ kanglei@bjmu.edu.cn

†These authors have contributed equally to this work

RECEIVED 20 January 2024
ACCEPTED 29 February 2024
PUBLISHED 21 March 2024

CITATION
Huang W, Zheng Z, Zhang Y, Qiu Y, Peng Y, Yang Q, Wang W and Kang L (2024) A rare case of primary cardiac diffuse large B-cell lymphoma imaged with ^{18}F-FDG PET/CT: a case report and literature review.
Front. Med. 11:1373773.
doi: 10.3389/fmed.2024.1373773

A rare case of primary cardiac diffuse large B-cell lymphoma imaged with ^{18}F-FDG PET/CT: a case report and literature review

Wenpeng Huang[1†], Zuohuan Zheng[2†], Yongbai Zhang[1], Yongkang Qiu[1], Yushuo Peng[1], Qi Yang[1], Wei Wang[3] and Lei Kang[1*]

[1]Department of Nuclear Medicine, Peking University First Hospital, Beijing, China, [2]Department of Traditional Chinese Medicine, The Seventh People's Hospital of Chongqing, Chongqing, China, [3]Department of Pathology, Peking University First Hospital, Beijing, China

Background: One of the exceptionally rare forms of non-Hodgkin's lymphoma (NHL) is primary cardiac lymphoma (PCL). The principal clinical manifestation in patients with PCL involves cardiac symptoms resulting from myocardial infiltration by lymphoma, including arrhythmias, heart failure, and chest pain. ^{18}F-FDG PET/CT serves as a reliable and indispensable imaging modality for assessing clinically staging NHL.

Case report: We present a rare case involving a 72-year-old woman diagnosed with primary intracardiac diffuse large B-cell lymphoma. For further staging, the patient underwent ^{18}F-FDG PET/CT, revealing multiple nodular soft tissue density lesions in the heart and pericardium exhibiting increased FDG metabolism (SUVmax = 12.1). The supradiaphragmatic and infradiaphragmatic segments of the inferior vena cava exhibited irregular morphology with localized nodular changes and increased FDG metabolism in the surrounding area (SUVmax = 9.7). Additionally, multiple enlarged lymph nodes were identified in the left axilla, mediastinum, and adjacent to the abdominal aorta, displaying heterogeneous FDG uptake with an SUVmax of 9.3, indicating lymphoma involvement. The above imaging findings suggested that the mass was a PCL. Hence, the patient underwent a combination of chemotherapy and immunotherapy using R-CDOP (rituximab, cyclophosphamide, liposomal doxorubicin, vincristine, and prednisone). Following two courses of treatment within a span of 2 months, there was a partial remission observed in the cardiac lymphoma and the enlarged lymph nodes.

Conclusion: The case elucidated in this report contributes to an enhanced understanding of the disease for clinicians, with ^{18}F-FDG PET/CT providing comprehensive insights into the extent of cardiac involvement, as well as the engagement of extracardiac organs and pathologic lymph nodes. The ^{18}F-FDG PET/CT examination not only visually delineates the lesion's location and extent but also serves as a cornerstone for clinical tumor staging, offering valuable support for treatment monitoring and subsequent follow-up.

KEYWORDS

malignant lymphoma, diffuse large B-cell lymphoma, primary cardiac lymphoma, computed tomography, ^{18}F-FDG PET/CT, case report

Introduction

Cardiac and pericardial involvement by malignant lymphoma constitutes approximately 1% of cardiac tumors and 0.5% of extra-nodal non-Hodgkin's lymphoma (NHL), representing a rare phenotype. Diffuse large B-cell lymphoma (DLBCL) is the most common type, but other cell types are also observed, such as T-cell lymphomas (1, 2). Epidemiological characteristics of primary cardiac lymphoma (PCL), according to a recent systematic review conducted in 2020, revealed a mean age of 62, a male preponderance, and a higher prevalence of cases in the Asian region followed by the European region (48% vs. 27%) (3).

One of the exceptionally rare forms of NHL is PCL. Defined by the WHO in 2015, PCL presents as a substantial lymphoma mass involving the heart and/or pericardium, with or without secondary lesions in other areas of the body. The incidence of PCL is a mere 0.056%, with only 10% identified as malignant, accounting for just 1% (4–6). While the right atrium and right ventricle are the most common sites of involvement, occurrences in the left ventricle have also been reported (4, 7). PCL exhibits a broad age range, primarily affecting the elderly and displaying a higher prevalence in men (8); it is more commonly observed in immunocompromised patients (9). The predominant symptoms are cardiac-related, contingent on the anatomical location within the heart. These include arrhythmias resulting from compressed cardiac conducting systems and manifestations of heart failure due to intra-cardiac blood flow obstruction. In some instances, PCL may even mimic myocardial ischemia or myocardial infarction (10). Petrich et al. (4) report constitutional symptoms, heart failure, and pericardial effusion as the most prevalent presenting symptoms and signs of PCL. Lymphoma-related symptoms, such as fever, night sweats, progressive weight loss, and other general systemic manifestations, are uncommon in PCL patients. Third-degree AV block constitutes an infrequent presentation of PCL. Complications may arise from mass effect, local invasion, or embolization (11).

The heart lacks lymphoid nodes, and PCL is believed to originate from the drainage of the epicardial lymph nodes (12). Although the pathogenesis of PCL remains elusive, it is potentially linked to recurrent infections and immune dysfunction, encompassing conditions like human immunodeficiency virus (HIV) infection, Epstein–Barr virus infection, congenital immunodeficiency, and allogeneic bone marrow and solid organ transplantation (2). Diagnosis hinges solely on histopathology and immunohistochemistry for precise identification, classification, and evaluation of proliferative activity (3, 5). Vogl et al. reported a successful CT-guided puncture of the cardiac tumor, enabling a prompt diagnosis of PCL and initiation of therapy without complications (13). Liquid cytology of cardiac or pleural effusion proves highly valuable. It's essential to note that pericardial effusion cannot be directly attributed to pericardial involvement due to a lack of specific details regarding effusion detection, as cardiac insufficiency may also contribute (3). While DLBCL is the most prevalent histopathology, documented cases include Burkitt lymphoma, T-cell lymphoma, and plasmablastic lymphoma (14). In our case, cytologic analysis of drained pericardial fluid revealed DLBCL, with immunohistochemical staining confirming positivity for CD5. Given the patient's comorbidities, including coronary artery disease and diabetes, no open chest biopsy was performed.

PCL is an extremely rare malignancy, constituting an oncologic emergency that proves fatal within a few months unless diagnosed and treated promptly (15). The principal clinical manifestation in patients with PCL involves cardiac symptoms resulting from myocardial infiltration by lymphoma, including arrhythmias, heart failure, and chest pain (4, 16). As of now, there is no specific biomarker for the early diagnosis of PCL. 2-Deoxy-2-[fluorine-18]-fluoro-D-glucose (^{18}F-FDG) positron emission tomography combined with computed tomography (PET/CT) serves as a reliable and indispensable imaging modality for assessing clinically staging of DLBCL. Despite the rarity of primary cardiac lymphoma, some reports detailing the findings of ^{18}F-FDG PET/CT imaging have been presented. Here, we present a rare case involving a 72-year-old woman diagnosed with primary intracardiac DLBCL, referred for ^{18}F-FDG PET/CT imaging for staging. According to the World Health Organization (WHO), PCL can be diagnosed if it meets one of the following criteria: (i) primary lymphoma of the heart or pericardium; (ii) lymphoma with the initial cardiac-related symptoms; and (iii) lymphoma dominated by a cardiac mass (17). However, in the early stages, its clinical manifestations do not significantly differ from ordinary chest and heart diseases, often leading to limited attention being paid to the disease when patients present with symptoms such as chest pain or dyspnea (18).

In our comprehensive literature search on the PubMed database spanning from 2009 to 2023, utilizing keywords related to diffuse large B-cell lymphoma and ^{18}F-FDG PET/CT, we identified a total of 20 available case reports. The summarized case reports are presented in Table 1.

Case presentation

A 72-year-old woman presented with chest tightness and breath-holding symptoms a month before seeking medical attention, aggravated by physical activity and hindering her ability to recline at night. The patient had a history of coronary artery disease and diabetes mellitus; however, she has no family history of genetic disorders or tumors. Acute coronary syndrome was initially ruled out. Laboratory tests revealed CK-MB level at 1.5 ng/mL (normal range: 0–5 ng/mL), high-sensitivity troponin I at 19.3 ng/L (normal range: 0–0.04 ng/mL), and natriuretic peptide at 127.00 pg./mL (normal range: 0–100 pg./mL). Blood gas analysis indicated hypoxemia. The patient initiated diuretic treatment with oral furosemide. However, her breath-holding symptoms intensified after 2 weeks, leading to her hospital admission. An electrophysiology study showed third-degree atrioventricular block. A chest CT scan disclosed an enlarged and dysmorphic heart, displaying multiple nodular and clumped slightly hypodense foci in the heart and pericardium, along with effusions in the pericardium and pleural cavity (Figures 1A,B). The diagnostic imaging physician suspected a malignant tumor of interlobar origin in the heart. Subsequent tumor marker panel analysis revealed elevated CA125 at 203 U/mL (normal range: 0–35 U/mL), CYFRA21-1 at 5.40 ng/mL (normal range: 0–3.3 ng/mL), and NSE at 17.75 ng/mL (normal range: 0–16.3 ng/mL). Cytologic examination of pericardial and pleural effusions exhibited microscopic cells characterized by large, deeply stained nuclei, scanty cytoplasm, moderate cellular anisotropy, visible small nucleoli, and distinct nuclear fission images and apoptosis (Figure 2A). Immunohistochemical staining demonstrated positive expression of CD5, CD10, CD20, MUM1, and

TABLE 1 ^{18}F-FDG PET/CT manifestations of primary cardiac lymphoma.

Case	References	Gender	Age	Clinical symptoms	Primary sites	Invasion and metastasis	Max diameter/cm	SUVmax	Management	Outcome
1	Venugopala et al. (5)	M	55 y	Fever	Pericardium, left ventricle, and right atrium	Superior mediastinum, and mediastinal, right cardio-phrenic, abdominal, bilateral inguinal, axillary, and cervical lymph nodes	4.7	NA	Chemotherapy	Alive at 2 mo
2	Thiagaraj et al. (7)	F	50 y	Abdominal pain, nausea, vomiting, and fever	Left ventricle	NA	4.5	10.7	Surgery + chemotherapy	Alive at 1 y
3	Alansari et al. (10)	M	81 y	Epigastric pain	Right atrium, right ventricle, and intra-pericardium	Lung and liver	4.5	NA	Chemotherapy	Alive at 6 mo
4	Lee et al. (11)	M	51 y	Syncope	Right atrium and right ventricle	NA	NA	NA	Chemotherapy	Alive at 7 mo
5	Imataki et al. (14)	M	62 y	Dyspnea	Right atrium	NA	8.3	NA	Surgery + chemotherapy	Alive
6	Kaida et al. (19)	F	80 y	Dyspnea	Right atrium	NA	NA	14.5	NA	NA
7	Qiang et al. (20)	M	71 y	Syncope, recurrent chest tightness, dyspnea, palpitations, and sweating	Left atrium and left ventricle	Mediastinum lymph nodes	6.7	28.7	Chemotherapy	Alive at 4 mo
8	Seval Erhamamcı et al. (21)	M	70 y	Dyspnea and weakness	Right atrium and auricula	Sternum	NA	26.6	Surgery + chemotherapy	Alive at 3 mo
9	Tong et al. (22)	F	80 y	Chest pain and breathlessness	Pericardium	Bone, peripheral nerves and mediastinal lymph node	NA	NA	Surgery + chemotherapy	Died at 3 mo
10	Chang et al. (23)	F	77 y	Chest tightness and dyspnea	Left atrium, right atrium, and tricuspid annulus	NA	4.9	NA	Chemotherapy	Alive at 3 mo
11	Higgins et al. (24)	F	72 y	NA	Pericardium	Left and right ventricle and brain	6	NA	Chemotherapy	Died
12	Su et al. (25)	M	43 y	Syncope	Interatrial septum, right atrium, and pericardium	Paratracheal, paraaortic regions, and the highest mediastinum lymph nodes	NA	9.24	Chemotherapy	Died at 3 mo
13	Goldman et al. (26)	F	73 y	Shortness of breath, fatigue, fever, and lower extremity swelling	Pericardium, right atrium, and right ventricle	NA	NA	37	Chemotherapy	Alive at 3 mo
14	Takaya et al. (27)	M	53	Penis mass	Penis	Left atrium and right femur	NA	NA	Chemotherapy + stem cell transplantation	Alive at 2 y

(Continued)

10.3389/fmed.2024.1373773

TABLE 1 (Continued)

Case	References	Gender	Age	Clinical symptoms	Primary sites	Invasion and metastasis	Max diameter/cm	SUVmax	Management	Outcome
15	Franc et al. (28)	F	67 y	Shortness of breath and fatigue	Pericardium, peri-orbit, and axillary lymph nodes	NA	NA	NA	Radiotherapy + chemotherapy + stem cell transplantation	Alive
16	Yang et al. (29)	M	46 y	Abdominal distension, acid reflux, and active chest tightness	Right ventricle, right atrium, stomach, jejunum, and colon	NA	7.8	26.7	Chemotherapy	Alive at 6 mo
17	Tsugu et al. (30)	F	57 y	Low-grade fever and night sweats	Right atrium and uterus	Mediastinum and para-aorta lymph nodes	2.5	22	Chemotherapy	Alive at 3 y
18	Panareo et al. (31)	M	71 y	Dyspnoea and superior vena cava syndrome	Right testicle	Right atrium	8	9.4	Surgery + chemotherapy	Alive at 3 y
19	Tagami et al. (32)	F	76 y	Swelling of the left upper eyelid	Left eyelid	Forehead, nasal cavity, right ventricle, and right atrium	NA	NA	Chemotherapy	Alive at 6 y
20	Kaderli et al. (33)	M	57 y	Mental confusion, weight loss, dyspnea, dizziness, and presyncope with effort	Right ventricle and right atrium	NA	NA	NA	Chemotherapy	Died at 5 mo

Bcl2 (Figures 2B–F). In addition, Ki-67 was observed to be positive in 40% of the tumor cells. *In situ* hybridization remained negative for Epstein–Barr virus (EBV)-encoded small RNAs (EBERs). The pathological diagnosis of cell smears and cell wax blocks in pericardial and pleural effusion confirms DLBCL.

For further staging, the patient underwent an ^{18}F-FDG PET/CT scan. The patient was instructed to follow a high-fat low-carbohydrate diet for 24 h prior to the ^{18}F-FDG PET/CT study and to avoid strenuous exercise (34, 35). Additionally, a low carbohydrate meal was advised before starting the 6-h fasting period to maintain blood glucose levels below 11.1 mmol/L. In this examination, 3,000 units of unfractionated heparin was intravenously administered 15 min before FDG administration. The ^{18}F-FDG PET/CT scan, performed utilizing Philips GXL-16 PET/CT machines, was conducted 60 min after the intravenous administration of ^{18}F-FDG. To ensure optimal hydration, patients were instructed to consume 1,000 mL of water and empty their bladders after 60 min of quiet rest. Routine scans were conducted from the head to mid-thigh, with separate acquisitions of the head and torso. In alignment with the European Association of Nuclear Medicine Research Limited (EARL) standards, we reconstructed the SUVmax for improved reproducibility and comparability (36, 37). This revealed multiple nodular soft tissue density lesions in the heart and pericardium, exhibiting increased FDG metabolism (SUVmax = 12.1). The supradiaphragmatic and infradiaphragmatic segments of the inferior vena cava exhibited irregular morphology with localized nodular changes and increased FDG metabolism in the surrounding area (SUVmax = 9.7). Additionally, multiple enlarged lymph nodes were identified in the mediastinum, left axilla, and near the left kidney, displaying heterogeneous FDG uptake with an SUVmax of 9.3, indicating lymphoma involvement (Figure 3). The above imaging findings suggested that the mass was a PCL.

Hence, the patient underwent a combination of chemotherapy and immunotherapy using R-CDOP (rituximab, cyclophosphamide, liposomal doxorubicin, vincristine, and prednisone). Following two courses of treatment within a span of 2 months, there was a partial remission observed in the cardiac lymphoma and the enlarged lymph nodes. She was closely monitored throughout the chemo-immunotherapy, with an established emergency plan in place to address potential complications, including arrhythmia and cardiac rupture.

Discussion

Clinical imaging examinations frequently provide crucial insights for the differential diagnosis of a cardiac mass. On CT, PCL typically manifests as multiple iso-attenuating to hypo-attenuating masses infiltrating the myocardium (15, 38). Noteworthy, CT reveals specific anatomical findings of unobstructed coronary arteries. In the case presented in this study, while CT served as the initial diagnostic modality for PCL, it fell short in revealing the details of myocardial and pericardial infiltration. Nevertheless, it did contribute additional information regarding extra-cardiac involvement. Presently, magnetic resonance imaging (MRI) stands as the preferred tomographic modality for investigating PCL, effectively distinguishing the mass from normal myocardial tissue through tissue characterization sequences (39). Beyond its radiation-free nature, MRI boasts advantages over CT, including high contrast and spatial resolution, making it the most useful modality for precisely defining the anatomy of the lesion. Kaida et al.

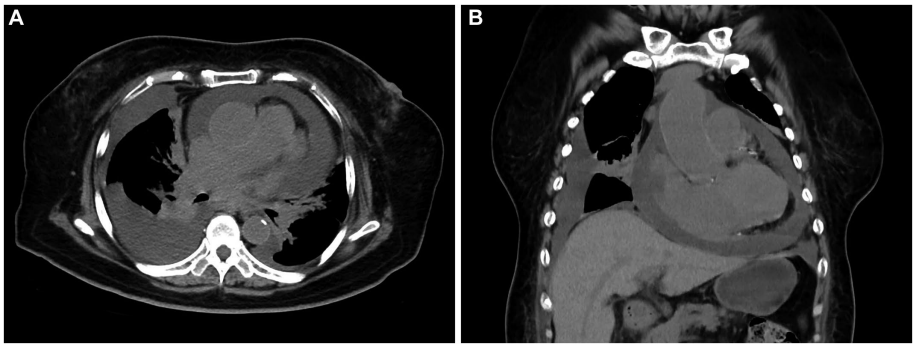

FIGURE 1
Computed tomography (CT) images of primary cardiac lymphoma (PCL). Transverse **(A)** and coronal **(B)** images revealed multiple nodular and clumped slightly hypodense foci in the heart and pericardium, along with effusions in the pericardium and pleural cavity.

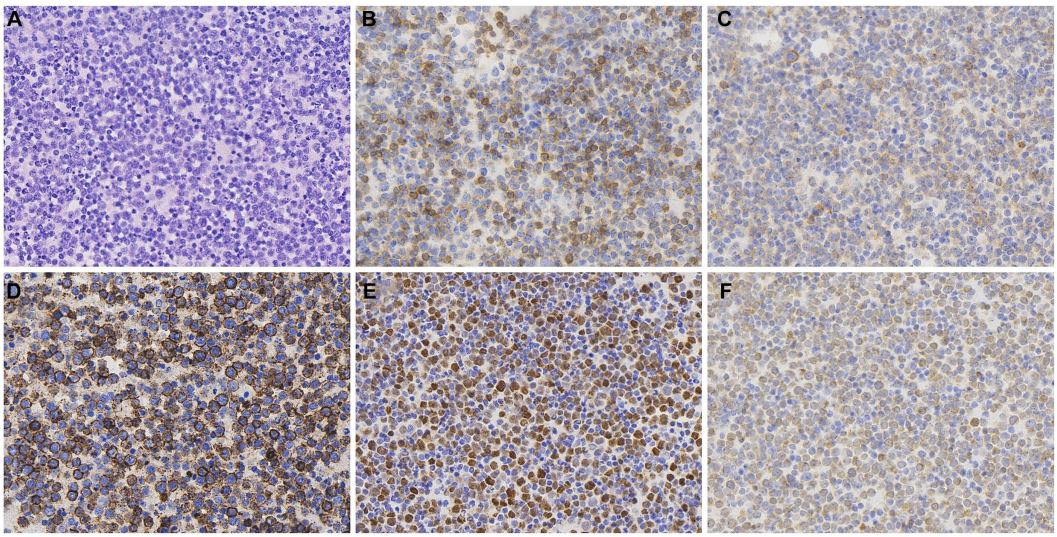

FIGURE 2
Histopathological and immunohistochemical images of PCL. Hematoxylin–eosin (HE) staining (magnification ×400) of the lesion **(A)** revealed microscopic cells characterized by large, deeply stained nuclei, scanty cytoplasm, moderate cellular anisotropy, visible small nucleoli, and distinct nuclear fission images and apoptosis. Immunohistochemical staining (400×) showed tumor cells were positive for the expression of CD5 **(B)**, CD10 **(C)**, CD20 **(D)**, MUM1 **(E)**, and Bcl-2 **(F)**.

(19) reported PCL to exhibit low signal on T1WI and high signal on both T2WI and fat suppression T2WI. Regrettably, our patient did not undergo a cardiac MRI examination.

^{18}F-FDG PET/CT stands out as a noninvasive tool for discerning the metabolic activity of tumors, proving exceptionally beneficial in delineating the staging of malignant lymphoma, tracking relapse, and evaluating therapeutic response (40, 41). When a patient is referred for evaluation of a heart lesion or an area very close to the myocardium, additional dietary recommendations can be helpful. While numerous options exist to reduce normal glucose uptake by the myocardium, common recommendations may include advising the patient to follow a low-carbohydrate diet for 24 h prior to the ^{18}F-FDG PET/CT study, or at the very least, consume a low-carbohydrate meal before the 6-h fasting period preceding the study (34, 35). A low-carbohydrate diet helps transition the myocardium from using glucose as its primary energy source to utilizing fatty acids, thereby reducing glucose uptake by the myocardium. Physiological FDG accumulation in the cardiac wall often interferes with the evaluation of cardiac lesions. Ishimaru et al. (42) underscored the significant role of heparin administration before FDG injection in detecting cardiac sarcoidosis. Heparin induces the release of free fatty acids into the circulation and serves to reduce the physiological FDG uptake by the myocardium (43, 44). Plasma glucose levels must be measured before administering FDG. If the plasma glucose level is 11 mmol/L (about 200 mg/dL) or higher, the ^{18}F-FDG PET/CT study should be rescheduled or the patient excluded based on individual circumstances and the nature of the study being conducted. For patients with Hodgkin and non-Hodgkin lymphoma, ^{18}F-FDG PET/CT has emerged as the standard procedure for staging, monitoring, and restaging the disease. During therapy assessment at mid-treatment and post-completion of chemotherapy, the Deauville score (DS) is recommended for distinguishing between responders and non-responders (45, 46). The DS is a clinical tool used to categorize patients with lymphoma based on the comparison between lesion and reference organ uptake of 18F-FDG, thus reflecting their disease status.

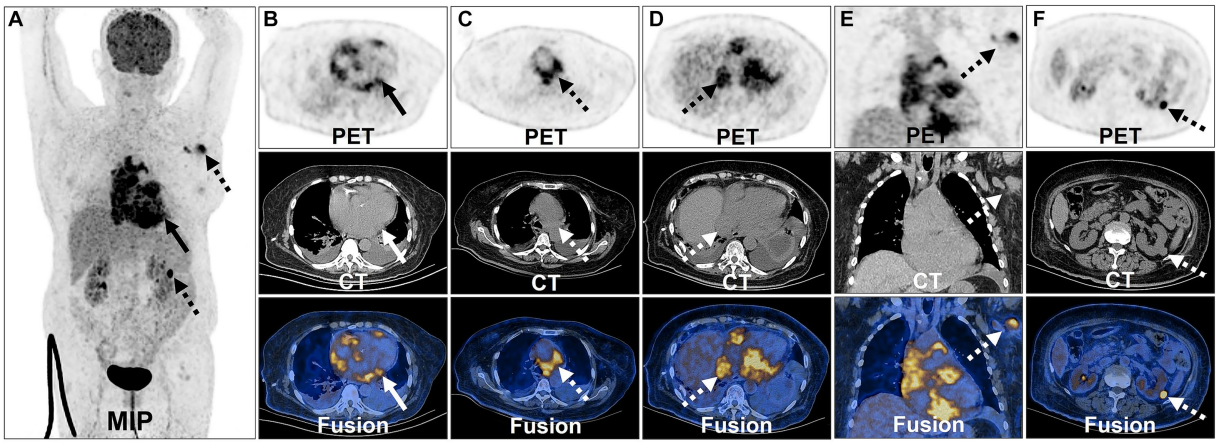

FIGURE 3
^{18}F-FDG PET/CT images of PCL. The anteroposterior 3-dimensional maximum intensity projection image (MIP) demonstrated FDG-avid lesions on the heart, pericardium (long arrows) and multiple lymph nodes (dash arrows) **(A)**. Transverse and coronal images showed multiple nodular soft tissue density lesions in the heart and pericardium exhibiting increased FDG metabolism **(B)**. Enlarged lymph nodes were identified in the mediastinum displaying heterogeneous FDG uptake **(C)**. The supradiaphragmatic segments of the inferior vena cava exhibited irregular morphology with localized nodular changes and increased FDG metabolism in the surrounding area **(D)**. Enlarged lymph node was identified in the left axilla displaying heterogeneous FDG uptake **(E)**. Enlarged lymph node was identified near the left kidney displaying heterogeneous FDG uptake **(F)**.

Notably, the existing literature on PCL predominantly comprises case reports, emphasizing its increased metabolic state with substantial FDG uptake (20). PCL may present as either multiple nodular lesions or extensive soft tissue masses (19, 21). The reported SUVmax range for cardiac lymphoma spans from 9.24 to 37 (5, 7, 10, 11, 14, 19–33). Kikuchi et al. (47) underscored a significantly elevated SUV in PCL patients compared to those with other cardiac malignant tumors (e.g., metastases, sarcoma) and benign tumors, demonstrating a lack of overlap. When imaging reveals increased ^{18}F-FDG uptake in multiple cardiac tumors alongside significant pericardial effusion, PCL should be a primary consideration. In the case under scrutiny, ^{18}F-FDG PET/CT provided comprehensive insights into both the extent of cardiac involvement and the absence of extracardiac organ participation. Another pivotal role of ^{18}F-FDG PET/CT in PCL management lies in its ability to monitor treatment response, a critical aspect in restaging numerous common lymphoma types (48). Adequate repeatability and reproducibility are essential for the clinical management of patients and the use of FDG PET/CT within multicenter trials. The new developments in PET/CT have been shown to affect the SUVmax in lesions (49). Consequently, it is conceivable that patients examined on various PET/CT scanners, utilizing different hardware, software, and acquisition parameters, may yield varied SUVmax. In future studies, we recommend that researchers adopt scan acquisition and image reconstruction protocols that are consistent with the EARL Coordination Program (36, 37). This approach will not only enhance the reproducibility and comparability of our findings but also facilitate the meaningful comparison of results across different PET/CT scanners.

In contrast, during the restaging of lymphoma, MRI may persist in exhibiting contrast enhancement, potentially linked to residual inflammation or scar, even when the tumor is no longer metabolically active. Consequently, PET/CT emerged as the preferred modality for assessing treatment response in this scenario. To ensure unequivocal findings, the post-chemotherapy scan was conducted after a 12-h abstinence from a high-fat low-carbohydrate diet, aiming to achieve a favorable tumor-to-background contrast and mitigate potential confounding physiological myocardial uptake in the ^{18}F-FDG PET/CT image. Differential diagnoses encompass benign myxoma, the most prevalent type of cardiac tumor, and angiosarcoma, the predominant malignant heart tumor typically located in the left cavities (50–52). While imaging examinations are valuable for detecting and characterizing cardiac masses, arriving at a definitive diagnosis remains challenging. Patient treatment and prognosis hinge significantly on the tissue type and biological behavior of the tumor.

The primary cause of mortality in PCL was heart failure, succeeded by sepsis and the progression of lymphoma. Less frequently observed causes included arrhythmia, embolism, cerebrovascular accidents, and sudden cardiac death (4). Existing strategies for PCL treatment encompass surgery, chemotherapy, radiotherapy, and immunotherapy. Complete resection was deemed unfeasible in our report due to the tumor's extensive involvement of the pericardium and diffuse infiltration of the myocardium. Early diagnosis and the precise selection of chemotherapy and immunotherapy, guided by cardiac imaging and pathological examination, may significantly improve the prognosis of PCL in atypical locations. Prognostic risk factors include extracardiac involvement, immune deficiency, arrhythmias such as complete atrioventricular block, and left heart involvement (3). The impact of surgical interventions proved limited, necessitating careful consideration of surgical decisions, especially in patients diagnosed with cardiac lymphoma (53). In cases where clinical and radiological suspicions of PCL exist, aggressive diagnostic procedures should be implemented, and therapy initiated before irreversible cardiac damage ensues.

The CHOP (cyclophosphamide, doxorubicin, vincristine, prednisone) regimen remains the conventional choice for treating DLBCL. However, the prognosis of PCL remains unfavorable; Rolla et al. (54) reported on 66 PCL patients, among whom 31 underwent a CHOP-based chemotherapy regimen, resulting in a median survival mean of 7 months. With the widespread use of rituximab (R), the integration of immunotherapy with chemotherapy (R-CHOP regimen) has become the preferred treatment for DLBCL, displacing surgical approaches, regardless of the tumor stage (55). Side effects, observed in approximately 10% of cases, include tumor lysis syndrome and sepsis. Additionally, chemotherapy carries the risk of significant thromboembolism, cardiac wall perforation, ventricular septal rupture, life-threatening arrhythmias, and pericardial effusion. While surgical

management does not constitute the primary treatment, prompt surgical debulking is indicated in patients with acute and severe presentations, especially those experiencing rapidly progressing heart failure. Therefore, clinicians must maintain a heightened vigilance index and provide timely interventions to optimize patient prognosis.

Conclusion

In conclusion, PCL is a rare entity in clinical practice, often associated with a poor prognosis. The advent of ^{18}F-FDG PET/CT has marked a significant stride, expanding the potential evaluation capabilities of conventional imaging (MRI and CT). When high ^{18}F-FDG uptake is evident in multiple cardiac tumors, accompanied by a considerable pericardial effusion, PCL should be considered a primary diagnostic consideration. The case elucidated in this report contributes to an understanding of the disease for clinicians, with ^{18}F-FDG PET/CT providing comprehensive insights into the extent of cardiac involvement, as well as the engagement of extracardiac organs and pathologic lymph nodes. The ^{18}F-FDG PET/CT examination not only visually delineates the lesion's location and extent but also serves as a cornerstone for clinical tumor staging, offering valuable support for treatment monitoring and subsequent follow-up.

Data availability statement

The original contributions presented in the study are included in the article/supplementary material, further inquiries can be directed to the corresponding author.

Ethics statement

The patients provided their written informed consent to participate in this study. Written informed consent was obtained from the individual for the publication of any potentially identifiable images or data included in this article.

Author contributions

WH: Conceptualization, Investigation, Writing – original draft, Writing – review & editing. ZZ: Investigation, Writing – original draft. YZ: Data curation, Writing – original draft. YQ: Conceptualization, Data curation, Writing – original draft. YP: Data curation, Writing – original draft. QY: Conceptualization, Writing – review & editing. WW: Conceptualization, Funding acquisition, Software, Validation, Writing – original draft. LK: Conceptualization, Writing – original draft.

Funding

The author(s) declare that financial support was received for the research, authorship, and/or publication of this article. This work was supported by the National Natural Science Foundation of China (82171970), the Beijing Science Foundation for Distinguished Young Scholars (JQ21025), the Beijing Municipal Science & Technology Commission (Z221100007422027), and National High Level Hospital Clinical Research Funding (Interdisciplinary Research Project of Peking University First Hospital, 2023IR17).

Conflict of interest

The authors declare that the research was conducted in the absence of any commercial or financial relationships that could be construed as a potential conflict of interest.

Publisher's note

References

1. Johri A, Baetz T, Isotalo PA, Nolan RL, Sanfilippo AJ, Ropchan G. Primary cardiac diffuse large B cell lymphoma presenting with superior vena cava syndrome. *Can J Cardiol*. (2009) 25:e210–2. doi: 10.1016/s0828-282x(09)70110-2

2. Hsueh S-C, Chung M-T, Fang R, Hsiung M-C, Young M-S, Lu H-F. Primary cardiac lymphoma. *J Chin Med Assoc*. (2006) 69:169–74. doi: 10.1016/S1726-4901(09)70200-X

3. Chen H, Qian S, Shi P, Liu L, Yang F. A presentation, treatment, and survival analysis of primary cardiac lymphoma cases reported from 2009 to 2019. *Int J Hematol*. (2020) 112:65–73. doi: 10.1007/s12185-020-02881-2

4. Petrich A, Cho SI, Billett H. Primary cardiac lymphoma: an analysis of presentation, treatment, and outcome patterns. *Cancer*. (2011) 117:581–9. doi: 10.1002/cncr.25444

5. Venugopala D, Dsouza NV, Acharya V, Rai M, Venkataramana CG, Boussios S. Constrictive pericarditis-a cloak camouflaging lymphoma. *Hematol Rep*. (2023) 15:166–71. doi: 10.3390/hematolrep15010017

6. Gowda RM, Khan IA. Clinical perspectives of primary cardiac lymphoma. *Angiology*. (2003) 54:599–604. doi: 10.1177/000331970305400510

7. Thiagaraj A, Kalamkar P, Rahman R, Farah V, Poornima I. An unprecedented case report of primary cardiac lymphoma exclusive to left ventricle: a diagnostic and therapeutic challenge. *Eur Heart J Case Rep*. (2018) 2:yty029. doi: 10.1093/ehjcr/yty029

8. Yin K, Brydges H, Lawrence KW, Wei Y, Karlson KJ, McAneny DB, et al. Primary cardiac lymphoma. *J Thorac Cardiovasc Surg*. (2022) 164:573–580.e1. doi: 10.1016/j.jtcvs.2020.09.102

9. Bulum J, Banfić L, Strozzi M, Aurer I, Jelasić D. Primary cardiac lymphoma presenting as atrial flutter and total heart block. *Heart Vessel*. (2007) 22:52–4. doi: 10.1007/s00380-006-0924-2

10. Alansari YE, Yudhistiara B, Michel RP, Elstein E. Case report: multimodality imaging to diagnose cardiac diffuse large B-cell lymphoma. *Eur Heart J Case Rep*. (2021) 5:ytab172. doi: 10.1093/ehjcr/ytab172

11. Lee JC, Platts DG, Huang Y-TT, Slaughter RE. Positron emission tomography combined with computed tomography as an integral component in evaluation of primary cardiac lymphoma. *Clin Cardiol*. (2010) 33:E106–8. doi: 10.1002/clc.20725

12. Economopoulos T, Asprou N, Stathakis N, Papageorgiou E, Dervenoulas J, Xanthaki K, et al. Primary extranodal non-Hodgkin's lymphoma in adults: clinicopathological and survival characteristics. *Leuk Lymphoma*. (1996) 21:131–6. doi: 10.3109/10428199609067590

13. Vogl TJ, Martin SS, Koch V, Scholtz J-E, Booz C, Leistner DM, et al. Letter to the editor: CT guided biopsy of a right ventricle primary cardiac lymphoma-a case report. *Cardiovasc Intervent Radiol*. (2023) 46:970–2. doi: 10.1007/s00270-023-03482-2

14. Imataki O, Kubo H, Fujita H, Uemura M. Metabolic steal of the myocardium by primary cardiac lymphoma. *Case Rep Oncol*. (2023) 16:7–12. doi: 10.1159/000527638

15. Coulier B, Colin GC, Tourmous H, Floris N, Van Eeckhout P, Scavée C. Imaging features of primary cardiac lymphoma. *Diagn Interv Imaging*. (2018) 99:115–7. doi: 10.1016/j.diii.2017.05.013

16. Jeudy J, Burke AP, Frazier AA. Cardiac lymphoma. *Radiol Clin North Am*. (2016) 54:689–710. doi: 10.1016/j.rcl.2016.03.006

17. Burke A, Tavora F. The 2015 WHO classification of tumors of the heart and pericardium. *J Thorac Oncol*. (2016) 11:441–52. doi: 10.1016/j.jtho.2015.11.009

18. Carras S, Berger F, Chalabreysse L, Callet-Bauchut E, Cordier J-F, Salles G, et al. Primary cardiac lymphoma: diagnosis, treatment and outcome in a modern series. *Hematol Oncol*. (2017) 35:510–9. doi: 10.1002/hon.2301

19. Kaida H, Kumode T, Kimura M, Ishii K. 18F-FDG PET/CT finding of primary cardiac lymphoma. *Clin Nucl Med*. (2020) 45:319–21. doi: 10.1097/RLU.0000000000002957

20. Qiang Y, Zeng K, Zhang B, Guan R, Liu Y, Liu Z, et al. Atypical location of primary cardiac lymphoma in the left heart with atypical clinical presentation: a case report and literature review. *Front Surg*. (2022) 9:1036519. doi: 10.3389/fsurg.2022.1036519

21. Erhamamcı S, Aslan N. A rare case of primary cardiac diffuse large B-cell lymphoma imaged with 18F-FDG PET/CT. *Mol Imaging Radionucl Ther*. (2022) 31:148–50. doi: 10.4274/mirt.galenos.2021.60590

22. Tong AK, Neo SH, Kok TY. Disseminated lymphoma evolving into neurolymphomatosis during mid-cycle of chemotherapy detected by $^{(18)}$F-FDG PET/CT. *Ann Acad Med Singap*. (2015) 44:545–7. doi: 10.47102/annals-acadmedsg.V44N11p545

23. Chang L, Gong C, Lu H, Liu Y, Kang L, Chen J, et al. Percutaneous intravenous catheter forceps biopsy in right atrial mass: two case reports and literature review. *BMC Cardiovasc Disord*. (2022) 22:63. doi: 10.1186/s12872-022-02507-x

24. Higgins AY, Taylor EP, Baldassarre LA, Miller EJ, Rosenfeld LE. Diagnosis of extensive myocardial infiltration by diffuse large B-cell lymphoma using 18F-fluorodeoxyglucose positron emission tomography (18-FDG PET). *J Nucl Cardiol*. (2018) 25:1869–71. doi: 10.1007/s12350-017-1099-1

25. Su H-Y, Huang H-L, Sun C-M, Hou S-M, Chen M-L. Primary cardiac lymphoma evaluated with integration of PET/CT and contrast-enhanced CT. *Clin Nucl Med*. (2009) 34:298–301. doi: 10.1097/RLU.0b013e31819e527c

26. Goldman M, Matthews R, Meng H, Bilfinger T, Kort S. Evaluation of cardiac involvement with mediastinal lymphoma: the role of innovative integrated cardiovascular imaging. *Echocardiography*. (2012) 29:E189–92. doi: 10.1111/j.1540-8175.2012.01746.x

27. Takaya T, Takeuchi Y, Nakajima H, Nishiki-Kosaka S, Hata K, Kijima Y, et al. Usefulness of transesophageal echocardiographic observation during chemotherapy for cardiac metastasis of non-Hodgkin lymphoma complicated with left ventricular diastolic collapse. *J Cardiol*. (2009) 53:447–52. doi: 10.1016/j.jjcc.2008.08.009

28. Franc B, Yoshida E, Herfkens R, Goris M. Pericardial lymph node involvement in lymphoma as identified on PET. *Clin Nucl Med*. (2004) 29:741–2. doi: 10.1097/00003072-200411000-00021

29. Yang Y, Chen P, Liu L, Lin J, Huang S. The value of 18F-FDG PET/CT in evaluating the efficacy of chemotherapy for diffuse large B-cell lymphoma with cardiac involvement. *J Nucl Cardiol*. (2022) 29:3548–53. doi: 10.1007/s12350-021-02551-8

30. Tsugu T, Nagatomo Y, Matsuyama E, Lancellotti P, Mitamura H. Very delayed sinus arrest during complete remission of diffuse large B-cell lymphoma invading right atrium. *Turk Kardiyol Dern Ars*. (2021) 49:414–8. doi: 10.5543/tkda.2021.57474

31. Panareo S, Urso L, Santi I, Rigolin GM, Cuneo A, Cittanti C, et al. Right atrium mass assessed with 18F-FDG PET/CT scan turns out to be an uncommon relapse of testicular diffuse large B-cell lymphoma: a case report. *Diagnostics*. (2020) 10:987. doi: 10.3390/diagnostics10110987

32. Tagami K, Tanda S, Kato H, Tashiro A, Saji K, Komaru T, et al. Detection of asymptomatic cardiac metastasis and successful salvage chemotherapy comprising a prednisone, etoposide, procarbazine, and cyclophosphamide regimen in an elderly Japanese patient suffering from a delayed recurrence of diffuse large B-cell lymphoma. *Case Rep Oncol*. (2012) 5:62–8. doi: 10.1159/000336447

33. Kaderli AA, Baran I, Aydin O, Bicer M, Akpinar T, Ozkalemkas F, et al. Diffuse involvement of the heart and great vessels in primary cardiac lymphoma. *Eur J Echocardiogr*. (2010) 11:74–6. doi: 10.1093/ejechocard/jep111

34. Lum DP, Wandell S, Ko J, Coel MN. Reduction of myocardial 2-deoxy-2-[18F]fluoro-D-glucose uptake artifacts in positron emission tomography using dietary carbohydrate restriction. *Mol Imaging Biol*. (2002) 4:232–7. doi: 10.1016/s1095-0397(01)00062-0

35. Coulden R, Chung P, Sonnex E, Ibrahim Q, Maguire C, Abele J. Suppression of myocardial 18F-FDG uptake with a preparatory "Atkins-style" low-carbohydrate diet. *Eur Radiol*. (2012) 22:2221–8. doi: 10.1007/s00330-012-2478-2

36. Kaalep A, Sera T, Oyen W, Krause BJ, Chiti A, Liu Y, et al. EANM/EARL FDG-PET/CT accreditation - summary results from the first 200 accredited imaging systems. *Eur J Nucl Med Mol Imaging*. (2018) 45:412–22. doi: 10.1007/s00259-017-3853-7

37. Boellaard R, Delgado-Bolton R, Oyen WJG, Giammarile F, Tatsch K, Eschner W, et al. FDG PET/CT: EANM procedure guidelines for tumour imaging: version 2.0. *Eur J Nucl Med Mol Imaging*. (2015) 42:328–54. doi: 10.1007/s00259-014-2961-x

38. Carter BW, Wu CC, Khorashadi L, Godoy MCB, de Groot PM, Abbott GF, et al. Multimodality imaging of cardiothoracic lymphoma. *Eur J Radiol*. (2014) 83:1470–82. doi: 10.1016/j.ejrad.2014.05.018

39. Asadian S, Rezaeian N, Hosseini L, Toloueitabar Y, Hemmati Komasi MM. The role of cardiac CT and MRI in the diagnosis and management of primary cardiac lymphoma: a comprehensive review. *Trends Cardiovasc Med*. (2022) 32:408–20. doi: 10.1016/j.tcm.2021.08.010

40. Zanoni L, Bezzi D, Nanni C, Paccagnella A, Farina A, Broccoli A, et al. PET/CT in non-Hodgkin lymphoma: an update. *Semin Nucl Med*. (2023) 53:320–51. doi: 10.1053/j.semnuclmed.2022.11.001

41. Yuan H, Qiu J, Chiu KWH, Chan LWC, Zhang F, Wei X, et al. PET/CT morphology and cardiac conduction disorders help discriminate primary cardiac lymphoma from primary cardiac sarcoma. *J Nucl Cardiol*. (2022) 29:2866–77. doi: 10.1007/s12350-022-03042-0

42. Ishimaru S, Tsujino I, Takei T, Tsukamoto E, Sakaue S, Kamigaki M, et al. Focal uptake on 18F-fluoro-2-deoxyglucose positron emission tomography images indicates cardiac involvement of sarcoidosis. *Eur Heart J*. (2005) 26:1538–43. doi: 10.1093/eurheartj/ehi180

43. Nuutila P, Koivisto VA, Knuuti J, Ruotsalainen U, Teräs M, Haaparanta M, et al. Glucose-free fatty acid cycle operates in human heart and skeletal muscle in vivo. *J Clin Invest*. (1992) 89:1767–74. doi: 10.1172/JCI115780

44. Minamimoto R, Morooka M, Kubota K, Ito K, Masuda-Miyata Y, Mitsumoto T, et al. Value of FDG-PET/CT using unfractionated heparin for managing primary cardiac lymphoma and several key findings. *J Nucl Cardiol*. (2011) 18:516–20. doi: 10.1007/s12350-011-9358-z

45. Barrington SF, Qian W, Somer EJ, Franceschetto A, Bagni B, Brun E, et al. Concordance between four European centres of PET reporting criteria designed for use in multicentre trials in Hodgkin lymphoma. *Eur J Nucl Med Mol Imaging*. (2010) 37:1824–33. doi: 10.1007/s00259-010-1490-5

46. Biggi A, Gallamini A, Chauvie S, Hutchings M, Kostakoglu L, Gregianin M, et al. International validation study for interim PET in ABVD-treated, advanced-stage hodgkin lymphoma: interpretation criteria and concordance rate among reviewers. *J Nucl Med*. (2013) 54:683–90. doi: 10.2967/jnumed.112.110890

47. Kikuchi Y, Oyama-Manabe N, Manabe O, Naya M, Ito YM, Hatanaka KC, et al. Imaging characteristics of cardiac dominant diffuse large B-cell lymphoma demonstrated with MDCT and PET/CT. *Eur J Nucl Med Mol Imaging*. (2013) 40:1337–44. doi: 10.1007/s00259-013-2436-5

48. Israel O, Keidar Z, Bar-Shalom R. Positron emission tomography in the evaluation of lymphoma. *Semin Nucl Med*. (2004) 34:166–79. doi: 10.1053/j.semnuclmed.2004.03.002

49. Hsu DFC, Ilan E, Peterson WT, Uribe J, Lubberink M, Levin CS. Studies of a next-generation silicon-photomultiplier-based time-of-flight PET/CT system. *J Nucl Med*. (2017) 58:1511–8. doi: 10.2967/jnumed.117.189514

50. Hoffmeier A, Sindermann JR, Scheld HH, Martens S. Cardiac tumors--diagnosis and surgical treatment. *Dtsch Arztebl Int*. (2014) 111:205–11. doi: 10.3238/arztebl.2014.0205

51. Kassab J, Gebrael G, Chedid El Helou M, El Dahdah J, Haroun E, Kassab R, et al. Case report: primary cardiac lymphoma manifesting as superior vena cava syndrome. *Front Cardiovasc Med*. (2023) 10:1257734. doi: 10.3389/fcvm.2023.1257734

52. Li X, Chen Y, Liu J, Xu L, Li Y, Liu D, et al. Cardiac magnetic resonance imaging of primary cardiac tumors. *Quant Imaging Med Surg*. (2020) 10:294–313. doi: 10.21037/qims.2019.11.13

53. Henn MC. Commentary: Don't mess with primary cardiac lymphoma. *J Thorac Cardiovasc Surg*. (2022) 164:582–3. doi: 10.1016/j.jtcvs.2020.09.049

54. Rolla G, Bertero MT, Pastena G, Tartaglia N, Corradi F, Casabona R, et al. Primary lymphoma of the heart. a case report and review of the literature. *Leuk Res*. (2002) 26:117–20. doi: 10.1016/s0145-2126(01)00092-3

55. Habermann TM, Weller EA, Morrison VA, Gascoyne RD, Cassileth PA, Cohn JB, et al. Rituximab-CHOP versus CHOP alone or with maintenance rituximab in older patients with diffuse large B-cell lymphoma. *J Clin Oncol*. (2006) 24:3121–7. doi: 10.1200/JCO.2005.05.1003

frontiers | Frontiers in Medicine

TYPE Case Report
PUBLISHED 29 April 2024
DOI 10.3389/fmed.2024.1353822

OPEN ACCESS

EDITED BY
Ramin Sadeghi,
Mashhad University of Medical Sciences, Iran

REVIEWED BY
Carmelo Caldarella,
Fondazione Policlinico Universitario A. Gemelli IRCCS, Italy
Damodara Naidu Kommi,
University of Virginia, United States
Giorgio Treglia,
Ente Ospedaliero Cantonale, Switzerland
Hushan Zhang,
3D Medicines Co., Ltd, China

*CORRESPONDENCE
Lei Kang
✉ kanglei@bjmu.edu.cn

RECEIVED 11 December 2023
ACCEPTED 08 April 2024
PUBLISHED 29 April 2024

CITATION
Song L, Qiu Y, Huang W, Sun X, Yang Q, Peng Y and Kang L (2024) Untypical bilateral breast cancer with peritoneal fibrosis on ^{18}F-FDG PET/CT: case report and literature review.
Front. Med. 11:1353822.
doi: 10.3389/fmed.2024.1353822

Untypical bilateral breast cancer with peritoneal fibrosis on ^{18}F-FDG PET/CT: case report and literature review

Lele Song, Yongkang Qiu, Wenpeng Huang, Xinyao Sun, Qi Yang, Yushuo Peng and Lei Kang*

Department of Nuclear Medicine, Peking University First Hospital, Beijing, China

Background: Retroperitoneal fibrosis, a condition of uncertain origin, is rarely linked to 8% of malignant cases, including breast, lung, gastrointestinal, genitourinary, thyroid, and carcinoid. The mechanism leading to peritoneal fibrosis induced by tumors is not well understood, possibly encompassing direct infiltration of neoplastic cells or the initiation of inflammatory responses prompted by cytokines released by tumor cells. We report a case of breast cancer with renal metastasis and retroperitoneal fibrosis detected using ^{18}F-FDG PET/CT, providing help for clinical diagnosis and treatment.

Case report: A 49-year-old woman was referred to the hospital with elevated creatinine and oliguria for over a month. Abdominal computer tomography (CT) and magnetic resonance imaging (MRI) showed a retroperitoneal fibrosis-induced acute kidney injury (AKI) was suspected. However, a percutaneous biopsy of the kidney lesion confirmed metastasis from breast cancer. The physical examination revealed inverted nipples and an orange peel appearance on the skin of both breasts. Ultrasonography revealed bilateral hyperplasia (BIRADS 4a) of the mammary glands and bilateral neck and axillary lymphadenopathy. Subsequently, ^{18}F-deoxyglucose positron emission tomography/computer tomography (^{18}F-FDG PET/CT) detected abnormally high uptake (SUVmax) in the bilateral mammary glands and axillary lymph nodes, suggesting bilateral breast cancer. Furthermore, abnormal ^{18}F-FDG uptake was detected in the kidney, suggesting renal metastasis. In addition, abnormal ^{18}F-FDG uptake was observed in the vertebrae, accompanied by an elevation in inhomogeneous bone mineral density, raising suspicion of bone metastases. However, the possibility of myelodysplasia cannot be dismissed, and further investigations will be conducted during close follow-ups. There was significant ^{18}F-FDG uptake in the retroperitoneal position indicating a potential association between retroperitoneal fibrosis and breast cancer. The final pathological diagnosis of the breast tissue confirmed bilateral invasive ductal carcinoma. The patient had been treated with 11 cycles of albumin-bound (nab)-paclitaxel (0.3 mg) and had no significant adverse reaction.

Conclusion: In this case, neither the bilateral breast cancer nor the kidney metastatic lesion showed typical nodules or masses, so breast ultrasound, abdominal CT, and MRI did not suggest malignant lesions. PET/CT played an important role in detecting occult metastases and primary lesions, thereby contributing to more accurate staging, monitoring treatment responses, and prediction of prognosis in breast cancer.

KEYWORDS

bilateral breast cancer, peritoneal fibrosis, renal metastasis, ^{18}F-FDG PET/CT, case report

Introduction

Retroperitoneal fibrosis is an uncommon disorder of unclear etiology, with 8% of cases associated with malignancies, among which breast cancer is a relatively common cause. The pathogenesis of peritoneal fibrosis caused by tumors remains unclear, potentially involving direct neoplastic cell infiltration or inflammatory reactions triggered by cytokines secreted by tumor cells. Retroperitoneal fibrosis is characterized by increased fibrotic deposition in the retroperitoneum, frequently leading to ureteral obstruction [1]. Herein, we report a case of breast cancer with retroperitoneal fibrosis and renal insufficiency as the first symptoms. Conventional imaging did not reveal any evidence of breast cancer or distant metastases. However, ^{18}F-deoxyglucose positron emission tomography/computer tomography (^{18}F-FDG PET/CT) images demonstrated increased ^{18}F-FDG uptake in the breast and kidney, which was suspicious of bilateral breast cancer (BBC) with diffuse renal metastatic lesions. PET/CT plays a crucial role in detecting primary lesions and metastatic lesions, monitoring relapses, managing treatment, and improving patient prognosis. In addition, we summarized the basic information and clinical details of some cases with tumor-associated retroperitoneal fibrosis in Table 1.

Case presentation

A 49-year-old woman was referred to the hospital with elevated creatinine and oliguria for over a month. The patient experienced abdominal pain and lower back pain with noticeable pitting edema in both lower extremities, along with decreased urine, without an

TABLE 1 Literature review of tumor-related retroperitoneal fibrosis.

Case	Primary tumor	Age	Authors	Sex	Clinical symptom	Management	Prognosis
1	Breast cancer (intraductal carcinoma of the breast)	73 years	Kava et al. (1)	F	Bilateral hydroureteronephrosis	Not mentioned	Not mentioned
2	Breast cancer (invasive lobular carcinoma)	73 years	MacNeil et al. (2)	F	Abdominal pain	Not mentioned	Not mentioned
3	Breast cancer (invasive lobular carcinoma)	68 years	Kane et al. (3)	F	Small bowel obstruction and hydronephrosis	Chemotherapy and operative treatments	Died
4	Breast cancer (invasive lobular carcinoma)	44 years	Kane et al. (3)	F	AKI and bilateral hydronephrosis	Not mentioned	Died
5	Breast cancer (invasive lobular carcinoma)	65 years	Gogas et al. (4)	F	Left hydronephrosis	Operative treatments	Good recovery
6	Lymphoma (follicular lymphoma)	56 years	Lan et al. (5)	F	Back pain and bilateral hydronephrosis	Chemotherapy	Complete remission
7	Lymphoma (B-cell non-Hodgkin lymphoma)	66 years	Alvarez et al. (6)		Back pain	Radiation therapy and rituximab therapy	Complete remission
8	Esophageal cancer (esophageal squamous cell carcinoma)	71 years	Mori et al. (7)	M	AKI	Chemotherapy	Died
9	Gastric cancer (gastric signet-ring-cell adenocarcinoma)	39 years	Benesch et al. (8)	M	Abdominal pain and dyspepsia	Palliative care	Died
10	Lung cancer (lung adenocarcinoma)	74 years	Nishiyama et al. (9)	F	Left lumbar backache	Chemotherapy	Died

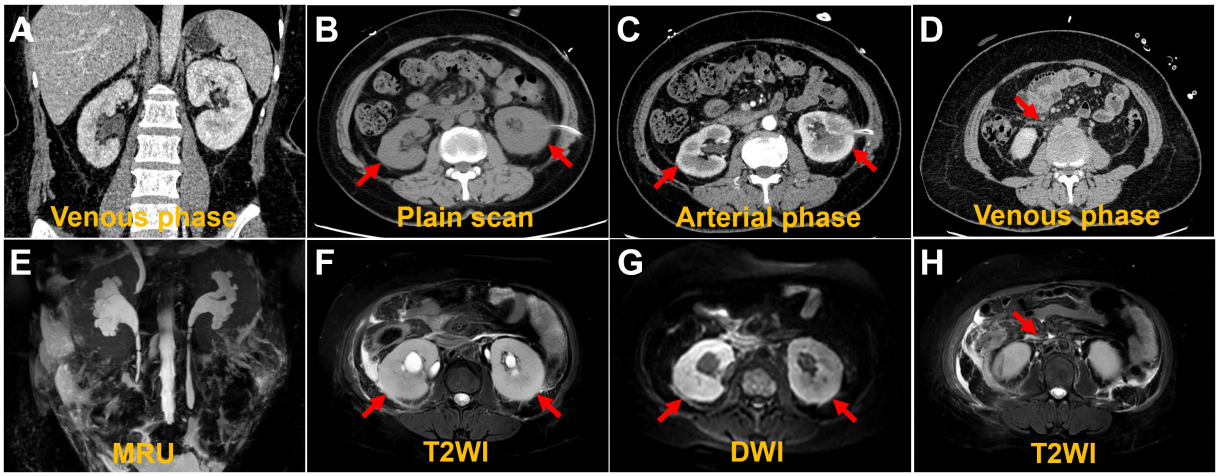

FIGURE 1
Computed tomography images and magnetic resonance images. The coronal image shows bilateral hydronephrosis and enlarged kidneys **(A,E)**. The axial images show diffuse lesions in the renal parenchyma, with no obvious masses detected **(B,C,F,G)**. The axial image shows retroperitoneal multiple exudation **(D,H)**.

apparent trigger over a month ago. The patient has no family history of the disease. Laboratory results revealed a serum creatinine level of 1,054 μmol/L and a hemoglobin level of 76 g/L, suggestive of acute kidney injury (AKI). Ultrasonography demonstrated bilateral hydronephrosis with widening of the proximal ureters and moderately low echogenicity around the abdominal aorta, suggesting that retroperitoneal fibrosis might be present. Abdominal CT and magnetic resonance imaging (MRI) (Figure 1) revealed bilateral kidney swelling, dilation of the bilateral kidneys, renal calyces, and upper ureters, accompanied by multiple retroperitoneal and bilateral perirenal exudations, suggestive of retroperitoneal fibrosis. No focal lesions were found in either kidney.

AKI is likely attributed to post-renal obstruction secondary to retroperitoneal fibrosis. To further define the histological features of renal lesions and exclude the probability of primary kidney disease, a biopsy was performed of the lower pole of the right kidney. The biopsy of the lower pole of the right kidney demonstrated acute renal tubular necrosis and heterotypic cells in the renal tissue. The tumor cells have moderate dysplasia, form adenoid arrangements, and show an invasive growth pattern. Immunohistochemical results showed that P120-, HER2-, PR 90%, ER 90%, E-Cadherin-, GATA (3+), CKpan (3+), and Vimentin-. Combined with the results of immunohistochemistry, it was consistent with breast cancer metastasis. Therefore, the mammary gland of the patient was further examined. A physical examination of the patient revealed an orange peel change on the skin of both breasts and a bilateral inverted nipple. Breast ultrasound showed bilateral hyperplasia (BIRADS 4a) of the mammary glands with a reduced echo. Contrast-enhanced breast MRI was precluded by the patient's compromised renal function and aimed at averting potential adverse reactions to the gadolinium contrast agent, including those associated with nephrogenic systemic fibrosis. Consequently, whole-body ^{18}F-deoxyglucose positron emission tomography/computed tomography (^{18}F-FDG PET/CT) imaging was conducted to pinpoint the most reliable clinical biopsy site. Moreover, ^{18}F-FDG PET/CT proves valuable in distinguishing between benign and malignant lesions, as well as in determining breast cancer staging, grading, and locating primary and metastatic tumor foci. The anteroposterior 3-dimensional maximum intensity projection (MIP) image demonstrated patchy metabolic elevation on both sides of the mammary glands, along with diffusely uneven metabolic foci in both kidneys (Figure 2A). Bilaterally dense mammary glands with a diffuse, mild ^{18}F-FDG uptake were seen, with a maximum standardized uptake value (SUVmax) of 4.7. Bilateral local thickening of the breast skin with an SUVmax of 2.3 was found, which was higher on the right side. BBC was considered (Figure 2B). Enlargement of both kidneys with various degrees of ^{18}F-FDG uptake is found, with an SUVmax at approximately 8.2 (Figure 2C). A patchy soft tissue density lesion is visible around the renal fascia and adjacent to the abdominal aorta, with mild ^{18}F-FDG uptake, and the SUVmax is approximately 3.3 (Figure 2D). Furthermore, diffuse inhomogeneous ^{18}F-FDG uptake was observed in bone lesions, characterized by an SUVmax of approximately 2.9. Additionally, inhomogeneous hyperintensities in bone mineral density were identified in the cones (Figures 2E,F), prompting suspicion of potential bone metastasis. Nevertheless, we cannot definitively exclude the possibility of myelodysplasia, and we will vigilantly monitor this concern during subsequent follow-up assessments. The lesions in the kidneys, bones, and retroperitoneal area were associated with the metastasis of breast cancer.

Subsequently, the bilateral mammary glands were examined histologically and immunohistochemically. Pathological examination (Figure 3) revealed grade II invasive lobular carcinoma with ER 90%, PgR 50%, P40-, E-cadherin-, P120++, GATA (3+), Ki67 15%, HER2-, and PD-L1- in both breasts. The clinician diagnosed stage IV invasive breast cancer. The presence of the BRCA1 gene mutation was identified in the germline of the BBC. Renal metastases due to breast cancer were diagnosed on the basis of immunohistochemistry. The patient was ultimately identified as having BBC accompanied by metastases to the bones, kidneys, and retroperitoneal location.

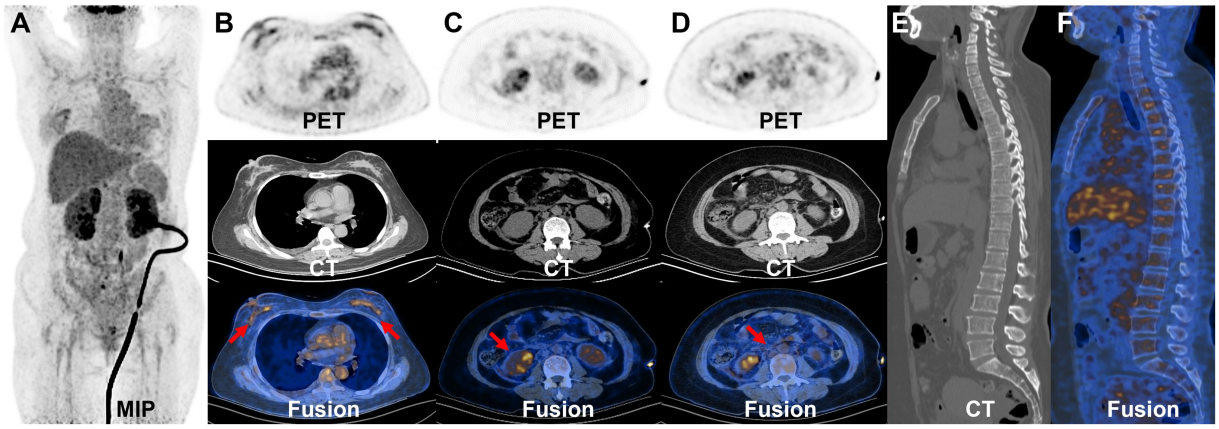

FIGURE 2
^{18}F-FDG PET/CT images. The MIP demonstrated patchy metabolic elevation on both sides of the mammary glands, as well as increased volume in both kidneys, accompanied by a diffusely uneven elevated metabolic lesion **(A)**. The bilateral dense breast tissue shows diffuse mild ^{18}F-FDG uptake, with an SUVmax of approximately 4.7. There is a local thickening of the skin in both breasts, with an SUVmax of 2.3, more prominent on the right side **(B)**. The transverse images show inhomogeneous ^{18}F-FDG uptake in the bilaterally enlarged kidneys, with an SUVmax of approximately 8.2 **(C)**. The transverse images show right perirenal fascia thickening with a significantly higher uptake of an SUVmax of approximately 3.3 **(D)**. The sagittal images show the heterogeneous bone density elevation with radioactive distribution, SUVmax of approximately 2.9 **(E,F)**.

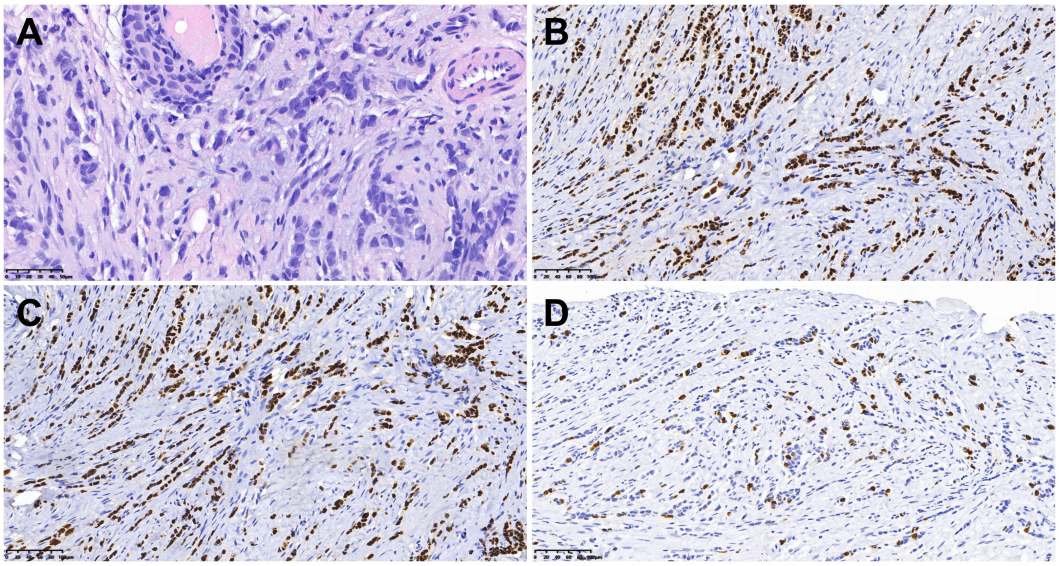

FIGURE 3
Histologic and immunohistochemical features of breast cancer. **(A)** Hematoxylin–eosin (HE) staining (×400). In immunohistochemical staining, the tumor cells were positive for ER **(B)** and GATA3 **(C)**. Moreover, 15% of them were positive for Ki-67 **(D)** [magnification **(B–D)** × 200].

Additionally, AKI was observed due to retroperitoneal fibrosis. A week later, after the contraindication of chemotherapy was excluded, the patient was treated with albumin-bound (nab)-paclitaxel (0.3 mg). At present, the chemotherapy has been 11 cycles, and the patient has had no obvious adverse reactions during the course of the chemotherapy. We are still following up.

Discussion

Breast cancer represents 24.5% of all cancer cases in women. In 2022, breast cancer will have the highest incidence and mortality in most countries (10). BBC is uncommon and accounts for 1.4–12% of all breast cancers (11). Based on the time interval between the diagnosis of bilateral malignant tumors, BBC can manifest synchronously or asynchronously (12). The primary risk factors associated with BRCA1-related breast cancer include a family history of breast cancer, younger age (under 40 years old), multifocal cancer, a history of lobular carcinoma, inherited genetic mutations such as those in the BRCA1 and BRCA2 genes, and exposure to radiation (13–16). For BRCA1 mutation carriers, the risk of breast cancer increases substantially between the ages of 30 and 50, while for women with a BRCA2 mutation, the risks are highest between ages 40 and 60 (16). BRCA-related breast cancer is characterized by a more aggressive

phenotype than sporadic breast cancer, with BRCA1-related breast cancer being more frequently high grade and triple negative, and BRCA2-related breast cancer being on average a higher histological grade than sporadic cases (17). The systematic review and meta-analysis conducted by Baretta et al. (17) showed that mutation carriers have worse overall survival than BRCA-negative/sporadic cases (hazard ratio, HR 1.30, 95% CI: 1.11–1.52) and worse breast cancer-specific survival than sporadic/BRCA-negative cases among patients with stage I–III breast cancer (HR 1.45, 95% CI: 1.01–2.07). In this particular case, the patient had no other risk factors, and genetic testing revealed a mutation in the BRCA1 gene. BRCA1 mutation carriers with breast cancer may benefit from treatment with cisplatinum (18) or olaparib (19) compared to those without a mutation. These data collectively indicate the important role of BRCA mutation status with respect to treatment decisions that may impact outcomes. Genetic mutation detection plays an essential role in the clinical management of breast cancer, as it enables physicians to more accurately identify the molecular characteristics of the disease, formulate personalized treatment plans, and predict the efficacy of therapy and patient prognosis (20, 21). Family members can understand their genetic risks through genetic counseling and undergo appropriate screening and management based on the recommendations of healthcare professionals. Moreover, studies have found that the infiltrating ductal type is the most common histology in BBC (22–24). Some studies indicate that the survival rates of patients with unilateral and BBC are comparable (25, 26). While routine radiological assessments, including mammography and ultrasonography, are conducted for women presenting with suspicious breast symptoms, these methods have certain limitations in diagnosing BBC (27). In addition, contrast-enhanced MRI is forbidden for patients with renal failure. In such a situation, PET/CT, in particular, is instrumental in detecting axillary extra-nodal disease and occult metastasis in patients with locally advanced breast cancer. Its role in assessing responses to neoadjuvant or adjuvant chemotherapy is continually evolving. In the detection of suspected recurrences, it proves more effective than traditional imaging modalities (28).

Retroperitoneal fibrosis is a rare condition of diverse etiology, associated with radiotherapy, aortic aneurysms, infections, and malignancy (29). Eight percent of cases are associated with malignancies (30). Common tumors leading to retroperitoneal fibrosis include breast, lung, gastrointestinal, genitourinary, thyroid, lymphoma, sarcoma, and carcinoid (31). The pathogenic mechanism of peritoneal fibrosis induced by tumors is unknown. It may result from a desmoplastic reaction of the retroperitoneum to malignant cells, an inflammatory reaction, or cytokines secreted by the tumor (30). We have compiled a subset of cases presenting with tumor-associated retroperitoneal fibrosis, and the basic information and clinical details are summarized in Table 1. In the literature, several cases of malignant retroperitoneal fibrosis associated with breast cancer have been documented, with the majority of reported cases featuring a history of breast cancer in the patients (1, 2, 4). Obstructive uropathy is typical of retroperitoneal fibrosis, and bilateral flank pain is the most frequent clinical presentation (1, 2, 4). Our patient presented classic symptoms of bilateral flank pain and hydronephrosis. CT reveals a diffusely infiltrative soft tissue mass enveloping retroperitoneal structures, which is a typical radiological manifestation of retroperitoneal fibrosis (32). ^{18}F-FDG PET/CT can be a valuable tool in evaluating the disease activity and lesion range of retroperitoneal fibrosis and monitoring the treatment of retroperitoneal fibrosis. Furthermore, as illustrated by our cases, in some patients with malignant tumors present with peritoneal fibrosis as the initial manifestation, PET/CT can assist in identifying the primary lesion and accurately staging and grading the condition.

Breast cancer metastasis to the kidneys is rarely seen (33). In one study, the incidence of metastasis of breast cancer to the kidneys was 12% (34). The mechanism of breast cancer metastasis to the kidneys can be attributed to the physiological characteristics of the kidneys. Specifically, the substantial proportion of cardiac output dedicated to renal blood flow makes it likely for circulating tumor cells to enter the renal capillaries (35). Common symptoms of renal metastasis are flank pain and hematuria (36, 37). The most common form of metastatic renal carcinomas is multiple bilaterally circumscribed, rounded masses (35). In patients with known primary tumors, diffuse enlargement of the kidney without a clear mass may suggest renal metastatic disease (38). In this case, the imaging findings were bilaterally enlarged kidneys without focal lesions. However, PET findings indicated various degrees of ^{18}F-FDG uptake in the bilateral kidneys with suspicions of breast cancer metastasis to the kidney, which was agreeable with the pathological diagnosis. In PET/CT imaging, renal metastasis may manifest as small, multiple, bilateral, circular lesions with high ^{18}F-FDG uptake and a diffusely invasive, large, single mass with high ^{18}F-FDG uptake. By the time the primary lesion was detected by PET/CT at some sites, especially tumors prone to renal metastasis (lymphomas and carcinomas of the lung, breast, stomach, pancreas, and colon), there was a high probability of renal involvement. A biopsy for histological analysis was performed if necessary. Conducting a thorough examination of the renal cortex through ^{18}F-FDG PET, coupled with a review of anatomical images such as CT and MRI results, plays a pivotal role in the identification of renal tumors.

Conclusion

In conclusion, we present a case study detailing the ^{18}F-FDG PET/CT imaging manifestations in a BBC patient with retroperitoneal fibrosis and renal metastasis. Compared with conventional imaging, PET can find systemic metastases based on the detection of primary foci, which can be used for disease staging and the evaluation of treatment efficacy.

Data availability statement

The original contributions presented in the study are included in the article/Supplementary material, further inquiries can be directed to the corresponding author.

Ethics statement

Written informed consent was obtained from the individual(s) for the publication of any potentially identifiable images or data included in this article. Written informed consent was obtained from the participant/patient(s) for the publication of this case report.

Author contributions

LS: Writing – original draft, Writing – review & editing. YQ: Conceptualization, Writing – original draft. WH: Data curation, Writing – original draft. XS: Investigation, Writing – original draft. QY: Methodology, Writing – original draft. YP: Project administration, Writing – review & editing. LK: Conceptualization, Funding acquisition, Investigation, Project administration, Supervision, Writing – review & editing.

Funding

The author(s) declare that financial support was received for the research, authorship, and/or publication of this article. This study was supported by the National Natural Science Foundation of China (82171970), the Beijing Science Foundation for Distinguished Young Scholars (JQ21025), the Beijing Municipal Science and Technology Commission (Z221100007422027), and the National High-Level Hospital Clinical Research Funding (Interdisciplinary Research Project of Peking University First Hospital, 2023IR17).

Conflict of interest

The authors declare that the research was conducted in the absence of any commercial or financial relationships that could be construed as a potential conflict of interest.

Publisher's note

Supplementary material

The Supplementary material for this article can be found online at: https://www.frontiersin.org/articles/10.3389/fmed.2024.1353822/full#supplementary-material

References

1. Kava BR, Russo P, Conlon KC. Laparoscopic diagnosis of malignant retroperitoneal fibrosis. *J Endourol*. (1996) 10:535–8. doi: 10.1089/end.1996.10.535

2. MacNeil JAB, Selegean S, Williams AS. Metastatic lobular carcinoma presenting as retroperitoneal fibrosis: a rare presentation detected using post-mortem cytology. *Pathology*. (2020) 52:387–90. doi: 10.1016/j.pathol.2019.12.004

3. Kane AJ, Wang ZJ, Qayyum A, Yeh BM, Webb EM, Coakley FV. Frequency and etiology of unexplained bilateral Hydronephrosis in patients with breast Cancer: results of a longitudinal Ct study. *Clin Imaging*. (2012) 36:263–6. doi: 10.1016/j.clinimag.2011.10.001

4. Gogas J, Markopoulos C, Kouskos E, Gogas H, Kiriakou V. Metastatic retroperitoneal and mediastinal fibrosis as first sign of recurrence of breast cancer. *Eur J Surg*. (2001) 167:715–8. doi: 10.1080/11024150152619408

5. Lan X, Hu R, Song T, Gan L, Sun W. A case of follicular lymphoma mimicking idiopathic retroperitoneal fibrosis. *Cureus*. (2022) 14:e32031. doi: 10.7759/cureus.32031

6. Alvarez Argote J, Bauer FA, Posteraro AF 3rd, Dasanu CA. Retroperitoneal fibrosis due to B-cell non-Hodgkin lymphoma: responding to rituximab! *J Oncol Pharm Pract*. (2016) 22:179–85. doi: 10.1177/1078155214543279

7. Mori T, Nabeshima S, Fujino S, Imoto A, Shima H, Yamamoto K, et al. A case of acute kidney injury due to secondary retroperitoneal fibrosis caused by direct invasion of esophageal squamous cell carcinoma. *CEN Case Rep*. (2015) 4:185–9. doi: 10.1007/s13730-014-0164-8

8. Benesch MGK, Mathieson A. Gastric signet-ring-cell adenocarcinoma with delayed retroperitoneal metastasis and fibrosis. *Case Rep Oncol*. (2022) 15:114–9. doi: 10.1159/000521888

9. Nishiyama A, Yoshioka H, Ikeo S, Morita M, Sone N, Ikeda S, et al. Retroperitoneal metastasis from lung adenocarcinoma mimics retroperitoneal fibrosis. *J Thorac Oncol*. (2016) 11:266–7. doi: 10.1016/j.jtho.2015.10.023

10. Sung H, Ferlay J, Siegel RL, Laversanne M, Soerjomataram I, Jemal A, et al. Global Cancer statistics 2020: Globocan estimates of incidence and mortality worldwide for 36 cancers in 185 countries. *CA Cancer J Clin*. (2021) 71:209–49. doi: 10.3322/caac.21660

11. Hartman M, Czene K, Reilly M, Adolfsson J, Bergh J, Adami HO, et al. Incidence and prognosis of synchronous and Metachronous bilateral breast Cancer. *J Clin Oncol*. (2007) 25:4210–6. doi: 10.1200/jco.2006.10.5056

12. Mishra S, Sable M, Das Majumdar SK, Mishra P, Muduly DK, Parida DK. Bilateral breast Cancer-its Clinicopathological profile and management: an experience from a tertiary care center from eastern India. *J Cancer Res Ther*. (2022) 18:S341–6. doi: 10.4103/jcrt.JCRT_1729_20

13. Mallory MA, Whiting K, Park A, Gönen M, Gilbert E, King TA, et al. Synchronous and Metachronous bilateral breast Cancer among women with a history of lobular carcinoma in situ. *Breast Cancer Res Treat*. (2022) 194:137–48. doi: 10.1007/s10549-022-06532-4

14. El Hanchi Z, Berrada R, Fadli A, Ferhati D, Brahmi R, Baydada A, et al. Bilateral breast Cancer. Incidence and risk factors. *Gynecol Obstet Fertil*. (2004) 32:128–34. doi: 10.1016/j.gyobfe.2003.01.002

15. Wang YA, Jian JW, Hung CF, Peng HP, Yang CF, Cheng HS, et al. Germline breast Cancer susceptibility gene mutations and breast Cancer outcomes. *BMC Cancer*. (2018) 18:315. doi: 10.1186/s12885-018-4229-5

16. Kotsopoulos J. Brca mutations and breast. *Cancer Prev* Cancers. (2018) 10:524. doi: 10.3390/cancers10120524

17. Baretta Z, Mocellin S, Goldin E, Olopade OI, Huo D. Effect of Brca germline mutations on breast Cancer prognosis: a systematic review and Meta-analysis. *Medicine*. (2016) 95:e4975. doi: 10.1097/md.0000000000004975

18. Byrski T, Gronwald J, Huzarski T, Grzybowska E, Budryk M, Stawicka M, et al. Pathologic complete response rates in young women with Brca1-positive breast cancers after neoadjuvant chemotherapy. *J Clin Oncol*. (2010) 28:375–9. doi: 10.1200/jco.2008.20.7019

19. Lee JM, Ledermann JA, Kohn EC. Parp inhibitors for Brca1/2 mutation-associated and Brca-like malignancies. *Ann Oncol*. (2014) 25:32–40. doi: 10.1093/annonc/mdt384

20. Kuchenbaecker KB, Hopper JL, Barnes DR, Phillips KA, Mooij TM, Roos-Blom MJ, et al. Risks of breast, ovarian, and contralateral breast Cancer for Brca1 and Brca2 mutation carriers. *JAMA*. (2017) 317:2402–16. doi: 10.1001/jama.2017.7112

21. Desai NV, Tung NM. Medical Management of Newly Diagnosed Breast Cancer in a Brca1/2 mutation carrier. *Breast J*. (2020) 26:1506–12. doi: 10.1111/tbj.13972

22. Li B, Xu W, Cao J, Guo D, Tao Z, Jin J, et al. A study of clinical and molecular characteristics in bilateral primary breast Cancer. *Cancer Med*. (2023) 12:15881–92. doi: 10.1002/cam4.6226

23. Vuoto HD, García AM, Candás GB, Zimmermann AG, Uriburu JL, Isetta JA, et al. Bilateral breast carcinoma: clinical characteristics and its impact on survival. *Breast J*. (2010) 16:625–32. doi: 10.1111/j.1524-4741.2010.00976.x

24. Li CI, Malone KE, Porter PL, Daling JR. Epidemiologic and molecular risk factors for contralateral breast Cancer among young women. *Br J Cancer*. (2003) 89:513–8. doi: 10.1038/sj.bjc.6601042

25. Nichol AM, Yerushalmi R, Tyldesley S, Lesperance M, Bajdik CD, Speers C, et al. A case-match study comparing unilateral with synchronous bilateral breast Cancer outcomes. *J Clin Oncol*. (2011) 29:4763–8. doi: 10.1200/jco.2011.35.0165

26. Irvine T, Allen DS, Gillett C, Hamed H, Fentiman IS. Prognosis of synchronous bilateral breast Cancer. *Br J Surg*. (2009) 96:376–80. doi: 10.1002/bjs.6553

27. Johnson L, Pinder S, Douek M. Multiple foci of invasive breast Cancer: can breast Mri influence surgical management? *Breast Cancer Res Treat*. (2011) 128:1–5. doi: 10.1007/s10549-011-1491-5

28. Hegarty C, Collins CD. PET/CT and breast cancer. *Cancer Imaging*. (2010) 10:S59–62. doi: 10.1102/1470-7330.2010.9031

29. Carloss H, Saab G. Breast Cancer and retroperitoneal metastasis. *South Med J*. (1980) 73:1570–1. doi: 10.1097/00007611-198012000-00009

30. Vega J, Ceriani A, Jensen D. Retroperitoneal fibrosis associated with malignancies: report of eight cases. *Rev Med Chile*. (2014) 142:791–8. doi: 10.4067/s0034-98872014000600015

31. Monev S. Idiopathic retroperitoneal fibrosis: prompt diagnosis preserves organ function. *Cleve Clin J Med*. (2002) 69:160–6. doi: 10.3949/ccjm.69.2.160

32. Kim J, Hwang JH, Nam BD, Park YW, Jeen YM. Mediastinal and retroperitoneal fibrosis as a manifestation of breast Cancer metastasis: a case report and literature review. *Medicine (Baltimore)*. (2018) 97:e11842. doi: 10.1097/md.0000000000011842

33. Huo Z, Gao Y, Yu Z, Zuo W, Zhang Y. Metastasis of breast cancer to renal cancer: report of a rare case. *Int J Clin Exp Pathol*. (2015) 8:15417–21.

34. Abrams HL, Spiro R, Goldstein N. Metastases in carcinoma; analysis of 1000 autopsied cases. *Cancer*. (1950) 3:74–85. doi: 10.1002/1097-0142(1950)3:1<74::aid-cncr2820030111>3.0.co;2-7

35. Ahmed Y, Aynaou M, El Houmaidi A, Mhanna T, Tombet C, Barki A. Breast Cancer metastatic to the kidney: case report. *Urol Case Rep*. (2020) 33:101302. doi: 10.1016/j.eucr.2020.101302

36. Cazacu SM, LD SĂ, Mitroi G, Neagoe DC, Streba C, Albulescu DM. Metastases to the kidney: a case report and review of the literature. *Curr Health Sci J*. (2020) 46:80–9. doi: 10.12865/chsj.46.01.11

37. Zhou C, Urbauer DL, Fellman BM, Tamboli P, Zhang M, Matin SF, et al. Metastases to the kidney: a comprehensive analysis of 151 patients from a tertiary referral Centre. *BJU Int*. (2016) 117:775–82. doi: 10.1111/bju.13194

38. Srisung W, Mankongpaisarnrung C, Warraich I, Sotello D, Yarbrough S, Laski M. Carcinoma of the lungs causing enlarged kidneys. *Proc (Baylor Univ Med Cent)*. (2015) 28:221–3. doi: 10.1080/08998280.2015.11929235

Frontiers in Medicine

Translating medical research and innovation into improved patient care

A multidisciplinary journal which advances our medical knowledge. It supports the translation of scientific advances into new therapies and diagnostic tools that will improve patient care.

Discover the latest Research Topics

See more →

Frontiers

Avenue du Tribunal-Fédéral 34
1005 Lausanne, Switzerland
frontiersin.org

Contact us

+41 (0)21 510 17 00
frontiersin.org/about/contact